N° d'ordre NNT : xxx

THESE de DOCTORAT DE L'UNIVERSITE DE LYON

opérée au sein de

L'Institut National des Sciences Appliquées de Lyon

Ecole Doctorale N° ED 162
Mécanique, Énergétique, Génie Civil, Acoustique

Spécialité de doctorat :
Mécanique – Génie Mécanique – Génie Civil

Soutenue publiquement le xx/02/2022, par :

Efoé Rodrigue WALLACE

On the rolling contact between multi-layered bodies, application to tire-pavement modelling

Devant le jury composé de :

David HILLS	Professeur	University of Oxford	Président
Giuseppe CARBONE	Professeur	Politecnico di Bari	Rapporteur
Antoine CHATEAUMINOIS	DR CNRS	ESPCI	Rapporteur
Anne MILLIEN	Maître de Conférences	IUT d'Égletons	Examinateur
Daniel NELIAS	Professeur	INSA-LYON	Dir. de thèse
Thibaut CHAISE	Maître de Conférences	INSA-LYON	Co-encadrant
Christophe PETIT	Professeur	Université de Limoges	Invité
Philippe REYNAUD	Maître de Conférences	IUT de Tulle	Invité

Département FEDORA – INSA Lyon - Ecoles Doctorales

SIGLE	ECOLE DOCTORALE	NOM ET COORDONNEES DU RESPONSABLE
CHIMIE	**CHIMIE DE LYON** **https://www.edchimie-lyon.fr** Sec. : Renée EL MELHEM Bât. Blaise PASCAL, 3e étage secretariat@edchimie-lyon.fr	**M. Stéphane DANIELE** C2P2-CPE LYON-UMR 5265 Bâtiment F308, BP 2077 43 Boulevard du 11 novembre 1918 69616 Villeurbanne **directeur@edchimie-lyon.fr**
E.E.A.	**ÉLECTRONIQUE, ÉLECTROTECHNIQUE, AUTOMATIQUE** **https://edeea.universite-lyon.fr** Sec. : Stéphanie CAUVIN Bâtiment Direction INSA Lyon Tél : 04.72.43.71.70 secretariat.edeea@insa-lyon.fr	**M. Philippe DELACHARTRE** INSA LYON Laboratoire CREATIS Bâtiment Blaise Pascal, 7 avenue Jean Capelle 69621 Villeurbanne CEDEX Tél : 04.72.43.88.63 **philippe.delachartre@insa-lyon.fr**
E2M2	**ÉVOLUTION, ÉCOSYSTÈME, MICROBIOLOGIE, MODÉLISATION** **http://e2m2.universite-lyon.fr** Sec. : Sylvie ROBERJOT Bât. Atrium, UCB Lyon 1 Tél : 04.72.44.83.62 secretariat.e2m2@univ-lyon1.fr	**M. Philippe NORMAND** Université Claude Bernard Lyon 1 UMR 5557 Lab. d'Ecologie Microbienne Bâtiment Mendel 43, boulevard du 11 Novembre 1918 69 622 Villeurbanne CEDEX **philippe.normand@univ-lyon1.fr**
EDISS	**INTERDISCIPLINAIRE SCIENCES-SANTÉ** **http://ediss.universite-lyon.fr** Sec. : Sylvie ROBERJOT Bât. Atrium, UCB Lyon 1 Tél : 04.72.44.83.62 secretariat.ediss@univ-lyon1.fr	**Mme Sylvie RICARD-BLUM** Institut de Chimie et Biochimie Moléculaires et Supramoléculaires (ICBMS) - UMR 5246 CNRS - Université Lyon 1 Bâtiment Raulin - 2ème étage Nord 43 Boulevard du 11 novembre 1918 69622 Villeurbanne Cedex Tél : +33(0)4 72 44 82 32 **sylvie.ricard-blum@univ-lyon1.fr**
INFOMATHS	**INFORMATIQUE ET MATHÉMATIQUES** **http://edinfomaths.universite-lyon.fr** Sec. : Renée EL MELHEM Bât. Blaise PASCAL, 3e étage Tél : 04.72.43.80.46 infomaths@univ-lyon1.fr	**M. Hamamache KHEDDOUCI** Université Claude Bernard Lyon 1 Bât. Nautibus 43, Boulevard du 11 novembre 1918 69 622 Villeurbanne Cedex France Tél : 04.72.44.83.69 **hamamache.kheddouci@univ-lyon1.fr**
Matériaux	**MATÉRIAUX DE LYON** **http://ed34.universite-lyon.fr** Sec. : Yann DE ORDENANA Tél : 04.72.18.62.44 yann.de-ordenana@ec-lyon.fr	**M. Stéphane BENAYOUN** Ecole Centrale de Lyon Laboratoire LTDS 36 avenue Guy de Collongue 69134 Ecully CEDEX Tél : 04.72.18.64.37 **stephane.benayoun@ec-lyon.fr**
MEGA	**MÉCANIQUE, ÉNERGÉTIQUE, GÉNIE CIVIL, ACOUSTIQUE** **http://edmega.universite-lyon.fr** Sec. : Stéphanie CAUVIN Tél : 04.72.43.71.70 Bâtiment Direction INSA Lyon mega@insa-lyon.fr	**M. Jocelyn BONJOUR** INSA Lyon Laboratoire CETHIL Bâtiment Sadi-Carnot 9, rue de la Physique 69621 Villeurbanne CEDEX **jocelyn.bonjour@insa-lyon.fr**
ScSo	**ScSo*** **https://edsciencessociales.universite-lyon.fr** Sec. : Mélina FAVETON INSA : J.Y. TOUSSAINT Tél : 04.78.69.77.79 melina.faveton@univ-lyon2.fr	**M. Christian MONTES** Université Lumière Lyon 2 86 Rue Pasteur 69365 Lyon CEDEX 07 **christian.montes@univ-lyon2.fr**

*ScSo : Histoire, Géographie, Aménagement, Urbanisme, Archéologie, Science politique, Sociologie, Anthropologie

Abstract

The purpose of this thesis has been the development of a dimensioning tool for pavement design. In order to better understand their surface degradations (mainly rutting and cracking), a modelling study is carried out. This modelling task has been performed with contact mechanics tools. Particularly, a semi-analytical model has been developed, based on Fast Fourier Transform (FFT) and Conjugate Gradient Method (CGM) algorithms. With view to achieve a more realistic modelling of the tire-pavement contact, the focus has been put on three aspects of the contact problem.

Firstly, the multi-layered aspect of the pavement has been considered. Using the Papkovich-Neuber potentials, the influence coefficients have been found in the Fourier frequency domain. A numerical inversion using FFT algorithms has allowed to find the influence coefficients in the space domain.

Secondly, the viscoelastic behaviour of asphaltic materials, used in roads construction, has been accounted. To this aim, an Elastic/Viscoelastic correspondence has been proposed. This correspondence imposes to recalculate the influence coefficients at every time step. These additional calculations imply an increase of the computation time; however, the simulations remain straight and fast. In addition, the proposed correspondence is exact in some cases (especially in steady-state regime); and it is an approximation in the other cases where the committed error has been shown to be marginal.

Thirdly, the effects of the tangential overall forces have been integrated to the rolling contact. The goal is that the present tool can be able to simulate acceleration, braking, turnaround, etc. cases where tangential forces and/or moment are applied on the wheel in addition to the normal force (which is generally the weight of the car or truck). This tractive rolling contact has been solved between elastically dissimilar bodies submitted not only to tangential forces but also to a spinning moment.

All these aspects, introduced together in the model, have allowed to perform various parametric analyses for a better grasp of their influence on general contacts. Furthermore, an application of the developed model has allowed to simulate realistic cases of rolling contact between the tire and the pavement. From examples such as acceleration, turnaround and drift, it has been proven that the tangential forces increase significantly the overall stresses.

Contents

Introduction

Maintenance of roads in cities implies both economical and ecological considerations. Indeed, in 2015 in France, 15 billions of Euro have been dedicated to the maintenance of road pavements in cities. Meanwhile, the bituminous materials used for road construction, are petroleum based. Thus, road construction processes generate pollution and high energy consumption. In this socio-economical and ecological context, the MACADAM project, supported by the ANR[1], aims at coupling experimental investigations from civil engineering, with numerical modelling from mechanical engineering, for a better understanding of the surface degradations of pavements.

MACADAM project

The MACADAM project has been initiated in 2017 by the laboratories GC2D[2] and LaMCoS[3] which are respectively from civil engineering and mechanical engineering. The project has two main goals:

- The first part is the conception of a modelling tool for the dimensioning of the surface of road pavements. It is endorsed by the LaMCoS which is specialised in developing efficient modelling tools for contact mechanics.
- The second part concerns an experimental platform for the qualification and the validation of industrial processes. This task is performed in the laboratory GC2D which is competent in civil engineering for roads and experimental research on the topic.

The first task of this project holds because the current methods, for the dimensioning of pavements, are unable to explain the early surface degradation of pavements. In fact, the actual normalised dimensioning method in France is based on the ALIZE software which makes the dimensioning at the base of layers without

[1]Agence Nationale de Recherche
The ANR financially supports the MACADAM project under the reference ANR-17-CE22-0 0 06-02.

[2]Laboratoire de Génie Civil, Diagnostic et Durabilité, Université de Limoges.

[3]Laboratoire de Mécanique des Contacts et des Structures, INSA Lyon.

solving the contact. Morevover, it only takes into account a normal force distributed over an idealised footprint. This dimensioning method has two flaws that it is important to underline.
On one side, using idealised footprints implies an uniform distribution of the applied stresses at the surface; and thus, the singularities of the real tire profiles which generate peaks of stress, are not considered. On the other side, applying only a normal load means to neglect the tangential loads. However, it is easy to remark that degradation of pavements are emphasized in transient phases of rolling (traffic lights, roundabout, etc.).

The present PhD work, performed in the LaMCoS, constitutes the first task of the MACADAM project.

The Modelling task of the MACADAM project

Degradations observed at the surface of road pavements are due to repeated solicitations from cars and trucks. Those solicitations occur under changing environmental conditions (seasons cycle, temperature, freeze-thaw cycles, etc.). Since roads are exposed to those various types of attacks, various physics are involved in their fatigue. The present work focuses on the mechanical aspects.

In this scope, the conception of a road pavement for a chosen life cycle imposes a modelling step during the process. To this aim, the civil engineer in charge of the conception is required to use a conception tool which has to be efficient and precise. The actual existing tools do not always show simultaneously these two important characteristics. Indeed, efficiency allows the engineer to make quickly all the calculations needed for a good dimensioning. Meanwhile, the precision is mandatory for building roads for the desired life cycle. Nowadays, the precision of the road conception software has appeared to be good except in the zone close to the surface.

Drawn from the above observations, the present study aims at building an efficient and precise tool which will allow to perform a good modelling including in the zone close to the road surface. For this purpose, modern contact mechanics tools are called upon. Since contact mechanics is completely dedicated to the development of tools for the understanding of contact between bodies, it is ideal for this topic. Then, a fast and efficient method for modelling the contact between the tire and the pavement is developed by coupling analytical solving with numerical techniques.

Therefore, in the present work, this civil engineering topic is treated as a mechanical problem with contact mechanics tools. The emphasis is put on three main aspects. Firstly, the multi-layered structure of the pavement is modelled. Secondly, the viscoelastic behaviour of the bodies in contact is taken into account. This is important for accounting the viscous behaviour of the asphaltic materials widely used in the road construction. Finally, the effects of the transient tractive rolling contact are highlighted. Previous researches have shown that the shear effects can

be significant even in a rolling motion. Thus, they must not be neglected as it is done currently in the pavement field.
Those aspects are treated throughout this document following the structure described below.

Manuscript outline

In the first chapter, a bird-eye view is given for the pavement field. The history of the tire-pavement modelling is presented. The experimental challenges through the history, as well as the actual modelling requirements are reviewed. The modelling of the tire-pavement contact are grouped into elastic modelling, viscoelastic modelling, dynamic modelling and other modelling containing non-linearities. In addition, the various methods used for those modelling are highlighted. Further, a general presentation of contact mechanics is performed with a particular interest put on the rolling contact.
The following chapters focus on the modelling where either material properties (elastic or viscoelastic), half-space structure (homogeneous, single layered, multi-layered) or type of loading (free rolling, tractive rolling, fretting) are changed and/or combined (see Fig. 1).

In the second chapter, the general method used throughout the present work is presented. The general contact problem is solved. The normal and the tangential contact problems are solved with a semi-analytical method. In this respect, Fast Fourier Transform (FFT) and Conjugate Gradient Method (CGM) algorithms are used as acceleration techniques. For the validation, classical partial slip problem are simulated and compared to analytical results.

The chapters 3 and 4 are dedicated to the contact between viscoelastic layered bodies. In chapter 3, the influence coefficients for a single layered half-space are determined. Using Papkovich-Neuber potentials, those influence coefficients are found in the Fourier frequency domain. Then, a numerical inversion is performed for finding them in the space domain. Further, after a brief introduction to viscoelasticity, an Elastic/Viscoelastic correspondence is proposed. In this way the contact between viscoelastic single layered bodies can be solved.
An extension of the works of chapter 3 is done in chapter 4 for multi-layered bodies. In the latter chapter, the influence coefficients are found for a multi-layered half-space. For this purpose, a matrix system is constructed and numerically solved in the frequency domain; and a numerical inversion is made.

In chapter 5, the rolling contact is analysed with the contact shear tractions effects. The so-called tractive rolling contact is solved in both transient and steady-state regimes. From the Kalker's theory, the present numerical tools allow to propose a fast and efficient algorithm for solving the problem. The proposed algorithm allows to impose not only tangential forces, but also a spinning moment. Moreover, the tractive rolling contact is solved between elastically dissimilar and multi-layered

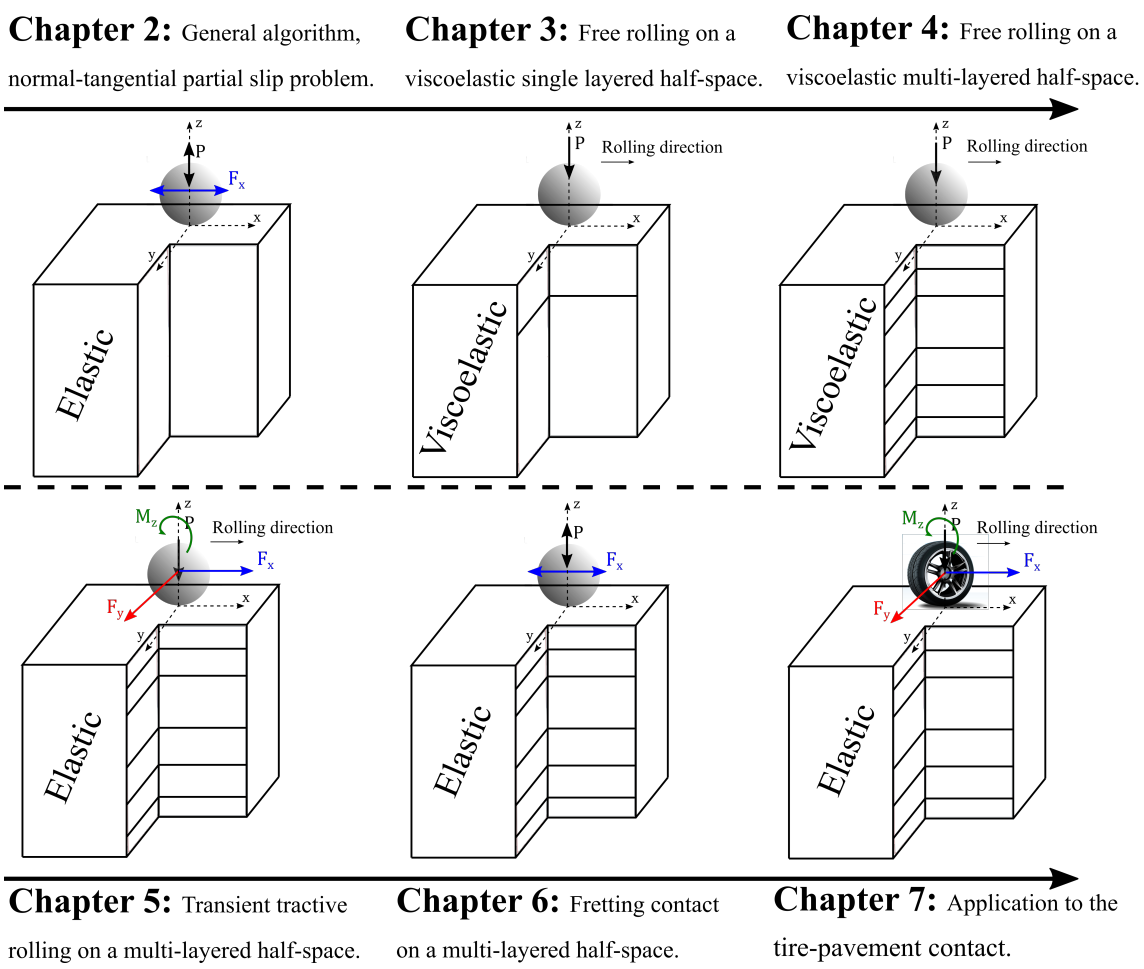

Figure 1: Summary of the manuscript outline.

bodies.

In the following chapter 6, the fretting contact problem is tackled between multi-layered bodies. The effects of a coating on the fretting contact is analysed through the observation of both contact surface and coating/substrate interface. The Spence and Cattaneo-Mindlin shifts are computed for multi-layered bodies, as well as a fretting loop in mode I.

In the last chapter, the developed model is applied to the tire-pavement modelling. The effects of real tire and real surface profiles are investigated. Further, the tractive rolling contact is simulated with a real tire profile on the pavement. Realistic cases (acceleration, turnaround, drift) are studied. Finally, an experimental validation is performed.

Chapter 1

Bibliography

In this chapter, the background of the present study is given. Firstly, the context of the study is drawn out from the historical considerations to the practical actual challenges. This being done, a review of the literature is performed. Finally, a brief introduction to the contact mechanics science is given, with a special view on the numerical methods in the field.

Sommaire

1.1 Context of the study

Roads certainly exist since animals and humans move. The first roads formed naturally because of the need to move from one point to another, avoiding obstacles and dangers. The pre-modern roads were built in the context of trades between people from different places. Those roads were paved soil, beaten-earth or made of crushed gravel. The road construction field which rose in the late Middle Ages, reached a key milestone with the industrial revolution (1800s).

In France, in 1764, Pierre Marie Jérôme Trésaguet brought a scientific eye to the road construction. He found out that the deeper layer of the road transfers all the charges to the ground. Thus, there was a need to add a coating to the road structure in order to protect the sub-layers.
In 1815, in England, John Loudon McAdam proposed to crush stones so that they have a specific size before introducing them in a mix of sand and water. This technique had a great impact by reducing the deterioration of roads under more traffic and heavier loads.
In the 1900s, with the beginning of democratisation of cars, there was a need for more and more roads. In the meantime, world wars allowed a terrific increase of roads and highways. From then, the road pavements have been improved in term of structure (engineer and scientists tried to adapt the conception to the usage) and in term of material (introduction of new materials, mix of materials; development of the material science).

Besides, the history of tires is definitely related to the industrial revolution. The first tire seems to have been invented by Robert William Thomson in 1845, but with no success at that time. In 1888, John Boyd Dunlop applied for the first pneumatic's patent [DUN 49]. His idea consisted in taking advantage of the vulcanisation of rubber, developed by Charles Goodyear in 1841 [COR 13], in order to change the full tire of bicycles by pneumatics full of air. That innovation brought out the tire type that is still known today. Further, industrials tried to optimise and to adapt tires to their different usages, and to reach better performances. In this respect, the shape, the surface profile as well as the materials have been improved to become the tires used today.
Evidently, the progress is continuing; and in 2021, in the numerical and smart technologies era, the improvement is not ended yet. Many firms are working on airless and smart tires such as Michelin Uptis [MIC 19], Goodyear Aero [GOO 19], Hankook Hexonic [HAN 18], etc. (see Fig. 1.1).

Finally, in the actual state, the development of the material science for roads and the efforts made for a better conception of roads are undeniable. Nevertheless, it seems that the pavement field is still lagging behind.
Figure 1.2 shows some of the many failures that one can observe at the surface of road pavements. The most commonly observed failures are cracking and rutting. For cracking, there are two frequently observed modes: the longitudinal cracking and the transversal cracking. The longitudinal cracking (in Fig. 1.2(a)) is the cracking of

Figure 1.1: Innovative tire projects. From left to right, Michelin Uptis [MIC 19], Goodyear Aero [GOO 19], Hankook Hexonic [HAN 18].

the road pavement in the rolling direction. Even if its origin is not clearly identified, the longitudinal cracking is generally said to be due to frost action, different volume changes in sub-layers or fatigue coming from an under-dimensioning. Meanwhile, the transversal cracking in Fig. 1.2(b) appears in the transverse direction to the rolling. This type of cracking is said to come from down to top and caused by thermal effects or localised weaknesses of the structure. As result of the combination of the longitudinal and the transversal cracking, one can observe what is called map cracking in Fig. 1.2(c).

Furthermore, rutting (see Fig. 1.2(d)) is frequently observed at the surface of road pavements. It is a permanent deformation of the road, also due to an under-dimensioning of the layers of the pavement structure.

Many other failures can appear on the roads as a result of other physical phenomena impacting the structure. In order to reduce the appearance of those failures, the present study aims at setting up a mechanical modelling for the development of a conception tool for civil engineers. The study focuses on road pavement structures since the goal is to reduce their degradations.

In fact, the conception of a road pavement involves the choice of a type of road structure, the analysis of operating conditions in order to determine the best materials, and then the choice of the right thicknesses for the layers. The engineer's goal is not to create new materials or to create new structure types. The previous engineering works coupled with experience and research works have lead to various indexes of possible pavement structures and existing materials. From a country to another, specific norms are used to select structure types corresponding to a set of criteria. Thus, the engineer is required to choose the best structure type for the application and then to play with the parameters in order to meet the requirements. In the present research work, the focus is put on developing a general tool which can be used to make calculations for any type of pavement structure and thickness of layers. This tool is intended to integrate a dimensioning method.

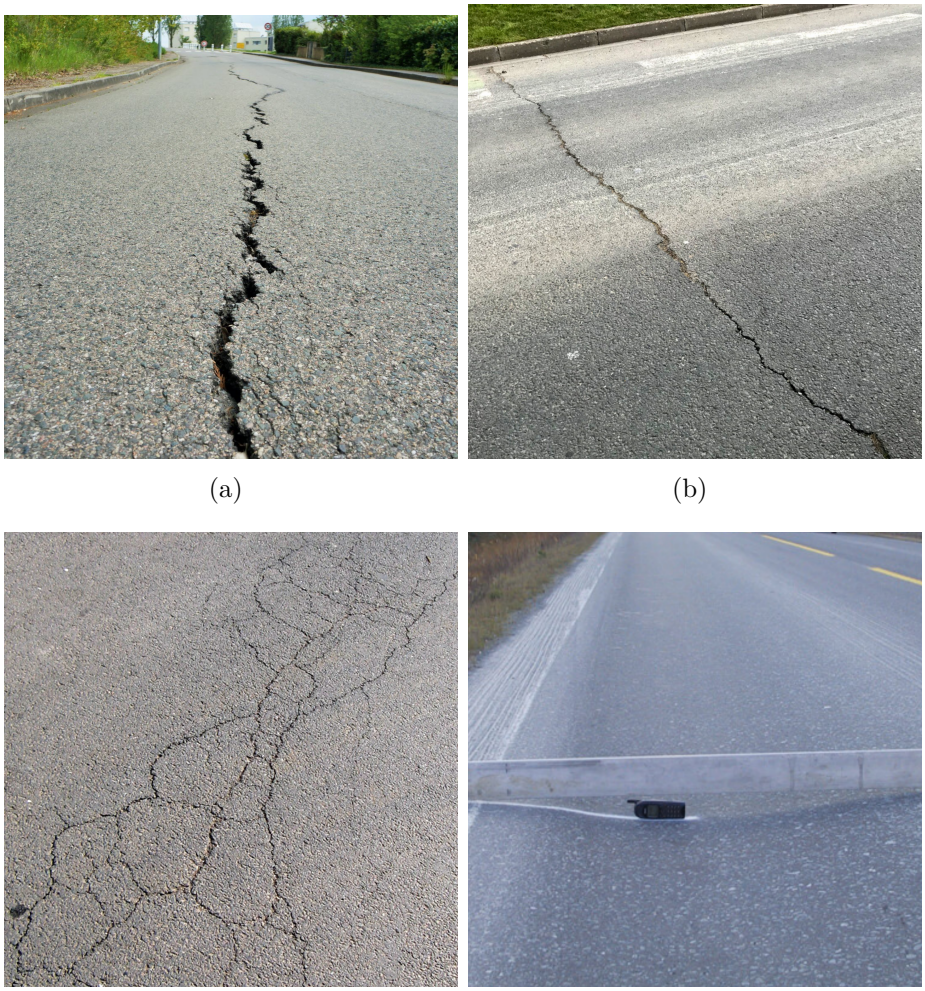

(a) (b)

(c) (d)

Figure 1.2: Some failures on the surface of road pavements. a) Longitudinal cracking; b) Transversal cracking; c) Map cracking; d) Rutting.

Therefore, in this chapter, a bird-eye view of the pavement field is given. Firstly, the general structure of road pavements is described, with a particular look on "flexible pavements". Secondly, the way those pavements are designed in a construction process is described. Further, a review of the literature concerning the tire-pavement topic is given with view to precise the domain on which this work holds. In a final section, generalities and a small review are given for the contact mechanics field which is the bedrock of the present study.

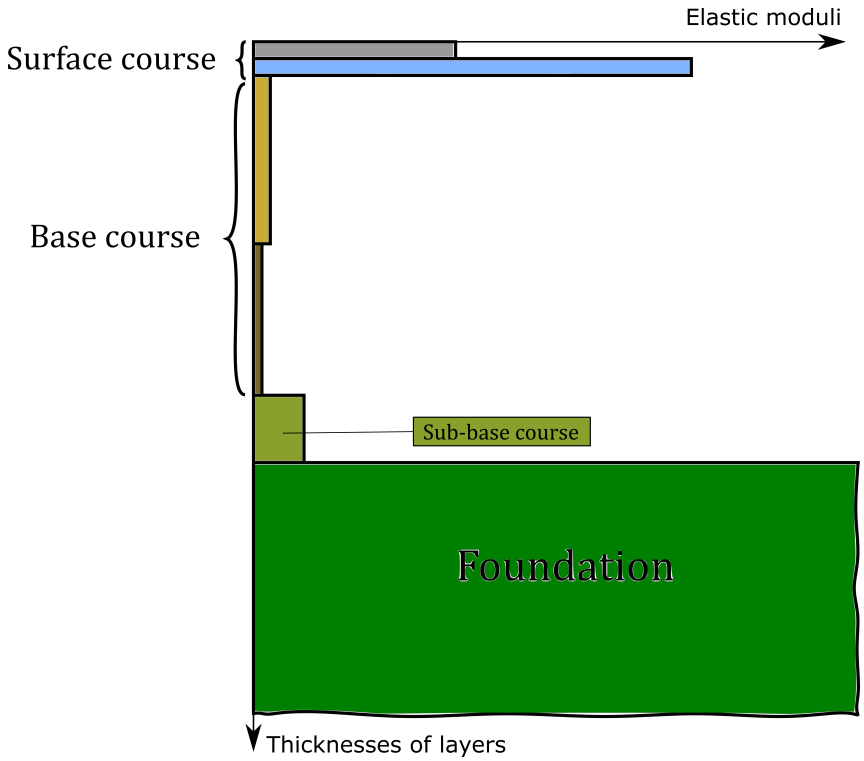

Figure 1.3: Flexible pavement structure. Average elastic moduli in the horizontal axis versus average thicknesses in the vertical axis.

1.2 Structure of road pavements

A road pavement is a multi-layered structure which consists of a certain number of layers lying or bounded to a soil or a foundation (see Fig. 1.3). In general, a distinction is made between *flexible* and *rigid* pavement structures. The *flexible pavements* consist of stone or gravel layers covered with asphaltic concrete, while the *rigid pavements* are made of an assembly of concrete layers on a foundation. For specific applications, engineers can combine rigid and flexible pavements components.
Whatever the case, road pavements are multi-layered structures, and thus it makes no difference in term of mechanical modelling if not only parametrisation. In the present work, flexible pavements are taken as the reference structure.

From the top to the bottom, a typical flexible pavement (see Fig. 1.3) structure consists of:

1. *Surface or wearing course:* it is the part of the pavement structure which is directly exposed to traffic. It is, most of the time, made of multiple layers. In one hand, this course is designed to resist to the abrasive effect of the traffic, the thermal attacks due to climate, accidental punchings, etc. In another hand, the wearing course should assure comfort to the user by having good adherence, evacuating water, limiting noise and being well integrated to the architectural

environment in cities. For the surface course, good quality aggregates and high dense bitumen or asphalt are recommended.

2. *Base course:* it is the main supporting layer for the transfer of stresses to the ground. The base course provides the required foundation stiffness and structural strength. It consists of a single or multiple layers placed on a sub-base, or lying directly on the foundation if a sub-base is not used. It aims at providing a uniform and stable support to the surface course. The base course is made of good quality crushed aggregates in line with technical specifications. If the crushed aggregate does not meet the required criteria it can be stabilised with cement, lime, or asphalt.

3. *Sub-base course:* this optional layer comes to strengthen the sub-grade and provides an answer to some functional requirements. In fact, it prevents the entry of finely graded sub-grade soil to the base course layer, prevents the capillary rise of water and enables free drainage of the water entering the pavement. It also provides insulation to sub-grade against frost and is used for raising the heights of pavements to be in line with the natural water table. Note that the sub-base course is optional since its use depends on the strength of the foundation. Thus, its usage might be limited to an adjusting layer.

4. *Sub-grade, road bed or pavement foundation:* it is the natural soil on which the pavement rests. It is the natural foundation made of the compacted, locally available, strong material.

In this study, three important mechanical aspects of the tire-pavement contact are taken into account: the multilayered characteristic of the pavement, the frictional effects in the contact and the viscoelastic behaviour of the pavement.
The latter aspect is due to the fact that the materials used for the construction of the pavement contain asphalt materials. Asphalt materials, also called bituminous materials, are sticky and highly viscous liquid or semi-solid forms of petroleum. They are mixed with aggregates and used as materials in the construction of pavements. In France, among the wide range types of asphaltic pavement structures that exist, four are mainly used: *flexible pavements*, *thick asphalt pavements*, *composite pavements* and *inverted pavements* [SET 94] (see Fig. 1.4).

This wide usage of asphalt materials in the pavement imposes to question the impact of their viscous behaviour on the general behaviour of the pavement structure. The answer to this question demands to model the viscoelasticity throughout the study.

Finally, the above summarised illustration of a flexible pavement known, the dimensioning can be performed. Generally, it is the job of a civil engineer to handle this conception. For building a road, not only the mechanical aspects have to be ensured, but also economical, environmental and social aspects. The socio-economical discussions are generally prior to the technical dimensioning. In the next section,

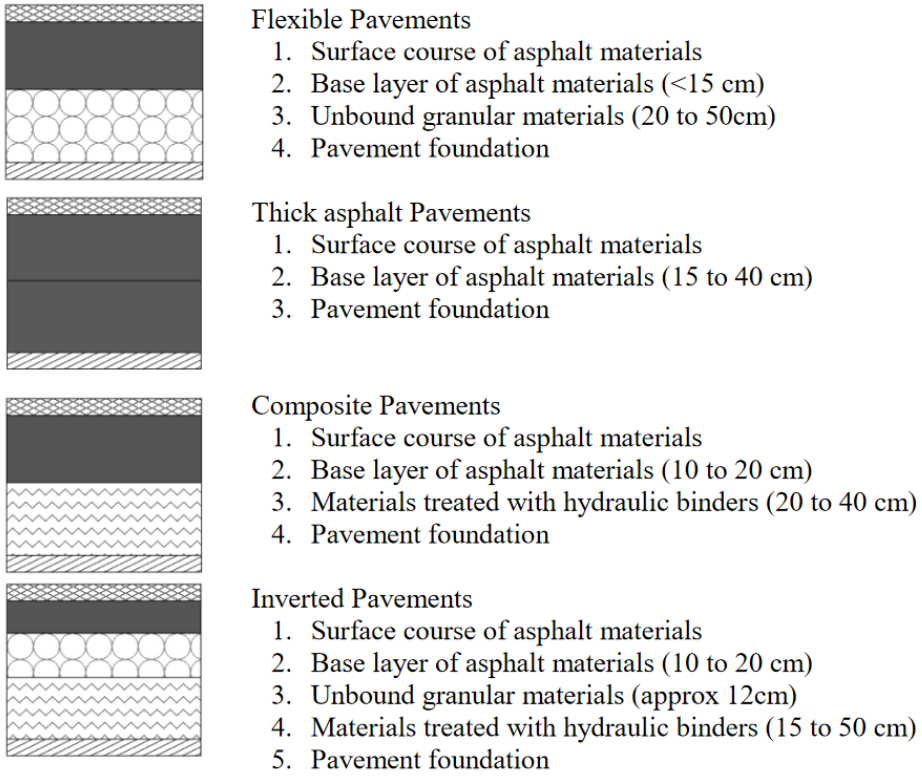

Figure 1.4: The different French asphalt pavements [SET 94].

the technical dimensioning of flexible pavement is discussed through various methods from different countries.

1.3 Flexible pavements dimensioning

Flexible pavements are the most used for big traffic zones. Their dimensioning is chosen here to exemplify the dimensioning of pavements. Note that the dimensioning of pavements may occur in rehabilitations cases also.
First of all, some commonly used dimensioning criteria are given. Then, normalised methods from several countries are examined.

1.3.1 The dimensioning criteria

The dimensioning of pavements is performed according to a set of criteria. A road pavement in the center of a city should not be build as highway; nor a road in France as one in Togo according to the cultural use of the structures and to the environmental conditions. The choice of the structure of a pavement regards a certain number of criteria related to the norm used by the engineer. Although, this

choice depends on the dimensioning method, some criteria are common to all the methods:

1. *The quality of the sub-grade*: the strength of the natural foundation available is to be verified by measuring the deflection under an applied normalised load. The deflection is the normal displacement at the surface induced by the loading. For new pavements, the deflection indicates directly the strength of the foundation; while in the case of rehabilitations, the original deflection (before the first pavement) is influenced by the remain courses.

2. *The service life*: it is a time generally between 10 and 50 years, function of the builder's strategy. This time depends on the investment and the maintenance strategies of the builder. The road is built to last for a service life time without any big rehabilitation work. In the strategy of the builder, the service life is coupled with the risk in calculation with regard to economical considerations.

3. *The risk in the calculations*: it is the probability (of risk) that a disorder appears in the pavement before the end of the service life. For a road built for a life time of 30 years for example, the road is not supposed to assure a perfect service for 30 years and then brutally break after the life service time. Of course, some damage will appear in the road before, without demanding to carry out a lot of maintenance work. A risk of 5%, for example, means that during the life time, there is 95% chance that no structural disorder will appear in the pavement. According to the initial investment, the builder chooses a couple service life-risk in the calculations that brings a corresponding "level of service". For instance, if the initial investment is high, corresponding to a high service life (20-30 years for example), a low risk will be taken. On contrary, for the same demand of service life, if the initial investment is low, the risk will be high with consequence that the traffic will be frequently interrupt for maintenance.

4. *The traffic*: it is often considered as the number of vehicles over a specific period. In the French method, it is the number of heavy vehicles per day in a year for a way and a direction. In UK, the design traffic is expressed in terms of millions of standard axles over the number of years for which the pavement is designed. For every country, there is a norm of the admissible charge of the axle and a maximum charge to be considered for a heavy vehicle.

5. *Climate and environmental conditions*: they are as various as impacting. The water status of the sub-grade, the seasons cycle, the temperatures, the freeze-thaw cycles, etc. have an undeniable impact on the overall resistance, deformability and durability of the pavement.

The above criteria are mainly based on the french dimensioning (see [SET 94]) but appear to be common in some way to many dimensioning methods.

1.3.2 Some dimensioning methods

The American Method The Americans were the first to rationalise the dimensioning process by performing experiments for the pavement design. From data gathered in the famous AASHO[1] Road Test [BOA 62], many reports have been made with view to use those data to improve the design of road pavements. The resulting book for the design engineer is the Mechanistic-Empirical Pavement Design Guide (MEPDG) by the AASHTO in 2008 [AAS 08]. In the MEPDG, the design is exposed as "an iterative process -the outputs from the procedure are pavement distresses and smoothness, not layer thicknesses". Three stages are to be considered:

- ✔ *Evaluation*: the site is investigated, soil properties are evaluated, environment and climate conditions are analysed as well as the traffic. In the case of rehabilitation, existing materials are re-evaluated and distress surveys are performed.
- ✔ *Analysis*: the engineer selects a trial design strategy. Stresses, strains, deflections and incremental damage are calculated. Then, the engineer can verify if the pavement meets the criteria. A reliability analysis is performed using developed models. If the criteria are not met, the design features or materials are modified and the process is started over. This step is repeated as needed until the performance criteria are met. When they are met, the trial design becomes a feasible design.
- ✔ *Strategy selection*: this step consists in analysing the engineering and constructability, evaluating the costs, the viability and the life-cycle of the chosen feasible strategy.

The British Method The British method is also based on an empirical approach which has been coupled further with the theory of structures and the material science. The reference documents for the pavement conception in United Kingdom are the "Design Manuel for Roads and Bridges"(DMRB) by the Highways Agency in 2006 [AGE 06]. In the DMRB, one can find a suit of reports concerning the requirements and advices for pavement design, maintenance, operation and disposal. The reports embody results from research and practical experience of constructing and operating. The dimensioning method described in the version of 2006 of the DMRB is a quite simple method for flexible, semi-rigid and rigid pavements. The graphs allow the engineer to find the thicknesses of the layers with regard to the traffic and the materials chosen for a type of pavement structure.

The South African Method The pavement dimensioning in South Africa began in 1970 with the South Africa Mechanistic Design Method (SAMDM). In an overview

[1]The American Association of State Highway Officials (AASHO) was renamed the American Association of State Highway and Transportation Officials (AASHTO) on November 13, 1973.

published in 1996, Theyse et al. [THE 96] have drawn the constitutive elements of the procedure. The design process in the SAMDM starts with the load and material characterisation. For each layer, the thickness and the elastic properties are found; and the structural analysis is performed. The pavement response in term of stresses and strains is then found at the critical positions of the structure. The response of the pavement structure serves as input to the transfer functions which allow to predict fatigue life, crack initiation, permanent deformations. This procedure is repeated by changing the materials, thicknesses of layers until the requirements are met.

The French Method In France, the dimensioning of pavements structures had begun in the 1950s, with empirical methods and some elements taken from the American method. In the meantime, the calculation of the critical stress in the pavement structure for the design, has been a real challenge. The evolution of the models used to do so is summarised below.

- **The model of Boussinesq (1885)**: The first model used for designing the pavements is the model of Boussinesq [BOU 85] which considers the pavement as a homogeneous half-space. The model of Boussinesq, developed to solve contact problems in solid mechanics is a good starting point for the road design. The idea is to determine a criteria at a depth z considered as the thickness of the top layer of the pavement structure. One may note that it is highly unrealistic to think the pavement structure as a homogeneous half-space.

- **The Westergaard's model (1926)**: Further, single layered structures have been proposed for the design. In this spirit, the Westergaard's model [WES 26b, WES 26a, WES 27] has been the first bi-layer model to be used. It consists of a plate resting on a ground which is considered as a set of springs. The interaction between the plate and the ground is represented by a proportionality relation. The model developed by Westergaard has been used by the U.S Bureau of Public Roads (in the USA) for investigations on the structural behaviour of concrete pavements. By comparing the critical corner stress obtained with the model and the measurements, it has been found that the Westergaard's formula always gives too small stress [HUA 04].

- **The Hogg's model (1938)**: The model developed by Hogg [HOG 38, HOG 44] is a bi-layer consisting of a plate resting on the Boussinesq half-space model. The plate is supposed to simulate the rheological behaviour of the pavement, while the half-space represents the ground.
  In the same way as the Westergaard's model, the plate theory is used to determine the tensile stress using the vertical displacements at the base of the plate. Thus, the result is applied to the half-space of Boussinesq.

❖ **The Burmister's model (1945)**: Burmister [BUR 45c, BUR 45a, BUR 45b] has treated the problem of an elastic layer resting on a half-space. Here, the layer is not a plate but an elastic solid. Further, the model has been extend to any n layers resting on a half-space. The french software Alizé-LCPC, developed by the "Laboratoire Central des Ponts et Chaussées (LCPC)" is based on the model of Burmister. Following the mechanical solution exposed above, stresses and strains are calculated and then compared to the admissible ones for the desired application. In addition, a reverse calculation has been developed so that equivalent moduli can be found from a normal displacement at the surface. The french method of dimensioning uses very widely the Alizé software for its quickness, the materials library and its relative simplicity. However, it presents some limitations such as:

- the loading considered is not the real profile of the tire but idealised footprints as contact zone,
- only a normal load is applied i.e. the tangential effects are not considered,
- the pavement is purely elastic.

Note that by the end of the 1950s, the model of Jeuffroy-Bachelez [JEU 62] had been very important in the design of pavements in France. This model is combination of the Hogg's model and the Burmister's model. In the Hogg's model, instead of applying the desired deflection to the half-space of Boussinesq, it is applied to the Burmister single layered half-space. Although this model does not seem relevant since it is possible in theory to have any number of layers with the Burmister's model, it had been very useful. In fact, in 1955, this model uses a bi-layer of Burmister since computation tools were not developed enough. Thus, it was a good alternative to set a plate resting on a layered half-space to have a tri-layer. The resulting tri-layer structure allowed to establish very complete abacus tables for engineers.

Furthermore, in 1971, a system of pre-computed index and validated with experiments, had been approved for the dimensioning method. The so-called "Catalogue des structures types de chaussées neuves" has been improved to reach its edition of 1998 [SET 98]. This revised edition is based on the "Conception et dimensionnement des structures de chaussées" [SET 94] which embodies the knowledges from the various stakeholders of the road topic in France. It is very important to cite the technical guide of the Sétra-LCPC (2003) [SET 03] which defines the criteria for the evaluations by the administration. The index of 1998 and the technical guide of 2003 are together the main documents of the French dimensioning method.
Nowadays, in the French dimensioning method, a pavement structure type is chosen according to the above documents and a pre-dimensioning is performed. Then, the dimensioning is done using the software Alizé which is based on the elastic Burmister's model for an indefinite number of layers. The goal of the calculations is to find the right thicknesses of the layers in order to support the charges during the life

cycle of the structure. The last step of the dimensioning is to verify the freeze-thaw of the pavement structure because the thaw of a huge quantity of water can mess the foundation. The reader may refer to the report of Berthier [BER 09] for more general informations on the French dimensioning method.

In summary, many dimensioning methods have been erected by responsible authorities in countries for conception and rehabilitation of pavement structures. All those methods are generally based on empirical observations, experimental and modelling research works. The contribution of research works to the progresses in the pavement conception field has been and is still significant. In the following section, a review of the literature is performed around this tire-pavement topic.

1.4 Tire-pavement in the research literature

In the history of physics, the first step has often been observation. According to the present tire-pavement subject, the observation of degradations on roads built by experience, brought out the need for a better understanding of those failures. From experience, experimental works have been carried out for a better grasp of those degradations. In the following lines a focus is put on some of the experimental works done in the early development of the tire-pavement field, as well as some innovative tests which have followed.

1.4.1 Tire-pavement Experiments

Before 1958, road pavements conception had been made with empirical methods based on observation of previous road pavements behaviour. Between 1958 and 1960 in the United States of America (precisely in Ottowa, Illinois), the American Association of States Highway Officials (AASHO) performed the first full-scale experiments for the tire-pavement conception(see Fig. 1.5). The so-called AASHO Road Test, was performed in specific environmental conditions, for a certain number of axle configurations, tire pressures, axle settings, and 1.1 million axle load repetitions [BOA 62]. The AASHO Road Test results have been largely used inside and outside of the USA. It is quite famous and is considered as the first data base for the dimensioning methods.

In the USA, other tests have followed such as the Westrack project [noa02], the Minnesota Road Research Project (Mn/Road) and the National Center for Asphalt Technology (NCAT) Test Track (Brown et al. [BRO 02]). Each of those tests had aimed to gather new informations for various environmental conditions and for different pavement structure types. Moreover, the performance of pavement structures under moving loads is analysed. For instance, the gathered data from the AASHO road test concern cracking (the amount of cracking at the pavement surface at a given time, rutting (the rut depth), pumping (the ejection of water and sub-base

material or embankment soil from beneath the pavement surfacing), displacements at the surface (slope, deflection, etc.), effects of frost, etc.

Figure 1.5: AASHO Road Test. Example of experiment comparing the effects of a low pressure-low silhouette tires (left) and conventional tires (right). [BOA 62]

In the meantime, following this novelty, innovative tests have been introduced throughout the world. One of the major challenges was to capture experimentally the stresses at contact interface. To achieve this goal, some innovative tests and sensors have been thought and built up.

For measuring the contact pressure distribution beneath a statically loaded truck, Marshek et al. [MAR 86] developed an experiment using a pressure sensitive film (see Fig. 1.6). The film consists of a coating with ink bubbles and a photocell which is able to read the intensity of the blots left by the ink bubbles burst under the pressure of the tire. Using the apparatus, the authors have highlighted the effect of the inflation on the pressures. It comes for example that the high inflation of the tire induces the move of the peak pressures from the tire shoulder toward the centerline.

The previous observations have also been made by Tielking and Abraham [TIE 94] by using another testing apparatus. They measured the contact stresses using triaxial load sensors in order to have the complete stress profile. The advantage in this case is the measurement of shears in the contact zone.

Further, the experiments have aimed at measuring the contact pressures and shears but for moving load. In this scope, de Beer et al. [BEE 96] developed the Vehicle-Road Surface Pressure Transducer Array (VRSPTA) system in association with the Laboratory of Advanced Engineering of the University of Pretoria, to measure vertical, longitudinal and transverse stresses at the surface of the pavement. The VRSPTA has allowed to record longitudinal and lateral stresses for a moving wheel in full scale experiments (see Fig. 1.7).

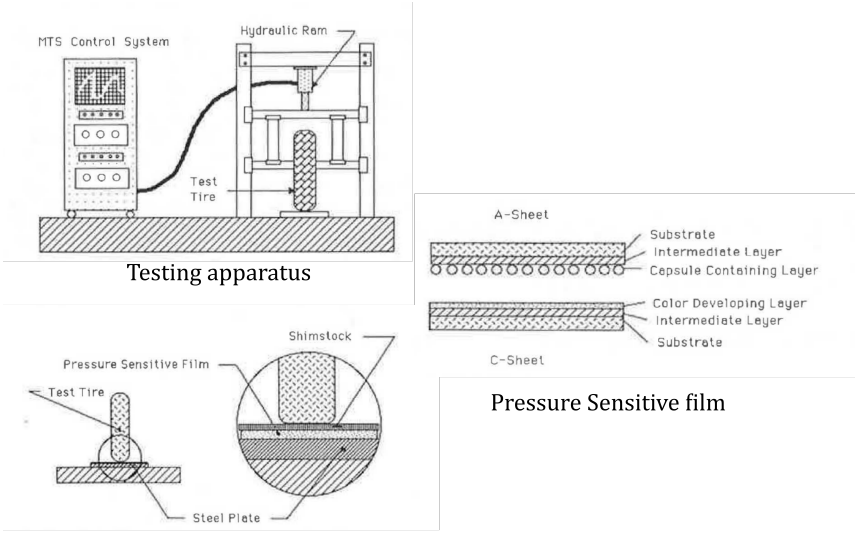

Figure 1.6: Testing apparatus for the measurement of the tire contact pressure using the a pressure sensitive film. [MAR 86]

Among other testing procedures for moving load on pavement structures, Howell et al. [HOW 86] used strain-gauged elements to quantify the stresses. The strain-gauged elements disposed in platen were suspended beneath the tire by cables. The purpose of those tests was to obtain forces in the footprint of commercial transport air-planes.

In recent technologies, electronic is coupled with software for the measurement of various footprints. In this respect, a commercial electronic based pressure sensor *TekScan* is used by Manyo et al. [MAN 19a] to capture the pressure field in the contact for a moving load. The sensor is in form of a thin film on which are distributed square elementary sensors. The variation of resistivity of the sensors allows to determine the pressure and so to have the global footprint under load. Figure 1.8 shows the sensor in the tire contact pressure measurement application. By coupling this technology to a semi-analytical model, the authors have highlighted the need for taking into account the real tire profile toward the understanding of the top-down cracking phenomena observed in pavements.

Apart from the capture of the fields in the tire-pavement contact, the experimental works have faced other challenges such as capturing the viscoelastic phenomena, reproducing the fatigue life cycle of the road pavement under specific controlled conditions, measuring the dynamic response of the pavement, etc.
Within these scopes, Hugo and Kennedy [HUG 85] have performed laboratory studies for a better grasp of the cracking phenomena observed at the surface of road pavements in South Africa. By performing full scale tests, they have showed in their experiments that the surface cracking of asphalt mixture in South Africa was due to aging, elasto-plastic behaviour and thermal effects. The latter result con-

firms the importance to investigate if the viscoelastic effects, due to temperature, are detrimental with respect to the elastic dimensioning.

The reader may have noted that the full scale testing is a common procedure in the tire-pavement field from the very beginning. This testing habit is justified by the overall behaviour of the pavement materials which is highly anisotropic at the mesoscopic scale. And this anisotropy makes difficult to scale down the structure to smaller apparatuses where it would be much difficult to find the right equivalent materials.

Around the experiments, various models have been erected. The models based only on the experiments are named *empirical* models since they are only based on observations and experimental measurements. Those models can be coupled with mathematical modellings to give *mechanistic-empirical* models. In practice, nowadays, only mechanistic-empirical models are used in the pavement conception processes. The empirical part has been reviewed briefly above; it is of certain interest to cast a look on the mechanistic part i.e. the modelling.

The modelling of tire-pavement contact has been performed widely under various hypothesis. In order to give a bird-eye view of those modelling within the literature, a review is performed with the following classification: elastic modelling (the pavement is considered elastic), viscoelastic modelling, dynamic modelling and finally other modelling taking into account non-linearities (mainly cracking and rutting).

1.4.2 Elastic Modelling of Road Pavements

By the materials used to build pavements and the arrangement of layers, roads are very complex structures from both local and global points of view. However, in modelling, the simplest way to grasp the structure is to consider that the material are elastic and then to focus on the structure. In the actual state of the art, for many mechanical topics, the models can be classified into four categories: empirical, analytical, semi-analytical and Finite Element based models. This classification is particularly relevant for the analysis of the elastic modelling of pavement structures.

- **The empirical models:** the empirical models are based on simple observation of the soils and existing roads, and relatively simple tests for the conception of new roads. In the USA, empirical methods have been used for the first time by the Public Roads (PR) by doing a classification of the soils, but without performing any strength test. In 1929, the empirical method with a strength test had been used by the Califoria Highway Department [POR 50]. The method is based on the California Bearing Ratio (CBR) which is defined as: the penetration resistance of a sub-grade soil relative to a standard crushed rock. The CBR method of design was studied extensively by the U.S. Corps of Engineers during World War II and became a very popular method after the war. However, it is limited because it is confined to a specific set of environmental, material and loading conditions. The change of one of those

parameters implies to start over the modelling.
To overcome this disadvantage, analytical models have been introduced.

- **The analytical models:** they are (from the beginning to the end) mathematically formulated and solved. Those models are usually limited to two-dimensions, to simple loadings and idealised geometries. They give simple criteria for dimensioning but are limited to some types of analysis. The models used in the design before software in France are analytical models.
  Another family of models, called the foundation models which use springs and dampers to represent the elastic and viscoelastic behaviour of the foundation are also analytical when solve under the two-dimension hypothesis (example in Fig. 1.10). They are discussed by Kerr [KER 64] who exposes the mathematical formulations and explains the physical problems and limitations involved.

  In addition, some analytical theories are discussed by Vesic and Saxena [VES 69] for rigid pavements. They are also divided into the ones based on the theory of elastic isotropic half-space, on one side; and those based on elastic springs, on the other side.

  To move forward to more complex solutions, there was a need to take advantage of the numerical procedures and computational science. Then, the methodology has consisted in coupling computation with analytical solutions in order to build fast and efficient models.

- **The semi-analytical models:** they use numerical strength to solve the analytical problems which are too complicated to be solved by hand. The analytical solutions are pushed till a certain complex point and then numerical tools are used to end the calculations. For instance, Reynaud et al. [REY 17] and Manyo et al. [MAN 21] used a semi-analytical contact model to solve the tractive rolling contact between the tire and pavement. Their model uses the Boussinesq and Love formulations coupled with Fast Fourier Transform algorithms and Conjugate Gradient Methods to solve the tire-pavement contact. Another example of semi-analytical model is the multi-asperity procedure of Dubois et al. [DUB 12], coupled with the Boussinesq half-space solution at a local level to find the contact pressures for different road textures. Note that in contact mechanics many semi-analytical models have been developed and might be use for the present tire-pavement contact (see section 1.5.5 for some semi-analytical methods in contact mechanics).

- **Finite Element Models (FEM):** they appear to be the very versatile tool for solving solid mechanics problems since the development of computational science. As the tire-pavement contact problem can certainly be considered as a mechanical problem, Finite Element based models have been developed to solve the problem for various points of view. In one hand, efforts were put by researchers to model the tire-pavement contact with a special focus on

either the pavement or the tire [TIE 87, FAR 92, BEC 97, SOO 04, NAC 04, WAN 11a, WOL 16]. Those studies aimed at analysing the impact of the elastic stresses used for the dimensioning. For example, Fig. 1.10 shows the contact stresses and slip for a FE modelling by Nackenhorst [NAC 04] using an Arbitrary Lagrangian Eulerian (ALE) formulation.

Another aspect is the analysis of the tire-pavement contact by setting a hyperelastic tire. This has been performed by some authors such as Bass [BAS 87], Hernandez et al. [HER 17]. For instance, Bass performed his studies by taking into account the friction at the contact interface between a hyperelastic cylinder and a rigid flat foundation with the purpose of analysing the effects of spinning and cornering. This modelling which pays a particular attention to the tire has also the advantage to have been performed in 3D. In fact, the spinning and cornering effects have to be modelled in 3D because of the out-of-plane effects ignored by a 2D model.
Despite its time consuming aspect, FEM allows to model numerically various complex and coupled phenomena. Thus, it has provided a lot of research works as we will see throughout this chapter and further in the document.

The elastic modelling has mainly allowed to understand the effects of a static load on the pavement. The impact of tire inflation, as well as the impacts of friction, tire type, structure type have been better caught with those modelling. However, the tire-pavement contact cannot be limited to elasticity scope. The use of asphaltic materials which are highly viscous, as seen in section 1.2, gives to the structure a non negligible viscoelastic behaviour.

1.4.3 Viscoelastic Modelling of Road Pavements

Viscoelastic effects can be briefly described as the time dependence of the material behaviour coupled with the load history. Pavement materials such as asphalt mixtures have viscous properties which are emphasised with temperature. Therefore, the stresses and strains have to be related with time dependent laws. The rheological response of the bituminous concrete has pushed the development of viscoelastic theories in the field. Among others, Hugo and Kennedy [HUG 85] have showed experimentally the effects of the temperature on the cracking near the surface of pavements. Then, it becomes important to take into account the thermal effects. To do so, an alternative way is chosen. It is based on the fact that the viscous behaviour of the pavements is dramatically increased with temperature. Therefore, for a given temperature the equivalent material properties are set for the modelling. Thus, the viscoelastic modelling allows to cover the thermal effects indirectly.

In term of modelling, analytical, semi-analytical and FE models still stand. For analytical and semi-analytical models, the elastic/viscoelastic correspondence of Lee [LEE 60] is often used to turn an existing elastic solution to a viscoelastic one. Many approaches have been developped on the basis of the elastic models.

One of the theories consists in a viscoelastic plate resting on a viscoelastic solid foundation (see [WES 67] and [PIS 61] for instance).

Another approach goes from the elastic bi-layer of Burmister [BUR 45c, BUR 45a, BUR 45b] in two-dimensions to a viscoelastic bilayer. Ishihara [ISH 62] used that approach to study two-layer systems where the base as well as the foundation can be viscoelastic. Chou and Larew [CHO 69] used a similar approach to model stresses and displacements under a moving load. Elliot and Moavenzadeh [ELL 71] performed the study of a tri-layer using the same technique to obtain the stationary solutions. Those works have been performed in 2D.

For the multi-layered viscoelastic case, the use of Fourier Transform is very helpful. Softwares such as VEROAD [HOP], ViscoRoute [CHA 10], KENLAYER [HUA 04] use the Burmister model and the frequency representation of viscoelastic materials to perform the calculations.

Further approaches have also been developped. The one of Papagiannakis et al. [PAP 96] couples the Burmister's model to viscoelasticity by using the Boltzman's superpostion principle to model stresses and displacements under a time dependent load. In this way, the authors had been able to apply a recorded load data from experiments to the model. It is also useful to remind viscoelastic modelling uses spring and dampers foundation to represent the viscoelastic behaviour. Some of them are recalled in the paper of Kerr [KER 64].
Note that all those works have been performed in two dimensions.

Beside the above analytical and semi-analytical models, FE models also have grown and improved. For some works on the subject the reader may refer to [ODE 86, KEN 87, PAD 87, NAK 87, BLA 02, MUL 07, ZIE 08, HOW 09, KIM 09, LIA 10, TAH 18, BAZ 20], where the viscoelastic effects are analysed in various contact configurations.

In summary, the modelling of viscoelastic behaviour of pavement structures allows not only to highlight the time effect related to the material behaviour, but also to take into account a history of loading and thus to take into accounts moving loads. For moving bodies, dynamics effects can appear depending on the relative velocity of the bodies. In the next section, the shady dynamic term is clarified and various modellings of dynamic effects within the literature are presented.

1.4.4 Dynamic Modelling of Road Pavements

First of all, it is essential to precise that a confusion might be made when using the term dynamic. In the literature, modelling of pavement under moving loads can sometimes be called dynamic modelling, in the same way as the modelling of the inertia effects.

In the first case, the studies are performed most of the time for an elastic or viscoelastic pavements with a time-dependent loading (dynamic loading); and then the so-called dynamic response of the pavement is in fact the viscoelastic response of the pavement under a moving (dynamic) load. For instance, Hardy and Ce-

bon [HAR 93] used Fourier Transforms to model the response of a pavement made of a Winkler foundation resting on a rigid foundation and topped by a beam. A 3D Finite Element in ABAQUS has been used by Zaghloul and White [ZAG 93] for the analysis of the response of flexible pavements at various moving speed.

The second type of modelling of the dynamic response of pavements takes into account the acceleration term (or the inertia term) in the equilibrium equation. Doing so, Stolle [STO 91] has developed a semi-analytical model in which an analytical explicit scheme is used and coupled with numerical integral calculation algorithms. He found out that the dynamic deflection is different from the static one and that the results of such a simulation can be used to interpret the Falling Weight Deflectometer (FWD) test.
In the same spirit, Fig. 1.11 shows a comparison between the quasi-static and dynamic response for a FEM analysis by Li et al. [LI 16] for the purpose of reproducing the FWD testing. The results show differences between the quasi-static and the dynamic analysis for the deflection-time histories. However, for the critical strain, the differences are not significant. This means that with view to build a conception tool for the engineer, it is not worth to perform a dynamic modelling because its ratio benefit/cost will not be interesting.

Furthermore, Pan and Atluri [PAN 95] have developed a coupled Boundary Element Method (BEM)-Finite Element Method (FEM) for the transient response of a finite elastic plate resting on an elastic-half space. The numerical method employed is a mix of: a time-domain BEM for the elastic foundation and a combination of a time-domain BEM for the soil and a semi-discrete finite element method for the finite sized elastic plate. Integration in time is carried out analytically and the solution for a moving point on an infinite elastic plate resting on an elastic half-space is derived.
Other FE models have been developped for the dynamic response of pavement and can be find in [UDD 04, ALQ 08, YOO 08, PIC 09, ASS 20a].

It is important to note that all those studies showed that the static response of the pavement is different from its dynamic response even for low frequencies.
However, the development of a real dynamic model is a completely different subject that will not be covered here. Focus will be put on taking into account the viscoelastic behaviour of the pavement and the time dependence aspect of the loading (i.e. the dynamic loading). In this way, the quasi-static response in viscoelasticity will be found for moving loads on the pavement structure.

Toward the understanding of the damages at the surface of the roads, not only the elastic, viscoelastic and dynamic modelling have been performed by the researchers. The modelling of the cracking, rutting, damage, aging and other phenomena have been investigated.

1.4.5 Modelling of Non-Linearities in Road Pavements

At the surface of the roads, the observable non-linearities are rutting and cracking (see Fig. 1.2).

Firstly, rutting is due to the accumulation of permanent deformations in the pavement structure. Those permanent deformations may appear in the layers within the structure, or they may appear at the surface. Surface rutting may be due to the low quality of the asphalt mixture, to the inflation pressure of tires and excessive loads [BRO 92, MYE 99, DRA 01]. The rutting is also very sensitive to shear stresses in the structure as showed by Deacon et al. [DEA 02] and Monismith et al. [MON 94].

Secondly, cracking of pavement structures is of two main types: the down-top cracking and the top-down cracking. The down-top cracking may be due to the traffic of heavy vehicles that provokes the initiation of cracking in the sub-layers of the structure. Meanwhile, the top-down cracking is not really well understood. However, it is possibly due to horizontal loadings at the surface [PET 09], or due to shear. Wang et al. [WAN 03] proposed that the top-down cracking may be due to both tensile and shear stresses; they are initiated when the mastic which binds the mixture is weaker or when the pavement temperature is higher. The authors add that "a mixture sensitive to rutting may also be sensitive to cracking" to explain that weak pavement structure favours potentially various non-linearities in the same time.

The above rutting and cracking as well as other non-linearities appear in the pavement after a considerable time of usage. Thus, the modelling of those non-linearities aims at building predictive laws to use in the dimensioning process. In this spirit, fatigue models based on experiments are the most used for the prediction of those failures in the dimensioning processes. Experiments have shown that damages are due, not only to the load, the number and location of axles, the type of tires, but also to pavement properties, operating conditions and environmental factors. The dimensioning methods aim to predict those rutting and cracking in order to avoid them in the structure's life time. Usually the strategy consists in using the elastic models to obtain the field under load, and then to build transfer or influence functions using experimental data to link the elastic field to the rutting and cracking prediction.
There are a variety of fatigue transfer functions that are used by the different agencies [SHE 98, BRO 92, MON 94, HAJ 05, AAS 08].
In research works, Deacon et al. [DEA 02] used the WesTack Test coupled with an elastic multilayered analysis, to find the coefficients to use for the prediction of permanent strain. Gillespie et al. [GIL 92] generated wheel load histories to build influence functions in order to predict the overall pavement damage caused by a truck. Shen and Carpenter [SHE 07a] incorporated the Fatigue Endurance Limit (FEL) concept to the design of pavement using an energy based fatigue model, on the basis of the material properties and load response. The model takes into account

the healing effect due to the rest periods between loads.

In another side, various approaches have been introduced for the fatigue modelling. In this respect, many models based on Finite Element modelling can be found in the literature [TRA 04, SOU 05, AKB 05, SHE 07b, CHA 09, PET 09, ABU 12, SUN 13, ELS 18] .

The non-linearities are of many kinds in reality and cannot be caught in totality by neither experiments nor modelling. For example, the modification of the microstructure of the materials during the lifetime, plasticity, visco-plasticity, the thermal effects, etc. Some multi-physics modelling have been carried to take into account those effects. For instance, Omairey et al. [OMA 21] have studied the oxidative ageing of asphalt pavements using a multi-physics FE model.

Ultimately, the non-linearities are various due to the multiple physics which can act on the roads. Most of the time, the conception will try to prevent from rutting and cracking. Since the purpose of the present work is the dimensioning part, the interest is not put in modelling those non-linearities.

In summary, a review has been done on the research works within the literature around the tire-pavement topic. Elastic, viscoelastic, dynamic modelling and the modelling of non-linearities have been successively covered, in a non exhaustive way though. However, the general concepts of the tire-pavement topic have been review. From those knowledges, the goal is to build up a numerical tool based on contact mechanics for the civil engineer in charge of pavements conception. Therefore, the next section is completely dedicated to quickly review the state of art of the contact mechanics field.

Figure 1.7: Images of the Vehicle Road Surface Pressure Transducer Array(VRSPTA) SIM MK II system during the UCB/NATC tests. [BEE 96]

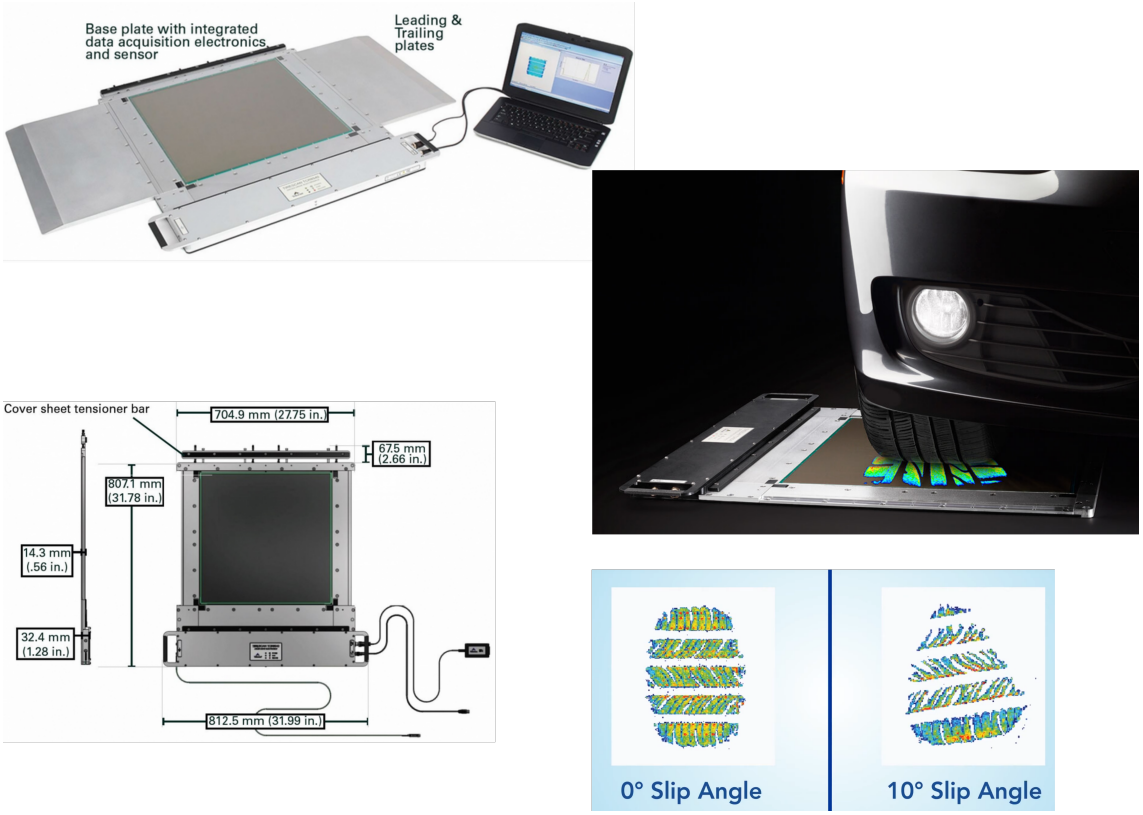

Figure 1.8: Tire contact pressures measurement using the Tekscan sensor (www.tekscan.com).

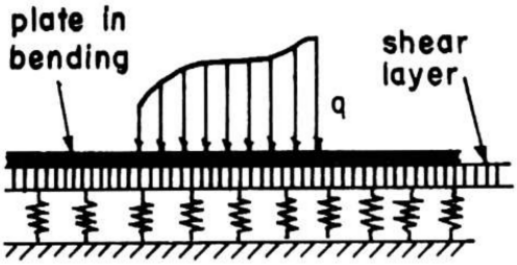

Figure 1.9: A plate resting on a Pasternak foundation which is made of elastic springs with shear interaction between them. [KER 64]

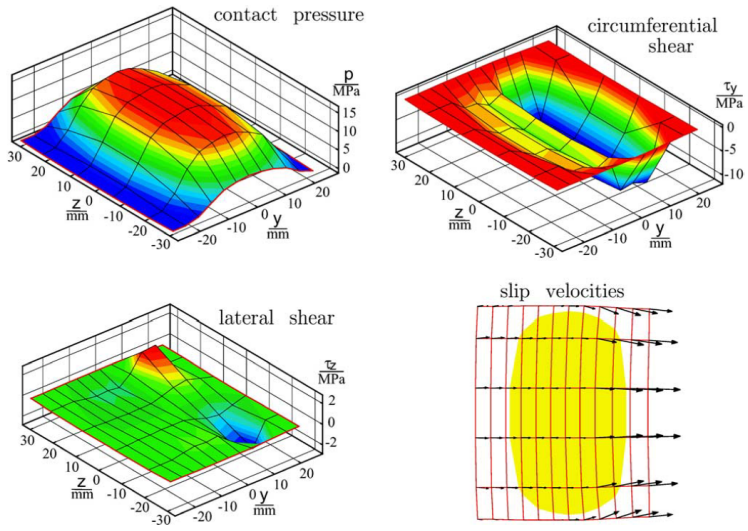

Figure 1.10: Contact stress distributions and distribution of slip-velocities at 15% driving slip. [NAC 04]

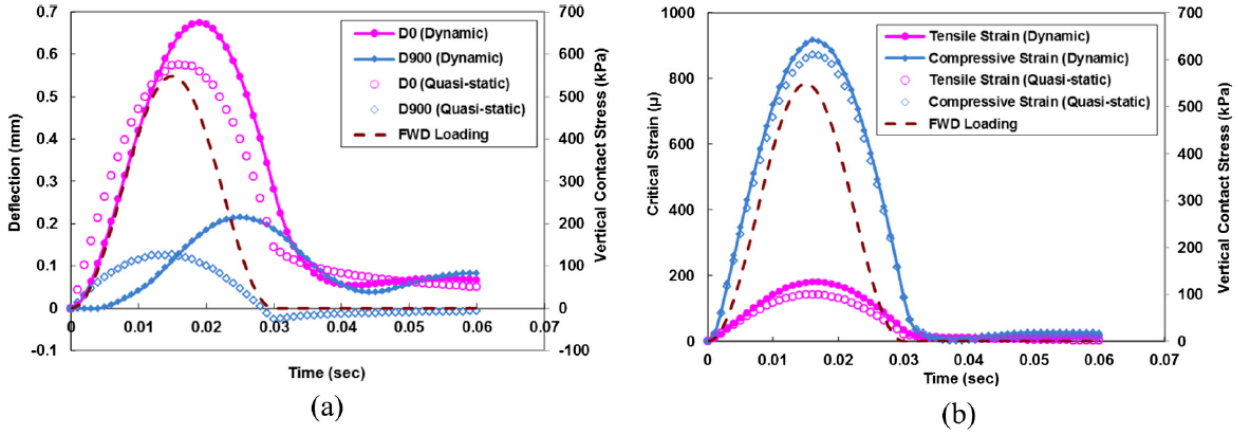

Figure 1.11: Comparison of dynamic and quasi-static analysis through (a) deflection-time histories and (b) strain-time histories (D0 is the surface deflection under the central load and D900 is the deflection 900 mm away from the central load). [LI 16]

1.5 Contact Mechanics

In this section, a rapid picture of contact mechanics is drawn. The history of contact mechanics as a specific part of mechanics had begun with the first formalisation by Hertz [HER 82]. Inspired by his works in optics, Hertz has treated the problem of an ellipsoidal contact pressure on elastic solid bodies under some hypotheses (see 1.5.2). Further, the industrial demand of knowledge for railways, rolling bearings and gears have boosted the field. Later, contact mechanics has been called upon to treat contact of frictional surfaces and inelastic bodies. The main historical progresses in the field, before the arrival of powerful numerical methods, are well exposed and summarised in the reference book of Johnson K. L. named "*Contact Mechanics*" [JOH 85].

In what follows next, the generalities of the contact mechanics are given. Then, the pioneering theory of Hertz is exposed. Further, non-Hertzian contact are presented with a particular stop on the rolling contact. Finally, the current numerical methods for solving contact problems are reviewed.

1.5.1 General Concept

In general, the contact problem considers two bodies of arbitrary surface shapes which touch each other under an applied load. Each body can behave elastically or inelastically (viscoelasticity, plasticity, etc.), be smooth or not, be moving or static, be homogeneous or not, isotropic or anisotropic, etc. . According to the profiles of the surfaces, a distinction is made between conforming (or conformal) and non-conforming contacts. If, when brought into contact without deformation, the bodies first touch at a point or a line, the contact will be called a non-conforming contact. One can also say that the surface profiles of the bodies are dissimilar. Otherwise, when the profiles fit together when there is no applied load, the contact is a conforming one.
The contact between two bodies happens under normal and tangential loads. The plane where the contact holds without load is to be considered when talking about tangential loads. Moreover, one or both bodies can be moving.
As usual in modelling processes, some assumptions allow to simplify a real problem to an approximative one which is relatively easier to solve.

1.5.2 Hertzian Contact

Hertzian contacts are the contacts that verify the conditions under which the pioneer H. Hertz developed the first analytical contact solutions. The five main conditions are:

- the materials are elastic, isotropic and homogeneous;
- the bodies are supposed continuous and non-conforming;

- the strains are small;
- the surfaces are smooth and frictionless ;
- the bodies are assimilated to half-spaces.

The last condition means that the bodies are large in comparison to the contact area. Thus, the stresses and the displacements vanish at infinity.
The theory of Hertz has been performed under those conditions for ellipsoidal contact areas. The reader may refer to Contact Mechanics [JOH 85] where Johnson recalls the solutions of Hertz and further developments that have been performed. Explicit solutions are found in two-dimension for solids of revolution. The Hertz solution of a circular contact region is recalled since it will be used very often for validation of the developed model.

1.5.2.1 Circular contact area

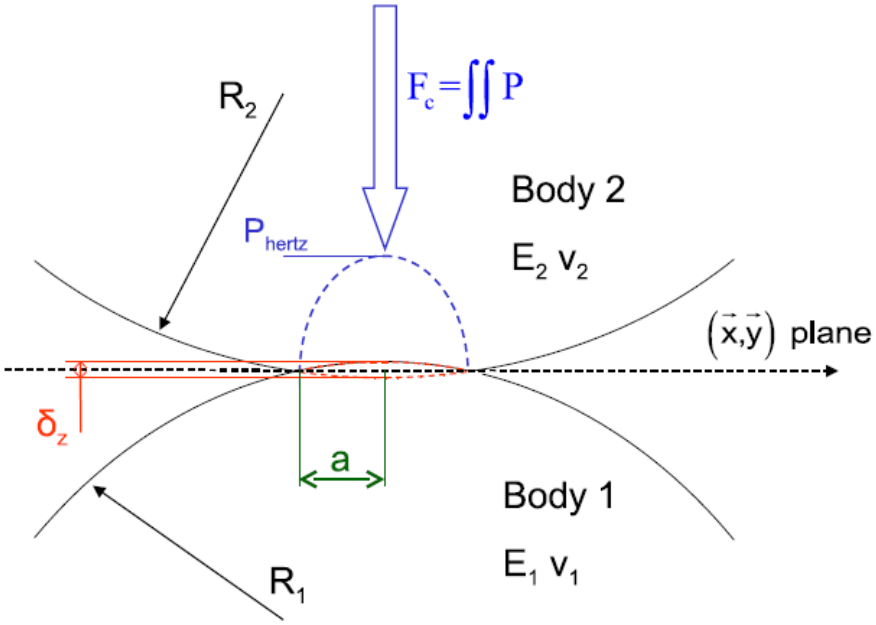

Figure 1.12: Schematic representation of the Hertzian contact problem for solids of revolution [CHA 11a].

The general problem is represented in Fig. 1.12. The relative curvature of the bodies is defined as:

$$\frac{1}{R_{eq}} = \frac{1}{R_1} + \frac{1}{R_2}, \tag{1.1}$$

where R_i is the radius of the body $i = 1,2$. Also, E_i and ν_i are respectively the Young modulus and the Poisson's ratio of the body i. Then, the equivalent Young modulus E_{eq} of the bodies is:

$$\frac{1}{E_{eq}} = \frac{1-\nu_1^2}{E_1} + \frac{1-\nu_2^2}{E_2}. \tag{1.2}$$

For an overall normal force F_c acting, the contact radius a, the rigid body displacement δ_z and the maximum contact pressure P_{Hertz} can be deduced. They are written as follow:

$$a = \left(\frac{3F_c R_{eq}}{4E_{eq}}\right)^{1/3} \tag{1.3}$$

$$\delta_z = \frac{a^2}{R_{eq}} = \left(\frac{9F_c^2}{16R_{eq}E_{eq}^2}\right)^{1/3} \tag{1.4}$$

$$P_{Hertz} = \frac{3F_c}{2\pi a^2} = \left(\frac{6F_c E_{eq}^2}{\pi^3 R_{eq}^2}\right)^{1/3} \tag{1.5}$$

Further in the studies, circular contacts will be used for validation and parametric studies. The above values will be useful to turn the results to dimensionless quantities.
Contact zones are very frequently not circular. For contacts involving solids of revolution, the general contact zone is elliptical.

1.5.2.2 Elliptic contact area

For the general elliptical case, finding the exact solution requires the use of elliptical integrals. It also exist approximated solutions. Let's recall the approximate solution using the approximation for elliptic integrals by Antoine et al. [ANT 06]. The contact conditions are the same as in the previous section apart from the geometry of the contacting bodies. Figure 1.13 shows the ellipsoids in contact in an elliptical region. ω is the angle between the planes $(O, \vec{x_1}, \vec{z})$ and $(O, \vec{x_2}, \vec{z})$. The same notations for the bodies are used as in the previous section: subscript $i = 1,2$ for the body i. In addition, for each body the radii r_{ix} and r_{iy} in the x and y direction respectively are defined. Thus, the curvatures are $\rho_i = 1/r_i$. The curvature for the contact geometry is defined with the curvature sum $\sum\rho$ and the curvature difference F_ρ:

$$\sum\rho = \rho_{1x} + \rho_{1y} + \rho_{2x} + \rho_{2y}, \tag{1.6}$$

$$F_\rho = -\left(\sqrt{R_I^2 + R_{II}^2 + 2R_I R_{II}\cos(2\omega)}\right) / \sum\rho, \tag{1.7}$$

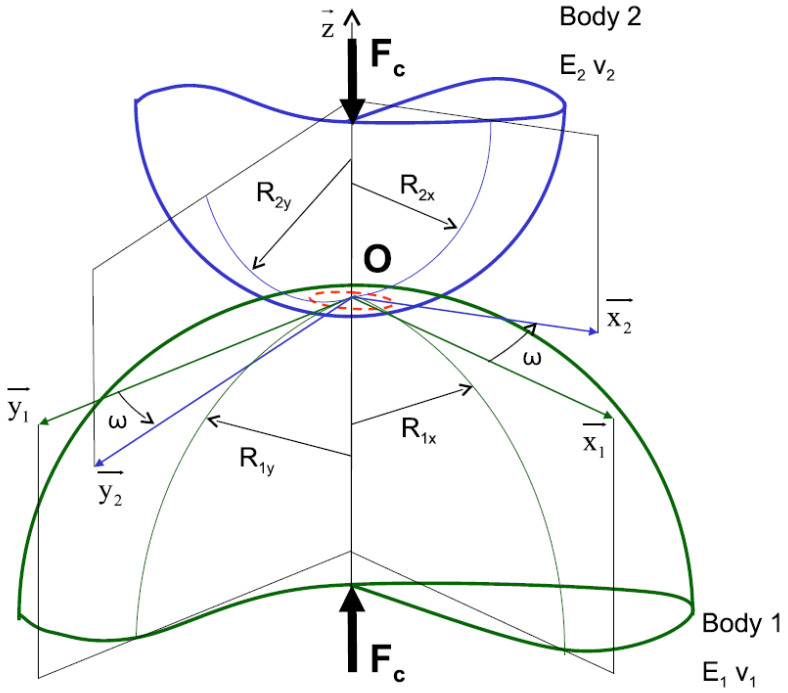

Figure 1.13: Schematic representation of the Hertzian contact problem for elliptical contact areas [ANT 06].

where $R_I = \rho_{1x} - \rho_{1y}$ and $R_{II} = \rho_{2x} - \rho_{2y}$. The relative curvatures of the contact are then:

$$\begin{aligned} A =& \frac{\sum \rho}{4}(1+F_\rho) \\ B =& \frac{\sum \rho}{4}(1-F_\rho). \end{aligned} \tag{1.8}$$

Suppose an ellipse of semi-axes a and b, and define the parameter $\kappa = a/b$. Then, the present approximate solution comes from the use of the elliptic integrals:

$$\begin{aligned} F_F(\kappa) &= \int_0^{\pi/2} \left(1 - \left(1 - \frac{1}{\kappa^2}\right)\sin^2\phi\right)^{-1/3} d\phi \\ F_\varepsilon(\kappa) &= \int_0^{\pi/2} \left(1 - \left(1 - \frac{1}{\kappa^2}\right)\sin^2\phi\right)^{1/2} d\phi \end{aligned} \tag{1.9}$$

to solve the problem since approximate solutions exist for them.
The Hertzian theory allows to find the geometrical parameter F_ρ by an implicit equation:

$$F_\rho = \frac{B/A - 1}{B/A + 1} = \frac{\left(\kappa^2+1\right)F_\varepsilon(\kappa) - 2F_F(\kappa)}{\left(\kappa^2-1\right)F_\varepsilon(\kappa)}. \tag{1.10}$$

In this way, the approximate functions of the elliptic integrals can be used to have an approximation of the solutions. The approximation of the elliptic integrals of

Eq. (1.9) are found to be:

$$\begin{aligned} F_F(\kappa) &= \left(\alpha_0 + \alpha_1 m_1 + \alpha_2 m_1^2\right) - \left(\alpha_3 + \alpha_4 m_1 + \alpha_5 m_1^2\right) \ln m_1, \\ F_\varepsilon(\kappa) &= \left(\beta_0 + \beta_1 m_1 + \beta_2 m_1^2\right) - \left(\beta_3 m_1 + \beta_4 m_1^2\right) \ln m_1, \end{aligned} \tag{1.11}$$

with

α_0	1.3862944	α_4	0.1213478	β_2	0.1077812
α_1	0.1119723	α_5	0.0288729	β_3	0.2452727
α_2	0.0725296	β_0	1	β_4	0.0412496
α_3	0.5	β_1	0.4630151		

Finally, the parameters, solution of the contact problem are found. The semi-axes of the contact area are:

$$\begin{aligned} a &= a^* \left(\frac{3F_c}{2(A+B)E^*}\right)^{1/3}, \\ b &= b^* \left(\frac{3F_c}{2(A+B)E^*}\right)^{1/3}, \\ \delta_z &= \delta_z^* \left(\frac{3F_c}{2E^*}\right)^{2/3} \frac{(A+B)^{1/3}}{2}, \end{aligned} \tag{1.12}$$

where the superscript * represents the dimensionless parameters:

$$\begin{aligned} a^* &= \left(\frac{2\kappa^2 F_\varepsilon(\kappa)}{\pi}\right)^{1/3}, \\ b^* &= \left(\frac{2F_\varepsilon(\kappa)}{\pi\kappa}\right)^{1/3}, \\ \delta_z^* &= \frac{2F_F(\kappa)}{\pi} \left(\frac{\pi}{2\kappa^2 F_\varepsilon(\kappa)}\right)^{1/3}. \end{aligned} \tag{1.13}$$

The force displacement relationship can be expressed as:

$$F_c = \left(\frac{2^{5/2}}{3} \frac{E^*}{(\delta_z^*)^{\frac{3}{2}} (A+B)^{\frac{1}{2}}}\right) \delta_z^{3/2}. \tag{1.14}$$

1.5.3 Non-Hertzian Contact

When a contact frame does not meet the conditions listed in 1.5.2, it is a non-Hertzian contact. In many works, the half-space condition has been maintained since it allows anyway to get good results for many practical applications.

Conforming contacts happen when the contact area grows rapidly and may become comparable with the significant dimensions of the bodies in contact. For

example, when a shaft is in a bearing, the convex surface of the shaft fits with the concave surface of the bearing, and this gives a conforming contact. The case of conforming contact of a frictionless sphere in a cavity has been studied by Goodman and Keer [GOO 65]. Hartnett [HAR 79], Nagatani and Imou [NAG 08] proposed other methods to solve the frictionless elements in bearing contact problem while Paul and Hashemi [PAU 81] have introduced numerical procedures to solve the conforming contact for wheel/rail contact application.

When dealing with asymmetric geometries or with singularities in the surface profiles, other mathematical approaches have been introduced to solve the two-dimensional contact problem. For instance, some authors such as Galin and Gladwell [GLA 08] treated geometries with singularities. In their book, Aleksandrov and Pozharskii [ALE 01] proposed some solutions to solve those problems in three-dimension. Greenwood [GRE 66, GRE 70] as well as many other authors [BUS 75, NÉL 06, RAD 19] analysed rough surface contacts.

In the case of inhomogeneous and/or inelastic bodies such as polymers, layered solids, etc., the Hertz theory cannot take place. The anisotropic contact problems in two dimensions are fully discussed in the book of Gladwell [GLA 08]. Gladwell resumes the use of "singular integral equations" and Fourier transform to solve the contact problems. Some other aspects of contact involving inhomogeneities and inelastic bodies are also discussed in [WIL 66, BOR 93, HWU 98, LI 06, BAG 12, KOU 14b, KOU 15b, AMU 16b, NGU 20]. Furthermore, viscoelasticity in the contact problems have been discussed extensively in the recent works. The modelling of viscoelastic contacts has been treated by many authors from Lee and Radok [LEE 60] to recent works [XU 20, ZHA 20, NGU 20, WAL 20, MEN 21], through [KAL 91, GOR 95, CHE 11, KOU 14a, PUT 14, MEN 14, PUT 15, KOU 15b, PUT 16, MEN 16, STE 16, KUS 17, SCA 17, PUT 18, STE 18, GOR 19, TOR 19], and others. The modelling of viscoelastic contacts is now widely known and solved for various motions (rolling, sliding, reciprocating, fretting), various punches (in terms of geometry and mechanical properties) and with different methods (Boundary Element Methods, Semi-Analytical Methods, Finite Element Methods).

Finally, layered bodies are of great interest in practice for thin films, coated bodies and multilayered structures as the pavement structure. This problem is usually treated using the Integral Transforms. The study of multi-layered half-spaces have begun with the works of Burmister [BUR 45a] and extended further to the axisymmetric and non-axisymmetric normal surface loadings by Chen [CHE 71]. Using an approximation technique, Chen and Engel [CHE 72] solved the normal frictionless contact for a multilayered half-space. Sneddon [SNE 51] and Gladwell [GLA 08] have studied the problem of an elastic layer resting on a frictionless rigid substrate. The same problem considering friction at the layer/substrate interface has been studied by Bentall and Johnson [BEN 68].
With the development of the computational science, new methods have been developed for solving numerically mechanical problems. O'Sullivan and King [O'S 88] have proposed a solution to the layered half-space problem using Papkovich-Neuber

Authors	Layer	Viscoelastic substrate	Viscoelastic coating	Shear traction	Method	2D/3D	Transient regime
O'Sullivan and King [O'S 88]	Yes	No	No	Yes	Numerical inverse transform	3D	-
Nogi and Kato [NOG 97]	Yes	No	No	No	CC-FFT	3D	-
Hu et al. [HU 99]	No	No	-	Yes	Direct method	3D	-
Plumet and Dubourg [PLU 98]	Yes	No	No	Yes	Direct method	3D	-
Ai and Sawamiphakdi [AI 99]	No	No	-	Yes	CC-FT + Decomposing	3D	-
Polonsky and Keer [POL 99]	Yes	No	No	No	CC-FT + Correction		-
Liu and Wang [LIU 02]	Yes	No	No	Yes	DC-FFT	3D	-
Chen et al. [CHE 11]	No	Yes	-	No	DC-FFT	3D	Yes
Kalker [KAL 91]	Yes	Yes	Yes	Yes	Numerical inversion	2D plane strain	No
Carbone and Putignano [CAR 13]	No	Yes	-	No	BEM	2D contact	No
Koumi et al. [KOU 15b]	No	Yes	-	Yes	DC-FFT	3D	Yes
Spinu and Cerlinca [SPI 16]	No	Yes	-	Yes	DC-FFT	3D	Yes
Stepanov and Torskaya [STE 18]	Yes	No	Yes	No	BEM	2D plane strain	No
Wallace et al. [WAL 20]	Yes	Yes	Yes	Yes	DC-FFT	3D	Yes

Table 1.1: List of some of the work on contact analyses for layered half-space and/or viscoelastic half-space

potentials and a numerical inverse transform. Drawn from that work, several methods have been proposed for the numerical inversion. A comparison of several methods for solving the contact problem on a viscoelastic layered half-space using numerical methods is performed in Tab. 1.1.
For a general case of L layers, L being any positive integer, most of the literature works are based on finite element methods [KOM 88, DJA 94, GOR 03, CHE 09, KOT 12, ASS 20b]. Yu et al. [YU 14] solved the problem analytically in the Fourier frequency domain by constructing a matrix system and used numerical algorithms to find a semi-analytical solution for the influence coefficients. Note that in geology science, the study of the ground have lead to the modelling of multi-layered systems (see for instance [KUO 69, BUF 71, FAR 72, PEL 74]) but in 2-D.

In summary, the non-Hertzian contact problems have been extensively studied analytically and with numerical tools. Conforming contacts, contacts involving particular surface profiles, inelastic bodies, inhomogeneous bodies, etc. have been analysed in the research literature.
Furthermore, the contact problem has been studied for moving bodies. Indeed, the tire pavement contact is a rolling contact. Thus, in the next part a rapid picture of the state of art is drawn around the rolling contact.

1.5.4 Rolling Contact

Considering two bodies in contact (see Fig. 1.14), a rolling motion between them is of interest. The rolling motion is a general angular motion about an axis parallel to their common tangent plane. In some cases, the rolling motion may be accompanied by the transmission of a tangential force. Then, two kinds of rolling motion can be defined:

- **Free rolling**: when there is no tangential force accompanying the rolling motion. In this case, considering a reference moving frame centred in the contact point O, the instantaneous tangential velocity of the particles in the contact is zero. This is the typical case where the contact is supposed frictionless.

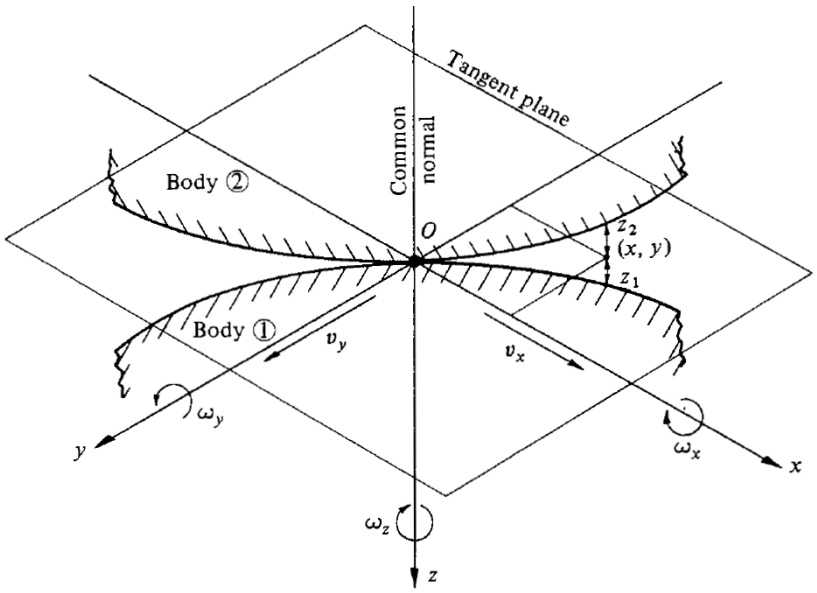

Figure 1.14: Kinematic of the contact between two bodies [JOH 85].

- **Tractive rolling**: when an overall tangential force is transmitted during the rolling motion. Due to friction, stick and slip zones coexist in the contact area. Further, according to the friction law used, when the tangential exceeds a certain value, the rolling motion turns into a sliding motion.

Solving the free rolling contact generally implies to solve only the normal contact problem. In function of the properties of the bodies, several additional manipulations of the solution can be performed. For example, in the case of viscoelastic bodies, a translation of the solution has to be performed in order to take into account the relaxation effect related to the history (see the solutions of Koumi et al. [KOU 15b] for example).

Meanwhile, the tractive rolling contact imposes to solve both the normal and the tangential components of the general contact problem. The tractive rolling contact has been firstly developed for the railways application. In 1926, Carter [CAR 26] studied the two-dimensional plane strain tractive rolling contact between elastic cylinders. In the same period of time (1927) the problem has been examined by Fromm [FRO 27].

1.5.4.1 Carter's Theory

The theory developed by Carter [CAR 26] is based on a superposition of two solutions. Firstly, the solution of a Hertzian contact is found for a stationary free rolling cylinder on a plane. Carter has shown that in presence of a friction coefficient f, there is an apparition of a slip zone in the contact area, beside an adhesion zone. Using the Coulomb's law for friction, he found out that the solution of the

problem is the superposition of two solutions q'_x and q''_x, where q''_x is displaced by a distance $d = (a - c)$ so that adhesion zone obtained is adjacent to the leading edge (see Fig. 1.15).

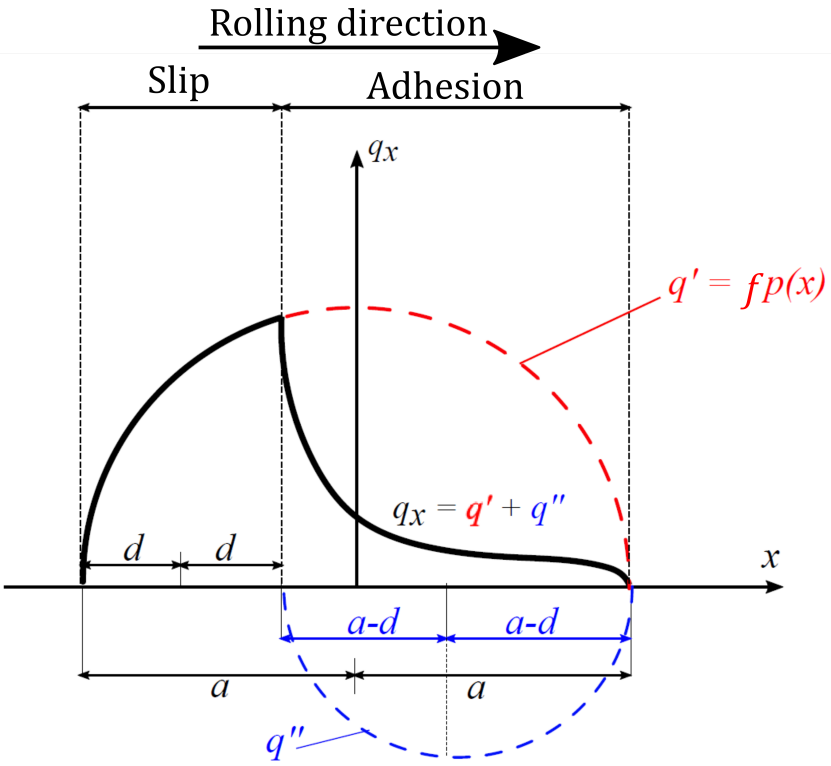

Figure 1.15: The solution of Carter for tractive rolling cylinder on a plane.

Finally, the contact shear stress in the rolling direction x is given by:

$$q_x = q'_x + q''_x, \tag{1.15}$$

where

$$q'_x = \mu p_0 \sqrt{1 - \left(\frac{x}{a}\right)^2} \quad -a \leq x \leq a, \tag{1.16a}$$

$$q''_x = -\frac{(a-d)}{a} \mu p_0 \sqrt{1 - \left(\frac{x-d}{a-d}\right)^2} \quad -a + 2d \leq x \leq a, \tag{1.16b}$$

with p_0 the maximum contact pressure of Hertz.
In order to link the overall tangential tractive force Q to the slip zone for an applied normal force F_c, the following relation is used:

$$d = a\left(1 - \sqrt{1 - \frac{Q}{fF_c}}\right). \tag{1.17}$$

Further, the micro slip ratio in the longitudinal direction is found to be:

$$\xi_x = -\frac{fa}{R}\left(1 - \sqrt{1 - \frac{Q}{fF_c}}\right), \tag{1.18}$$

where R is the radius of the rolling cylinder.
Therefore, the stick/slip problem in the rolling contact has been solved in one-dimension. It has been later improved by Haines and Ollerton [HAI 63] with a strip theory in two-dimension, followed by the theory of Vermeulen and Johnson [VER 64]. The limits of these last two theories will be demonstrated later by Kalker [KAL 68a]. Earlier, Cattaneo [CAT 38] then Mindlin [MIN 49] studied the problem of partial slip but for a shift motion. Their analytical solution is also one-dimensional. A spherical contact surface on which a normal and tangential force is applied is considered. A micro slip ring is then observed around a central grip area.

The works of Carter have given a good basis for the study of the slip in a rolling contact. Further, another main highlight of the rolling contact has been brought by the works of Kalker. Throughout his research works, Kalker has progressively developed a very complete theory for solving the rolling contact problem.

1.5.4.2 Kalker's theory

Joost J. Kalker developed a theory *"On the Rolling Contact of Two Elastic Bodies in the Presence of Dry Friction"* [KAL 68a] in his PhD dissertation. The works were mainly motivated by the wheel-rail contact application. From this first theory, Kalker has developped the linear theory which will be upgraded progressively to reach the exact theory based on the principle of virtual work [KAL 90]. A review can be found in Zaazaa and Schwab [ZAA 09] which pays tribute and underlines the key lines of the brilliant works of Kalker. The main points in the development of his theory are recalled here.

Consider a wheel rolling with a velocity $\mathbf{v}$ on a rail in a fix coordinate system. For a circumferential velocity $\mathbf{c}$ relative to the center of the wheel, the *rigid slip* is defined as :

$$\dot{\mathbf{s}} = \mathbf{v} + \mathbf{c} = |\mathbf{v}| \begin{pmatrix} \xi_x - \varphi y \\ \xi_y + \varphi x \end{pmatrix} \tag{1.19}$$

in a moving coordinate system. ξ_x, ξ_y and φ are longitudinal, lateral and spin creepages respectively. The creepages are the quantities used to describe the tangential micro rigid body displacements. They can be seen as micro slips. The slip zone Γ_{slip} and the adhesion or stick zone Γ_{stick} are defined using the Coulomb's law for friction:

$$\begin{array}{ll} |\mathbf{q}| = \sqrt{q_x^2(x,y) + q_y^2(x,y)} < fp(x,y); & |\dot{\mathbf{w}}| = 0; \quad (x,y) \in \Gamma_{stick} \\ \mathbf{q} = -\frac{fp(x,y)\dot{\mathbf{w}}}{|\dot{\mathbf{w}}|}; & |\dot{\mathbf{w}}| \neq 0; \quad (x,y) \in \Gamma_{slip} \end{array} \tag{1.20}$$

where f is the friction coefficient, p the contact pressure and $\mathbf{q}$ the shear vector. The total shear forces F_x and F_y and moment M_φ around the normal axis are expressed

as sums over the contact area Γ_c:

$$\begin{aligned} F_x &= \int\int_{\Gamma_c} q_x(x,y)dxdy \\ F_y &= \int\int_{\Gamma_c} q_y(x,y)dxdy \\ M_\varphi &= \int\int_{\Gamma_c} (xq_y(x,y) - yq_x(x,y))dxdy \end{aligned} \tag{1.21}$$

The linear theory Taking into account the displacement vector $\mathbf{u}$ due to the deformation of the material, the true slip is defined as:

$$\begin{aligned} \dot{\mathbf{w}}(x,y) &= \dot{\mathbf{s}} + \dot{\mathbf{u}}(x,y,t) \\ &= |\mathbf{v}| \begin{pmatrix} \xi_x - \varphi y \\ \xi_y + \varphi x \end{pmatrix} - |\mathbf{v}|(\partial\mathbf{u}/\partial x) + (\partial\mathbf{u}/\partial t). \end{aligned} \tag{1.22}$$

The linear theory of Kalker is based on the assumption that the true slip (Eq. (1.22)) becomes zero. Note that in the steady state rolling, $(\partial\mathbf{u}/\partial t) = 0$. Kalker determine the well known Kalker coefficients C_{11}, C_{22}, C_{33} and C_{23}, to link the global applied tangential forces and spin moment to the creepages with the system:

$$\begin{pmatrix} F_x \\ F_y \\ M_\varphi \end{pmatrix} = -Gab \begin{pmatrix} C_{11} & 0 & 0 \\ 0 & C_{22} & \sqrt{ab}C_{23} \\ 0 & -\sqrt{ab}C_{23} & abC_{33} \end{pmatrix} \begin{pmatrix} \xi_x \\ \xi_y \\ \varphi \end{pmatrix} \tag{1.23}$$

where a and b are the semi-axes of the ellipsoidal contact region; G is the equivalent shear modulus of the bodies in contact.
From the works of De Pater who solved the problem for a circular region and a Poisson ration $\nu = 0$, Kalker has extended the results to a general ellipsoidal contact region and for $\nu \neq 0$ [KAL 71]. The main downside of the linear theory is its limitation to handle large spin and large creepages.

The empirical theory The empirical method introduced by Kalker in 1968 [KAL 68b] defines a relation between the longitudinal and lateral creepages and the overall tangential forces. Thus the creepages are found to be a function of the the semi-axes of the ellipsoidal contact zone, some elliptical integrals and the normal applied force. The empirical method of Kalker had been compared to that of Johnson and Vermeulen [VER 64] with good agreement. In addition, the empirical theory of Kalker shows good agreements for relatively low value of creepage but estimates higher total force for greater values.

The simplified theory The program FASTIM well known for its speed is based on the simplified theory developed by Kalker in the years 1973-1982 [KAL 82]. The

elastic body is replaced by a set of springs so that the displacements are linked to the tractions with compliant parameters L:

$$\begin{pmatrix} u_x \\ u_y \end{pmatrix} = \begin{pmatrix} L_x q_x \\ L_y q_y \end{pmatrix}. \tag{1.24}$$

By replacing the above equation in the true slip in Eq. (1.22), a relation is found between the overall tractions F_x, F_y and the creepages:

$$\begin{aligned} F_x &= \int_{-b}^{b} dy \int_{-x_1}^{x_1} q_x dx = -\frac{8a^2 b}{3L_1}\xi_x = -abGC_{11}\xi_x \\ F_y &= \int_{-b}^{b} dy \int_{-x_1}^{x_1} q_y dx = -\frac{8a^2 b}{3L_2}\xi_y - \frac{\pi a^3 b\varphi}{4L_3} \\ &= -abGC_{22}\xi_y - (\sqrt{ab})^3 GC_{23}\varphi \end{aligned} \tag{1.25}$$

where the notations of the previous paragraphs are used, and the complaint parameters L_1, L_2 and L_3 are:

$$L_1 = \tfrac{8a}{3C_{11}G}, \quad L_2 = \tfrac{8a}{3C_{22}G}, \quad \text{and } L_3 = \tfrac{\pi a\sqrt{a/b}}{4C_{23}G}. \tag{1.26}$$

The numerical solving of the equations has been done by transferring the shape of the contact area to circular. The simplified theory give results with an expected error of 15% and is widely used in railroad.

The exact theory By the use of the variational formulations, the problem is turned into an optimisation problem where the complementary work is to be maximised. The resulting program is the well known CONTACT described in his book [KAL 90]. The variational problem to solve is then:

$$\begin{aligned} &\min \int_{\Gamma_c} \left(h^* + \frac{1}{2}\bar{u}_z\right) p dS + \int_{\Gamma_c} \left(\mathbf{W}_\tau^* + \frac{1}{2}\overline{\mathbf{u}}_\tau^t - \overline{\mathbf{u}}_\tau^{t-1}\right) \mathbf{q} dS, \\ &p \geq 0 \\ &\|\mathbf{q}\| \leq \mu p \end{aligned} \tag{1.27}$$

In addition, the displacements are found using the influence coefficients for an homogeneous isotropic half-space. Numerical tools are then used to solve the problem. In CONTACT, the normal contact problem is solve with the algorithm NORM. Influence coefficients are used to link surface displacement and constant pressure on each element of the discretised potential contact area. The tangential part is implemented with the algorithm called TANG. To solve the general problem, the normal contact and the tangential contact are uncoupled and solved successively using the KOMBI process. KOMBI is a solving process based on the modification of the Panagiotopoulos process. The Panagiotopoulos process consists in solving alternatively the normal problem and the tangential problem until the convergence is

reached. KOMBI supposes no shear tractions and solve the normal problem. Then, the tangential problem is solve by taking into account the contribution of the normal pressures. After, it iterates between the normal and the tangential algorithms until convergence by taking into account the effect of one solution on the other.

The final exact theory developed will be considered further in this work. The idea is to use the exact theory for solving the three-dimensional rolling contact problem, coupled with the actual efficient numerical tools.
The use of the various numerical tools has lead to various numerical methods for solving the contact problem. The most common ones are briefly presented in the next section.

1.5.5 Numerical Approaches for Solving Contact Problems

Computational science has hugely improved the use of numerical methods in mechanics. In contact mechanics, apart from the analytical methods, the main numerical methods that are used are: *Finite difference and multigrid methods*, *Finite Element methods* and *Semi-analytical methods*.

- **Finite difference and multigrid methods**: In one hand, the finite difference method is the numerical technique for solving differential equations using the finite differences to approximate the partial derivatives. In the other hand, the multigrid method (MG method) is an algorithm for solving differential equations by accelerating the convergence of a basic iterative method doing a global correction of the fine grid solution approximation from time to time.
  Terzopoulos et al. [TER 87] used the finite differences to study the contact between two purely elastic bodies. They were the first to use this approach for contact mechanics. After applying it to elastic contact, they applied it to inelastic deformation: viscoelasticity, plasticity and fracture [TER 88]. The limitation is that it is difficult to model complex geometries by finite differences. Indeed, the diagrams of the latter are not flexible enough since they impose the use of a regular grid. It is therefore also difficult to manage the boundary conditions in the correct ways. Alternatives to finite differences are the multigrid methods used by Lubrecht and Ioannides [LUB 91]. However, for the development of these methods, it is mandatory for them to become capable of handling anisotropy, plasticity, viscoleasticity, etc. In this spirit, for example Boffy et al. [BOF 12, BOF 14] have proposed a 3D modelling based on the multigrid technique for heterogeneous materials.

- **Finite Element methods:** It is a versatile method which is widely used in various fields in physics, including contact mechanics.

  Finite Element Method (FEM) has radically changed the calculations in both research and industry. FEM is a numerical approach for solving physical prob-

lems by approximation in a space domain using a set of constitutive equations and some boundary conditions. The FEM can be used when bodies are continuous and the phenomenon can be described by partial derivatives equations. The method generally consists in four main steps (see Fig. 1.16):

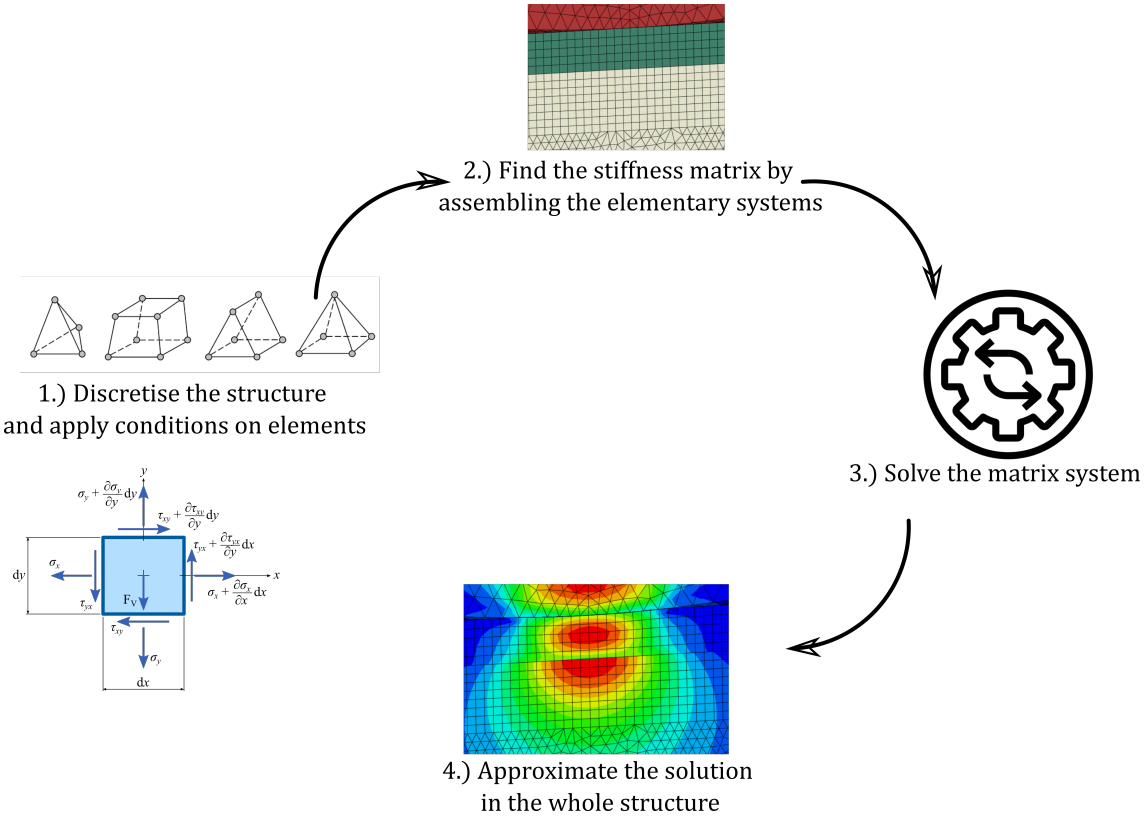

Figure 1.16: Summary of the concept of Finite Element Methods.

1. **Analysis of the problem**: the unknown of the problem is defined and the discretisation of the studied structure is performed. The particular data of the problem are set: type of analysis (plane strain, plane stress, axisymmetric, etc.), elements types, material properties and geometry.
2. **Calculation of the stiffness matrix**: the matrix system to solve is found by assembling the elementary matrices and then the stiffness and mass matrices are written in their optimal form for the solver. The boundary conditions are taken into account mathematically in this process.
3. **Solving**: the matrix system is solved to give the deformed structure and the stresses at boundaries.
4. **Post-processing**: the stresses in the structure and at all the nodes of the discretised structure are deduced.

This method can be applied to one, two or three-dimensional problems. It allows in theory to treat various aspects of the contact modelling such as dynamic, viscoelasticity, fracture, finite structures, transient problems, etc. Nevertheless, it can be time consuming; and this prevents it from being an efficient design tool for engineers. However, it is the most studied and used in both research and industrial areas because of its good user-friendliness.

Nowadays, there are a lot of commercial softwares (Abaqus [SIM 19], Ansys [ANS 19] for instance) with simple graphical interfaces making it easy to handle. With the FEM, there is the possibility of simultaneously taking into account several physical phenomena. This can be interesting for this tire-pavement contact in modelling coupled complex phenomena.

Several researchers have used the FEM method to solve the contact problem. Among the first to use the FEM method for the resolution of the contact problem, Oden and Martins [ODE 84] developed models for the study of dynamic friction phenomena, Oden and Lin [ODE 86] studied the rolling contact for a viscoelastic cylinder on a rigid plane, and Padovan [PAD 87] had also developed a model for a rolling contact in the transition and stationary phase of nonlinear viscoelastic structures. Recently, Blanco-Lorenzo et al. [BLA 16, BLA 18] have developed a finite element model of the rolling contact between two elastic materials to validate an extension of the Kalker numerical code for conformal contacts.

With the FEM, a good user-friendliness of the results is guaranteed. However, the smoothness of the mesh in the singular zones of the contact causes serious problems and the computing time is sometimes very high compared to the other methods. An alternative method is the Boundary Element Method (BEM) where only the surfaces of the bodies are meshed. It is widely used for solving problems in contact mechanics. The first application of the BEM to contact problems can be traced back to the early 1980s [AND 81]. Later works [KAR 87, PAR 85] used both continuous and discontinuous quadratic elements to solve contact problems. A fully incremental formulation was developed in [MAN 93a], where it was shown that linear elements should be used in place of higher order elements in the contact area [MAN 93b]. Application of the method to axisymmetric and three-dimensional problems can be found in [ABD 86, LAC 00, WRO 02].

- **Semi-analytical methods**: The semi-analytical models are the best alternative for obtaining solutions in a small amount of time when the analytical formulations become complex. Those methods have been boosted by acceleration techniques such as the Fast Fourier Transform (FFT) and the Conjugate Gradient Methods (CGM) used in the present work. Semi-analytical methods are applied in contact mechanics for solving Hertzian and non-Hertzian contacts, to treat inhomogeneities, thermal modelling, etc.

In the first semi-analytical models the main numerical side was the discretisation and the numerical calculation of integrals. Among the first semi-analytical models, Bentall and Johnson [BEN 68] have developed a model for the study of an elastic strip passing between two elastic rollers. Paul and Hashemi [PAU 81] have developed a semi-analytical model for both non-conformal and conformal contacts. Further, Nowell et al. [NOW 98, DIN 04] have also proposed the use of numerical tools to study fretting and layers problems in 2D. Note that the model proposed by Kalker [KAL 90] (see section 1.5.4.2) is a semi-analytical method using a Newton-Raphson algorithm.

With the use of acceleration techniques, a new generation of semi-analytical methods have appeared. The main advantages are brought by the use of *Fast Fourier Transform (FFT)* and *Conjugate Gradient Method (CGM)* algorithms. While FFT is used for its capacity for calculating efficiently convolution products, the CGM is used for solving the contact problem which is shown to be a constrained minimisation problem. Indeed, when the contact problem is formulated in its variational form (see Kalker [KAL 90]), it becomes a constrained minimisation problem where a CGM algorithm can be used for solving it.

Polonsky and Keer [POL 99] have proposed a CGM algorithm to solve the problem for arbitrary rough surfaces. While solving the contact problem, there is a need for calculating the displacements and stresses. To do so, various numerical techniques can be used. In [POL 99], Polonsky and Keer have used a two-dimensional multi-level multi-summation algorithm. Further, in [POL 00] they have proposed to use FFT with a correction which erases the error due to the periodicity property of the FFT. The use of FFT decreases significantly the computation time. In this respect, the method combining the CGM and the FFT is extensively used in semi-analytical methods nowadays. Improvements of FFT algorithm for solving the contact have been studied by Liu et al. [LIU 00] who proposed an efficient and versatile algorithm for the calculation of convolution products using FFT in 2D.

Using the CGM and FFT algorithms, various aspects of the contact problem can be analysed. For instance, Jacq et al. [JAC 02] have proposed a three dimensional algorithm for solving the elastic-plastic contact problem. Gallego et al. [GAL 06, GAL 10b] have studied the normal-tangential general problem through the fretting contact problem. Recently, Koumi et al. [KOU 15a], Spinu et al. [SPI 17a, SPI 17b, SPI 18b] have proposed to take into account the viscoelasticity of the materials in the modelling. Koumi et al. [KOU 14b, KOU 15b], Amuzuga et al. [AMU 16b] have studied the effects of inhomogeneities on the contact problem, and Bagault et al. [BAG 12, BAG 13] the effect of an anisotropic material.

Note that the inhomogeneities problems impose to deal with three dimensional quantities. A Galerkin vectors technique [YU 91, LIU 05] can be used for solving the problem. However, an extension of the FFT algorithm to 3D

has been proposed by Chaise [CHA 11a] in 3D Discrete Convolution FFT algorithm.

Many other phenomena have been studied with the help of the CGM and FFT algorithms. For example, layered bodies problem have been studied in [POL 00, WAN 11b, WAN 10, YU 14], tractive rolling contact in [MAN 21, XI 21], etc.

In the present work, a semi-analytical method is used. It is based on the CGM and FFT algorithms for the acceleration of the computations.

1.6 Conclusion

In this chapter, the context and the general concepts of the study have been exposed. The general definition of the pavement structure has been given as a multi-layered structure. From this definition, the difference between the rigid and the flexible pavements has been highlighted.

Further, a general overview of pavement dimensioning methods has been presented. Several examples of the methods from the USA, the UK, South Africa and France have been given to illustrate the variety of the methods as well as their common points.

Furthermore, a quick review of the state of art has been performed on the tire-pavement topic. The experimental and the various modelling aspects have been reviewed.

Ultimately, an important section has been dedicated to the Contact Mechanics which is the bedrock of the present work. In general, from the pioneer theory of Hertz to the actual numerical improvements, the main lines of the contact mechanics field have been presented. A particular look has been cast on the rolling contact as the tire-pavement contact is a rolling contact.

Chapter 2

A Semi-analytical Contact Model

This chapter is dedicated to the general semi-analytical model on the basis of which the present work is done. The contact problem, subdivided in its normal and tangential components, is solved in elasticity. For this purpose, the numerical tools are introduced and the general algorithm is presented.

Sommaire

2.1 Introduction

The developments in the PhD work are performed in a home made code named *Isaac*. Isaac is a semi-analytical code which embodies various aspects of the contact modelling. It takes into account any type of geometry for the bodies in contact, takes as input either forces or rigid body displacements, and any combination of them. The 3D problem is solved in Isaac for both static and moving loads, in both transient and steady-state regime.

In the beginning, Jacq [JAC 01] has developed the 3D model for solving the elastic-plastic contact. In this first version of Isaac, only the normal contact was solved. In 2007, Gallego [GAL 07b] has added the tangential component of the contact problem with view to solve the fretting contact problem. He succeeded in taking into account all the three modes of the fretting contact. Further, Boucly [BOU 08] has worked on plasticity and thermal effects. Chaise [CHA 11a] later tackled the impact problem. He extended the 2D-DC-FFT algorithm to 3D for solving the latter problem. The inhomogeneities problem have been studied later by Fulleringer [FUL 11], Leroux [LER 13], Koumi [KOU 15a] and Amuzuga [AMU 16a]. Also, in 2011 Fulleringer [FUL 11] worked on the wearing coupled with inclusion effects on the contact.

More recently, Koumi [KOU 15a] has introduced the viscoelastic behaviour of the materials in Isaac; and Manyo [MAN 19b] developed the tractive rolling contact in steady-state regime for elastic bodies.

In the present document, three new aspects are introduced:

- Coated bodies and multi-layered elastic bodies will be introduced. Coating has been earlier modelled in Isaac [FUL 11] but by using inhomogeneities. This technique is perfectly adapted to simulate wear of coating or the behaviour of a layer of not uniform thickness, however it is costly in terms of CPU time. To make it faster, the influence coefficients corresponding to coated bodies will be calculated (chapter 3). An extension to the multi-layered case for any number of layers will be made in chapter 4.

- An Elastic/Viscoelastic correspondence will be introduced for those layered bodies in order to solve the rolling contact between viscoelastic layered bodies.

- Finally, the transient tractive rolling contact will be solved between multi-layered elastic bodies (chapter 5). All the cases of tangential loading during the rolling motion will be taken into account.

The above new aspects are introduced in Isaac beside the existing code. Here, the focus is put on the general normal-tangential problem that will be modified later. Therefore, the goal of this chapter is to clearly expose the general formulations and algorithms used for solving the contact general problem in Isaac.

2.2 Formulation

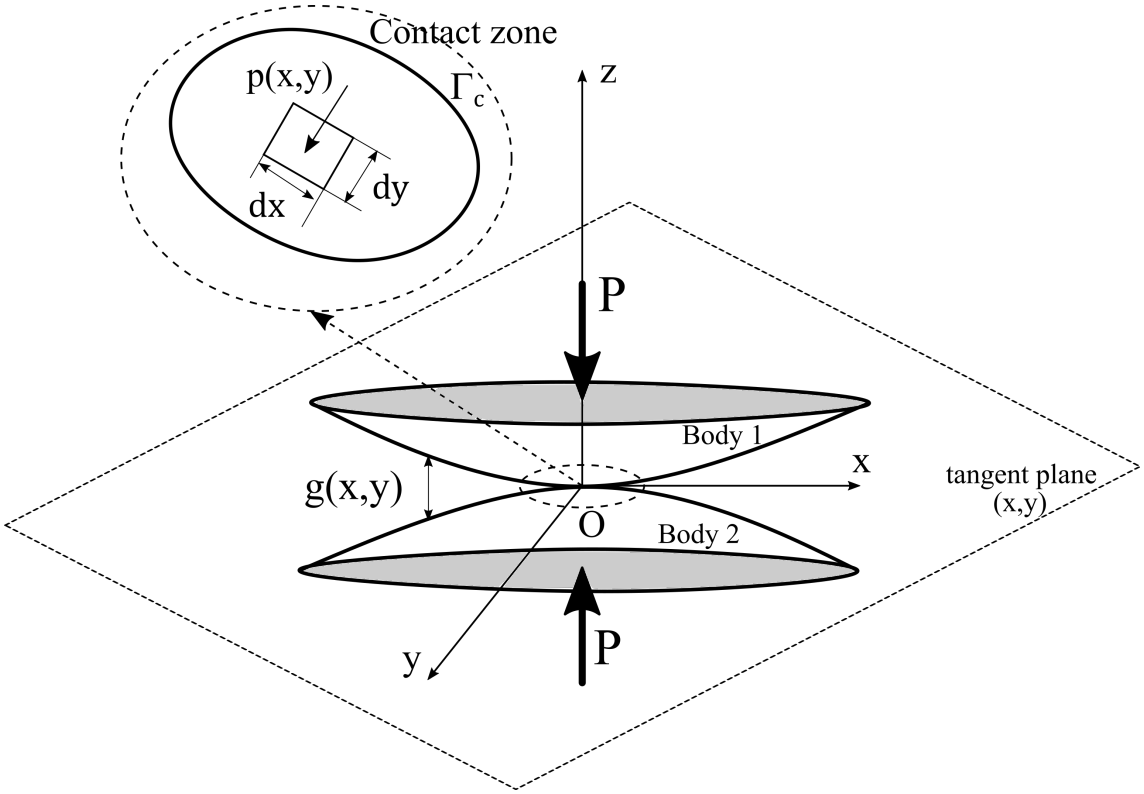

Figure 2.1: Illustration of the contact problem involving two elastic bodies B_1 and B_2 defined by the profile of their surfaces. The bodies are in contact over an area Γ_c in a tangent plane (x, y).

In theory, the general contact problem has to be solved in one procedure. Since this would be tedious, it is broken down into its two components: the *normal contact* and the *tangential contact* problems.

2.2.1 The normal contact problem

First of all, consider the contact between purely elastic bodies. The two elastic bodies B_1 and B_2 in contact are defined by their surface profiles in an orthonormal coordinate system $(Oxyz)$ (see Fig. 2.1). Note that only the non-conformal contact is considered. A contact is said conformal or conforming when the curvature of the surfaces in contact is such that in absence of applied loading the contact is a point or a line (or several points on the same line). Then, the (x, y) plane is the tangent plane of the contact, in which lies the first point or the first line of the contact when

no load is applied. For surface profiles defined with the functions:

$$z_1 = f_1(x,y) \tag{2.1}$$
$$z_2 = f_2(x,y), \tag{2.2}$$

where subscript 1 and 2 correspond to body 1 and body 2 respectively. Then, the initial separation function can be written as:

$$h(x,y) = f_1(x,y) - f_2(x,y). \tag{2.3}$$

The slopes of the surfaces of the bodies are supposed small enough to be confused with the tangent plane (x,y). In addition, the assumption of small strains is made such that the quadratic term in the Lagrangian strain formulation can be neglected. Then, the linearised strains are obtained as:

$$\varepsilon_{ij} = \frac{1}{2}(u_{i,j} + u_{j,i}), \tag{2.4}$$

where $u_{i,j}$ are the displacement gradients. Subscripts i and j take the values x,y,z; and $_{,j} = \partial/\partial x_j$. For the contact to happen, a force P normal to the tangent plane (x,y) is applied. Then, the contact occurs over an area Γ_c in which a pressure field $p(x,y)$ appears. Under the pressure field, the bodies deform with a displacement $u_z = u_{z1} + u_{z2}$. By taking into account the previous definitions, one can write the actual gap between the bodies as:

$$g(x,y) = h(x,y) + u_z + \delta, \tag{2.5}$$

where δ is the normal rigid body displacement. This δ allows to impose not only a normal force, but also a normal displacement as input of the simulations. Note that in this work, no interpenetration, magnetic or adhesion effects are considered.

From the previous remarks, it comes that the gap and the pressure are always positive quantities:

$$g(x,y) \geq 0 \qquad \text{and} \qquad p(x,y) \geq 0. \tag{2.6}$$

Considering a potential contact zone, where each point (x,y) in the tangent plane is either in the contact area or not, the contact conditions are defined as follow:

$$g(x,y) = 0 \quad - \quad (x,y) \in \Gamma_c, \quad \Rightarrow p(x,y) > 0 \tag{2.7a}$$
$$g(x,y) > 0 \quad - \quad (x,y) \notin \Gamma_c, \quad \Rightarrow p(x,y) = 0 \tag{2.7b}$$

The set of equations (2.5), (2.6) and (2.7), added to the equilibrium equation:

$$P = \int_{\Gamma_c} p(x,y) dx dy, \tag{2.8}$$

define the normal contact problem.

The problem as described above, considers only an applied normal load and solves the contact pressure. In fact, the general contact problem frequently involves a tangential component, since even a normal applied load can induce tangential displacements. Moreover, tangential loads can be applied at a macroscopic scale to the system; and in those cases it is mandatory to solve the tangential problem.

2.2.2 The tangential contact problem

The tangential component of the contact problem aims at finding the shear tractions in the contact zone. Those shear tractions are induced by the contact conditions: material properties, loading, friction between the bodies in contact, etc.

Consider two particles in the contact zone, having rigid body displacements x'_{1i} and x'_{2i}, and elastic displacements u'_{1i} and u'_{2i}, respectively for bodies 1 and 2. In an undeformed state, if the particles are facing each other, their position is given by $x'_{1i}+u'_{1i} \equiv x'_{2i}+u'_{2i}$ at the time step t'. At the next time step t, the particles are located at the positions $x_{1i}+u_{1i}$ and $x_{2i}+u_{2i}$. Hence, the notion of shift e is given by the difference:

$$e_i = (x_{1i}+u_{1i}) - (x_{2i}+u_{2i}) \qquad i = x, y. \tag{2.9}$$

The slip vector is related to the shift with the relation:

$$e_i = s_i(t-t') \tag{2.10}$$

Using the notation $\dot{\cdot} = \frac{d}{dt}$, the derivative with respect to time, after some developments, Kalker [KAL 90] found the form of the slip as:

$$s_i = (\dot{x}_{1i} - \dot{x}_{2i}) + \frac{1}{2}(\dot{x}_{1j} + \dot{x}_{2j})(u_{1i,j} - u_{2i,j}) + \partial(u_{1i} - u_{2i})/\partial t. \tag{2.11}$$

With $u_i = u_{1i} - u_{2i}$ the displacement difference, $v_i = -\frac{1}{2}(\dot{x}_{1i} + \dot{x}_{2i})$ the rolling velocity and $w_i = \dot{x}_{1i} - \dot{x}_{2i}$ the rigid slip, the slip can be rewritten in a simpler form as:

$$s_i = w_i - v_j u_{i,j} + \partial u_i/\partial t. \tag{2.12}$$

This equation embodies all the tangential motions: transient rolling, steady state rolling and shift motion. In the case of a transient rolling, the original Eq. (2.12) is retained. The steady state rolling occurs when the rolling motion does not depend on time. Thus, the slip during the steady state rolling is defined by suppressing the contribution of the time t:

$$s_i = w_i - v_j u_{i,j} \qquad \text{(Steady state rolling)}. \tag{2.13}$$

The shift motion is characterised by the fact that the rigid slip w_i is of the same order as the rolling velocity v_i. Thus the term $v_j u_{i,j}$ becomes negligible compared to the single term w_i. Then, the slip can be approximated by:

$$s_i = w_i + \partial u_i/\partial t \qquad \text{(Shift motion)}. \tag{2.14}$$

The above definition of slip (Eq. (2.12)) describes the relative tangential motion between two bodies in contact. This relative motion depends on the friction that is present at the contact interface. The concept of friction allows to establish how and

when the slip occurs.
The slip occurs when the tangential force $F_{\tan}$ reaches or exceeds a certain value $F_{\lim}$. On contrary, when $F_{\tan}$ is below that same force $F_{\lim}$, there is adhesion.
In order to give a value of that bound force, Coulomb [COU 85] proposed a law which states that the bound force $F_{\lim}$ is proportional to the normal force with a *friction coefficient* f ($F_{\lim} = f \times P$).
Using this coefficient of friction, the Coulomb's law is described as follow:

- When the magnitude of shear force is proportional to the magnitude of the normal force with a friction coefficient, the contact totally slips:

$$\|F_\tau\| = f \times P \qquad \Rightarrow \qquad \text{Slip} \tag{2.15}$$

- When the magnitude of shear force has a lower value compared to the magnitude of the normal force multiplied by the coefficient of friction, the contact sticks:

$$\|F_\tau\| < f \times P \qquad \Rightarrow \qquad \text{Stick.} \tag{2.16}$$

This law will be used throughout this work for the tangential contact modelling. It is used not only at a global scale i.e. for the overall applied force F_τ and P, but also at the local scale i.e. for local shear tractions $q_\tau(x,y)$ and pressure $p(x,y)$. It comes that the friction law at the local scale can be written as:

- When the magnitude of the contact shear vector is proportional to the pressure with the friction coefficient, the point slips:

$$\sqrt{q_x^2(x,y) + q_y^2(x,y)} = f \times p(x,y) \qquad \Rightarrow \qquad (x,y) \in \text{Slip zone } \Gamma_{slip} \tag{2.17}$$

- When the magnitude of the contact shear vector has a lower value compared to the pressure multiplied by the coefficient of friction, the point sticks:

$$\sqrt{q_x^2(x,y) + q_y^2(x,y)} < f \times p(x,y) \qquad \Rightarrow \qquad (x,y) \in \text{Stick zone } \Gamma_{stick} \tag{2.18}$$

with $\Gamma_{stick} \cup \Gamma_{slip} = \Gamma_c$.

Finally, the tangential contact problem is solved using the Eq. (2.12), the above Coulomb's law for friction and the equilibrium equations for the tangential forces F_x and F_y and the spinning moment M_z:

$$\begin{aligned} F_x &= \int\int_{\Gamma_c} q_x(x,y)dxdy \\ F_y &= \int\int_{\Gamma_c} q_y(x,y)dxdy \\ M_z &= \int\int_{\Gamma_c} (xq_y(x,y) - yq_x(x,y))dxdy. \end{aligned} \tag{2.19}$$

THE CONTACT PROBLEM	
NORMAL	TANGENTIAL
$g(x,y) = h(x,y) + u_z + \delta$	$s_i = w_i - v_j u_{i,j} + \partial u_i / \partial t$
$g(x,y) \geq 0; p(x,y) \geq 0$	$\|F_\tau\| \leq f \times P$
$g(x,y) = 0$ – $(x,y) \in \Gamma_c, \Rightarrow p(x,y) > 0$	$\|q_\tau(x,y)\| = f \times p(x,y) \Rightarrow (x,y) \in \Gamma_{slip}$
$g(x,y) > 0$ –$(x,y) \notin \Gamma_c, \Rightarrow p(x,y) = 0$	$\|q_\tau(x,y)\| < f \times p(x,y) \Rightarrow (x,y) \in \Gamma_{stick}$
	$\Gamma_{stick} \cup \Gamma_{slip} = \Gamma_c$
$P = \int_{\Gamma_c} p(x,y) dxdy$	$F_x = \int \int_{\Gamma_c} q_x(x,y) dxdy$
	$F_y = \int \int_{\Gamma_c} q_y(x,y) dxdy$
	$M_z = \int \int_{\Gamma_c} (x q_y(x,y) - y q_x(x,y)) dxdy$

Table 2.1: Constitutive equations for the general contact problem.

In summary, the constitutive equations of the contact problem are given in Tab. 2.1.

At this point, the contact problem is mathematically formulated through the equations that constitute the problem. In the formulation, we have hypothesised that the displacements can be calculated. However, the calculation of the displacements requires some assumptions. For finding those displacements, the notion of influence coefficients is used. This notion is described in the next section when considering the bodies in contact as semi-infinite.

2.2.3 The Half-space approximation

In contact mechanics, the bodies are usually considered as semi-infinite according to the assumption of Hertz [HER 82]. This hypothesis means that the dimensions of the bodies are large in comparison with the dimension of the potential contact area. The assumption has been kept since it has allowed to get widely acceptable results. Thus, in the present work, the bodies are considered as semi-infinite.
Under this assumption, the elastic field (stresses and displacements) has to be found.

For this purpose, consider an elastic half-space limited by the surface defined by the plane $z = 0$. The methodology consists in applying unit pressure and shears at the surface and then to find the response (generally analytically). With the solution for the a unit load, the solution for an applied field is found by superposition i.e. by integration. Figure 2.2 shows the response at a point $\bar{M}$ of the surface and at a point M in the subsurface, due to an applied unit force at the point O. The stresses and displacements found that way in the whole solid, are called *influence coefficients*, *unit response* or *Green functions*.

Once the influence coefficients are found, the response of the half-space under pressure and shear fields are obtained by an integration. For example, the displace-

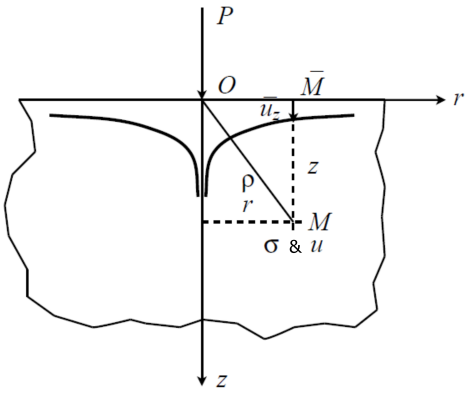

Figure 2.2: Illustration of the unit response of a half space for the determination of influence coefficients [JOH 85].

ment u_I induced by a pressure field at the contact surface is given by

$$u_I(x,y,z) = \int\int_{\Gamma_c} p(x',y')G_I^p(x-x',y-y',z)dx'dy' \tag{2.20}$$

where G_I^p are the influence coefficients of the displacements induced by a unit pressure. Equivalent forms stand for the other stresses. In practice, the influence coefficients can be found for any kind of problem such as inhomogeneities, layers, impact, etc.

In the case of an elastic homogeneous isotropic half-space, the influence coefficients have been explicitly found. Boussinesq [BOU 85] and Cerruti [CER 82] developed a theory of potentials for elasticity in solid mechanics. The resulting potentials of Boussinesq and Cerruti with further development by Love [LOV 52] are summarised in the book of Johnson [JOH 85].
The key solutions of the potential theory of Boussinesq are briefly exposed in a general form. We are seeking for the effects of a loaded point $C(\xi,\eta)$ in a loaded region S, on a general point $A(x,y,z)$ in the homogeneous elastic isotropic half-space of elastic constants E and ν (Fig. 2.3). For pressure and shear fields $p(\xi,\eta)$, $q_x(\xi,\eta)$ and $q_y(\xi,\eta)$ acting on S, the following potential functions have been defined:

$$\begin{aligned} F_1 &= \iint_S q_x(\xi,\eta)\Omega d\xi d\eta, \\ G_1 &= \iint_S q_y(\xi,\eta)\Omega d\xi d\eta, \\ H_1 &= \iint_S p(\xi,\eta)\Omega d\xi d\eta, \end{aligned} \tag{2.21}$$

where

$$\Omega = z\ln(\rho+z) - \rho, \tag{2.22}$$

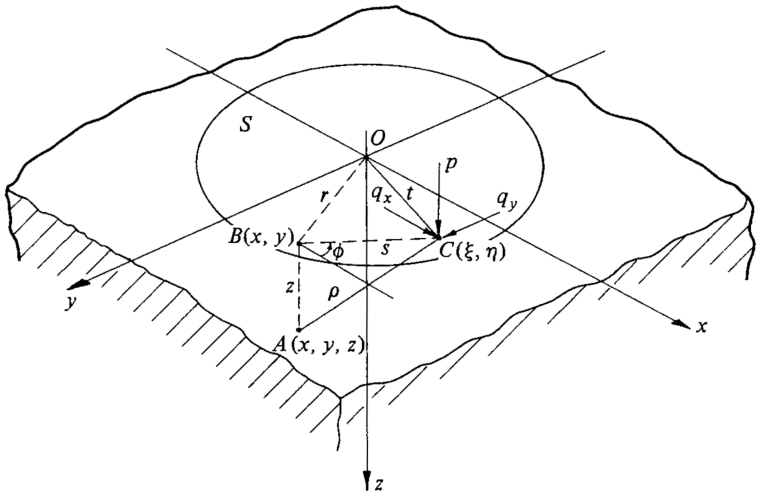

Figure 2.3: Half-space solution for the theory of potentials of Boussinesq [JOH 85].

with

$$\rho = [(\xi - x)^2 + (\eta - y)^2 + z^2]^{1/2}. \tag{2.23}$$

The partial derivatives of the above potential functions, give additional potential functions:

$$\begin{aligned} F &= \frac{\partial F_1}{\partial x} = \iint_S q_x(\xi,\eta)\ln(\rho+z)d\xi d\eta, \\ G &= \frac{\partial G_1}{\partial x} = \iint_S q_y(\xi,\eta)\ln(\rho+z)d\xi d\eta, \\ H &= \frac{\partial H_1}{\partial x} = \iint_S p(\xi,\eta)\ln(\rho+z)d\xi d\eta, \\ \psi_1 &= \frac{\partial F_1}{\partial x} + \frac{\partial G_1}{\partial y} + \frac{\partial H_1}{\partial z}, \\ \psi &= \frac{\partial \psi_1}{\partial z} = \frac{\partial F}{\partial x} + \frac{\partial G}{\partial y} + \frac{\partial H}{\partial z}. \end{aligned} \tag{2.24}$$

Thus the displacements have been shown by Love [LOV 52] to be given by:

$$\begin{aligned} u_x &= \frac{1}{4\pi G}\left\{2\frac{\partial F}{\partial z} - \frac{\partial H}{\partial x} + 2v\frac{\partial \psi_1}{\partial x} - z\frac{\partial \psi}{\partial x}\right\}, \\ u_y &= \frac{1}{4\pi G}\left\{2\frac{\partial G}{\partial z} - \frac{\partial H}{\partial y} + 2v\frac{\partial \psi_1}{\partial y} - z\frac{\partial \psi}{\partial y}\right\}, \\ u_z &= \frac{1}{4\pi G}\left\{\frac{\partial F}{\partial z} - (1-2v)\psi - z\frac{\partial \psi}{\partial z}\right\}, \end{aligned} \tag{2.25}$$

and the equivalent stresses related with the Hooke's law can be written as:

$$\begin{aligned}
\sigma_x &= \frac{2vG}{1-2v}\left(\frac{\partial u_x}{\partial x}+\frac{\partial u_y}{\partial y}+\frac{\partial u_z}{\partial z}\right)+2G\frac{\partial u_x}{\partial x},\\
\sigma_x &= \frac{2vG}{1-2v}\left(\frac{\partial u_x}{\partial x}+\frac{\partial u_y}{\partial y}+\frac{\partial u_z}{\partial z}\right)+2G\frac{\partial u_y}{\partial y},\\
\sigma_x &= \frac{2vG}{1-2v}\left(\frac{\partial u_x}{\partial x}+\frac{\partial u_y}{\partial y}+\frac{\partial u_z}{\partial z}\right)+2G\frac{\partial u_z}{\partial z},\\
\tau_{xy} &= G\left(\frac{\partial u_x}{\partial y}+\frac{\partial u_y}{\partial x}\right),\\
\tau_{yz} &= G\left(\frac{\partial u_y}{\partial z}+\frac{\partial u_z}{\partial y}\right),\\
\tau_{zx} &= G\left(\frac{\partial u_z}{\partial x}+\frac{\partial u_x}{\partial z}\right).
\end{aligned} \tag{2.26}$$

For the purpose of finding the influence coefficients, it only takes to apply a unit pressure and further unit shears. Doing so, and over a unit discretised rectangular element, leads to the elastic field given in appendix A.
Finding influence coefficients for layered bodies has been a non negligible part of the present work. The influence coefficients for a layered body and for a multi-layered body have been found. Those influence coefficients used for the modelling of elastic and viscoelastic contacts are exposed in details in chapters 3 and 4. In what follows, the influence coefficients are supposed found for the calculation of the displacements needed for solving the contact problem formulated in section 2.2. To solve the problem, numerical procedures have been put together. The discretisation needed for the numerical resolution is presented in the next section.

2.3 Discretisation procedure

The numerical resolution of a problem imposes to turn the continuous functions into discretised variables. This induces some constraints in the methodology.

The problem to solve is not only the contact problem but also a volume problem, as the stresses in the bodies are of undeniable interest, particularly for the purpose of this document which is the pavement modelling. From the previous section, the elastic field can be calculated by using the influence coefficients. However as one can observe in Fig. 2.2, a singularity appears when a load is applied on a point. In order to be able to use the numerical tools which are going to be presented, there is a need of doing a discretisation of the solids. Therefore, it is important to keep the continuity of the loading while avoiding the singularities.

In this respect, firstly, a discretisation of the contact surface is performed with rectangular elements and the volume with hexahedrons. Each element of the discretisation is taken in such a way that it is centred in the calculation point. Thus,

the contact surface is discretised with $N_p = N_x \times N_y$ elements of size $dS = \Delta_x \times \Delta_y$. Figure 2.4 shows the example of a repartition of pressure on a discretised contact surface. A constant pressure is applied on every rectangular element.

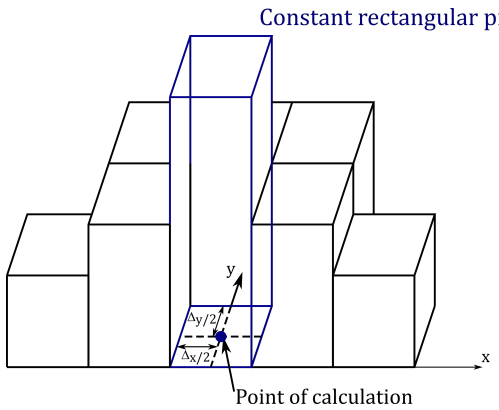

Figure 2.4: Discretisation of the contact zone with rectangular elements centred in the calculation points.

Secondly, a dimension Δ_z is added to the discretisation for the calculation of the elastic field in the volume. Two important precisions have to be brought out:

- ✧ The methodology using influence coefficients has been explained analytically for a loading on a point. However, a singularity is observed at the loaded point. In order to avoid that singularity, the influence coefficients are to be found on the single rectangular element. In the case of a homogeneous half-space, those influence coefficients have been developed by Love for a constant pressure on a rectangular surface and extended by Vergne [VER 85] for a constant shear loading. The reader may find those results in appendix A.

- ✧ The use of *Fast Fourier Transform (FFT)* (FFT is described in section 2.4.1) imposes to keep constant and regular the discretisation in each direction.

The FFT are extensively used in this work coupled with other numerical methods. In order to understand the above constraints for the discretisation and further to understand the numerical solving, the next section is devoted to the main numerical tools.

2.4 Numerical tools

The present semi-analytical model for solving the contact problems is mainly based on analytical solutions coupled with acceleration algorithms. Those numerical tools are chosen for their efficiency. The two main tools used throughout the work are the *Fast Fourier Transform (FFT)* algorithms and the *Conjugate Gradient Method (CGM)*.

The first one is mainly used because it allows to calculate efficiently convolution products such as in Eq. (2.20) (which allows to evaluate the displacements). The FFT based on the Fourier integral transformation is described below.

2.4.1 The Fourier Transform(FT)

The Fourier Transform (FT) is an integral transformation which transforms an integrable function into its frequency spectrum. The Fourier Transform in one dimension for a function $y(t)$ is defined by the following equation:

$$\tilde{y}(w) = \int_{-\infty}^{+\infty} y(t) e^{-iwt} dt, \tag{2.27}$$

where i is the imaginary unit symbol of complex numbers. Alternative definitions exist, the only difference being a multiplying factor. If the function $\tilde{y}$ is an integrable function, then can be defined the *inverse Fourier Transform* (IFT):

$$y(t) = FT^{-1}(\tilde{y})(t) = \frac{1}{2\pi} \int_{-\infty}^{+\infty} \tilde{y}(w) e^{+iwt} dw. \tag{2.28}$$

To illustrate the interest put on the FT in the present work, let's take the example of a convolution product in one dimension:

$$y(t) = \int_{-\infty}^{+\infty} x(t) h(t-\tau) d\tau \equiv x(t) * h(t). \tag{2.29}$$

$y(t)$ is a linear convolution (sign $*$) between the functions $x(t)$ and $h(t)$.
With the definition of the FT, one can demonstrate that a convolution is transformed into a term-to-term product in the frequency domain. Thus the FT of Eq. (2.29) becomes:

$$\tilde{y}(w) = \tilde{x}(w).\tilde{h}(w). \tag{2.30}$$

This property of the FT is one of the key tools to use efficiently the influence coefficients.

FT as defined above concerns a *continuous* function defined in $]-\infty;+\infty[$. Nevertheless, one can observe that the contact problem is defined and solve in a *discrete finite* domain. To overcome the limitations brought out by the latter remark, Fourier transform algorithms have been developed to calculate numerically the FT integrals. Their interest is huge for signal processing in electronics, in optics, for sounds and images, for data compression, etc. and for calculations in computational mechanics In all these areas, there is a need to have a discrete definition of the above continuous definitions of the FT. In this respect, let's state the discrete functions h_r and x_r equivalent to $h(t)$ and $x(t)$ respectively. For a discrete sample of N values in a zone L_0, the discrete Fourier transform is defined by:

$$\widehat{h}_s = \sum_{r=0}^{N-1} h_r e^{-2\pi irs/N}, \quad s = 0, \ldots, N-1 \tag{2.31}$$

and the discrete inverse Fourier transform is:

$$h_j = (1/N) \sum_{r=0}^{N-1} \widehat{h}_r e^{2\pi i r j/N}, \quad j = 0, \ldots, N-1. \tag{2.32}$$

In the same way as the continuous definition, the convolution property stands:

$$y_j = \sum_{r=0}^{N-1} x_r h_{j-r}, \quad j = 0, \ldots, N-1. \tag{2.33}$$

Note that, from the very first definition of the Fourier transform, the transform is implicitly performed over an infinite domain. By the discretisation, this assumption has not been removed. The discretisation only changes the discrete finite signal into a periodic signal with the same length L_0. A convolution in this case is called a circular or cyclic convolution. Thence, the convolution can be rewritten by using the Heaviside step function H as:

$$y_j = \mathbf{x} \otimes \mathbf{h} = \sum_{r=0}^{N-1} x_r h_{j-r+NH(r-j)}, \quad j = 0, \ldots, N-1 \tag{2.34}$$

where

$$H(t) \begin{cases} =0 \text{ if } t < 0 \\ =1 \text{ if } t \geq 0 \end{cases}. \tag{2.35}$$

Note again that $\mathbf{x}$ and $\mathbf{h}$ have the same number of elements $j \in [0, N-1]$. The Heaviside function introduced in the convolution allows to avoid the non positive values. Finally, there is a cyclic sum and thus a periodicity of length L_0 has been introduced in the signal.

The discrete FT calculation have lead to Fast Fourier Transform (FFT) algorithms which are so-called because of their efficiency in term of computation time. In the following subsection, a quick bird-eye view of the FFT algorithms is presented.

2.4.1.1 Fast Fourier Transform methods

Fast Fourier Transforms (FFT) are methods based on the Fourier transform properties with acceleration based on the reduction of the number of operations needed. For given functions, the calculation of their FT based directly on the discrete definitions of Eqs. (2.31) and (2.32) are not interesting in practice. In fact, doing that would demand $(N-1)^2$ complex products and $N \times (N-1)$ complex sums. To counteract this disadvantage, a rapid version is proposed. In this version, only are needed $\frac{N}{2} \times (\log N - 2)$ products and $N \times \log N$ sums. The algorithms depend generally on the factorial of N. One can find a wide range of FFT algorithms nowadays: the algorithm of Cooley and Tukey [COO 65] (for sizes power of 2), the PFA algorithm of Good-Thomas based on the Chinese remainder theorem, the algorithm of Winograd which uses a Cyclotomic polynomial, etc. In the present work, the FFT algorithms

of Singleton [SIN 69] based on the algorithms of Cooley and Tukey extended to sizes non power of 2 are used.

In the same manner, the inverse Fourier Transform (IFT) are performed using the FFT algorithms with a cost in $O(N \log N)$ instead of $O(N^2)$. Thus a convolution in the Fourier frequency domain costs $O(N)$ operations against $O(N^2)$ in the space domain.
Finally, using FFT algorithms, one needs $O(N + 3N)$ instead of $O(N^2)$, which is very interesting, especially for large N.

Nevertheless, a cost is paid for the rapidity of a method. This cost is related to the possible errors that have to be controlled when using FFTs. Those errors are discussed in the following lines.

2.4.1.2 Possible errors due to the use of FFT

In most cases, the functions to be convoluted are not periodic. Thus, an error is introduced when using FFT since this method supposes that the functions are periodic in order to cover the infinite domain. Therefore, the main problem which appears is the *recovery problem*. Liu et al. [LIU 00] have studied the origin of this error for the contact problem and proposed improvement to avoid it.
Figure 2.5 illustrates this phenomenon for a discrete one-dimensional convolution of a sample of pressures p and coefficients of influence K. The convolution being cyclic, the pressure field becomes periodic. At the beginning and at the end of the convolution process, the pressures added to the left and to the right interfere with the influence coefficients. The result will therefore be modified because of this phenomenon.
The appropriate method for avoiding this recovery problem is to perform a "zero-padding" [PRE 92].

The zero-padding technique consists in expanding the size of the two samples from N to $2N$ using zeros. In this way, as shown in figure Fig. 2.6, recovery is no longer possible. This technique is proposed by Liu et al. [LIU 00] coupled with the DC-FFT. However, authors like Ju and Farris [JU 96] have extended the contact area at least five times to avoid the errors. Liu et al. clarifies this fact by describing the method used by Ju and Farris. The latter method is called *Cyclic Convolution and Fourier Transform (CC-FFT)*. It consists in,

- finding the frequency spectrum of the pressures with the FFT;
- then, the influence coefficients are directly determined by sampling the frequency response obtained by a continuous Fourier transform of the continuous function associated to the influence coefficients.

An error then appears following the latter sampling: this is the phenomenon of *aliasing*. The frequency response obtained does not correspond to that which should have been obtained if the sampling had been done upstream of the FFT. Then the

product of the two samples is made, followed by the IFFT to obtain the result in the space domain. This methodology therefore leads to an error which cannot be limited without a significant extension of the contact zone.

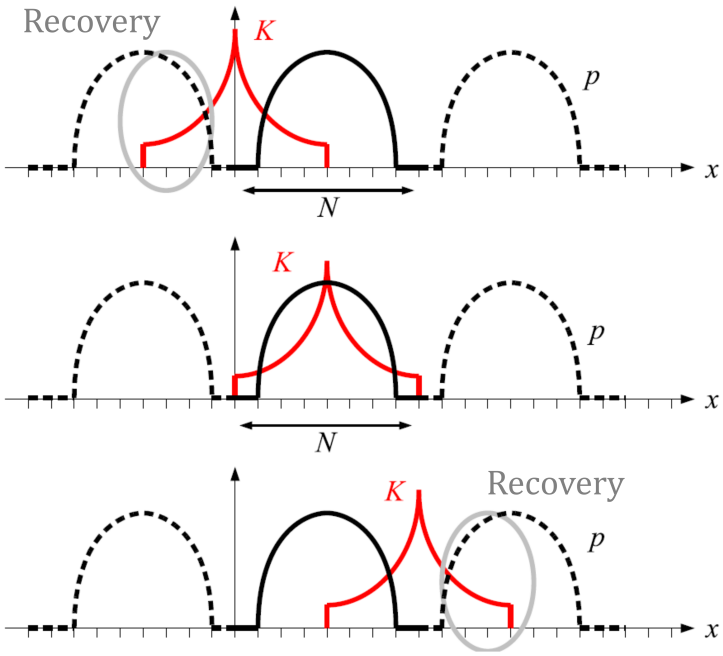

Figure 2.5: Illustration of the recovery phenomenon due to periodicity of the signal when performing discrete convolutions [GAL 07b].

In this work, the proposed discrete convolution with fast Fourier transform method (DC-FFT) from Liu et al. [LIU 00] is used. It avoids the above problems and is described below.

2.4.1.3 The DC-FFT method

The Discrete Convolution and Fast Fourier Transform (DC-FFT) method proposed, embodies the wrap-around order and zero-padding techniques explained further. The steps of the method are:

a) Find the influence coefficients, $\{K_j\}_N$;

b) Extend the influence coefficients by wrap-around order, $\{K_j\}_{2N}$;

c) Apply the FFT to the extended influence coefficients, $\{\tilde{K}_s\}_{2N}$;

d) Enter the pressures, $\{p_j\}_N$;

e) Extend the pressures using the zero-padding, $p_j = p_j, \quad j \in [0, N-1]$ and $p_j = 0, \quad j \in [N, 2N-1]$;

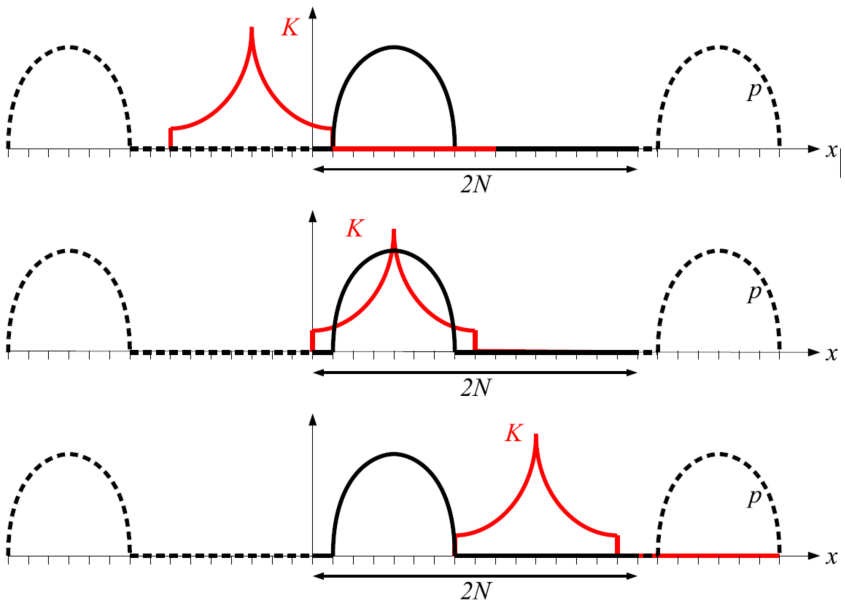

Figure 2.6: Illustration of the zero padding technique to avoid the recovery phenomenon for discrete convolutions [GAL 07b].

f) Apply the FFT to the extended pressures, $\{\tilde{p}_j\}_{2N}$;

g) Perform a term to term product in the Fourier frequency domain, $\{\tilde{\nu}_j\}_{2N}$;

h) Apply the IFFT to obtain the wanted quantity $\{u_j\}_{2N}$;

i) Truncate the result to keep $\{u_j\}_{2N}$, $j \in [0, N-1]$.

Zero-padding The distribution is extended with zero values for the indices N to $2N+1$ while the initial values are kept in the range 0 to $N-1$. This is particularly done in this work for the surface fields (the pressure and shear distributions).

Wrap-around order Applied to the influence coefficients, the wrap-around order consists in two steps.

➢ Firstly, the initial coefficients are extended with zero values for the index N.

➢ Secondly, for the indices $N+1$ to $2N-1$ the initial (0 to $N-1$) indices are written symmetrically with respect to the index N. In function of the parity of the influence coefficients, an opposite sign is applied to the extended range of coefficients. For even coefficients the coefficients have to be extended like in Fig. 2.7 and for odd coefficients they should be extended like in Fig. 2.8.

The DC-FFT method presented above for one dimension can be applied for the two dimensional case. For the 2D-DC-FFT, a transform is performed in both

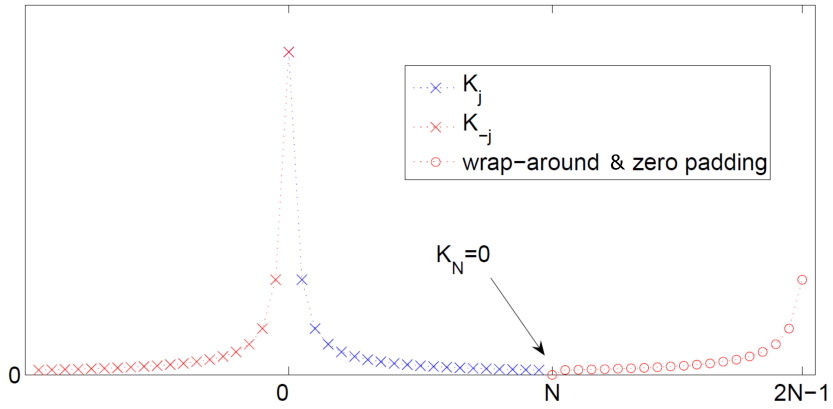

Figure 2.7: Illustration of the wrap-around and zero padding of the even influence coefficients while doing the DC-FFT [GAL 07b].

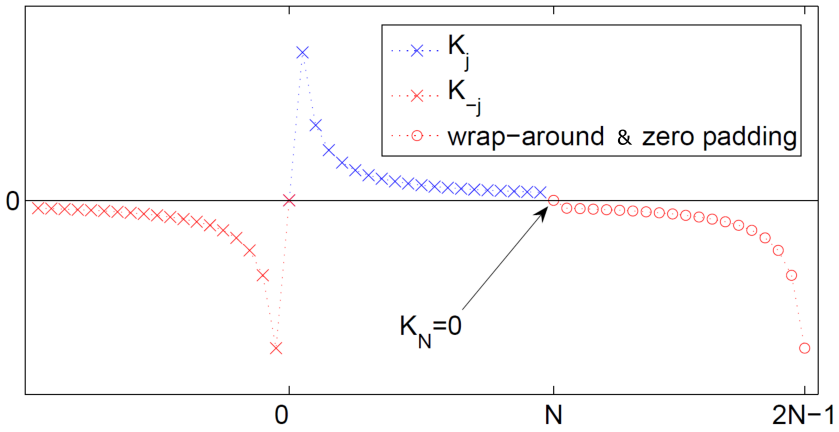

Figure 2.8: Illustration of the wrap-around and zero padding of the odd influence coefficients while doing the DC-FFT [GAL 07b].

directions. Then, a reduction of the number of operations is obtained from $O(N_1^2 \times N_1^2)$ to $O(2N_1 \times 2N_2 \times \log 2N_1 \times 2N_2)$. The convolution in the frequency domain demands $O(2N_1 \times 2N_2 \times \log 2N_1 \times 2N_2)$ operations as well as the IFT. Thus, for a 2D-DC-FFT, the need for $O(N_1^2 \times N_1^2)$ operations is turned into a total need for $O(2N_1 \times 2N_2 + 3 \times (2N_1 \times 2N_2) \times \log 2N_1 \times 2N_2)$ operations.
The 2D-DC-FFT will allow to calculate 2D fields particularly in the contact zone. For calculation of the 3D fields, two possibilities arise:

- ❖ use the 2D-DC-FFT for every value of the third component or
- ❖ implement the 3D-DC-FFT in analogy with what has been done previous.

The latter technique is mainly used when dealing with inhomogeneities or when 3D images are involved. In the context of this study, the use of only the 2D-DC-FFT

algorithm is sufficient to have a good gain in term of simulation time.

In summary, the DC-FFT algorithm proposed allows to calculate efficiently the elastic fields. The reduction of the number of operations needed implies a significant decrease of computation time. The wrap-around and zero-padding techniques considerably reduce the errors. However, in order to calculate the elastic fields, the contact problem has to be solved. For this purpose, the numerical process used is the Conjugate Gradient Method (CGM).

2.4.2 The Conjugate Gradient Method

The Conjugate Gradient Method (CGM) is an optimisation method developed by Hestenes and Stiefel [HES 80] based on Conjugate Direction methods. It allows to solve systems of linear equations. It can also be used to solve unconstrained optimisation problems such as energy minimisation.
The problem to solve is a system of linear equations. For instance, let $\mathbf{A}$ be a real symmetric (i.e. $\mathbf{A}^T = \mathbf{A}$) and positive-definite (i.e. $\mathbf{x}^T\mathbf{A}\mathbf{x} > 0$ for all non-zero vectors $\mathbf{x} \in \mathbb{R}^N$) matrix of size $N \times N$; and $\mathbf{b}$ a real vector of size N. Note that the superscript ^{T} stands for the transpose. The system to solve can be written as:

$$\mathbf{A}\mathbf{x} = \mathbf{b} \tag{2.36}$$

for the unknown $\mathbf{x}$.
In order to introduce the concept of conjugacy, consider two vectors $\mathbf{u}$ and $\mathbf{v}$. Those vectors are conjugate if $\mathbf{u}^T\mathbf{A}\mathbf{v} = 0$. For a set of mutually conjugate vectors $Q = \{\mathbf{p}_1, \cdots, \mathbf{p}_N\}$ with respect to $\mathbf{A}$, the solution $\mathbf{x}_*$ of the system in Eq. (2.36) has been proven to be:

$$\mathbf{x}_* = \sum_{i=1}^{N} \alpha_i \mathbf{A}\mathbf{p}_i \tag{2.37}$$

with $\alpha_i = \frac{\mathbf{p}_k^T\mathbf{b}}{\mathbf{p}_k^T\mathbf{A}\mathbf{p}_k}$. This solution is the direct solution for a well chosen set of conjugate vectors Q. When N is large, the direct method becomes very consuming. However, if Q is chosen well enough, it might not be necessary to find all of the $\mathbf{p}_k$ to obtain a good approximation of the solution. Then, the CGM can be regarded as an iterative method.

The iterative way to formulate the CGM needs to start from an initial point $\mathbf{x}_0$ and then use a metric to get closer to the solution $\mathbf{x}_*$. The procedure consists in writing the problem as a quadratic function

$$\phi(\mathbf{x}) = \frac{1}{2}\mathbf{x}^T\mathbf{A}\mathbf{x} - \mathbf{x}^T\mathbf{b}, \qquad \mathbf{x} \in \mathbb{R}^N \tag{2.38}$$

that has to be minimised. The gradient of the quadratic function solves the initial problem since:

$$\nabla\phi(\mathbf{x}) = \mathbf{A}\mathbf{x} - \mathbf{b}. \tag{2.39}$$

For the first basis vector $\mathbf{p}_0$, one obtain $\mathbf{p}_0 = \mathbf{b} - \mathbf{A}\mathbf{x_0}$ which is the gradient. The name of Conjugate Gradient Method comes from the fact that the other vectors will be conjugated to this vector $\mathbf{p}_0$.
Note that the gradient in Eq. (2.39) is also the residue $\mathbf{r}(\mathbf{x})$ of the system:

$$\mathbf{r}(\mathbf{x}) = \nabla\phi(\mathbf{x}) = \mathbf{A}\mathbf{x} - \mathbf{b}. \tag{2.40}$$

At the step k, the optimal next location is given by:

$$\mathbf{x}_{k+1} = \mathbf{x}_k + \alpha_k \mathbf{p}_k \tag{2.41}$$

where

$$\alpha_k = \frac{\mathbf{p}_k^T(\mathbf{A}\mathbf{x_k} - \mathbf{b})}{\mathbf{p}_k^T\mathbf{A}\mathbf{p_k}} = \frac{\mathbf{p}_k^T\mathbf{r_k}}{\mathbf{p}_k^T\mathbf{A}\mathbf{p_k}}. \tag{2.42}$$

The CGM method as presented above is an exact method where the solution can be obtain in N iterations. However, one of its main advantage is the speed of descent, which allows to obtain a good approximation in few steps. This aspect is very useful for large size systems. The second main advantage is the fact that for the approximation at a certain step, there is only a need of recording the data of the previous step. In this way, it generally uses a low amount of memory.
Finally the CGM algorithm can be summarised as:

Conjugate Gradient Method (CGM) general algorithm:
`Choose the starting point` $\mathbf{x}_0$ `and the error` ε

$$\mathbf{r}_k \leftarrow \mathbf{A}\mathbf{x_0} - \mathbf{b}$$

`if` $\mathbf{r}_0 < \varepsilon$`, then return` $\mathbf{x}_0$ `as result`
$\mathbf{p}_0 \leftarrow \mathbf{r}_0$
$k \leftarrow 0$
`repeat`

$$\alpha_k \leftarrow \frac{\mathbf{r}_k^T\mathbf{r_k}}{\mathbf{p}_k^T\mathbf{A}\mathbf{p_k}};$$
$$\mathbf{x}_{k+1} \leftarrow \mathbf{x}_k + \alpha_k\mathbf{p}_k;$$
$$\mathbf{r}_{k+1} \leftarrow \mathbf{r}_k + \alpha_k\mathbf{p}_k;$$

`if` $\mathbf{r}_{k+1} < \varepsilon$`, then exit loop`

$$\beta_k \leftarrow \frac{\mathbf{r}_{k+1}^T\mathbf{r}_{k+1}}{\mathbf{r}_k^T\mathbf{r}_k};$$
$$\mathbf{p}_{k+1} \leftarrow -\mathbf{r}_{k+1} + \beta_k\mathbf{p}_k;$$
$$k \leftarrow k+1$$

```
end repeat
return x_{k+1} as the result
```

The CGM algorithm developed for solving unconstrained problem has been extended to constrained linear systems as:

$$\min_{\mathbf{x}\in\Re^n} \phi(\mathbf{x}) = \frac{1}{2}\mathbf{x}^T\mathbf{A}\mathbf{x} - \mathbf{b}^T\mathbf{x}, \quad \text{with} \begin{cases} c_i(\mathbf{x}) = 0, & i \in \mathcal{E} \\ c_i(\mathbf{x}) \geq 0, & i \in I \end{cases} \tag{2.43}$$

The contact problem is constrained by the contact conditions as defined for example in Eq. (2.7) for the normal contact.
To be able to apply the CGM algorithm to the contact problem, it is important to write it in the adequate form in Eq. (2.43) with the corresponding constrains.

Then, the contact problem has to be formulated in the form of a minimisation problem so that it can be solved with the CGM. This form is called the variational formulation of the contact problem. It is given for both the normal and the tangential components of the contact problem. And the resulting algorithms for solving the general normal and tangential problems are presented.

2.5 A Semi-analytical method for solving the Contact Problem

The contact problem is divided into a normal and a tangential part. Their constitutive equations are described in Tab. 2.1. However, those forms are not adequate for the use of the CGM algorithm.
Firstly, let us focus on the normal component of the problem. Its variational formulation is given and then the algorithm for solving it are presented.

2.5.1 Variational Formulation of the Normal Contact

The variational formulation of a problem is the formulation which turns it into an optimisation problem. Duvaut and Lions [DUV 72] have developed those formulations for the contact problem using the virtual work and complementary virtual work. Further, Kalker [KAL 90] has extended the conventional extremum principle to all frictionless contact problems and to quasi-identical frictional contact problems. The existence and uniqueness of the contact solution is also well proved [DUV 72, KAL 90].
In summary, the normal contact problem in its variational formulation can be written as:

$$\min\left(\frac{1}{2}\mathbf{p}^T\mathbf{A}_\mathbf{z}^\mathbf{p} + \mathbf{h}^{*T}\mathbf{p} + c_\tau\right), \tag{2.44a}$$

$$p_{ij} \geq 0, \tag{2.44b}$$

where $\mathbf{p}$ is the vector for the pressure field; $\mathbf{A}_\mathbf{z}^\mathbf{p}$ the influence coefficients for the normal displacement at the surface due to the pressure; $\mathbf{h}^*$ the vector for the initial

gap, the rigid body displacement and the normal displacements induced by the shear fields at the surface since they do not induce any work. c_τ is the complementary energy due to the tangential problem that is supposed already solved.

For solving this problem (Eq. (2.44)), consider a general constrained minimisation problem defined as:

$$\min_{\mathbf{x}\in\Re^n} \phi(\mathbf{x}), \text{ with } \begin{cases} c_i(\mathbf{x}) = 0, & i \in \mathcal{E}, \\ c_i(\mathbf{x}) \geq 0, & i \in \mathcal{I}. \end{cases}$$

In this definition, there are equality constraints and inequality constraints. The latter are active when $c_i(\mathbf{x}) = 0$, $i \in I$. The active set is then given by

$$\mathcal{A}(\mathbf{x}) = \mathcal{E} \cup \{i \in I \mid c_i(\mathbf{x}) = 0\}. \tag{2.45}$$

In the contact problem, the active set cannot be defined *a priori* since the contact zone is not known in advance. Thus, to control the active set, the Lagrangian method is used.
For the problem in Eq. (2.45), the general Lagrangian formulation is given by:

$$\mathcal{L}(\mathbf{x}, \lambda) = \phi(\mathbf{x}) - \sum_{i\in\mathcal{E}\cup\mathcal{I}} \lambda_i c_i(\mathbf{x}) \tag{2.46}$$

where λ_i are the Lagrange multipliers. Those multipliers will allow to solve the constraints since the problem is now equivalent to solving the Karush Kuhn and Tucker optimality conditions:

$$\begin{aligned} \nabla_x \mathcal{L}(x, \lambda) &= 0, \\ c_i(x) &= 0, \quad \forall i \in \mathcal{E} \\ c_i(x) &\geq 0, \quad \forall i \in \mathcal{I} \\ \lambda_i(x) &\geq 0, \quad \forall i \in \mathcal{I} \\ \lambda_i(x) c_i(x) &= 0, \quad \forall i \in \mathcal{E} \cup \mathcal{I} \end{aligned} \tag{2.47}$$

The last equation in the above relations is the complementary condition that can also be written as:

$$c_i(\mathbf{x}) > 0, \quad \lambda_i = 0, \tag{2.48a}$$

$$c_i(\mathbf{x}) = 0, \quad \lambda_i \geq 0, \tag{2.48b}$$

Finally, the variational formulation of the normal contact problem with the Lagrangian method reads:

$$\min\left(\frac{1}{2}\mathbf{p}^T \mathbf{A}_z^p \mathbf{p} + \mathbf{h}^{*T}\mathbf{p} + c_\tau - \sum \lambda_{ij} p_{ij}\right) \Leftrightarrow \mathbf{A}_z^p \mathbf{p} + \mathbf{h}^{*T} - \lambda = 0 \tag{2.49a}$$

$$p_{ij} > 0, \quad \lambda_{ij} = 0 \tag{2.49b}$$

$$p_{ij} = 0, \quad \lambda_{ij} \geq 0 \tag{2.49c}$$

This variational formulation suits well for the use of the CGM described in the numerical tools (section 2.4). Gathering all the methods described to solve this variational problem in Eq. (2.49), a general algorithm is proposed for solving the normal contact problem.

2.5.2 General algorithm of the normal contact

The algorithm for solving the normal contact in the home made code ISAAC has been developped by Gallego [GAL 07b]. It is based on the CGM algorithm used by Polonsky and Keer [POL 99, POL 00] with improvements brought with (i) the possibility to impose either a force or a displacement, (ii) taking into account the moments transmitted through the contact if the applied force is not centred. Here, the contribution of moments is voluntarily ignored. The normal contact for an applied normal force or an applied normal displacement is proposed.
For an applied force P, the equilibrium equation in Eq. (2.8) is to be verified as a condition in the algorithm, while in the case of an applied displacement δ_z, it becomes an output of the algorithm.

1. `Initialisation of the pressure field` $\mathbf{p}$. `A potential contact zone` Γ_c' `is supposed in contact.` $\lambda_{ij} = 0$, $\zeta = 0$

2. `DC-FFT for the calculation of` $\bar{\mathbf{u}}_z^p$. `For applied force, the rigid body displacement` δ_z `is approximated. This approximation is done by calculation of the summation of the gaps in the contact zone which should give` 0:

$$\sum_{(i,j)\in\Gamma_c} \bar{u}_{zij}^p + h_{ij}^* = 0. \tag{2.50}$$

3. `The gap is calculated in the actual contact zone:`

$$g_{ij} = \bar{u}_{zij}^p + h_{ij}^*, \quad (i,j) \in \Gamma_c'. \tag{2.51}$$

   `The gap is also the residue of the linear system.`

4. `The descent direction is calculated function of the residue and the previous descent direction`

$$d_{ij} \leftarrow -g_{ij} + \zeta \frac{G}{G_{old}} d_{ij}, \quad (i,j) \in \Gamma_c' \tag{2.52a}$$

$$d_{ij} \leftarrow 0, \quad (i,j) \notin \Gamma_c' \tag{2.52b}$$

   `with`

$$G = \sum_{(i,j)\in\Gamma_c'} g_{ij}^2 \tag{2.52c}$$

   `and finally` $G_{old} \leftarrow G$ `and` $\zeta \leftarrow 1$.

5. The DC-FFT is applied to the descent direction

$$\mathbf{r}_z^p = \mathbf{A}_z^p \mathbf{d} \tag{2.53}$$

and the descent step is

$$\alpha = \frac{\sum_{(i,j)\in\Gamma_c'} g_{ij}^2}{\sum_{(i,j)\in\Gamma_c'} d_{ij} r_{ij}} \tag{2.54}$$

6. The pressures are updated

$$p_{ij} \leftarrow p_{ij} + \alpha d_{ij} \tag{2.55}$$

7. The complementary conditions are enforced:

$$\text{if } p_{ij} < 0, \quad (i,j) \in \Gamma_c' \quad \text{then } p_{ij} \leftarrow 0, \quad \Gamma_c' \leftarrow \Gamma_c' \setminus (i,j), \tag{2.56a}$$

$$\text{if } g_{ij} = \lambda_{ij} < 0, \quad (i,j) \notin \Gamma_c' \quad \text{then } p_{ij} \leftarrow -\alpha g_{ij}, \quad \zeta \leftarrow 0, \quad \Gamma_c' \leftarrow \Gamma_c' \cup (i,j). \tag{2.56b}$$

8. The equilibrium equation in Eq. (2.8) is enforced by multiplying the pressure field by a factor $a = \frac{P}{\sum_{\Gamma_c'} p_{ij} S}$ and then the convergence criteria is tested

$$\varepsilon = \frac{\sum_{(i,j)\in\Gamma_c'} (p_{ij} - p_{ijold})}{\sum_{(i,j)\in\Gamma_c'} p_{ij}} < \varepsilon_0 \tag{2.57}$$

The variable ζ allows the reinitialisation of the algorithm for $\zeta = 0$. At step 7, if a point which is not in the contact zone has a negative gap, then it should get into the potential contact zone Γ_c' and so the latter changes. Thus, the conjugate gradient is reinitialised at the next iteration. The new point entering the contact zone takes the pressure value $-\alpha g_{ij}$ which is a positive value. The convergence criteria is a stabilisation criteria coupled with the equilibrium equation for an applied force. Figure 2.9 shows the general algorithm for the normal contact problem.

To complete the contact problem, its tangential component has then to be solved.

2.5.3 General algorithm for the tangential problem

The tangential and the normal contacts should be solved simultaneously in theory since they are coupled. In fact, they are usually solved one after the other by following a Panagiotopoulos process [PAN 75] which consists in iterating between the normal and the tangential algorithms by taking into account the result from one problem on the other, until convergence. Briefly, the Panagiotopoulos process can be written as:

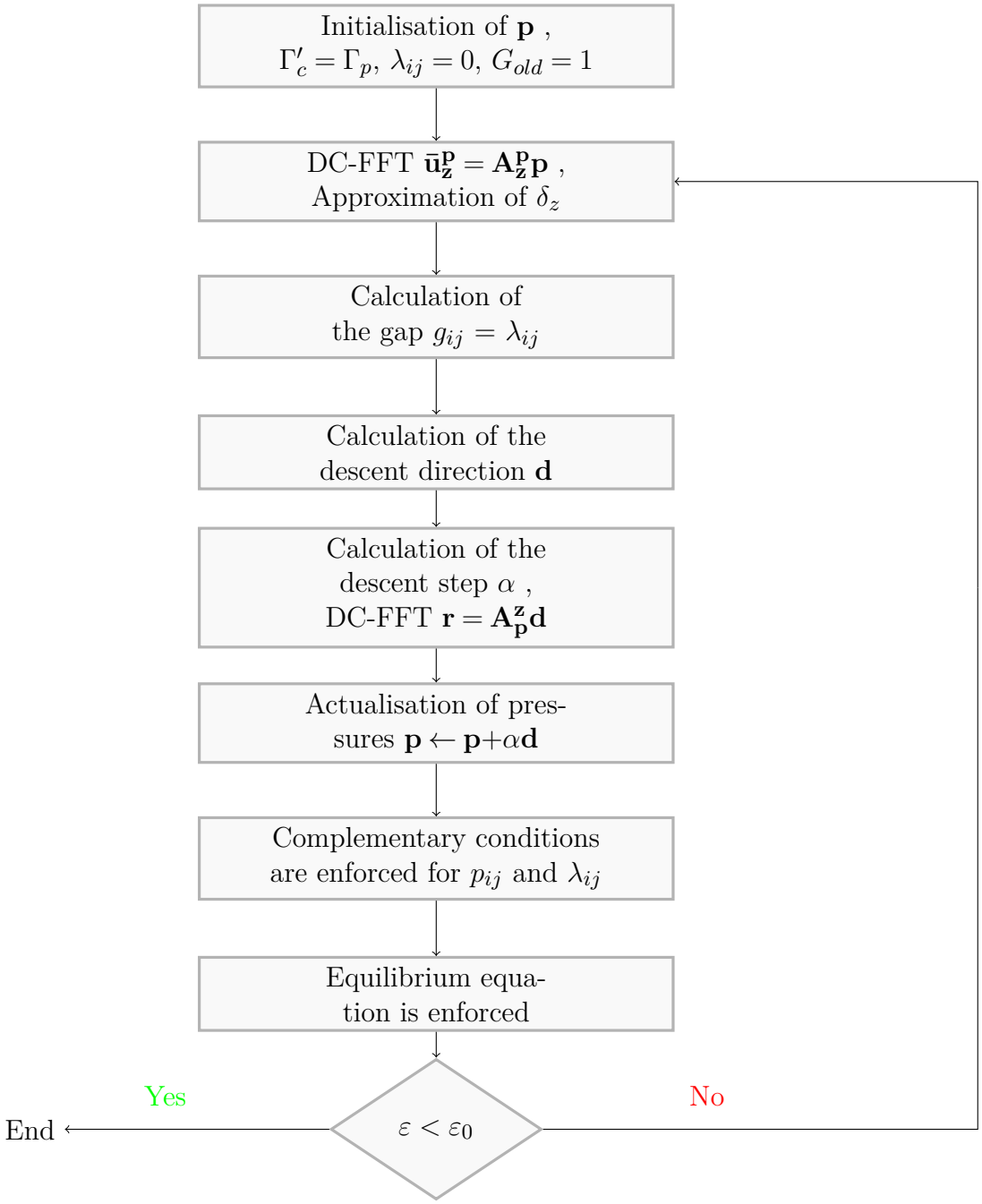

Figure 2.9: General algorithm for solving the Normal Contact Problem.

i) the normal contact problem is solved by assuming that there is no tangential traction;

ii) the tangential contact is then solved using the previous output from the normal problem;

iii) the normal contact problem is solved with the output shears from the tangential contact problem.
If the results are close enough to those of the previous step, return the results.
If not, go back to the second step.

The tangential problem as the normal one needs to be put into an appropriate form for the application of the CGM. Thus, the variational formulation for the tangential contact problem is given by:

$$\min\left(\frac{1}{2}\mathbf{q}^T\mathbf{A}_\tau^{\mathbf{q}}+\mathbf{W}^{*T}\mathbf{q}+c_p\right), \tag{2.58a}$$

$$\|\mathbf{q}_{ij}\|\geq fp_{ij}, \tag{2.58b}$$

where f is the friction coefficient, $\mathbf{W}^*$ is the vector containing the creepages or rigid tangential body displacements and the contribution of the normal loading on tangential displacements. c_p is the complementary energy due to the normal problem. Here again, the problem is a constrained minimisation problem. However the constraints on the shear tractions are not linear. Thus, it is appropriate to write them in the form: $\frac{q_x^2+q_y^2}{2fp}-\frac{fp}{2}$. Then, the problem can be written as:

$$\min\left(\frac{1}{2}\mathbf{q}^T\mathbf{A}_\tau^q\mathbf{q}+\mathbf{W}^{*T}\mathbf{q}+c_p-\sum\lambda_{ij}\left(\frac{q_x^2+q_y^2}{2fp}-\frac{fp}{2}\right)\right)\Leftrightarrow\mathbf{A}_\tau^q\mathbf{q}+\mathbf{W}^{*T}-\begin{pmatrix}\vdots\\ \lambda_{ij}\frac{q_{xij}}{fp_{ij}}\\ \vdots\\ \lambda_{ij}\frac{q_{yij}}{fp_{ij}}\\ \vdots\end{pmatrix}=0 \tag{2.59a}$$

$$\|\mathbf{q}_{ij}\|<fp_{ij},\quad \lambda_{ij}=0 \tag{2.59b}$$

$$\|\mathbf{q}_{ij}\|=fp_{ij},\quad \lambda_{ij}\geq 0 \tag{2.59c}$$

This variational formulation holds for the tangential contact problem in general. The CGM presented in this chapter has been developed and used by Gallego [GAL 07b] to the shift motion in the contact. The shift motion occurs when the velocity of the particles in the contact zone is of the same order as their velocity with respect to the contact zone. In this frame, the slip is given by:

$$\mathbf{s}=\begin{pmatrix}\Delta\bar{u}_x-\Delta\delta_x+y.\Delta\phi_z\\ \Delta\bar{u}_y-\Delta\delta_y-x.\Delta\phi_z\end{pmatrix} \tag{2.60}$$

where $\Delta\bar{u}_i$ is the variation of the surface tangential displacement, $\Delta\delta_i$ and $\Delta\phi_z$ the variation of the rigid body displacements between two consecutive time steps. Finally, for applied forces F_x and F_y and twisting moment around z M_z, the tangential contact algorithm reads:

1. Initialisation of the shear field $\mathbf{q}$. The contact zone Γ_c is supposed in adhesion. Thus, $\lambda_{ij} = 0$.

2. DC-FFT for $\bar{\mathbf{u}}_\tau^p$ and $\bar{\mathbf{u}}_\tau^q$. For applied forces and moment, the rigid body displacements δ_i are approximated using the Lagrangian formulation equations. The matrix system in Eq. (2.61) is found and solved with a Gauss-Jordan algorithm:

$$\begin{pmatrix} \sum_{\Gamma_c} 1 & 0 & \sum_{\Gamma_c} y_j \\ 0 & \sum_{\Gamma_c} 1 & -\sum_{\Gamma_c} x_i \\ -\sum_{\Gamma_c} y_j & \sum_{\Gamma_c} x_i & -\sum_{\Gamma_c} \left(x_i^2 + y_j^2\right) \end{pmatrix} \begin{pmatrix} \Delta\delta_x \\ \Delta\delta_y \\ \Delta\phi_z \end{pmatrix} = \begin{pmatrix} \sum_{\Gamma_c} \left(\Delta\bar{u}_{xij} + \lambda_{ij} \frac{q_{xij}}{fp_{ij}}\right) \\ \sum_{\Gamma_c} \left(\Delta\bar{u}_{yij} + \lambda_{ij} \frac{q_{yij}}{fp_{ij}}\right) \\ \sum_{\Gamma_c} \left[-y_j \left(\Delta\bar{u}_{xij} + \lambda_{ij} \frac{q_{xij}}{fp_{ij}}\right) + x_i \left(\Delta\bar{u}_{yij} + \lambda_{ij} \frac{q_{yij}}{fp_{ij}}\right)\right] \end{pmatrix}. \tag{2.61}$$

3. The true slip between the bodies is calculated in the contact zone:

$$\mathbf{s}_{ij} = \Delta\bar{\mathbf{u}}_\tau^q + \Delta\bar{\mathbf{u}}_\tau^p - \Delta\delta_\tau, \quad (i,j) \in \Gamma_c. \tag{2.62}$$

4. The Lagrange multipliers are calculated for the slip zone Γ'_{slip}

$$\lambda_{ij} = \|\mathbf{s}_{ij}\| \times sign(\mathbf{s}_{ij}.\mathbf{q}_{ij}); \tag{2.63}$$

5. The complementary conditions are tested:

$$\text{If } \lambda_{ij} < 0, \text{ then } \Gamma'_{stick} \leftarrow \Gamma'_{stick} \cup (i,j) \text{ and } \zeta = 0. \tag{2.64}$$

An error is evaluated with respect to the angle between the shear vectors and the slip in the slip zone:

$$\varepsilon^{slip} = \frac{\sum_{(i,j)\in\Gamma'_{slip}} \|\mathbf{s}_{ij} + \lambda_{ij} \frac{\mathbf{q}_{ij}}{fp_{ij}}\|}{\sum_{(i,j)\in\Gamma'_{slip}} \lambda_{ij}} \tag{2.65}$$

6. The descent direction is calculated function of the residue which is the slip, and the previous descent direction

$$\mathbf{d}_{ij} \leftarrow \mathbf{s}_{ij} + \zeta \frac{G}{G_{old}} \mathbf{d}_{ij}, \quad (i,j) \in \Gamma'_{stick} \tag{2.66a}$$

$$\mathbf{d}_{ij} \leftarrow (\mathbf{s}_{ij} + \lambda_{ij}\mathbf{q}_{ij}) + \zeta \frac{G}{G_{old}}\mathbf{d}_{ij}, \quad (i,j) \in \Gamma'_{slip} \tag{2.66b}$$

with

$$G = \sum_{(i,j)\in\Gamma'_c} \left(\mathbf{s}_{ij} + \lambda_{ij}\frac{\mathbf{q}_{ij}}{fp_{ij}}\right).\left(\mathbf{s}_{ij} + \lambda_{ij}\frac{\mathbf{q}_{ij}}{fp_{ij}}\right) \tag{2.66c}$$

and finally $G_{old} \leftarrow G$ and $\zeta \leftarrow 1$.

7. The DC-FFT is applied to the descent direction

$$\mathbf{r}^q_\tau = \mathbf{A}^q_\tau \mathbf{d} \tag{2.67}$$

and then,

$$\mathbf{r}^q_\tau \leftarrow \mathbf{r}^q_\tau + \lambda_{ij}\mathbf{d}_{ij}/(fp_{ij}). \tag{2.68}$$

The descent step is

$$\alpha = \frac{\sum_{(i,j)\in\Gamma_c} \left(\mathbf{s}_{ij} + \lambda_{ij}\frac{\mathbf{q}_{ij}}{fp_{ij}}\right).\left(\mathbf{s}_{ij} + \lambda_{ij}\frac{\mathbf{q}_{ij}}{fp_{ij}}\right)}{\sum_{(i,j)\in\Gamma_c} \mathbf{d}_{ij}\mathbf{r}_{ij}}; \tag{2.69}$$

8. The shears are updated

$$\mathbf{q}_{ij} \leftarrow \mathbf{q}_{ij} + \alpha\mathbf{d}_{ij} \quad (i,j) \in \Gamma_c \tag{2.70}$$

9. The complementary conditions are enforced:

$$\text{if } \|\mathbf{q}_{ij}\| > fp_{ij}, \quad (i,j) \in \Gamma'_{stick} \quad \text{then}, \quad \Gamma'_{slip} \leftarrow \Gamma'_{slip} \cup (i,j), \quad \zeta = 0, \quad \mathbf{q}_{ij} \leftarrow fp_{ij}\frac{\mathbf{q}_{ij}}{\|\mathbf{q}_{ij}\|}; \tag{2.71}$$

10. The equilibrium equations in Eq. (2.19) are enforced by adding the quantity a, b and c to the shear field: $q_{xij} \leftarrow q_{xij} + a - c.y_j$ and $q_{xij} \leftarrow q_{yij} + b + c.x_i$ where a, b and c are found by solving the system (5.9) with $S = dxdy$.
Then the convergence criteria is tested with (2.73).

$$\begin{pmatrix} \sum_{\Gamma'_{stick}} 1 & 0 & -\sum_{\Gamma'_{stick}} y_j \\ 0 & \sum_{\Gamma'_{stick}} 1 & \sum_{\Gamma'_{stick}} x_i \\ -\sum_{\Gamma'_{stick}} y_j & \sum_{\Gamma'_{stick}} x_i & \sum_{\Gamma'_{stick}} \left(x_i^2 + y_j^2\right) \end{pmatrix} \begin{pmatrix} a \\ b \\ c \end{pmatrix} = \begin{pmatrix} F_x/S - \sum_{\Gamma_c} q_{xij} \\ F_y/S - \sum_{\Gamma_c} q_{yij} \\ M_z/S + \sum_{\Gamma_c} (y_j \cdot q_{xij} - x_i \cdot q_{yij}) \end{pmatrix} \tag{2.72}$$

$$\varepsilon = \frac{\sum_{(i,j)\in\Gamma_c} \sqrt{(q_{xij} - q_{xoldij})^2 + (q_{yij} - q_{yoldij})^2}}{\sum_{(i,j)\in\Gamma_c} \sqrt{q_x ij^2 + q_{xij}^2}} \tag{2.73}$$

Finally, $\mathbf{q}_{old} \leftarrow \mathbf{q}$.

In the same way as for the normal contact algorithm, the variable ζ is used to reinitialise the CGM. When a point goes from the stick zone to slip zone or from the slip zone to the stick zone, $\zeta \leftarrow 0$.

The general algorithm for the tangential contact problem is presented in Fig. 2.10.

At this point, the contact problem is completely solved for both the normal and the tangential aspects. To validate the proposed algorithms, some classical results have been simulated and compared to the literature. The results of those simulations are presented next.

2.6 Classical Results

A validation of the general algorithm of the coupled normal-tangential problem is proposed here. For this purpose two interesting examples are simulated for their physical interest and because they stand as reference results in the literature, namely the *Spence shift* and the *Cattaneo shift*.

2.6.1 The Spence shift

The first studied case of coupled normal-tangential problem is the Spence shift from Spence [SPE 75].
The normal contact exposed by Hertz in his pioneering theory considers frictionless contact surfaces. In fact, contact surfaces are very often frictional and then it is relevant to take it into account. When friction is considered at the surface, shear tractions appear in the contact area even for only an applied normal load if the bodies are *elastically dissimilar*. The problem has been studied by Spence [SPE 75] who showed that the slip zone in such a case is a disc with external radius a and internal radius c. a is the contact zone and the c is the stick zone radius, function of the Dundurs' parameter [1].

A simulation of the contact between a rigid sphere and an elastic half-space is performed for different values of friction coefficient f (see Fig. 2.11). There is no tangential force nor displacement applied. The simulation is force driven (for the normal load) and performed in one step. The details of the study of the Spence shift case is performed using the present semi-analytical method by Gallego [GAL 07b] with good agreements with the Spence theory. Note that for the same simulation performed in many steps, a rounded profile is observed in the stick/slip zones transition zone.

[1] The Dundurs' parameter β describes the elastic similarity between the bodies in contact: $\beta = \frac{1}{2}\left[\frac{(1-2\nu_1)/G_1-(1-2\nu_2)/G_2}{(1-\nu_1)/G_1+(1-\nu_2)/G_2}\right]$.
When $\beta = 0$, then the bodies are elastically similar or incompressible. The limit values -0.5 and $+0.5$ are reached when one of the bodies is rigid and the other has a zero Poisson's ratio.

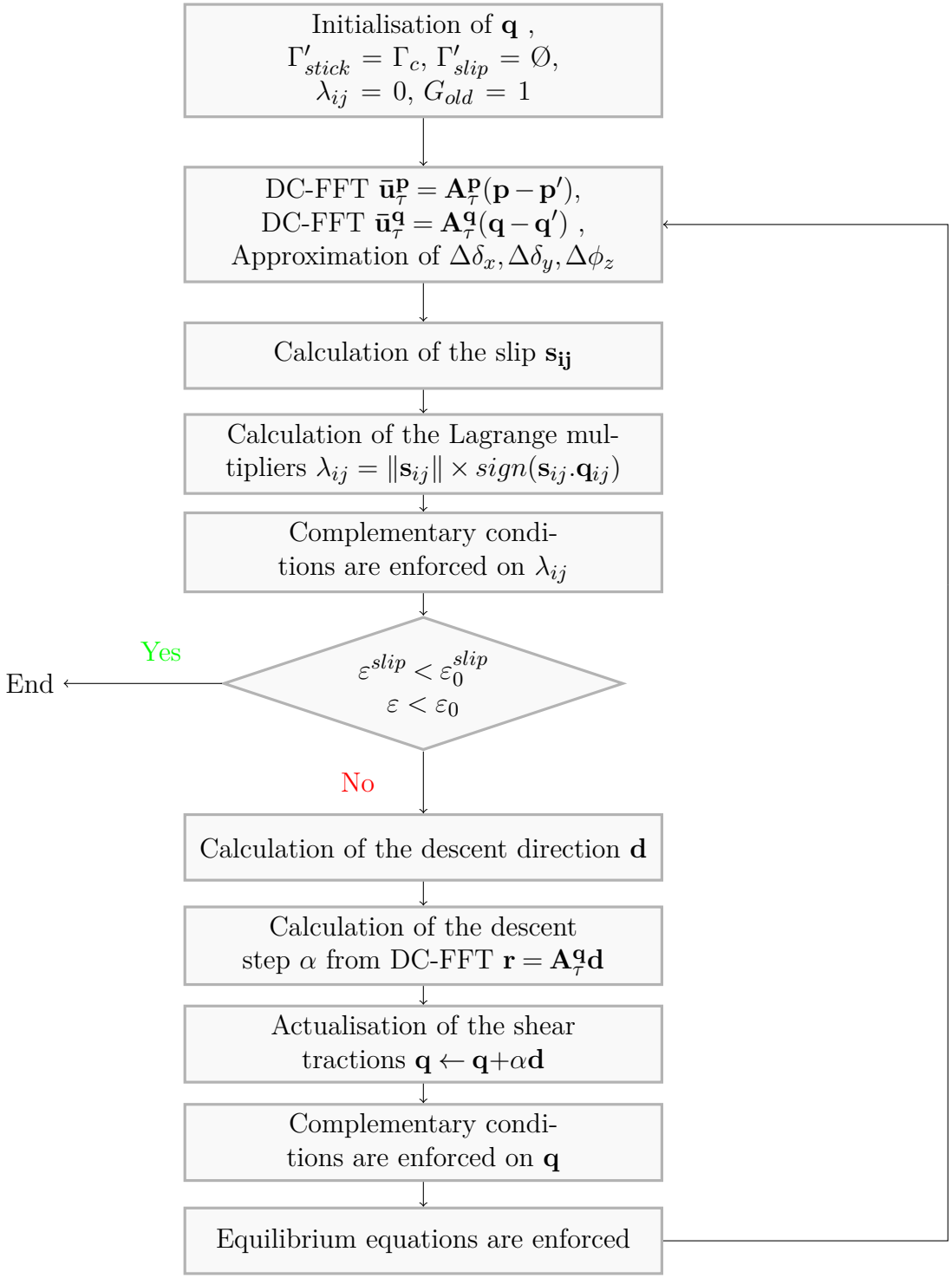

Figure 2.10: General algorithm for solving the Tangential Contact Problem for the shift motion.

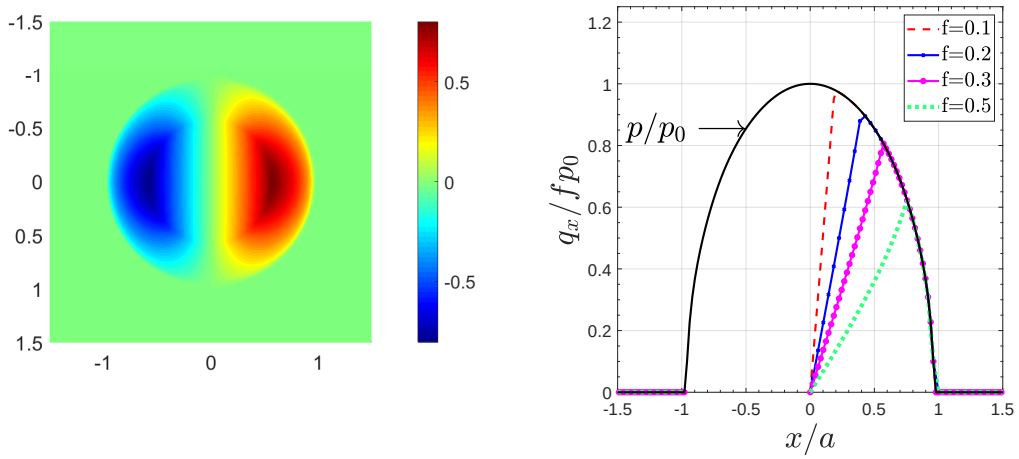

(a) (b)

Figure 2.11: Shear traction for the Spence shift for a rigid sphere on a flat elastic half-space. The 2D view of the shear dimensionless q_x/fp_0 at the left, and the profile of the same q_x/fp_0 along the line x in the plane $y = 0$ for different values of the friction coefficient f at the right.

2.6.2 The Cattaneo-Mindlin shift

The Cattaneo-Mindlin problem is the contact problem where both a normal force P and a tangential force F_x are applied at the same time so that $F_x < fP$, f being the friction coefficient. According to the Coulomb's law, at an overall scale, the bodies are in an equilibrium state. However, in the contact zone, slip zones appear beside the adhesion zones. Cattaneo [CAT 38] and Mindlin [MIN 49, MIN 53] have studied the problem for Hertzian geometries, showing the appearance of singularities at the edge of the contact leading to infinite shear tractions. The problem studied by Cattaneo considers quasi-identical equal spheres pressed together and then shifted with respect to the $x-$axis.
For a circular contact area, the slip appears over a disc with greater radius a and lower radius c. Then, the shear is given as a superposition of two shears: $q_x = q'_x + q''_x$. The first term is found when a total slip is supposed in the contact area:

$$q'_x = fp_0(1-(r/a)^2)^{1/2} \quad r \leq a \tag{2.74}$$

In order to verify the equilibrium with respect to the overall shear, the second term is found to be:

$$q''_x = -f\tfrac{c}{a}p_0(1-(r/c)^2)^{1/2} \quad r \leq c \tag{2.75a}$$

$$q''_x = 0 \quad r > c \tag{2.75b}$$

where p_0 is the maximum Hertz pressure and c is given by:

$$c = a\,(1 - F_x/fP)^{1/3} \tag{2.76}$$

Using the present contact model, the contact has been simulated for a rigid sphere on an elastic half-space. The friction coefficient is $f = 0.25$ and the tangential force applied is $F_x/fP = 0.5$, P being the normal force applied. The results are compared in Fig. 2.12 showing a good agreement with the theory.

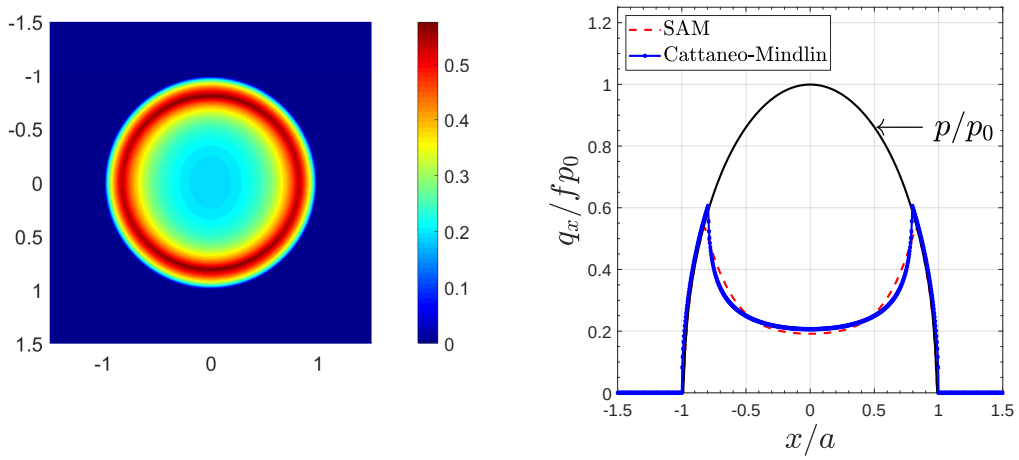

(a) (b)

Figure 2.12: Shear traction for the Cattaneo-Mindlin shift for a rigid sphere on a flat elastic half-space. The 2D view of the shear dimensionless q_x/fp_0 at the left, and the profile of the same q_x/fp_0 along the line x in the plane $y = 0$ compared to the formula of Cattaneo at the right.

Note again that the simulation can be driven in term of force or displacement for both normal and tangential contacts. This is particularly interesting for the simulation of fretting. The fretting motion is a repeated shift motion with small amplitudes. The fretting contact is studied further for a layered half-space in chapter 6.

2.7 Conclusion

In summary, the general algorithms for solving the contact basic contact problem have been given.

Firstly, the formulations have been recalled for both the normal and the tangential components of the contact problem. The half-space approximation and the notion of influence coefficients have been exposed.

Secondly, the numerical approach has been described. The numerical acceleration techniques, Conjugate Gradient Method (CGM) and Fast Fourier Transform (FFT) have been presented. The CGM is used for solving the contact problem while the FFT is used for the calculation of the displacement and stress fields involved.

Thirdly, the general algorithms for solving the normal and tangential contacts are presented. The variational formulation needed is presented before, for both cases.

Finally, two normal-tangential problems are studied for the validation of the proposed algorithms: the Spence shift and the Cattaneo-Mindlin shift. The first one consists in applying only a normal load on the bodies in contact. The second one consists applying simultaneously normal and tangential loads in such a way that the overall system is static. The two reference cases show a good agreement with the theory.

Chapter 3

Pure Rolling Contact on a Viscoelastic Layered Half-space

This chapter discusses the contact on a viscoelastic layered half-space where coating and substrate have different viscoelastic behaviours. The influence coefficients are calculated using the Papkovich-Neuber potentials coupled with a Fast Fourier Transform (FFT) algorithm. Then, an Elastic/viscoelastic correspondence is applied to move the elastic solutions into viscoelastic ones. Further, a validation is made and a parametric study performed to highlight the influence of different parameters such as the elastic modulus ratio, the relaxation time ratio, the coating thickness or the rolling velocity.

Sommaire

3.1 Introduction

The use of coatings is more and more common in the industry with view to improve surface properties like appearance, adhesion, wettability, resistance to corrosion, resistance to wear and mechanical behaviour in term of admissible stresses. Since ecological and economical topics are more actual than ever, it is important to optimise the conception of the layered materials. For this aim, contact mechanics develops tools for modelling the contact problems between bodies of different geometries, under various types of loads and for different materials.

The previous works concerning the modelling of coatings have been made mainly in elasticity [BUR 45a, CHE 71, CHE 72, O'S 88, YU 14, SPI 18a, WAN 11b]. In viscoelasticity, the models concern homogeneous viscoelastic half-spaces, thin films and viscoelastic films bonded to an elastic or a rigid base [GOR 95, KOU 14a, KOU 15b, MIF 18, PUT 15, PUT 18, STE 15, STE 16, STE 18, TOR 19]. The originality in this work lies in the fact that the contact is modelled for a viscoelastic layered half-space where coating and substrate have different viscoelastic behaviours.

The model proposed in this chapter is able to solve the rolling/sliding contact on viscoelastic layered half-space. This implies that the present model is able to handle the following limit cases: Viscoelastic coating/Elastic substrate, Viscoelastic coating/Rigid substrate and Elastic coating/Viscoelastic substrate. It is also capable of solving the problem in both transient and steady-state regimes. Note that the counterface material - that can be either a sliding indenter or a rolling body of revolution - can be of any material, i.e. rigid, elastic, visco-elastic or elastic-plastic (see [CHA 11b, JAC 02]). For sake of simplicity it will be assumed here only rigid or elastic.

The novelty of the present work lies in accounting for a layered viscoelastic half-space with the coating and substrate having different viscoelastic properties. This is done with a proposed Elastic/viscoelastic correspondence. The previous works on coatings mainly focus on viscoelastic layers over elastic or rigid bases; or are dedicated to rough contacts where the approach as well as the analysed phenomena are not the same. Therefore, none of previous models has provided detailed results for this framework. The analysis of the contact pressure, the stresses and especially at the interface are completely new for the studied framework.

In what follows next, the model formulation is briefly recalled first and a validation is performed. Then a parametric study is made to highlight the effect of the shear modulus ratio, the relaxation time ratio, the coating thickness and the rolling/sliding velocity. Coating/substrate interface stresses are computed as well as three-dimensional stresses.

3.2 Formulation

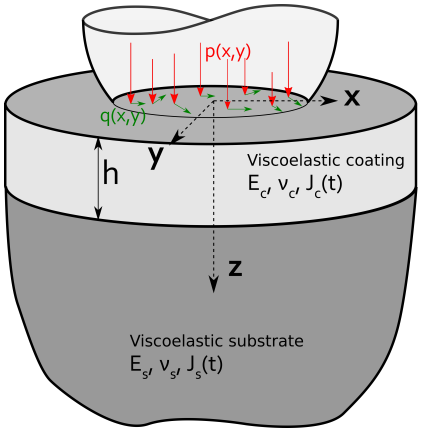

Figure 3.1: System being considered. A pressure and shear distributions at the surface of a viscoelastic layered half-space, where coating and substrate have different viscoelastic behaviours.

The problem is shown in Fig. 3.1. It consists of two bodies in contact where pressure and shear distributions are holding. To solve the problem, it is important to know the behaviour of the layered half-space. For this aim, consider pressure and shear fields imposed at the top surface of a viscoelastic layered half-space. In what follows next, the normal contact model is recalled. The influence coefficients are found so that the displacements can be calculated in the contact algorithm. Those influence coefficients are found in the Fourier frequency domain with the potentials of Papkovich-Neuber and then an IFT is performed. Later, for the viscoelasticity, an Elastic/viscoelastic correspondence is proposed.

3.2.1 Contact formulation

For two non-conforming bodies B_1 and B_2, the classical contact model is well explained in chapter 2. Let's recall the three main points of that contact formulation:

- ✧ The load balance: The applied charge $W(t)$ must be equal to the sum of the contact pressure $p(x,y,t)$ in the contact zone Γ_c.

$$W(t) = \int_{\Gamma_c(t)} p(x,y,t)dxdy \tag{3.1}$$

- ✧ The surface separation: The distance between the two bodies is defined at every point as the sum of the initial separation $h_i(x,y)$, the elastic normal displacement of both bodies under load $u_3^{(B_1+B_2)}(x,y,t)$ and -eventually- the rigid body displacement $\delta(t)$ at every time t.

$$h(x,y,t) = h_i(x,y) + \delta(t) + u_3^{(B_1+B_2)}(x,y,t) \tag{3.2}$$

✧ The contact conditions: Since bodies in contact cannot interpenetrate, the gap $h(x,y,t)$ defined above is always positive. The pressure is also assumed always positive what ever is the type of physics we are dealing with. Then, two zones can be identified:

$$\begin{array}{c} \text{Contact zone: } h(x,y,t) = 0 \text{ and } p(x,y,t) > 0 \\ \text{Separation zone: } h(x,y,t) > 0 \text{ and } p(x,y,t) = 0 \end{array}$$

Since the goal is the viscoelastic modelling of the contact, the time variable has been introduced for all the quantities involved in the formulation. Taking into account the time allows to take into account every kind of load and so to solve transient problems.
To find the displacements u_i $(i = x,y,z)$, the Green functions G_J $(J = x,y,z)$ or influence coefficients are used. Green functions have been used extensively for homogeneous elastic half-space using mainly the potential functions of Boussinesq (see the book of Johnson [JOH 85]) . When G_J are known, for an applied pressure field $p(x,y)$, the displacements are given by:

$$u_J^p(x,y) = \int\int_{-\infty}^{\infty} G_J^p(x-x',y-y')p(x',y')dx'dy' = G_J^p * p \tag{3.3}$$

where * represents the Convolution.
In the present chapter, the focus is put on layered bodies. Therefore, before all, it is important to find the elastic influence coefficients of a single layered half-space.

3.2.2 Influence coefficients for layered elastic half-space

To implement the contact formulation for a layered elastic half-space, the adequate Green functions have to be brought out.
In this case, the half-space consists in an elastic coating of shear modulus μ_c and Poisson's ratio ν_c perfectly bounded to an elastic substrate of shear modulus μ_s and Poisson's ratio ν_s. Note that the coating thickness h is constant throughout the modelling.
The influence coefficient are found using the method exposed by O'Sullivan and King [O'S 88]. The approach uses the Papkovich-Neuber potentials ϕ and ψ_i. Those potentials are the result of the combination of Helmotz representation and Navier equations (see Malvern [MAL 69]). ϕ and ψ_i are the harmonic functions of (x,y), and when no body forces, Malvern [MAL 69] showed that ψ_2 vanishes. Then, the displacements and stresses take the following forms, function of the potentials ϕ, ψ_1 and ψ_3 :

$$2\mu u_i^r = \phi_{,i}^r + x\psi_{x,i}^r + z\psi_{z,i}^r - (3-4\nu)\psi_i^r \tag{3.4a}$$

$$\sigma_{ij}^r = \phi_{,ij}^r - 2\nu(\psi_{x,x}^r + \psi_{z,z}^r)\delta_{ij} - (1-2\nu)(\psi_{i,j}^r + \psi_{j,i}^r) + x\psi_{x,ij}^r + z\psi_{z,ij}^r \tag{3.4b}$$

where $r = s$ (substrate), c (coating).
In the above equations, it appears partial derivatives of the Papkovich-Neuber potentials. Those forms are difficult to handle as they stand. To bypass this barrier, a linearisation of the Eqs. (4.4) is to be performed. Many linearisation processes can be used, generally with integral transforms such as Laplace and Fourier transforms. Here, the choice has been put on Fourier transform since the numerical corresponding algorithms are already used in the contact model (see chapter 2). For an integrable function f, recall the useful properties:

$$FT_x\left[\frac{\partial}{\partial x} f(x)\right] = im\tilde{f}(m), \tag{3.5a}$$

$$FT_x[-ixf(x)] = \frac{\partial}{\partial m}\tilde{f}(m), \tag{3.5b}$$

where x is the coordinate in the space domain and m its equivalent in the frequency domain.

Then, Eqs. (4.4) become:

$$2\mu\tilde{\tilde{u}}_i^r = FT_{xy}\left[\phi_{,i}^r + x\psi_{x,i}^r + z\psi_{z,i}^r - (3-4\nu)\psi_i^r\right] \tag{3.6a}$$

$$\tilde{\tilde{\sigma}}_{ij}^r = FT_{xy}\left[\phi_{,ij}^r - 2\nu(\psi_{x,x}^r + \psi_{z,z}^r)\delta_{ij} - (1-2\nu)(\psi_{i,j}^r + \psi_{j,i}^r) + x\psi_{x,ij}^r + z\psi_{z,ij}^r\right]. \tag{3.6b}$$

The FT of the potentials are chosen as follow:

$$\tilde{\tilde{\phi}}^r = A^r \exp(-\alpha z_r) + \overline{A}^r \exp(\alpha z_r) \tag{3.7a}$$

$$\tilde{\tilde{\psi}}_1^r = B^r \exp(-\alpha z_r) + \overline{B}^r \exp(\alpha z_r) \tag{3.7b}$$

$$\tilde{\tilde{\psi}}_3^r = C^r \exp(-\alpha z_r) + \overline{C}^r \exp(\alpha z_r) \tag{3.7c}$$

Using the above properties in Eq. (3.5) and the above forms, linear equations of the elastic displacements and stresses are found in the Fourier frequency domain. Let's introduce some notations:

$$D^r = A^r + B'^r i, \qquad \overline{D}^r = \overline{A}^r + \overline{B}'^r i$$
$$w_+^r = e^{\alpha z_r}, \qquad w_-^r = e^{-\alpha z_r}$$

where $\alpha = \sqrt{m^2+n^2}$ is the radius in the frequency domain; (m,n) represents the Fourier Transform of (x,y).

With the formula and the notations introduced above, one can infer the forms of displacements and stresses in the Fourier frequency domain as:

$$\begin{aligned}2\mu_r\tilde{\tilde{u}}_x^r =& im\left(D^r w_-^r + \overline{D}^r w_+^r\right) - 4\left(1-\nu_r\right)\left(B^r w_-^r + \overline{B}^r w_+^r\right)\\ &+ m^2 z_r \alpha^{-1}\left(B^r w_-^r - \overline{B}^r w_+^r\right) + imz_r\left(C^r w_-^r + \overline{C}^r w_+^r\right)\end{aligned} \tag{3.8a}$$

$$2\mu_r\tilde{\tilde{u}}_y^r = in\left(D^r w_-^r + \overline{D}^r w_+^r\right) - mnz_r\alpha^{-1}\left(B^r w_-^r - \overline{B}^r w_+^r\right) + inz_r\left(C^r w_-^r + \overline{C}^r w_+^r\right) \tag{3.8b}$$

$$\begin{aligned}2\mu_r\tilde{\tilde{u}}_z^r =& -\alpha\left(D^r w_-^r - \overline{D}^r w_+^r\right) - im\alpha^{-1}\left(B^r w_-^r - \overline{B}^r w_+^r\right) - (3-4\nu_r)\left(C^r w_-^r + \overline{C}^r w_+^r\right)\\ &+ imz_r\left(B^r w_-^r + \overline{B}^r w_+^r\right) + z_r\alpha\left(-C^r w_-^r + \overline{C}^r w_+^r\right)\end{aligned} \tag{3.8c}$$

$$\begin{aligned}\tilde{\tilde{\sigma}}_{xx}^r =& -m^2\left(D^r w_-^r + \overline{D}^r w_+^r\right) - 2im\left(2-\nu_r\right)\left(B^r w_-^r + \overline{B}^r w_+^r\right) - 2\alpha\nu_r\left(-C^r w_-^r + \overline{C}^r w_+^r\right)\\ &+ im^3 z_r\alpha^{-1}\left(B^r w_-^r - \overline{B}^r w_+^r\right) - z_r m^2\left(C^r w_-^r + \overline{C}^r w_+^r\right)\end{aligned} \tag{3.8d}$$

$$\begin{aligned}\tilde{\tilde{\sigma}}_{yy}^r =& -n^2\left(D^r w_-^r + \overline{D}^r w_+^r\right) - 2im\nu_r\left(B^r w_-^r + \overline{B}^r w_+^r\right) - 2\alpha\nu_r\left(-C^r w_-^r + \overline{C}^r w_+^r\right)\\ &+ imn^2 z_r\alpha^{-1}\left(B^r w_-^r - \overline{B}^r w_+^r\right) - z_r n^2\left(C^r w_-^r + \overline{C}^r w_+^r\right)\end{aligned} \tag{3.8e}$$

$$\begin{aligned}\tilde{\tilde{\sigma}}_{zz}^r =& \alpha^2\left(D^r w_-^r + \overline{D}^r w_+^r\right) + 2im\left(1-\nu_r\right)\left(B^r w_-^r + \overline{B}^r w_+^r\right) - 2\alpha\left(1-\nu_r\right)\left(-C^r w_-^r + \overline{C}^r w_+^r\right)\\ &- imz_r\alpha\left(B^r w_-^r - \overline{B}^r w_+^r\right) + z_r\alpha^2\left(C^r w_-^r + \overline{C}^r w_+^r\right)\end{aligned} \tag{3.8f}$$

$$\begin{aligned}\tilde{\tilde{\sigma}}_{xy}^r =& -mn\left(D^r w_-^r + \overline{D}^r w_+^r\right) - 2in\left(1-\nu_r\right)\left(B^r w_-^r + \overline{B}^r w_+^r\right)\\ &+ im^2 nz_r\alpha^{-1}\left(B^r w_-^r - \overline{B}^r w_+^r\right) - z_r mn\left(C^r w_-^r + \overline{C}^r w_+^r\right)\end{aligned} \tag{3.8g}$$

$$\begin{aligned}\tilde{\tilde{\sigma}}_{xz}^r =& -im\alpha\left(D^r w_-^r - \overline{D}^r w_+^r\right) + \left(2\alpha\left(1-\nu_r\right) + m^2\alpha^{-1}\right)\times\left(B^r w_-^r - \overline{B}^r w_+^r\right)\\ &- im\left(1-2\nu_r\right)\left(C^r w_-^r + \overline{C}^r w_+^r\right) - m^2 z_r\left(B^r w_-^r + \overline{B}^r w_+^r\right) + iz_r\alpha m\left(-C^r w_-^r + \overline{C}^r w_+^r\right)\end{aligned} \tag{3.8h}$$

$$\begin{aligned}\tilde{\tilde{\sigma}}_{yz}^r =& -in\alpha\left(D^r w_-^r - \overline{D}^r w_+^r\right) + mn\alpha^{-1}\left(B^r w_-^r - \overline{B}^r w_+^r\right) - in\left(1-2\nu_r\right)\left(C^r w_-^r + \overline{C}^r w_+^r\right)\\ &- mnz_r\left(B^r w_-^r + \overline{B}^r w_+^r\right) + inz_r\alpha\left(-C^r w_-^r + \overline{C}^r w_+^r\right)\end{aligned} \tag{3.8i}$$

Remark: $\overline{B}^s = \overline{C}^s = \overline{D}^s = 0$ because the half-space condition implies that at the infinity, the elastic field vanishes.

The equations in Eq. (3.8) are made of unknowns B^r, $\overline{B}^r$, C^r, $\overline{C}^r$ and D^r. To find them, a system of 9 independent equations has to be determined.
The system to solve is given by the boundary conditions of the problem which can be split into two sets:

- ➢ At the top surface of the coating i.e. the contact surface of the whole half-space $z_c = 0$, pressure and shear fields are imposed:

$$\sigma^c_{zz}(x,y,0) = -p(x,y), \quad \sigma^c_{zx}(x,y,0) = -q(x,y), \quad \sigma^c_{zy}(x,y,0) = 0. \tag{3.9}$$

- ➢ At the interface between coating and substrate, tractions and displacements continuity is required:

$$\begin{aligned} \sigma^c_{zx}(x,y,h) &= \sigma^s_{zx}(x,y,0) \quad u^c_x(x,y,h) = u^s_x(x,y,0) \\ \sigma^c_{zy}(x,y,h) &= \sigma^s_{zy}(x_x y,0) \quad u^c_y(x,y,h) = u^s_y(x,y,0) \\ \sigma^c_{zz}(x,y,h) &= \sigma^s_{zz}(x,y,0) \quad u^c_z(x,y,h) = u^s_z(x,y,0) \end{aligned} \tag{3.10}$$

Note that the results for the shear $\sigma^c_{zy}(x,y,0)$ can be found by taking advantage of the results for an applied $\sigma^c_{zx}(x,y,0)$ and with the good analysis of the symmetries. By applying a double Fourier Transform (2D FT) to the above boundary conditions, a system of 9 equations with 9 unknowns $(B^c, B^s, C^c, C^s, D^c, D^s, \overline{B}^c, \overline{C}^c, \overline{D}^c)$ comes out. This system has been solved first by O'Sullivan and King [O'S 88] for an elastic coating on an elastic substrate. The solution of the system is consigned in appendix A.

From there, the Green functions are found in the Fourier frequency domain and can be specified in the case of an applied pressure and in the case of an applied shear, setting respectively $p(x,y) = \delta(x,y)$, $q(x,y) = 0$ or $p(x,y) = 0$, $q(x,y) = \delta(x,y)$.
The challenge of the next step is to find the Green functions in the space domain, by operating an Inverse Fourier Transform (IFT). Using FFT algorithms, it is possible to use the Continuous Convolution FFT (CC-FFFT) or the Discrete Convolution FFT (DC-FFT) according to the definitions of Liu et al. [LIU 00]. The reader may read a brief explanation of those differences in chapter 2.
The present work is based on the Discrete Convolution based on Fast Fourier Transform (DC-FFT) method. Therefore, the IFT is handled with Fast Fourier Transform (FFT) algorithms as proposed by Liu et al. [LIU 00].

At this point, the elastic influence coefficients are found for a layered half-space. A validation of those influence coefficients can be performed by using them in several contact cases.

3.2.3 Validation of the Elastic single layered half-space

In this section, a validation of the elastic influence coefficients of a layered half-space is performed. For this purpose, some contact cases are simulated and the results

compared to the results from the literature.
For the validation, the contact cases from O'Sullivan and King [O'S 88] are simulated. Consider a spherical indenter of radius R with a very high modulus that can be considered rigid, in contact with the elastic layered half-space. The coating has a thickness $h = a$, where a is the contact radius given by the contact on a homogeneous half-space with the elastic properties of the substrate. The elastic modulus of the substrate and the coating is noted E_i with $i = c, s$ and the the Poisson's ratio is ν_i. The Poisson's ratios are fixed: $\nu_s = \nu_c = 0.3$. The substrate's Young modulus is also fixed and then only changes the Young modulus of the coating.

Figure 3.2(a) shows the dimensionless contact pressure along the x line in the middle plane $y = 0$ for various ratio of E_c/E_s. Meanwhile, Fig. 3.2(b) shows the effect of the same ratio E_c/E_s on the coating/substrate interface stress σ_{xz} when friction is $f = 0.25$ in a pure sliding contact ($F_x = f \times P$, full slip condition). The figures show a good agreement with the results of O'Sullivan and King [O'S 88].

Convergence and time: Solving the contact by the use of the new influence coefficients for the layered half space has induced a slight increase of the computation time $\approx 24\%$. This increase is due to the calculations for finding the influence coefficients and particularly the inverse Fourier calculations. Since the Fourier Transform of the influence coefficients is used to solve the contact further, an improvement could be to keep those coefficients in the frequency domain from the analytical solutions. To do so, a particular attention would be put, not only in making them well correspond to the coordinate in the space domain, but also on the numerical FFT procedures which have some subtleties.
In term of convergence, there is no issue to highlight. The convergence occurs in comparable way as for the homogeneous case.

At this point, the validation has been performed for the whole three-dimensional elastic field (stresses and displacements). The solution of a contact involving a layered elastic body has been found. With the same influence coefficients, one can impose that one or both the bodies in contact are layered.
The next step is to find the solution for a viscoelastic layered body. To this aim, an *Elastic/Viscoelastic correspondence* is introduced. In the next lines, a brief bird-eye view is given on viscoelasticity before the correspondence method is exposed.

3.2.4 Viscoelasticity

3.2.4.1 Introduction to viscoelasticity

The purpose here is to draw a rapid picture of what is viscoelasticity in mechanics and to specify the assumptions that hold in the present work.
First of all, viscoelasticity concerns materials behaviour, characterised by the combination of their elastic and viscous response under load. Pure elastic materials

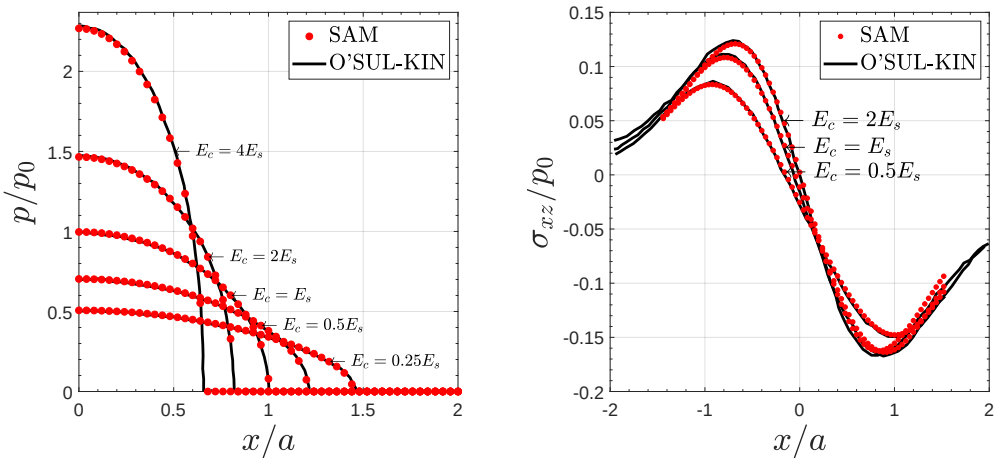

(a) (b)

Figure 3.2: Validation of the influence coefficients of a layered half-space.

deform instantaneously under a load and recover instantaneously when the load is removed. Meanwhile, a viscous fluid like engine oil will continuously deform in time under an applied same load.
A viscoelastic material is an elastic material to which a viscosity is added in such a way that under an applied load it deforms instantaneously and if the load is maintained, the deformation continues. When the load is removed, the material takes a certain time to recover. Thus, viscoelasticity means that the response of a material depends on the history of the loading. For a solicitation at high velocity, a viscoelastic material will tend to behave like an elastic material, while for lower velocity of solicitation, the viscous behaviour will clearly come out.

Example: The silly putty is a very relevant example of such behaviour. If one throws a ball of silly putty on the ground it rebounds 25% higher than a same ball in rubber. But the same ball in silly putty resting on a surface for few minutes will spread on the surface.

To link the solicitation to the deformations, the science of *rheology* is called upon. In rheology, the viscoelasticity uses two types of description: "non-linear viscoelasticity" and "linear viscoelasticity".

Non-linear viscoelasticity: This concerns large strains or materials that change properties under deformations. It also treats the case of solids that change dimensions under load. Non-linear viscoelasticity leans on empirical works since the control factors of such a behaviour are various and difficult.

Linear viscoelasticity: It is the description used for small strains. In that case, at a time t the stress $\sigma(t)$ and the strain $\varepsilon(t)$ are related by the equations :

$$\sigma(t) = \int_0^t R(t-\xi)\frac{d\varepsilon(\xi)}{d\xi}d\xi, \tag{3.11a}$$

$$\varepsilon(t) = \int_0^t J(t-\xi)\frac{d\sigma(\xi)}{d\xi}d\xi, \tag{3.11b}$$

where $R(t)$ and $J(t)$ are respectively the relaxation and the creep functions. Those functions are found by tests among which three are the most common:

- ✧ Relaxation test: the goal here is to find the relaxation function by applying a constant strain on a sample and by measuring the stress. In the above Eq. (3.11a), the strain ε_0 is constant and then the relaxation function is deduced by:

$$R(t) = \frac{\sigma(t)}{\varepsilon_0} \tag{3.12}$$

- ✧ Creep test: in the same way as above, a constant stress σ_0 is applied on a sample and the strain is measured. This gives the creep function as:

$$J(t) = \frac{\varepsilon(t)}{\sigma_0} \tag{3.13}$$

  In theory, when one of the creep or the relaxation functions is known, the other can be deduced by the use of the relation:

$$\int_0^t J(\xi)R(t-\xi)d\xi = 0. \tag{3.14}$$

  In practice, it is easier to find the creep from relaxation function than the converse.

- ✧ Another testing procedure is the *Dynamic Mechanical Analysis (DMA)* which consists in applying a sinusoidal load and then analysing the frequency response of the material. In the tire-pavement domain, this is a common procedure which allows to gather various information for elasticity, viscoelasticity, plasticity for different temperatures. For the viscoelasticity, the behaviour is given by the complex modulus. It is a complex number $G^*(t) = \frac{\sigma(t)}{\varepsilon(t)}$ which gives the behaviour of material in function of the loading frequency.
  However, the present model is not built around the use of the complex modulus but around the Prony series. Prony series representation is described in the next lines (see section 3.2.4.2).

In linear viscoelasticity, strain is presumed to be a linear function of stress, so the total effect of applying several stresses is the sum of the effects of applying each one separately: this is the *Boltzman superposition principle*. This principle allows the discretisation without hypothetically any lost of information.
In order to have a rheological modelling of the behaviour of a material, several models are used, based on spring and dampers.

3.2.4.2 Rheological Models

The rheological models used in linear viscoelasticity are based on the coupling of the elastic effects represented by springs ($\sigma = E\varepsilon$) and the viscous effects represented by dampers ($\sigma = \eta\dot{\varepsilon}$). The models are obtained by combination of springs and dampers in various configurations. The common models which are used in both research and industrial context are:

- *The Kelvin-Voigt model*: Also called the model of Voigt, it describes the viscoelastic behaviour by one spring and one damper placed in parallel (see Fig. 3.3). By using the procedure described in the previous section to determine the creep and the relaxation functions, one obtains:

$$J(t) = \frac{1}{\mu}\left(1 - \exp(-\frac{t}{\eta/\mu})\right) \tag{3.15a}$$

$$R(t) = \mu + \eta\delta(t). \tag{3.15b}$$

  where $\delta(t)$ is the Dirac distribution. This model does not well describe the instantaneous elastic behaviour as one can see in the relaxation formulae; and thus, it is not adequate to describe the relaxation phenomena.

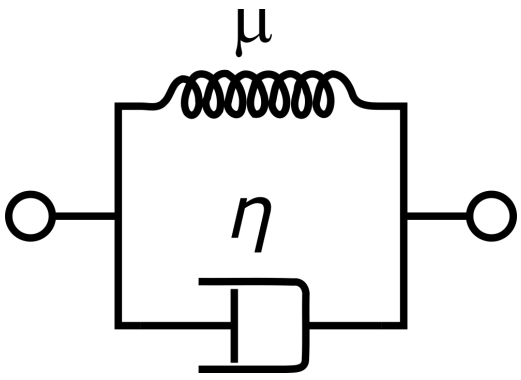

Figure 3.3: The Kelvin-Voigt rheological model for linear viscoelasticity.

- *The Maxwell model*: This model, proposed in 1867, consists of one spring and one damper in series as shown in Fig. 3.4. The creep and relaxation functions are given by:

$$J(t) = \frac{t}{\eta} + \frac{1}{\mu} \tag{3.16a}$$

$$R(t) = \mu \exp(-\frac{t}{\eta/\mu}) \tag{3.16b}$$

With this model, when a stress is applied, the spring gives immediately the elastic response and with time the damper adds the viscous contribution.

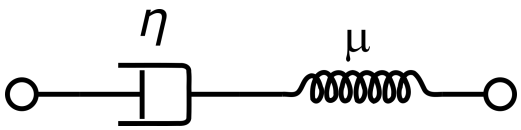

Figure 3.4: The Maxwell rheological model for linear viscoelasticity.

❖ *The Zener model*: This model put together the ability to represent the relaxation and the creep phenomena by using a spring in parallel with the model of Maxwell as presented in Fig. 3.5. It is a particular form of the generalised Maxwell model that is used in this work.

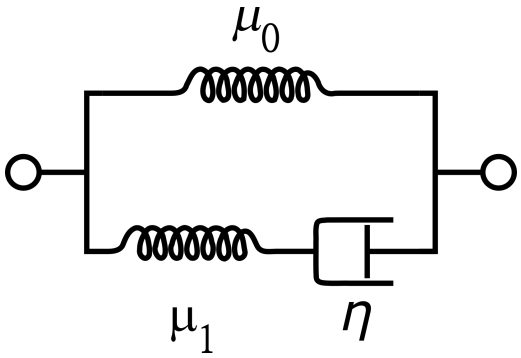

Figure 3.5: The Zener rheological model for linear viscoelasticity.

❖ *The generalised Maxwell model*: This model consists of a finite number n of Maxwell elementary models placed in parallel and in parallel with a single spring as shown in Fig. 3.6. This model allows to describe the behaviour of almost any linear viscoelastic material. The creep and relaxation functions are written as:

$$J(t) = \frac{\varepsilon(t)}{\sigma_0} = \left[j_0 - \sum_{i=0}^{n} j_i exp(-t/\lambda_i) \right] H(t) \tag{3.17a}$$

$$R(t) = \frac{\sigma(t)}{\varepsilon_0} = \left[\mu_0 + \sum_{i=0}^{n} \mu_i \exp(-t/\tau_i) \right] H(t), \tag{3.17b}$$

where:
μ_i is the spring stiffness,
η_i the damper viscosity,
$\tau_i = \eta_i/\mu_i$ the relaxation time of one elementary model and
$H(t)$ the Heaviside function.

Those forms are known as Prony series decomposition for the relaxation and creep functions.
Recall that creep and relaxation functions are connected through the relation of Eq. (3.14). Most of the time, it is easier to have the relaxation function and to infer the creep function. To do so, a code has been developed based on the interconversion algorithm of Loy et al. [LOY 15]. Their algorithm is based on the Laplace transform of the relaxation function in order to derive analytical formula for the coefficients j_i in terms of the derivative $d\hat{R}(s)/ds$ of the Laplace transform $\hat{R}(s)$ of the relaxation function $R(t)$.

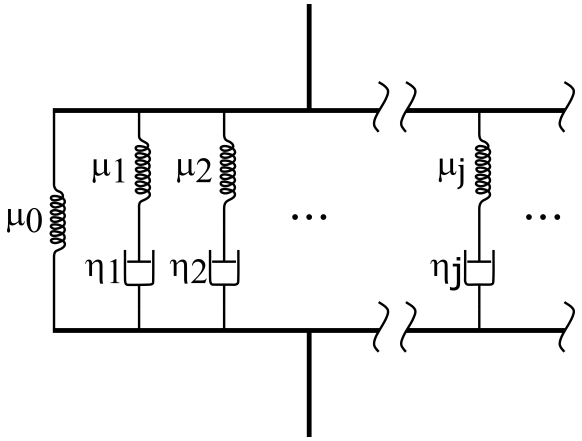

Figure 3.6: The generalised Maxwell rheological model for linear viscoelasticity.

Other models exists such as the *generalised Kelvin-Voigt* model that, as his name indicates, is a generalisation of the Kelvin-Voigt model. Elementary Kelvin-Voigt models are put in series together and with a single spring and a single damper.

In the road pavement modelling field, the frequency behaviour of the asphalt materials is usually analysed and specific models are used to describe the viscoelasticity. For instance the model of Huet and Sayegh (1963) is used to describe the coupled thermo-viscoelastic behaviour.

❖ *The Huet-Sayegh model*: This model proposed in 1963 is made of a spring and two parabolic dampers giving the instantaneous and retarded elasticity of the material, in parallel with a single spring for the long-term elasticity (see Fig. 3.7). Note that a parabolic damper of parameter k has a creep law: $f(t) = bt^k$, where b is a dimensionless constant. For a temperature θ and a frequency w, the complex modulus of the Huet-Sayegh models is given by:

$$E^*(\omega,\theta) = E_0 + \frac{E_\infty - E_0}{1+\delta(j\omega\tau(\theta))^{-k}+(j\omega\tau(\theta))^{-h}}, \tag{3.18}$$

where E_∞ is the instantaneous elastic modulus; E_0 the long-term modulus; k and h are the exponents of the parabolic dampers; and δ is a positive dimensionless coefficient balancing the contribution of the first damper on the overall behaviour. j is the complex number $j^2 = -1$ and $\tau(\theta)$ is a function of the temperature. Sometimes the Huet-Sayegh model is modified by adding for example a damper to the branch with the parabolic elements to build model named *2S2P1D model*.

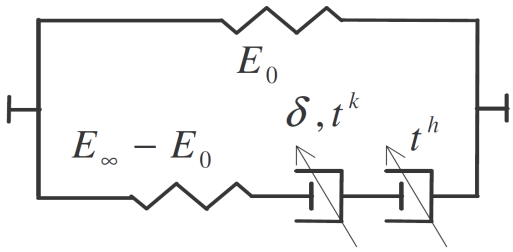

Figure 3.7: The Huet-Sayegh rheological model for linear viscoelasticity, used for asphalt materials.

In this work, the viscoelastic behaviour is described by the generalised Maxwell model and its Prony series representation. In what follows next, it is assumed that the creep and relaxation functions are known. Therefore, an Elastic/Viscoelastic correspondence can be proposed to turn the elastic solution for the contact involving an elastic layered body into its viscoelastic equivalent.

3.2.4.3 Elastic/Viscoelastic correspondence

The goal is to solve the contact in viscoelasticity. For this purpose, a correspondence method is proposed. The Elastic/viscoelastic correspondence is inspired by the one used in the case of homogeneous half-space. It allows to use the elastic solutions to solve the corresponding viscoelastic problem. The solution proposed by Lee and Radok [LEE 60] is based on the following property: *In the Laplace or Fourier transform domain, viscoelastic constitutive equations are equivalent to their corresponding elastic ones.* Hence, the correspondence is performed by applying the following points to the elastic solution as summarised by Chen et al. [CHE 11]:

- ✧ replace the elastic modulus $\frac{1}{2\mu}$, with the viscoelastic creep compliance $J(t)$,
- ✧ discretise the time domain and the load history,
- ✧ integrate the hereditary integral $\int_{-\infty}^{\infty}()dt$.

Let's recall first the correspondence in the case of homogeneous bodies.
For any viscoelastic body, the displacement u_i at a time t can be written as:

$$\begin{aligned} u_i(x,y,t) &= \int_0^t \int\int_{\mathbb{R}^2} \mathcal{F}_{ij}(x-x',y-y',t-t')\dot{\sigma}_j(x',y',t')dx'dy'dt' \\ &= \int_0^t \int\int_{\mathbb{R}^2} \mathcal{F}_{ij}(x',y',t-t')\dot{\sigma}_j(x-x',y-y',t')dx'dy'dt' \end{aligned} \tag{3.19}$$

where σ_j are the components of the applied stress at the surface and $\mathcal{F}_{ij}(x,y,t)$ the viscoelastic influence coefficients. The dot $\dot{}$ represents the partial derivative with respect to time.
Considering a homogeneous semi-infinite body, the viscoelastic influence coefficients $\mathcal{F}_{ij}(x,y,t)$ can be written as:

$$\mathcal{F}_{ij}(x,y,t) = J(t)\bar{G}_{ij}(x,y), \tag{3.20}$$

where the term $\bar{G}_{ij}$ is included in the elastic influence coefficient and does not depend on the elastic modulus of the body. $J(t)$ is the creep function defining the viscoelastic behaviour of the body. The reader may find this correspondence method for a homogeneous half-space in [CHE 11] for instance. Thus the above displacement can be written as:

$$u_i(x,y,t) = \int_0^t J(t-t') \int\int_{\mathbb{R}^2} \bar{G}_{ij}(x',y')\dot{\sigma}_j(x-x',y-y',t')dx'dy'dt'. \tag{3.21}$$

This means that a convolution is performed between the elastic influence coefficients $\bar{G}_{ij}$ - which are constant - and the applied stress at every time step. And then the time integral, containing the creep function and the history of the loading, is calculated.

Now, when moving to the case of a multi-layered half-space, the factorisation in Eq. (3.20) is not possible in that same way.
What has been done for the present model is:

- ✧ Firstly, one may observe that the use of the potentials of Papkovich-Neuber implies the following forms of the displacements:

$$2\mu^r u_i^r = \phi_{,i}^r + x\psi_{x,i}^r + z\psi_{z,i}^r - (3-4\nu)\psi_i^r, \tag{3.22}$$

  where μ is the shear modulus of the layer r and ϕ and ψ_i are the potentials of Papkovich-Neuber.
  In the left hand, the factor 2μ is ideal for the correspondence since it has to be replaced by its viscoelastic equivalent $J(t)$.

- ✧ Secondly, solving the boundary conditions, it has come that the right hand depends on the ratio μ^c/μ^s. Since the Poisson's ratios are assumed constant, the change of behaviour of the materials is given only by those ratios μ^c/μ^s.

✧ The last remark have lead to propose the following equation for the viscoelastic displacements:

$$u_i(x,y,t) = \int_0^t J^c(t-t') \int\int_{\mathbb{R}^2} \bar{G}^c_{ij}(x',y',J^c(t')/J^s(t'))\dot{\sigma}_j(x-x',y-y',t')dx'dy'dt'. \tag{3.23}$$

This equation is an approximation of the exact solution. It meets the exact solution in steady-state regime and in some other cases as discussed in appendix C. In transient regime, the error made is marginal with regard to the behaviour of the Fourier transform (see appendix C for details).

Therefore, the correspondence can be performed but it is mandatory to recalculate the right hand of Eq. (3.22) at every time step. This recalculation of the influence coefficients has an additional cost on the overall simulation time. However, the simulation remains straight and fast.

The resulting equation for the normal displacement can then be written as:

$$u_z^{B_2}(x,y,t) = \int_0^t J^c(t-\xi) \left[\bar{G}^c(x,y,\xi) * \frac{\partial p(x,y,\xi)}{\partial \xi} \right] d\xi \tag{3.24}$$

where,

- $*$ represents the convolution product,
- $J^c(t)$ is the creep function of the top layer,
- $\bar{G}^c$ is contained - as explained above - in the Green function (the influence coefficients) for the normal displacement at the surface $z=0$ of the half-space, in which the ratio μ^c/μ^s are replaced by their equivalent $J^c(\xi)/J^s(\xi)$.

In the case of a single layered half-space, the recalculation of the influence coefficient at every time step has as consequence an *increase of the calculation time by approximately 50%.*

The logic exposed above for the displacement u_z due to a pressure field, is the same to use for the displacements u_x and u_y; and when a shear field is imposed. It can also be applied for the body 1.

3.2.4.4 Pure rolling procedure

The rolling and sliding of bodies in a viscoelastic contact demand to shift one or both bodies in order to have the adequate relaxation phenomena related to the history of loading. For the pure rolling (with no friction), let's introduce a coordinate system $R^0(O^0, X_1^0, X_2^0, X_3^0)$ for the initial time $t=0$ and a moving coordinate system $R(O, X_1, X_2, x_3)$ for every time $t \neq 0$. When the time range of simulation is divided into N_t uniform time steps of size Δt, the elementary shift of the rolling body is

$\Delta\vec{r} = \vec{v} \times \Delta t$. Then the contact solution at every time step is found in the frame centred on the projection of the center of pressure of the rolling body, on the tangent plane of the contact. The contact fields at the surface of the half-space are translated into the actual frame to keep the history of the solution available. Figure 3.8 shows the translation procedure for a rolling sphere.

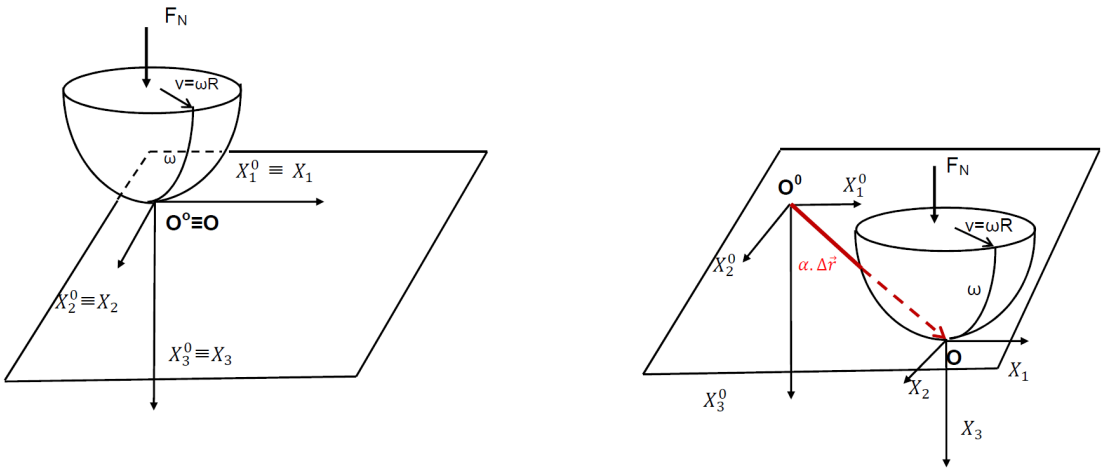

Figure 3.8: Rolling procedure by the example of a rolling sphere on a plane.

Therefore, the surface normal displacement at every time $t = \alpha\Delta t$ can be written as:

$$u_z^{B_2}(x,y,t) = \int_0^t J^c(t-\xi)\left[\bar{G}^c(x,y,\xi) * \frac{\partial p(x-\alpha\Delta r_x, y-\alpha\Delta r_y, \xi)}{\partial \xi}\right] d\xi \qquad (3.25)$$

One can identify that the above equation means that the previous pressure field is translated backward, accompanied by its relaxation.

With the above formulation of the contact considering viscoelasticity, the numerical approach demands to take into account the time dimension. This numerical task is described below.

3.2.4.5 Numerical approach

The numerical implementation needs a discretisation of both space and time. The contact surface is discretised into $N_1 \times N_2$ elements, while the time domain is subdivided into N_t time steps Δt. Then, using the finite difference method for $\frac{\partial p}{\partial \xi}$ the discretised form of Eq. (3.25) becomes:

$$u_z^{B_2}(i,j,\alpha) = \sum_{k=0}^{\alpha} J^c[(\alpha-k)\Delta t] \times \left[\sum_{i'=1}^{N_1}\sum_{j'=1}^{N_2} \bar{G}^c\left(i-i', j-j', k\Delta t\right) \times \left(p(i',j',k) - p(i',j',k-1)\right)\right], \qquad (3.26)$$

where one can infer that i, j and α are the indices for x, y and t respectively. For $k=0$, the term with $k-1$ has to be zero.

Note that the translation process explained in the previous section does not clearly appear in the notation of the pressure here; so, the reader should make sure to perform the translation between the actual and the precedent time steps.

At the time step α, the only unknown in the above equation is the actual pressure field. The implementation gives:

1. For $\alpha=0$, the elastic solution of the contact is found: $p(i,j,0)$.
2. For any α, the Green functions are recalculated $\bar{G^c}\,(i-i',j-j',(\alpha)\Delta t)$. Then, the term

$$\mathcal{H}(\alpha)=\sum_{k=0}^{\alpha-1} J^c[(\alpha-k)\Delta t]\times\left[\sum_{i'=1}^{N_1}\sum_{j'=1}^{N_2}\bar{G^c}\left(i-i',j-j',k\Delta t\right)\times\Big(p(i',j',k)-p(i',j',k-1)\Big)\right]$$
$$-J^1[(\alpha-\alpha)\Delta t]\times\left[\sum_{i'=1}^{N_1}\sum_{j'=1}^{N_2}\bar{G^c}\left(i-i',j-j',(\alpha)\Delta t\right)\times\Big(p(i',j',\alpha-1)\Big)\right] \tag{3.27}$$

   is calculated and stored.
   The remaining term $J^1[(\alpha-\alpha)\Delta t]\times\left[\sum_{i'=1}^{N_1}\sum_{j'=1}^{N_2}\bar{G^c}\,(i-i',j-j',(\alpha)\Delta t)\times(p(i',j',\alpha))\right]$ contains the unknown pressure field and so is solved with the CGM algorithm.

After the contact is solved, one may want to calculate the volume quantities especially the three-dimensional stresses.

3.2.4.6 3D stresses calculation

When surface field is known at the time step α, the 3D stresses calculation uses this contact field and the elastic Green functions of stress. The consequence of this modelling procedure is that any change in the volume cannot be observe in without observing a change at the contact surface. Moreover, it implies that the change in the contact surface is sufficient for the modelling of the viscoelasticity. In other words, the Elastic/Viscoelastic correspondence is not applied to the stresses in the volume. This is the reason why the influence coefficients of the elastic layered half-space are used for the calculation of the stresses by convolution with the pressure field output of the viscoelastic contact. The stresses for the pure frictionless normal contact can then be written for example as:

$$\sigma_{ij}=K_{ij}^{p}*p \tag{3.28}$$

where K_{ij}^{p} are the influence coefficients for the stress component σ_{ij} due to normal pressure; and $*$ the sign for convolution.
Finally, the whole numerical approach of this contact on viscoelastic layered half-space is summarised in the algorithm displayed in Fig. 3.9.

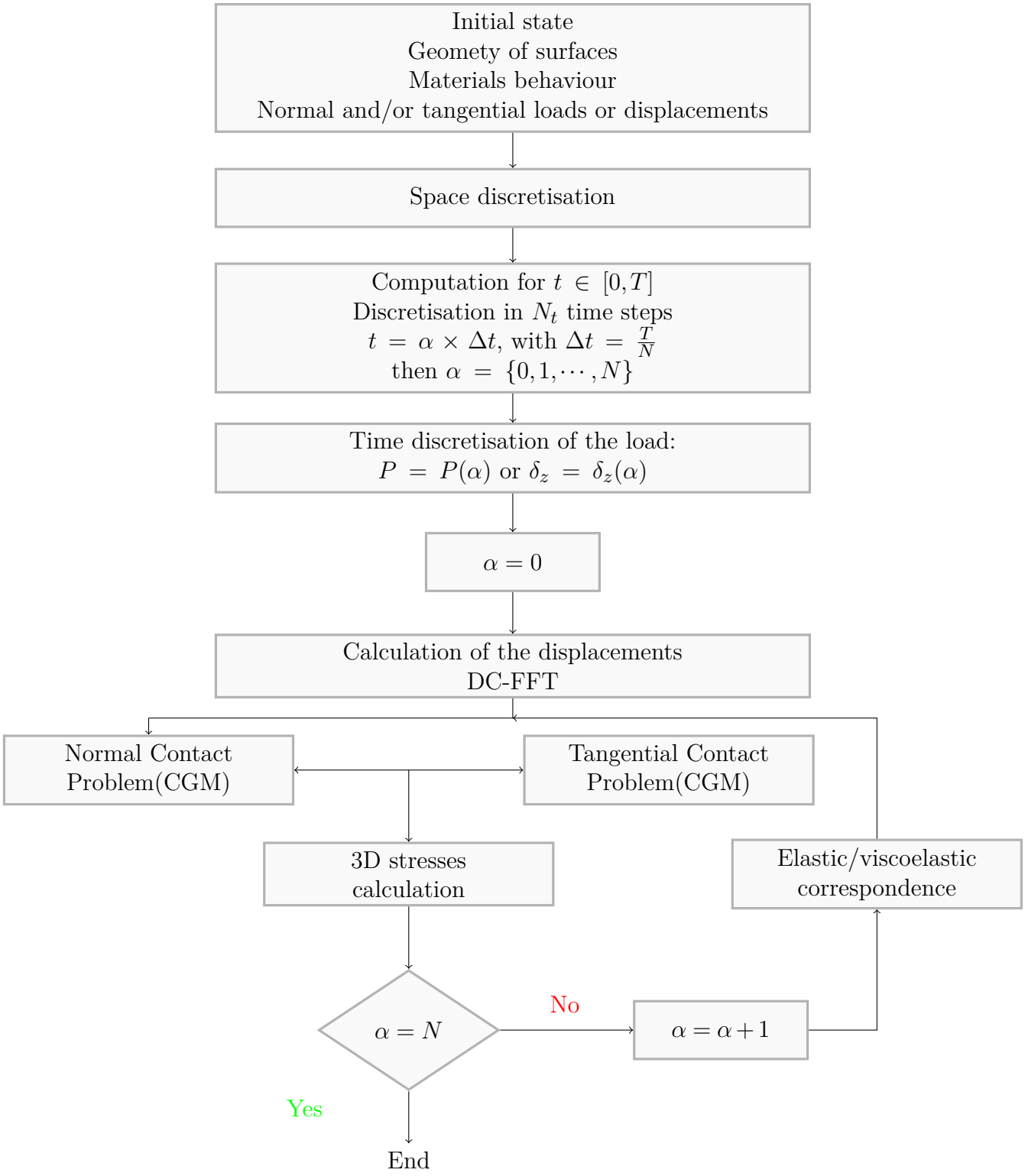

Figure 3.9: Algorithm of resolution of the contact on a viscoelastic layered half-space.

In summary, the elastic influence coefficients for solving the contact problem involving a layered half-space have been determined, a correspondence method has been proposed to get the viscoelastic solutions from the elastic ones and finally a rolling procedure has been proposed to translate the contact field without lost of informations related to the history of loading. In the next section, a validation of the model is to be performed especially for the viscoelastic part.

3.3 Validation

To perform a complete validation, the present semi-analytical model has been confronted to other models in three different contact cases: viscoelastic homogeneous contact cases, the viscoelastic layer bounded to a rigid base and a Finite Element model. The first comparison regarding the rolling contact on a homogeneous viscoelastic half-space has been relevant to verify that the above rolling procedure works well. The second validation for a viscoelastic layer on a rigid base has allowed to begin falling into the novelty of this work even if it is a limiting case. The last case which is presented here is a complete case of validation with Finite Element Method. The other cases are presented in appendix B.

Contact on a viscoelastic layered half-space (FEM validation)

For the validation of a complete case of contact on a viscoelastic layered half-space, a Finite Element Model (FEM) has been built using the commercial software Abaqus v6.17. The configuration is shown in Fig. 3.10: a rigid sphere of radius $R = 31$ mm is in contact with a viscoelastic layered solid of dimensions $100 \times 50 \times 60$ mm^3. The coating of thickness $h = 1$ mm is a partition of the solid and its material is PolyMethylMetAcrylate (PMMA) of relaxation function:

$$R_{PMMA}(t) = 1429.71 + 184.62 \times \exp\left(-\frac{t}{8.93}\right) + 191.06 \times \exp\left(-\frac{t}{117.96}\right) \quad (3.29)$$

The substrate material is a *fictitious viscoelastic steel* with one relaxation time:

$$R_{STEEL}(t) = \mu \times \exp\left(\frac{-t}{\tau}\right) \quad (3.30)$$

where the units of R and t are MPa and s respectively; μ is the shear modulus $\mu = 80769\ MPa$ and τ is the relaxation time of the substrate (fictitious steel): $\tau = \tau_s = 10\ s$. This value of τ has been choosen so that it can be comparable to the relaxation times of the PMMA. The Poisson's ratios are $\nu_{PMMA} = 0.38$ and $\nu_{STEEL} = 0.3$. A friction coefficient $f = 0.25$ is considered for the surfaces in contact. To reduce computation time, the symmetry of the model is considered with respect to the plane $y = 0$. A zone of interest (zoom in Fig. 3.10) in the solid of dimensions $7 \times 3.5 \times 2.5$ mm^3 is meshed with eight-node brick elements with reduced integration

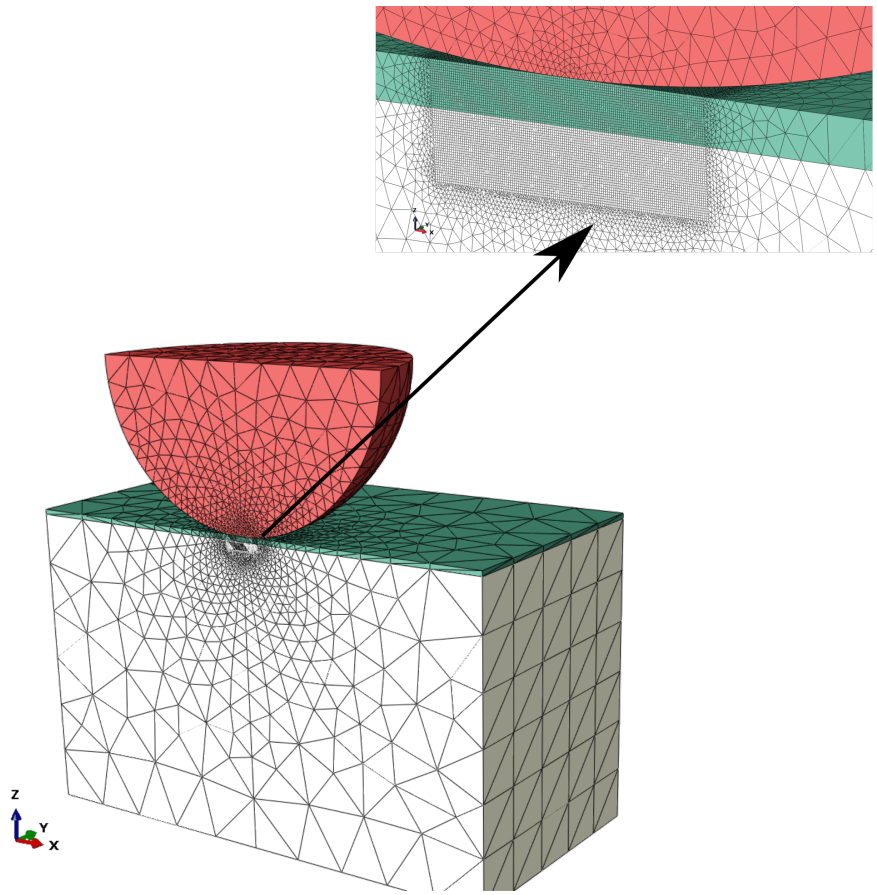

Figure 3.10: Finite element model for validation

(C3D8R) of size 0.05. The rest of the solid is meshed with four-node tetrahedral elements (C3D4) and the sphere with ten-node tetrahedral elements (C3D10). The calculation is made in 3 steps (see Fig.3.11):

1. **Normal charge**: Application of a normal displacement $\delta = 0.1$ mm,
2. **Sliding**: Application of a tangential displacement $\xi = 0.1$ mm,
3. **Visco**: Viscoelastic relaxation of the stresses. The viscoelastic simulation time is $2 \times \tau$, divided in 40 time steps.

Figure 3.12 shows the comparison of the normalised contact pressure p/p_0 and shear σ_X/p_0 obtained by the Finite Element Method and the results by the Semi-Analytical Method for different time steps. One can observe a correct agreement between the two methods except for the shear at $t = \varepsilon$. In fact, when applying a normal force on a half-space, finding the induced shears is a non-linear problem. This non-linear problem strongly depends on the mesh and needs to be handled with care.

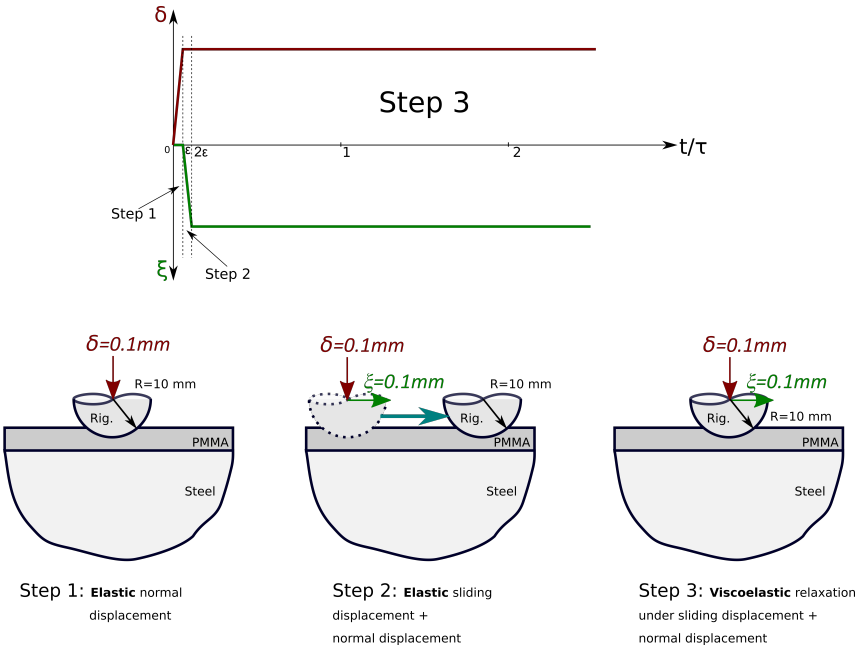

Figure 3.11: Finite element model steps

Thus, the differences come from the average method of calculation of quantities with Abaqus in presence of friction, and the mesh which slightly differs between the two methods. But the results match enough to state that the model is validated.
Finally it should be noted that here the computation time by the Finite Element Method is approximately 800 time the one by the present method (semi-analytical method).

Now, with this semi-analytical model, the goal is to to try to understand various effects on the contact when a viscoelastic layered half-space is involved in the contact. In this spirit, a parametric study is performed in the following section.

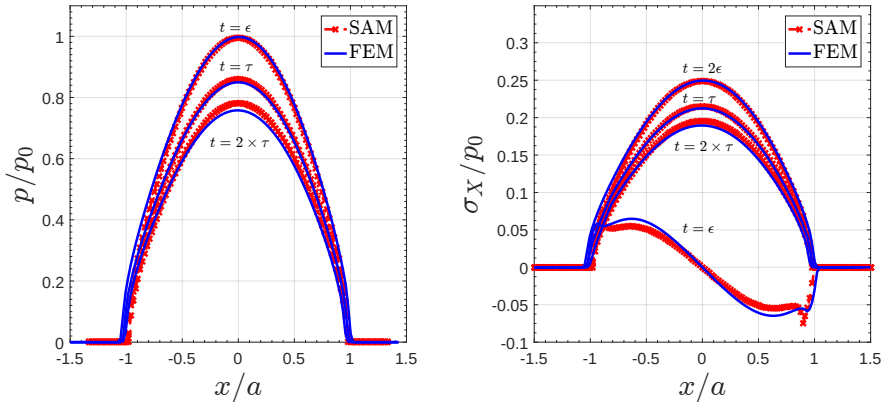

Figure 3.12: Validation with Finite Element Method: Normalised contact pressure comparison (a) and normalised shear x (b) at different time steps.

3.4 Results

3.4.1 Description of the problem

Although the model can take into account frictional contact, in this part a free rolling or pure sliding (friction coefficient $f = 0$) contact is considered between a rigid sphere of radius $R = 10$ mm moving at constant velocity v on a viscoelastic layered half-space. The substrate viscoelastic properties are kept constant and are given by Eqs. (3.31) and (3.32), with $\mu_{\infty s} = 3.86$ MPa, $\mu_{\infty s}/\mu_{0s} = 11/2$. The reference case is the contact over the substrate for a prescribed normal displacement $\delta = 0.1$ mm; p_0 the reference contact pressure and a the reference contact radius are given at $t = 0$.
The coating thickness is h and its viscoelastic properties are noted $\mu_{\infty c}$, μ_{0c}. The Poisson's ratio is considered constant and the same for coating and substrate: $\nu_{c,s} = 0.3$.

$$J(t) = \left[\frac{1}{\mu_0} - \frac{1}{\mu_1}\exp\left(-\frac{t}{\tau}\right)\right] = \left[\frac{1}{\mu_\infty} + \frac{1}{\mu_1}\left(1 - \exp\left(-\frac{t}{\tau}\right)\right)\right] \tag{3.31}$$

$$R(t) = \left[\mu_0 + (\mu_\infty - \mu_0)\exp\left(-\frac{t}{\frac{\mu_0}{\mu_\infty}\tau}\right)\right] \tag{3.32}$$

A parametric study is made with the following parameters:

1. $\mu_{\infty c}/\mu_{\infty s} = 0.25$; 0.5 ; 1 ; 2 ; 4.

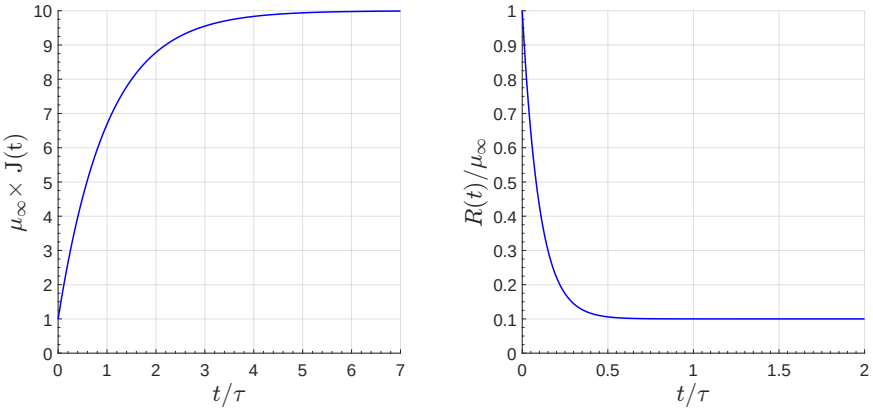

(a) (b)

Figure 3.13: Creep function (a) and relaxation function (b)

2. $\tau_c/\tau_s = 0.5$; 1 ; 2 ; where τ_c and τ_s are the relaxation times of coating and substrate, respectively.

3. $h = 0.1a$; $0.25a$; $0.5a$; a ; ∞ ; where a is the elastic contact radius for the homogeneous half-space with substrate properties.

4. $v\tau_s/a = 0.4$; 0.8 ; 1.2.

For every case, the following data will be analysed:

✧ The contact pressure distribution normalised by p_0, the Hertz's pressure for the homogeneous half-space with substrate properties

✧ The coating/substrate interfacial stresses σ_{11} and σ_{13} considered relevant since the sphere rolls/slides along x_1. The second invariant J_2 is also plotted as the overall stress state in the volume. The stresses will be plotted versus x_1 in the plane $x_2 = 0$

✧ The apparent friction coefficient μ_{app} and resisting torque M. They are a representation of the hysteresis losses in the viscoelastic material. These losses induce a tangential force given by:

$$F_V(t) = \int_{\Gamma_c(t)} \frac{\partial u_3(x_1, x_2, t)}{\partial x_1} p(x_1, x_2, t)\, dx_1 dx_2 \tag{3.33}$$

where $\Gamma_c(t)$ is the real contact area at time t.
Then the apparent friction coefficient is $\mu_{app} = F_t/F_N$, where F_N is the normal load. The above integral is evaluated using rectangle rule while a Finite Difference Method is used to calculate $\partial u_3(x_1, x_2, t)/\partial x_1$.

In the case of a rolling/sliding sphere in direction x_1, the resisting torque is given by:

$$M(t) = \int_{\Gamma_c(t)} x_1 p(x_1, x_2, t)\, dx_1 dx_2 \tag{3.34}$$

This equation is evaluated by the rectangle rule. Moreover, at a macroscopic scale, for a rolling/sliding sphere the two variables (apparent friction coefficient and resisting torque) are related by the following equation:

$$M(t) = \mu_{app}(t) \times F_N \times R \tag{3.35}$$

Note that what is called here the apparent friction coefficient is observed for a frictionless contact. For more details on the differences between rolling and sliding, also depending on which body behaves viscoelastically, the reader may refer to Fig. 3 in Koumi et al. [KOU 15b].

3.4.2 Effect of the ratio of shear modulus $\mu_{\infty c}/\mu_{\infty s}$

For this study, a normal body displacement $\delta = 0.1$ mm is prescribed at $t = 0$. The dimensionless velocity of the sphere is $v\tau_s/a = 0.8$. For both coating and substrate $\mu_{\infty c,s}/\mu_{0c,s} = 11/2$; $\tau_c/\tau_s = 1$; and the computation time domain is $[0, 2\tau_s]$.

Figure 3.14 shows the contact pressure distribution normalised by p_0, the Hertz's pressure for the homogeneous half-space with substrate properties. The results are plotted at (a) t=$\tau_s/10$, (b) t=$\tau_s/4$, (c) t=τ_s, (d) t=$2 \times \tau_s$. One can see that the contact pressure increases significantly with the ratio $\mu_{\infty c}/\mu_{\infty s}$.
The apparent friction coefficient and the resisting torque plotted in Fig. 3.15 show a minor variation with the ratio $\mu_{\infty c}/\mu_{\infty s}$. However, a slight decrease can be observed when increasing the ratio. The steady-state regime which is reached when $t = \tau/2$ approximately; and at this regime the apparent friction coefficient is close to 0.04.

The coating/substrate interface stresses are plotted in Fig. 3.16. σ_{xx} (Fig. 3.16(a)) shows a profile near to a normal law distribution but slightly different with two main zones. A middle zone which is in compression when $\mu_{\infty c}/\mu_{\infty s} < 1$ and in traction when $\mu_{\infty c}/\mu_{\infty s} > 1$; and a peripheral zone which is always in compression and where stresses logically vanish when far from the contact area. It is also interesting to remark the abrupt increase of the maximum of the σ_{xx} component when $\mu_{\infty c}/\mu_{\infty s} > 1$ while the decrease of the ratio $\mu_{\infty c}/\mu_{\infty s}$ from 0.5 to 0.25 implies a slight change.
Besides, the curves of σ_{xz} (Fig. 3.16(b)) show a compression zone at the front in the rolling direction and a traction zone behind. The absolute value of shear σ_{xz} at the interface increases with the ratio $\mu_{\infty c}/\mu_{\infty s}$. But it increases less rapidly for $\mu_{\infty c}/\mu_{\infty s} > 1$.
To have an overall representation of the stresses, the second invariant is plotted in Fig. 3.16(c). A global increase of J_2 in respect to the ratio $\mu_{\infty c}/\mu_{\infty s}$ is observed; meaning the stiffness of the coating drives the stresses at the coating/substrate interface.

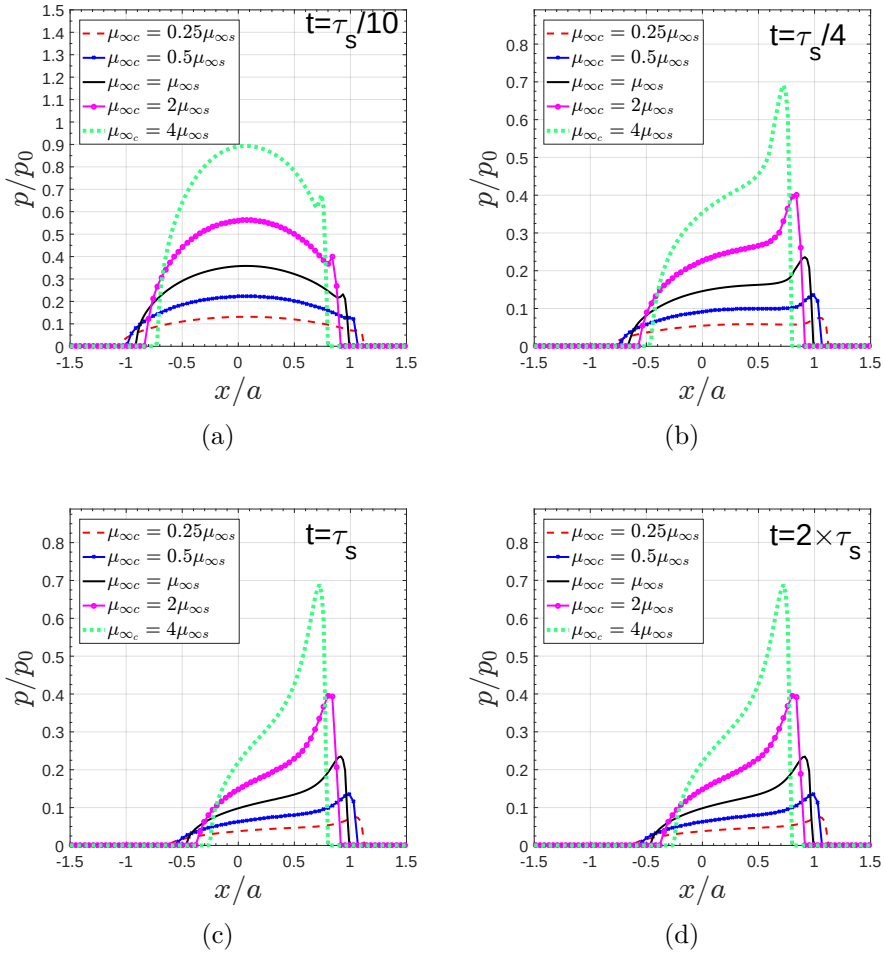

Figure 3.14: Distribution of normalised contact pressure for layered viscoelastic half-space for different ratios $\mu_{\infty c}/\mu_{\infty s}$; prescribed normal body displacement $\delta =$ 0.1 mm and dimensionless velocity $v\tau_s/a = 0.8$ at (a) t=$\tau_s/10$, (b) t=$\tau_s/4$, (c) t=τ_s, (d) t=$2 \times \tau_s$.

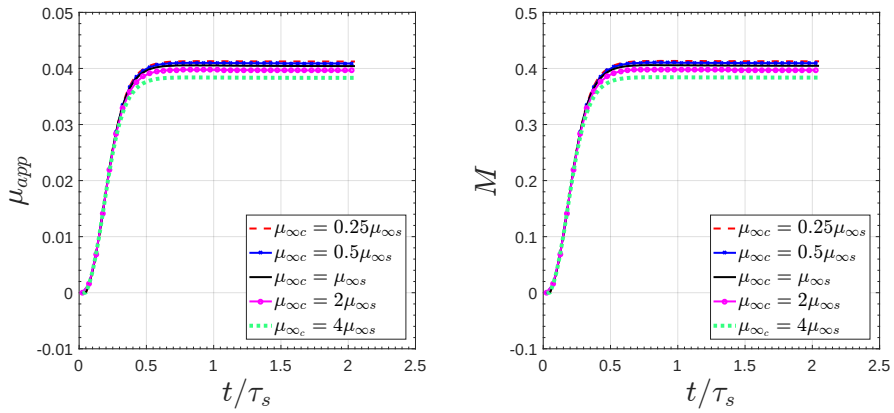

(a) (b)

Figure 3.15: Apparent friction coefficient (a) and resisting torque (b) for different ratios $\mu_{\infty c}/\mu_{\infty s}$; prescribed normal body displacement $\delta = 0.1$ mm and dimensionless velocity $v\tau_s/a = 0.8$.

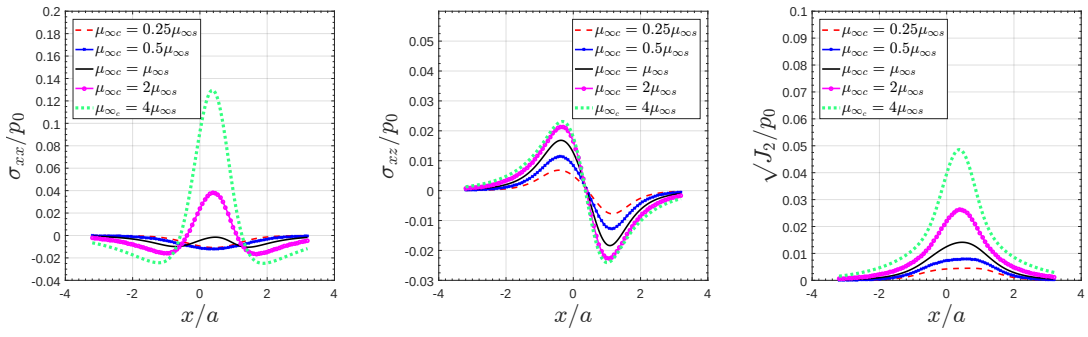

(a) (b) (c)

Figure 3.16: Normalised coating/substrate interface stresses (a) σ_{xx}, (b) σ_{xz} and (c) second invariant J_2 ; for different ratios $\mu_{\infty c}/\mu_{\infty s}$, for prescribed normal body displacement $\delta = 0.1$ mm and dimensionless velocity $v\tau_s/a = 0.8$.

3.4.3 Effect of the ratio of relaxation times τ_c/τ_s

In this section, the effect of the relaxation time ratio is investigated. For this aim, it is kept $\mu_{\infty c} = 0.25 \times \mu_{\infty s}$; $\mu_{\infty c,s}/\mu_{0c,s} = 11/2$; while $\tau_c/\tau_s = 0.5$; 1 ; 2. A normal body displacement $\delta = 0.1$ mm is prescribed, and the dimensionless rolling velocity is set at $v\tau_s/a = 0.8$.
The normalised contact pressure profile is plotted in Fig. 3.17 and the apparent friction coefficient in Fig. 3.18. Both show that the steady-state regime is achieved more rapidly when the ratio τ_c/τ_s decreases. This is why the pressure distribution for $\tau_c/\tau_s = 0.5$ is almost the same at the four time steps plotted. One can also observe that at steady-state regime, the highest peak of pressure appears for the highest relaxation time ratio. This may mean that the increase of the relaxation time ratio is somewhat equivalent to an increase of the coating stiffness. In addition, the relaxation time ratio drives the time to spend before reaching the steady-state regime, or the speed with which it is reached. It is very important to remark the very strong impact of the relaxation time on the apparent friction: when τ_c is greater, greater is the resisting tangential force induced; then μ_{app} increases.

The analysis of the coating/substrate interface in Fig. 3.19 shows that the fluctuation and magnitude of the stresses increase with the ratio τ_c/τ_s. This means that when the coating relaxes more rapidly than the substrate, its deformation induces additional stresses at the interface. On contrary, when the coating relaxes less rapidly, stresses are reduced. These observations confirm the idea of adding a certain stiffness to the coating when increasing the relaxation time ratio.

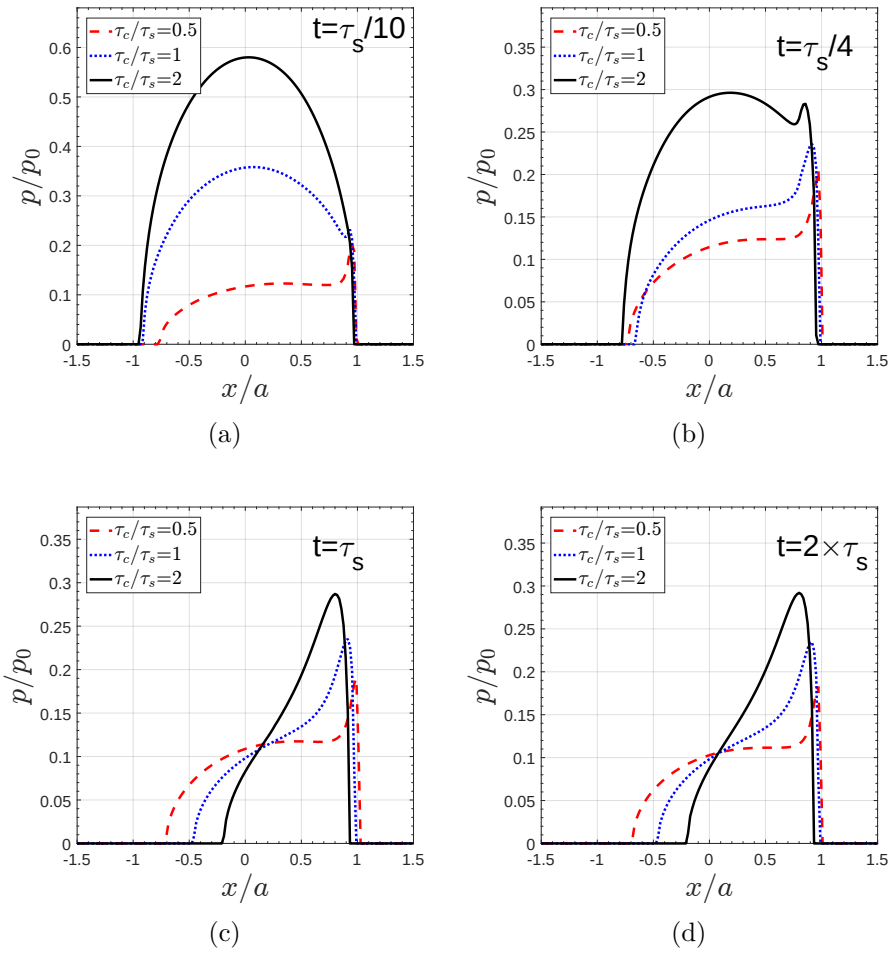

Figure 3.17: Distribution of normalised contact pressure for layered viscoelastic half-space for different ratios τ_c/τ_s ; $\mu_{\infty c} = 0.25 \times \mu_{\infty s}$; prescribed normal body displacement $\delta = 0.1$ mm and dimensionless velocity $v\tau_s/a = 0.8$ at (a) t=$\tau_s/10$, (b) t=$\tau_s/4$, (c) t=τ_s, (d) t=$2 \times \tau_s$.

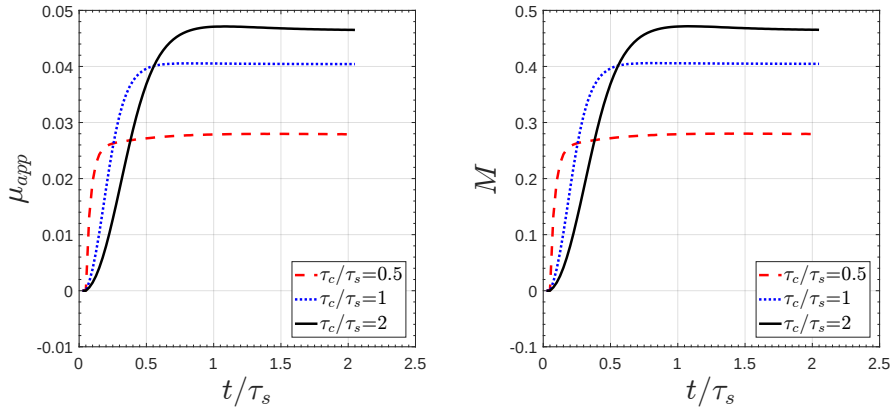

(a) (b)

Figure 3.18: Apparent friction coefficient (a) and resisting torque (b) for different ratios τ_c/τ_s ; $\mu_{\infty c} = 0.25 \times \mu_{\infty s}$; prescribed normal body displacement $\delta = 0.1$ mm and dimensionless velocity $v\tau_s/a = 0.8$.

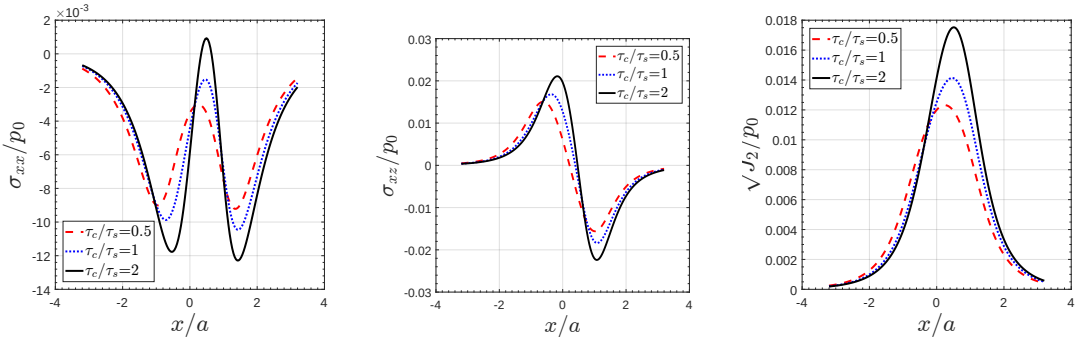

(a) (b) (c)

Figure 3.19: Normalised coating/substrate interface stresses (a) σ_{xx}, (b) σ_{xz} and (c) second invariant J_2 ; for different ratios τ_c/τ_s ; $\mu_{\infty c} = 0.25 \times \mu_{\infty s}$; prescribed normal body displacement $\delta = 0.1$ mm and dimensionless velocity $v\tau_s/a = 0.8$.

3.4.4 Effect of the coating thickness

This section focuses on the effect of the coating thickness, while keeping constant the following ratios: $\mu_{\infty c} = 0.25 \times \mu_{\infty s}$; $\mu_{\infty c,s}/\mu_{0c,s} = 11/2$ and $\tau_c/\tau_s = 1$. A normal body displacement $\delta = 0.1$ mm is prescribed, and the dimensionless rolling velocity is $v\tau_s/a = 0.8$. Figures 3.20, 3.21 and 3.22 are plotted for $h = 0.1a$, $0.25a$, $0.5a$, a , ∞ ; where a is the contact radius for the homogeneous half-space with substrate properties.
When h is increasing, the solution will tend towards the homogeneous solution with the coating properties. In Figs. 3.20 and 3.22, when increasing h the pressure decreases to reach the homogeneous half space solution. Besides, the coating/substrate interface stresses decrease to reach zero because the interface becomes far in the half-space and does not feel the stresses anymore. One can observe in Fig. 3.22(b) that for $h = 0.1a$, there is a perturbation of the shear stress σ_{xz}. This is due to our parametrisation where the prescribed normal displacement coincides with the thickness of the coating. This result shows that the models can handle this special case of loading.
In the same time, one can observe that the influence of the thickness on the apparent friction coefficient (see Fig. 3.21) is not significant.

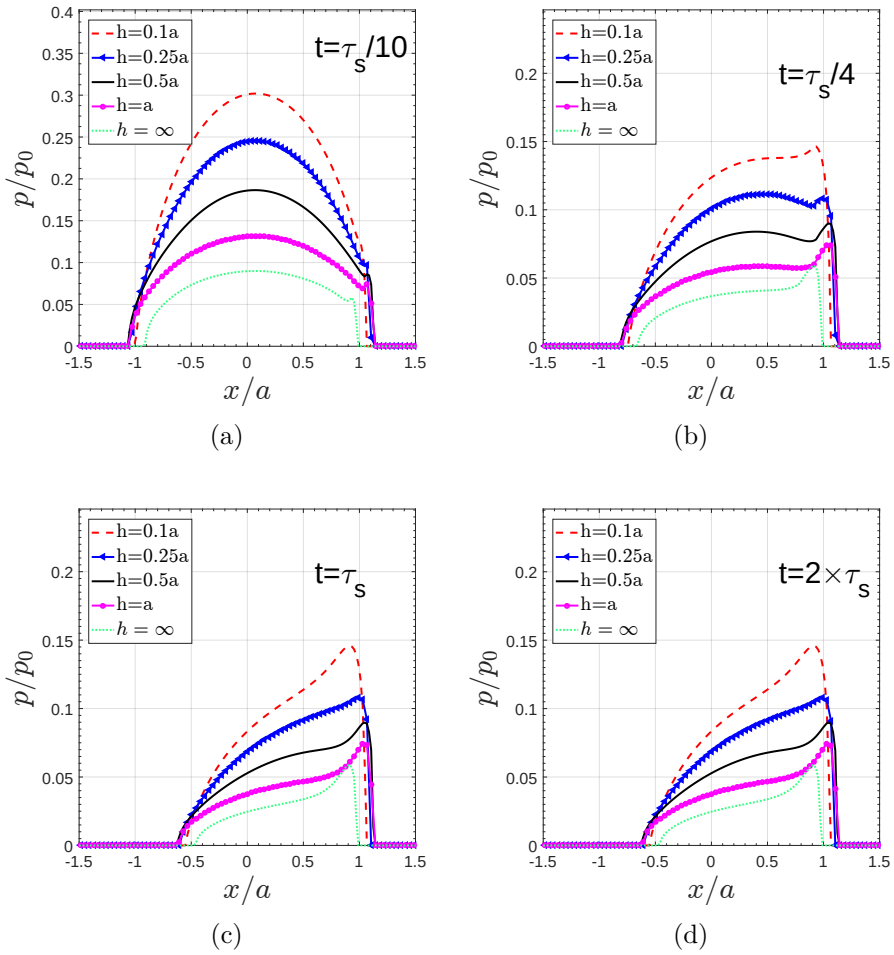

Figure 3.20: Distribution of normalised contact pressure for layered viscoelastic half-space for different thicknesses h; $\mu_{\infty c} = 0.25 \times \mu_{\infty s}$; prescribed normal body displacement $\delta = 0.1$ mm and dimensionless velocity $v\tau_s/a = 0.8$ at (a) t=$\tau_s/10$, (b) t=$\tau_s/4$, (c) t=τ_s, (d) t=$2 \times \tau_s$.

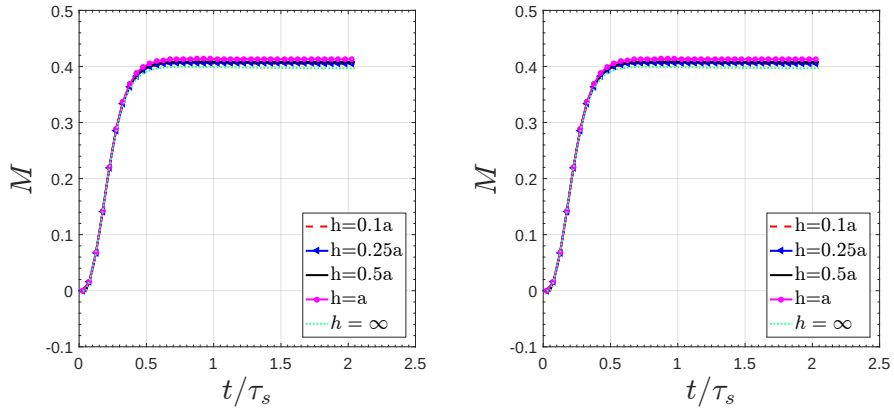

Figure 3.21: Apparent friction coefficient (a) and resisting torque (b) for different thicknesses h; $\mu_{\infty c} = 0.25 \times \mu_{\infty s}$; prescribed normal body displacement $\delta = 0.1$ mm and dimensionless velocity $v\tau_s/a = 0.8$.

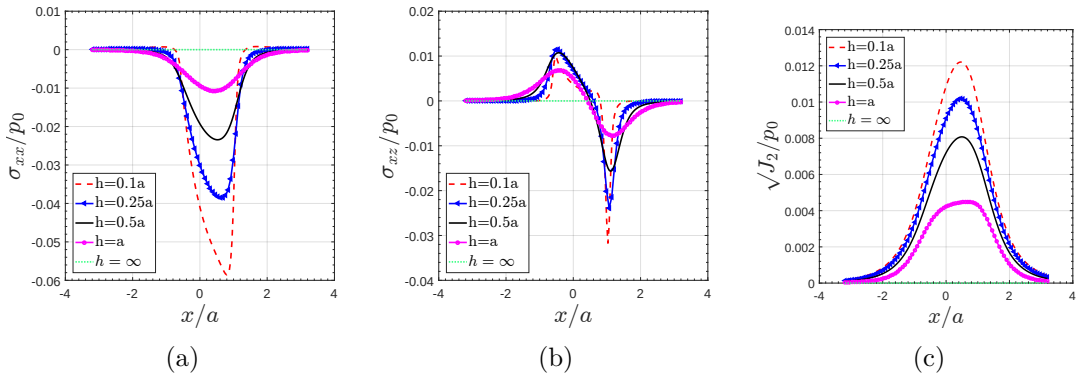

Figure 3.22: Normalised coating/substrate interface stresses (a) σ_{xx}, (b) σ_{xz} and (c) second invariant J_2 ; for different thicknesses h; $\mu_{\infty c} = 0.25 \times \mu_{\infty s}$; prescribed normal body displacement $\delta = 0.1$ mm and dimensionless velocity $v\tau_s/a = 0.8$.

3.4.5 Effect of the velocity

In this section, the effect of the velocity is studied. It is kept constant the following ratios: $\mu_{\infty c} = 0.25 \times \mu_{\infty s}$; $\mu_{\infty c,s}/\mu_{0c,s} = 11/2$ and $\tau_c/\tau_s = 1$. A normal body displacement $\delta = 0.1$ mm is prescribed, and the dimensionless rolling velocity is set to $v\tau_s/a = 0.4$; 0.8 or 1.2.
Results are plotted in Figs. 3.23, 3.24 and 3.25. In one hand, when the velocity is low the stresses have time to relax and then the pressure decreases with the velocity. In another hand, the apparent coefficient curves show that the steady-state regime is achieve near $t = \tau/2$ independently of the velocity.
Concerning the stresses at the coating/substrate interface, an increase of the absolute value is observed when increasing the velocity. Nevertheless, the values of the stresses are not very high themselves because of the set of parameters applied.

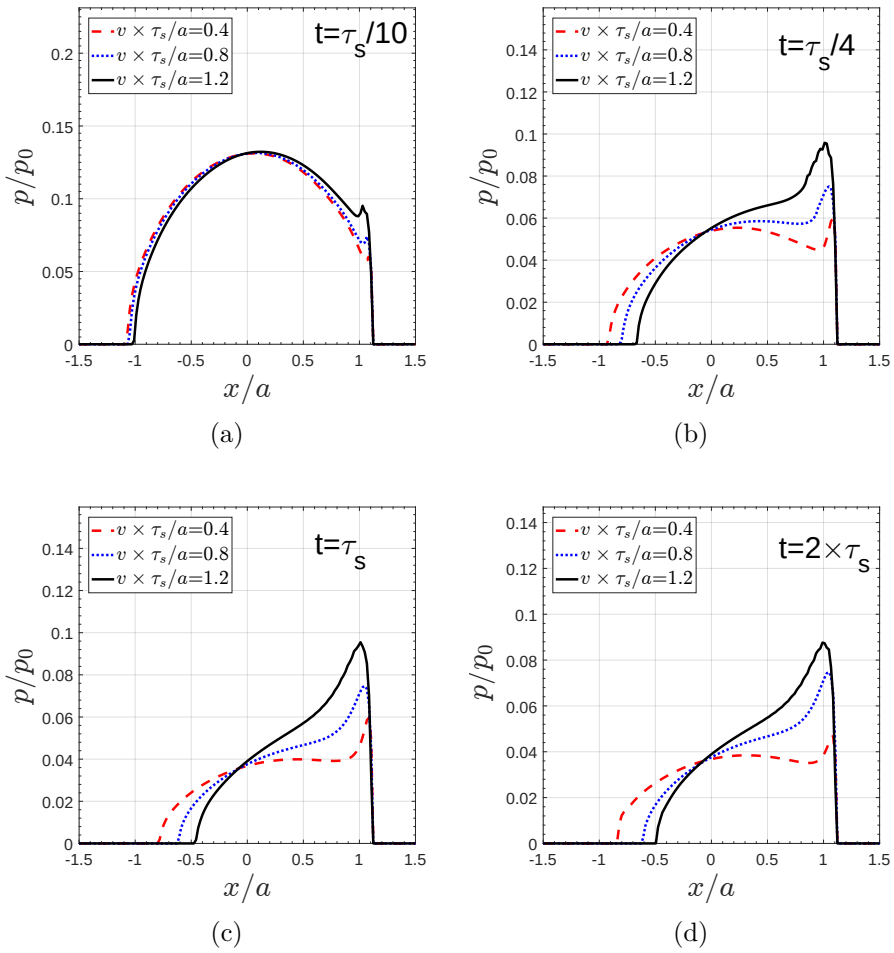

Figure 3.23: Distribution of normalised contact pressure for layered viscoelastic half-space for different dimensionless velocities $v\tau_s/a$; for $\mu_{\infty c} = 0.25 \times \mu_{\infty s}$ and a prescribed normal body displacement $\delta = 0.1$ mm at (a) t=$\tau_s/10$, (b) t=$\tau_s/4$, (c) t=τ_s, (d) t=$2 \times \tau_s$.

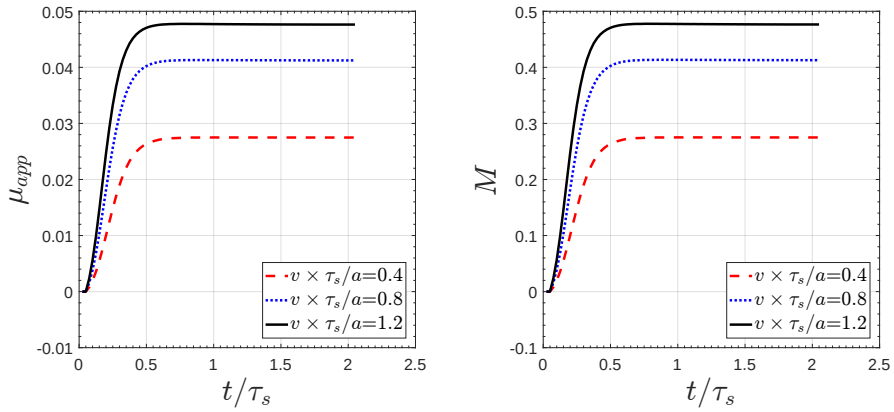

(a) (b)

Figure 3.24: Apparent friction coefficient (a) and resisting torque (b) for different dimensionless velocities $v\tau_s/a$; for $\mu_{\infty c} = 0.25 \times \mu_{\infty s}$ and prescribed normal body displacement $\delta = 0.1$ mm.

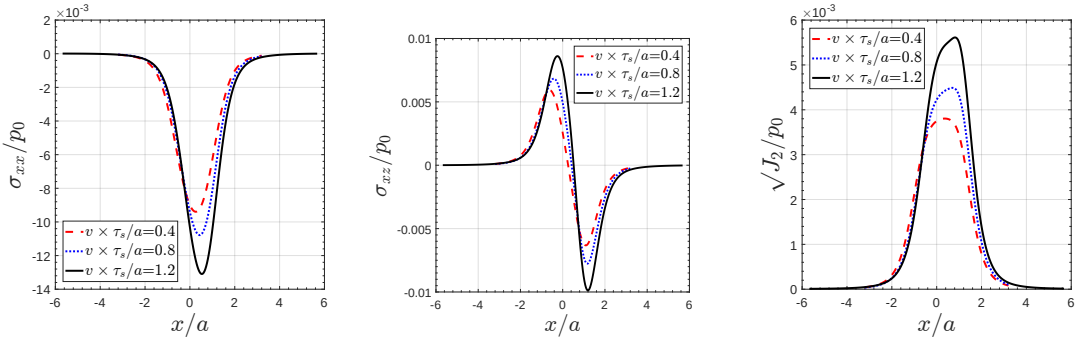

(a) (b) (c)

Figure 3.25: Normalised coating/substrate interface stresses (a) σ_{xx}, (b) σ_{xz} and (c) second invariant J_2 for different dimensionless velocities $v\tau_s/a$; for $\mu_{\infty c} = 0.25 \times \mu_{\infty s}$ and prescribed normal body displacement $\delta = 0.1$ mm.

3.4.6 Prescribed normal force: creep

The above work was done for a prescribed normal body displacement δ implying relaxation effects. In the present part a normal force $P = 1.48$ N is applied to move into the creep case. The parameters of section 3.4.5 are kept. The results are plotted in Figs. 3.26 and 3.27 in terms of pressure profile, apparent friction coefficient and resisting torque.

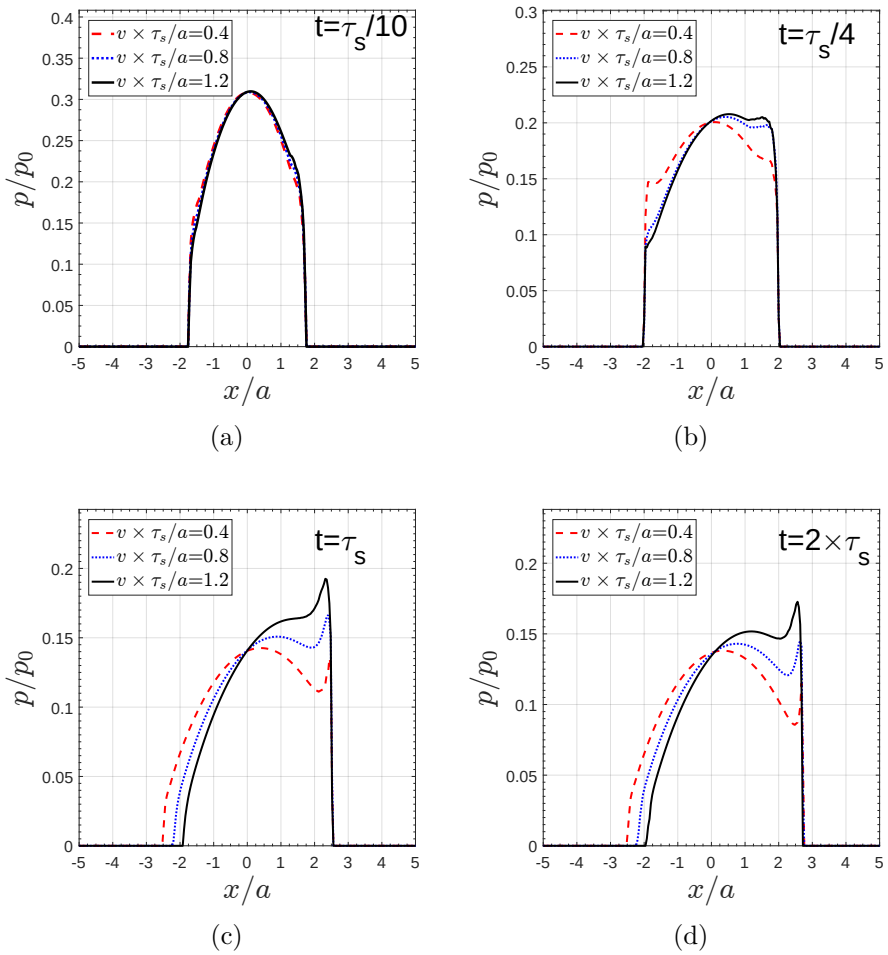

Figure 3.26: Distribution of normalised contact pressure for layered viscoelastic half-space for different dimensionless velocities $v\tau_s/a$; for $\mu_{\infty c} = 0.25 \times \mu_{\infty s}$ and prescribed normal force $P = 1.48$ N at (a) t=$\tau_s/10$, (b) t=$\tau_s/4$, (c) t=τ_s, (d) t=$2 \times \tau_s$.

One can observe in Fig. 3.27 that the steady-state regime is hardly acheived near $t/\tau = 4$ against $t/\tau = 0.5$ in the case of a prescribed normal body displacement. This behaviour is a result of the creep function effect (see Fig. 3.13(a)); while when a normal body displacement is prescribed, there is a relaxation effect.

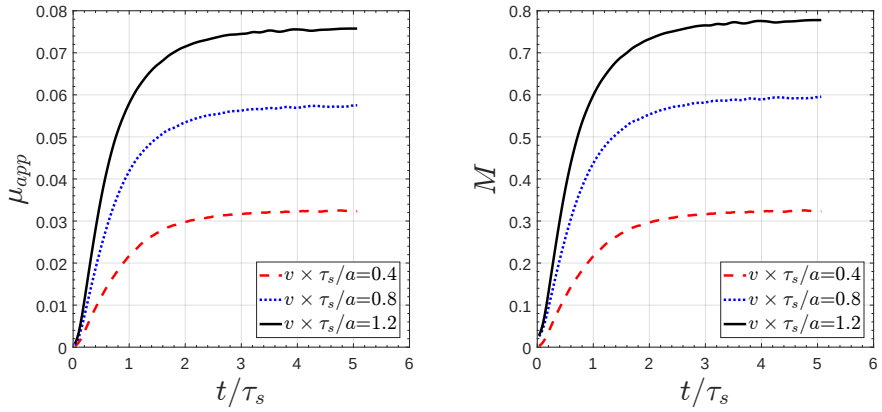

Figure 3.27: Apparent friction coefficient (a) and resisting torque (b) for different dimensionless velocities $v\tau_s/a$; for $\mu_{\infty c} = 0.25 \times \mu_{\infty s}$ and prescribed normal force $P = 1.48$ N.

3.4.7 3D stress analysis

The present model described with equations in section 6.2 allows the calculation of 3D stresses. When the contact is solved, the contact pressure distribution is the input of the 3D stress calculation. This procedure considers that there is no change of the material with time, but only a change of the pressure distribution which influences the stresses.
In the present section the parametric study of section 3.4.2 is considered but with $\tau_c/\tau_s = 0.25$ and $\mu_{\infty c}/\mu_{\infty s} = 0.25$.
Here a cut view in the plane $Y = 0$ is presented. In Fig. 3.28, stresses (a) σ_{xx}/p_0, (b) σ_{xz}/p_0 and (c) J_2/p_0 are plotted at time steps $t = \tau_s/10$ (left) and $t = 2 \times \tau_s$ (right).
The solution at $t = \tau_s/10$ is at the beginning of the movement and in the transient regime; while at $t = 2 \times \tau_s$ it is clearly the steady-state regime and, a peak appears at the front of the contact zone in the direction of the rolling at a certain distance under the surface.
The coating/substrate interface is visible at $z/h = 1$, showing a jump of stress as a result of interaction between substrate and coating.

3.4.8 Frictional (dry friction) sliding on a viscoelastic layered half-space

The tangential viscoelastic contact modelling is based on the same global approach presented for the normal viscoelastic contact. The tangential contact algorithm used is based on the Conjugate Gradient Method CGM described in [GAL 10b].

Here some preliminary results of the sliding in presence of dry friction on the viscoelastic layered half-space are presented. For this aim,the set of parameters of the section 3.4.5 is considered with $v\tau_s/a = 0.4$. The dry friction coefficient is $f = 0.25$.

Figure 3.29 shows the frictional sliding on a homogeneous half-space with the material properties of the substrate ($\mu_c/\mu_s = 1$) and on a coated half-space with $\mu_c/\mu_s = 0.25$.

It can be observed that before achieving the slip regime, there is a partial slip regime (see Fig. 3.29(a)). Forward to the stick-slip regime, where $Q < f \times W$ (Q stands for the applied tangential load and W for the applied normal load), the full slip regime appears. One can then observe at the early stage (when $t = \tau_s/20$) the loss of the classical shape of the shear curve due to the relaxation phenomenon. It is important to note that the coupling between the normal and the tangential problems is taken into account. Thus, an asymmetric shear profile appears due to the fact that the sphere and the half-space are elastically dissimilar (see [GAL 07b]). By comparing the homogeneous half-space and the coated half-space solutions, it can be seen that adding a soft coating leads in a decrease of the overall pressures and shears.

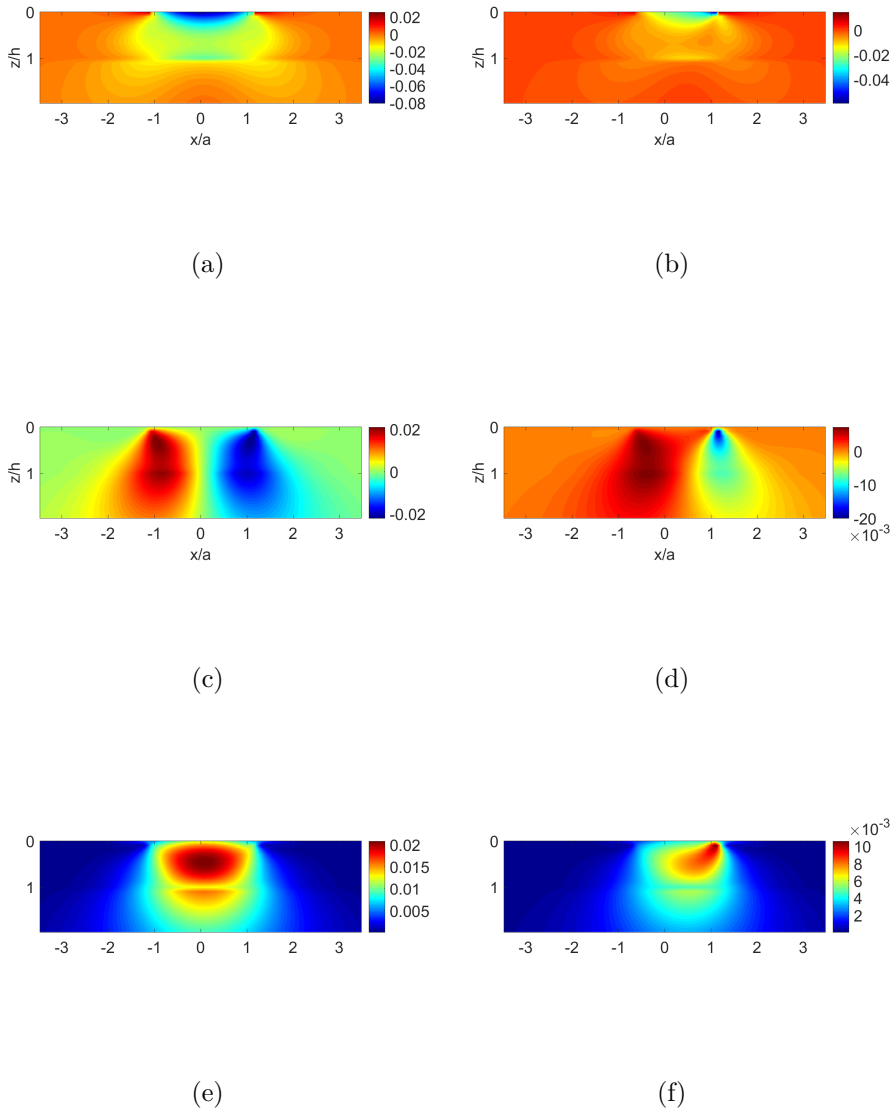

(a) (b)

(c) (d)

(e) (f)

Figure 3.28: Dimensionless stresses (a) & (b) σ_{xx}/p_0 , (c) & (d) σ_{xz}/p_0 and (e) & (f) J_2/p_0 in the plane Y=0, plotted at time steps $t = \tau_s/10$ (left) and $t = 2 \times \tau_s$ (right)

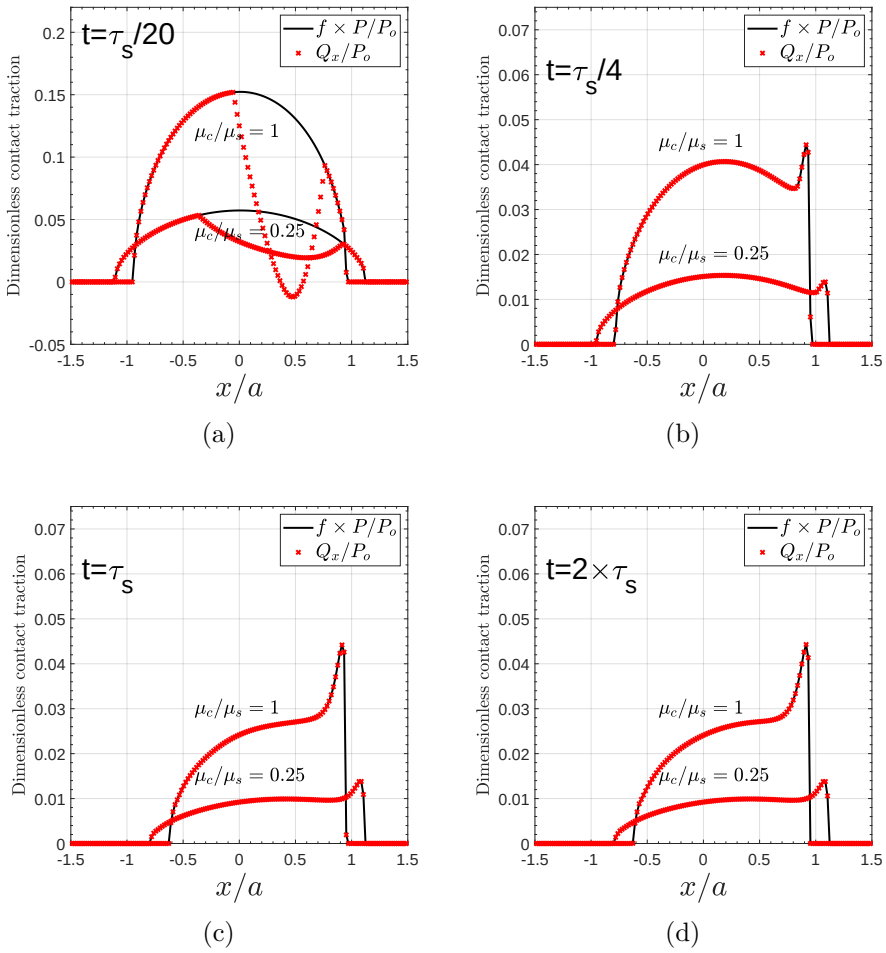

Figure 3.29: Dimensionless contact tractions for a frictional ($f = 0.25$) sliding contact of a rigid sphere on a viscoelastic layered half-space. The sphere slides at a dimensionless velocity $v\tau_s/a = 0.4$ (tangential effort is driven in term of displacement) under a prescribed normal displacement. The dimensionless contact shear in the direction of the sliding and the dimensionless contact pressure are plotted over the line $y = 0$ at (a) t=τ_s/20, (b) t=τ_s/4, (c) t=τ_s, (d) t=2×τ_s.

3.5 Conclusion

In this chapter, a semi-analytical model has been developed to solve the contact on a viscoelastic layered half-space, where coating and substrate have different viscoelastic behaviours. The influence coefficients for an elastic coated half-space have been calculated first, using Papkovich-Neuber potentials. Then an elastic/viscoelastic correspondence has been proposed. For validation, the model is confronted to the elastic layered half-space solution of O'Sullivan and King [O'S 88], the homogeneous viscoelastic half-space solutions of Koumi et al. [KOU 15b] and Carbone and Putignano [CAR 13], the viscoelastic layer on rigid base of Stepanov and Torskaya [STE 18] and finally a Finite Element Model. Contact pressure distribution, apparent friction coefficient, stresses at the interface and subsurface stresses have been analysed and the main results are:

1. The coating drives the stresses at the coating/substrate interface; and when the coating relaxes more rapidly than the substrate, its deformation produces additionnal stresses at the interface.

2. The steady-state regime is reached more rapidly in relaxation case (i.e. when a displacement is imposed) than in the creep case (when a force is imposed).

3. The relaxation time ratio and rolling/sliding velocity have a very significant impact on the apparent friction coefficient.

4. The coating/substrate shear modulus ratio and thickness do not have a significant effect on hysteresis losses (apparent friction coefficient).

Chapter 4

Pure Rolling on a Viscoelastic Multi-layered Half-space

The purpose of this chapter is the contact of a rolling body on a viscoelastic multi-layered half-space. The influence coefficients are found for an elastic multi-layered half-space using the Papkovich-Neuber potentials. An Elastic/Viscoelastic correspondence is used in order to take into account not only the change of behaviour of the half-space during time, but also to superimpose the load history. The numerical Conjugate Gradient Method (CGM) coupled with FFT algorithms are used to solve the variational problem that yields from the contact problem definition. Finally, a parametric study is performed to highlight the effect of a gradient of property in the half-space.

Sommaire

4.1 Introduction

The modelling of multi-layered structures is certainly of great interest for those who work with coated bodies or composites for example. The pavement structure which is the desired application of the works presented in this document is also a multi-layered body. Multi-layered structures are widely popular and used in many fields and thus, it is important to model the possible viscoelastic behaviour they can take.

Note that the case of a single layered half-space is presented in the previous chapter. In elasticity, for two elastic layers on an elastic substrate, Chen et al. [CHE 71] performed an exact analysis for a two dimensional case. For a general case of L layers, L being any positive integer, Yu et al. [YU 14] solved the problem analytically in the Fourier frequency domain by constructing a matrix system and used numerical algorithms to find a semi analytical solution for the influence coefficients.

In this chapter, a method is proposed to solve the 3D contact problem with a viscoelastic multi-layered half space. The general method is an extension of the Elastic/viscoelastic correspondence exposed in the previous chapter, coupled with the influence coefficients for a multi-layered half-space.

Some examples are also provided to illustrate the performances of the numerical techniques used to tackle the problem. The free rolling contact is studied in viscoelasticity for both transient and steady-state regime.

In the following, firstly the general problem and its formulation are recalled quickly. Then, the elastic influence coefficients for a multi-layered half-space are found analytically in the Fourier frequency domain and numerically obtained in the space domain. A validation is performed and finally, a parametric study allows to highlight the viscoelastic effects on some examples of viscoelastic multi-layered bodies.

4.2 Formulation

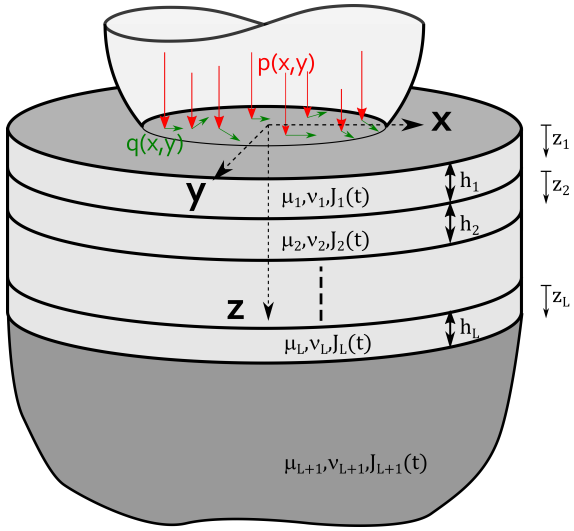

Figure 4.1: System being considered. A pressure and a shear distributions are applied at the surface of a viscoelastic multi-layered half-space, where the L layers and substrate have different viscoelastic behaviours

This formulation is similar to the one of the previous chapter. The system being considered consists of two bodies (1 and 2) in contact over a region Γ_c. Both bodies can be of any kind of geometry, and here body 2 is the actual viscoelastic multi-layered half-space. In this framework, the layers are considered perfectly bonded to one another. It means that the displacements are continuous at the interfaces. In addition, the tractions continuity condition is set at all the interfaces.
Let us recall quickly the classical definition of the contact for numerical applications. It begins with the definition of the gap between the bodies: the surface separation $g(x,y,t)$ between the two bodies is defined at every point at the contact surface as the sum of the initial separation $h_i(x,y)$, the elastic and the viscoelastic normal displacements of both bodies under the load history $u_3^{(B_1+B_2)}(x,y,t)$ and (if there is some,) the rigid body displacement $\delta(t)$ at every time t. Then, the following equation reads:

$$g(x,y,t) = h_i(x,y) + \delta(t) + u_3^{(B_1+B_2)}(x,y,t) \tag{4.1}$$

Once the gap is defined, for $p(x,y,t)$ the locale pressure at a point (x,y) on the surface at a time t, the contact conditions can be identified as:

$$(x,y) \in \Gamma_c; \quad h(x,y,t) = 0 \quad \text{and} \quad p(x,y,t) > 0 \tag{4.2a}$$

$$(x,y) \notin \Gamma_c; \quad h(x,y,t) > 0 \quad \text{and} \quad p(x,y,t) = 0 \tag{4.2b}$$

The above contact conditions take into account the non-penetration and the pressure positivity conditions. Moreover, the load balance added to the set of equations: If

a force $P(t)$ is applied on the system, it must be equal to the sum of the contact pressure distribution $p(x,y,t)$ over the contact zone Γ_c. That reads as follow:

$$P(t) = \int_{\Gamma_c(t)} p(x,y,t)dS \tag{4.3}$$

It is important to remark that the contact is solved at every time step. It means that whatever the load history is, it is taken into account at the present step. This allow to solve transient problem shown later in the results.
In the above contact definition, the elastic and viscoelastic displacements remain unknown. In the next part, the elastic response of the multi-layered half-space under an unit pressure and an unit shear has to be found. This response is the influence coefficients that will be formulated with Papkovich-Neuber potentials.

4.2.1 Influence coefficients for multi-layered elastic half-space

This part is the original part of this chapter. Consider a multilayered half-space with L linear elastic and homogeneous layers on a linear elastic and homogeneous substrate. From the top to the bottom, the layer j has a shear modulus μ_j; its Poisson's ratio is ν_j and its thickness is h_j $(j = 1,...,L)$. For the substrate, the shear modulus is μ_{L+1} or μ_{sub} and the Poisson's ration is ν_{L+1} or ν_{sub}. The Papkovich-Neuber potentials ϕ^j and ψ_i^j are used to express the elastic field. ϕ^j and ψ_i^j are harmonic functions of (x,y), and when no body forces, ψ_2^j vanish. Then, as for the single layered case seen in the previous chapter, one can write displacements and stresses as function of the potentials ϕ^j, ψ_x^j and ψ_z^j :

$$2\mu_j u_i^j = \phi_{,i}^j + x\psi_{x,i}^j + z_j\psi_{z,i}^j - (3-4\nu_j)\psi_i^j \tag{4.4a}$$

$$\sigma_{ik}^j = \phi_{,ik}^j - 2\nu_j(\psi_{x,x}^j + \psi_{z,z}^j)\delta_{ik} - (1-2\nu_j)(\psi_{i,k}^j + \psi_{k,i}^j) + x\psi_{x,ik}^j + z_j\psi_{z,ik}^j \tag{4.4b}$$

where Einstein's notation is used and $j = 1,...L+1$.
In the above equations, the coma stands for the partial derivative (eg: $\phi_{,x} = \frac{\partial\phi}{\partial x}$). To avoid performing those partial derivatives, a linearisation of the Eqs. (4.4) is done using Fourier Transform (FT). Furthermore, the transformed Papkovich-Neuber potentials using bi-harmonic functions are defined as:

$$\tilde{\tilde{\phi}}^j = A^j \exp(-\alpha z_j) + \overline{A}^j \exp(\alpha z_j) \tag{4.5a}$$

$$\tilde{\tilde{\psi}}_x^j = B^j \exp(-\alpha z_j) + \overline{B}^j \exp(\alpha z_j) \tag{4.5b}$$

$$\tilde{\tilde{\psi}}_z^j = C^j \exp(-\alpha z_j) + \overline{C}^j \exp(\alpha z_j). \tag{4.5c}$$

Therefore, yield linear equations to solve in the Fourier frequency domain.
Let's introduce again the following notations: $w_+^j = e^{\alpha z_j}$ and $w_-^j = e^{-\alpha z_j}$, where

$\alpha = \sqrt{m^2+n^2}$ is the radius in the frequency domain; (m,n) representing the Fourier Transform of (x,y).
Thence, the forms of displacements and stresses in the Fourier frequency domain can be inferred (see chapter 3).
With those forms of the elastic field, a system might be found for which the solution will be the coefficients A^j, $\overline{A}^j$,B^j, $\overline{B}^j$,C^j and $\overline{C}^j$. Note that $\overline{A}^{L+1} = 0$, $\overline{B}^{L+1} = 0$ and $\overline{C}^{L+1} = 0$ because the elastic field must vanish at infinity.
To construct the system to solve, the boundary conditions are used. They are:

- At the top surface i.e. the contact surface of the whole multi-layered half-space $z_1 = 0$, pressure and shear fields are imposed:

$$\sigma^1_{zz}(x,y,0) = -\delta(x,y), \qquad \sigma^1_{zx}(x,y,0) = -\delta(x,y), \qquad \sigma^1_{zy}(x,y,0) = 0. \tag{4.6}$$

  δ is the Dirac distribution.

- At all the interfaces, tractions and displacements continuity is required:

$$\begin{aligned} \sigma^j_{zx}(x,y,h_j) &= \sigma^{j+1}_{zx}(x,y,0) & u^j_x(x,y,h_j) &= u^{j+1}_x(x,y,0) \\ \sigma^j_{zy}(x,y,h_j) &= \sigma^{j+1}_{zy}(x_xy,0) & u^j_y(x,y,h_j) &= u^{j+1}_y(x,y,0) \\ \sigma^j_{zz}(x,y,h_j) &= \sigma^{j+1}_{zz}(x,y,0) & u^j_z(x,y,h_j) &= u^{j+1}_z(x,y,0). \end{aligned} \tag{4.7}$$

  This continuity at the interfaces means a perfect bounding of the layers to one another.

Further, applying a double Fourier Transform (FT) to the above boundary conditions, a system of $6L+3$ equations with $6L+3$ unknowns comes out. Following the steps of Yu et al. [YU 14], the system can be split into two matrix systems: one keeping the applied shear contribution and the other, the contribution of the applied pressure.
Applying the FT to the boundary conditions, leads to:

$$\tilde{\tilde{\sigma}}^1_{zz}(m,n,0) = -\tilde{\tilde{p}}(m,n), \tag{4.8}$$
$$\tilde{\tilde{\sigma}}^1_{zx}(m,n,0) = -\tilde{\tilde{q}}(m,n), \tag{4.9}$$
$$\tilde{\tilde{\sigma}}^1_{zy}(m,n,0) = 0, \tag{4.10}$$

and

$$\tilde{\tilde{\sigma}}^j_{zx}(m,n,h_j) = \sigma^{j+1}_{zx}(x,y,0), \tag{4.11}$$
$$\tilde{\tilde{\sigma}}^j_{zy}(m,n,h_j) = \sigma^{j+1}_{zy}(x_xy,0), \tag{4.12}$$
$$\tilde{\tilde{\sigma}}^j_{zz}(m,n,h_j) = \sigma^{j+1}_{zz}(x,y,0), \tag{4.13}$$
$$\tilde{\tilde{u}}^j_x(x,y,h_j) = u^{j+1}_x(m,n,0), \tag{4.14}$$
$$\tilde{\tilde{u}}^j_y(x,y,h_j) = u^{j+1}_y(m,n,0), \tag{4.15}$$
$$\tilde{\tilde{u}}^j_z(x,y,h_j) = u^{j+1}_z(m,n,0). \tag{4.16}$$

Then the system is built using those equations by a construction procedure of matrix systems. The construction procedure is as follow:

- ✧ By subtracting the shear stresses in Eqs. (4.9) and (4.10), all the unknowns are cancelled except B^1 and $\bar{B}^1$. This gives the first row of the matrix system in Eq. (4.17).
- ✧ By subtracting the continuity conditions of shear stresses between the layers (Eqs. (4.11) and (4.12)) and the continuity conditions of the displacements Eqs. (4.14) and (4.15), a 2×4 sub-matrix is obtained along the diagonal of the system in Eq. (4.17).
- ✧ For the last interface before the half-space $\bar{B}^{L+1}=0$. By applying the subtraction procedure as for the previous interfaces, for the shear stresses and displacements, a sub-matrix 2×3 is obtained.

The system for finding the unknowns B^j, $\bar{B}^j$, B^{j+1} and $\bar{B}^{j+1}$ is:

$$\begin{pmatrix} 2\alpha(1-\nu_1) & -2\alpha(1-\nu_1) & & & & & & & & \\ \ddots & & \ddots & & & & & & & \\ & & -4(1-\nu_j)\theta_-^j & -4(1-\nu_j)\theta_+^j & 4(1-\nu_{j+1})\mu^{(j,j+1)} & 4(1-\nu_{j+1})\mu^{(j,j+1)} & & & & \\ & & 2\alpha(1-\nu_j)\theta_-^j & -2\alpha(1-\nu_j)\theta_+^j & -2\alpha(1-\nu_{j+1}) & 2\alpha(1-\nu_{j+1}) & & & & \\ & & & & \ddots & & \ddots & & & \\ & & & & \ddots & & \ddots & & & \\ & 0 & & & & & -4(1-\nu_L)\theta_-^L & -4(1-\nu_L)\theta_+^L & 4(1-\nu_{L+1})\mu^{(L,L+1)} & \\ & & & & & & 2\alpha(1-\nu_L)\theta_-^L & -2\alpha(1-\nu_L)\theta_+^L & -2\alpha(1-\nu_{L+1}) & \end{pmatrix} \begin{pmatrix} B^1 \\ \vdots \\ \overline{B}^j \\ B^{j+1} \\ \vdots \\ \overline{B}^L \\ B^{L+1} \end{pmatrix} = \begin{pmatrix} -\bar{q} \\ \vdots \\ 0 \\ 0 \\ \vdots \\ 0 \\ 0 \end{pmatrix} \tag{4.17}$$

Using the same technique of construction, the system in Eq. (4.18) is formed by using the normal stresses and displacements. The two first rows are given by the use of Eqs. (4.8) and (4.10). Along the diagonal, the sub-matrices X_{1j} and X_{2j} are found by using the continuity conditions in Eqs. (4.15), (4.16), (4.12) and (4.13). At the bottom of the matrix, four rows contain the continuity conditions at the last interface with $\bar{A}^{L+1}=0$ and $\bar{C}^{L+1}=0$.

$$\begin{pmatrix} \alpha & \alpha & 2(1-\nu_1) & -2(1-\nu_1) & & & & & & & \\ \alpha & -\alpha & 1-2\nu_1 & 1-2\nu_1 & & & & & & & \\ & \ddots & & & \ddots & & & & & & \\ & & & & X_{1j} & X_{2j} & & & & & \\ & & & & & \ddots & & \ddots & & & \\ & & & & & & \alpha & \alpha(\theta_+^L)^2 & \alpha h_L & \alpha h_L(\theta_+^L)^2 & -\alpha\mu^{(L,L+1)}\theta_+^L & 0 \\ & & & & & & \alpha & -\alpha(\theta_+^L)^2 & 3-4\nu_L+\alpha h_L & (3-4\nu_L+\alpha h_L)(\theta_+^L)^2 & -\alpha\mu^{(L,L+1)}\theta_+^L & -\mu^{(L,L+1)}(3-4\nu_{L+1})\theta_+^L \\ & & 0 & & & & \alpha & -\alpha(\theta_+^L)^2 & 1-2\nu_L+\alpha h_L & (1-2\nu_L-\alpha h_L)(\theta_+^L)^2 & -\alpha\theta_+^L & -(1-2\nu_{L+1})\theta_+^L \\ & & & & & & \alpha & \alpha(\theta_+^L)^2 & 2(1-\nu_L)+\alpha h_L & -[2(1-\nu_L)-\alpha h_L](\theta_+^L)^2 & -\alpha\theta_+^L & -2(1-\nu_{L+1})\theta_+^L \end{pmatrix} \begin{pmatrix} A^1 \\ \overline{A}^1 \\ \vdots \\ C^j \\ \overline{C}^j \\ A^{j+1} \\ \overline{A}^{j+1} \\ \vdots \\ C^L \\ \overline{C}^L \\ A^{L+1} \\ C^{L+1} \end{pmatrix} = \begin{pmatrix} S_1^0 \\ S_2^0 \\ \vdots \\ S_1^j \\ S_2^j \\ S_3^j \\ S_4^j \\ \vdots \\ S_1^L \\ S_2^L \\ S_3^L \\ S_4^L \end{pmatrix} \tag{4.18}$$

where $\theta_+^j = e^{\alpha h_j}$, $\theta_-^j = e^{-\alpha h_j}$, $\mu^{(j,j+1)} = \dfrac{\mu_j}{\mu_{j+1}}$ and the sub-matrices X_{1j} and X_{2j} are written as follow:

$$X_{1j} = \begin{pmatrix} \alpha & \alpha(\theta_+^j)^2 & \alpha h_j & \alpha h_j(\theta_+^j)^2 \\ \alpha & -\alpha(\theta_+^j)^2 & 3-4v_j+\alpha h_j & (3-4v_j-\alpha h_j)(\theta_+^j)^2 \\ \alpha & -\alpha(\theta_+^j)^2 & 1-2v_j+\alpha h_j & (1-2v_j-\alpha h_j)(\theta_+^j)^2 \\ \alpha & \alpha(\theta_+^j)^2 & 2(1-v_j)+\alpha h_j & -[2(1-v_j)-\alpha h_j](\theta_+^j)^2 \end{pmatrix} \quad X_{2j} = \begin{pmatrix} -\alpha\mu^{(j,j+1)}\theta_+^j & -\alpha\mu^{(j,j+1)}\theta_+^j & 0 & 0 \\ -\alpha\mu^{(j,j+1)}\theta_+^j & \alpha\mu^{(j,j+1)}\theta_+^j & -\mu^{(j,j+1)}(3-4v_{j+1})\theta_+^j & -\mu^{(j,j+1)}(3-4v_{j+1})\theta_+^j \\ -\alpha\theta_+^j & \alpha\theta_+^j & -(1-2v_{j+1})\theta_+^j & -(1-2v_{j+1})\theta_+^j \\ -\alpha\theta_+^j & -\alpha\theta_+^j & -2(1-v_{j+1})\theta_+^j & 2(1-v_{j+1})\theta_+^j \end{pmatrix} \tag{4.19}$$

In Eqs. (4.18), the second hands remain to be defined. Those $S_1^0, \cdots, S_4^L$ are functions of the B^j and $\overline{B}^j$ (found solving Eqs. (4.17)) and their derivatives. Those functions are given in appendix A.
Whether it is possible to find analytic solution of the Eqs. (4.17) and (4.18), the choice has been to find the analytic exact solution of Eqs. (4.17) and then to make a numerical inversion of the system in Eqs. (4.18). This will help to avoid errors that can be made since the solutions are long and complex. Thus, a Gauss-Jordan algorithm is used to make the inversion of the $(4L+2)\times(4L+2)$ matrix. The cost of the numerical inversion depends on the number of layers and also on the size of the computation area.
At this point, the Green functions are found in the Fourier frequency domain and can be found numerically by applying an Inverse Fourier Transform (IFT) (see [LIU 02]). In the present work, the IFT is handled with Fast Fourier Transform (FFT) algorithms as done in the previous chapter 3.

Once the solution is found, the solution of the elastic contact on a multi-layered half-space with any L layers can be obtained.

Before moving forward in the viscoelastic multi-layered half-space modelling, it is important to perform a validation of the elastic influence coefficients found by using the method described previously.

4.2.2 Validation

For the validation of the elastic influence coefficients of the multi-layered half-space, the contact results are compared to the results in [YU 14]. For this purpose, two configurations are considered: a tri-layer and a multi-layer (with ten layers).

Firstly, a contact is simulated between a rigid sphere of radius $R = 31$ mm and a half-space on the top of which two layers are bounded. For a being the contact radius of Hertz for the contact considering the properties of the substrate, each of the layers has a thickness $h_i = 0.5a$. The Poisson's ratio of all the materials is fixed to 0.3. A normal load $P = 10000$ N is applied and the shear moduli take the values $\mu_1 = 2\mu_2 = 4\mu_{sub}$, $\mu_1 = \mu_2 = \mu_{sub}$ and $\mu_1 = \mu_2/2 = \mu_{sub}/4$. Figure 4.2 shows the comparison of the resulting dimensionless contact pressure along the line x in the middle plane $y = 0$. p_0 is the Hertz contact maximum pressure for the contact on the homogeneous half-space ($\mu_1 = \mu_2 = \mu_{sub}$). The results show a good agreement with the results of yu et al. [YU 14]. Further, for the validation of the stresses influence coefficients, a sliding contact has been simulated. The pure sliding contact is considered for various friction coefficient at the contact interface: $f = 0$, 0.25, 0.5. The results of the simulations are shown in appendix B.

Secondly, a multi-layer configuration is considered. The cases of decreasing, increasing and alternate modulus are studied in viscoelasticity in the results section. For $t = 0$ the viscoelastic case is equivalent to the elastic one where a good agreement is observed with the results in [YU 14].

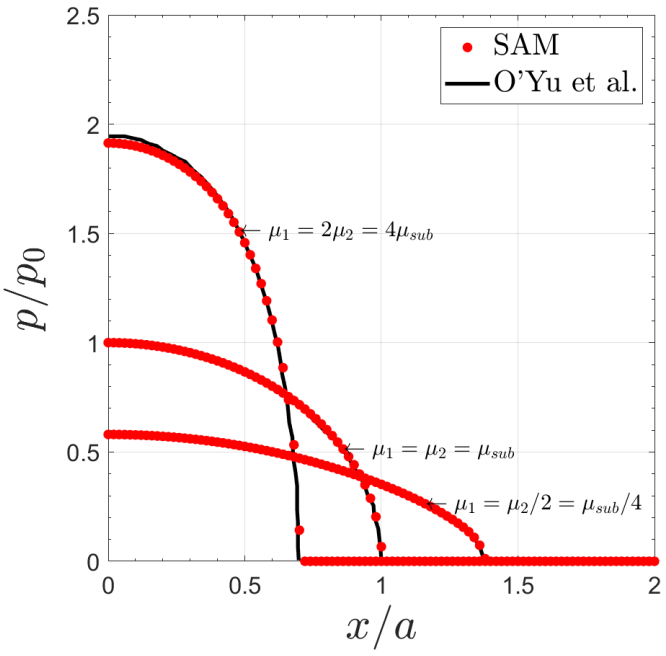

Figure 4.2: Validation of the influence coefficients for an elastic multi-layered half space.

4.3 Results

4.3.1 Framework

For the presentation of some illustrative cases, let's first describe the chosen framework.
A normal force P or a normal rigid displacement δ is applied on a sphere of radius $R = 10$ mm which goes in contact with a multi-layered viscoelastic half-space. The sphere is free-rolling at a velocity v in the direction x. Since the focus is put on the effects related to the viscoelastic multi-layered half-space, for the sphere a shear modulus $\mu_{sphere} = 10^{20}$ MPa is set and its Poisson's ratio is $\nu_{sphere} = 0.3$; this very high shear modulus allows to assume the sphere as rigid. For the layered half-space, the notations in Fig. 4.1 is used and $L = 10$ layers are set, each of thickness $h_j = a_0/10$ $(j = 1, \cdots, 10)$. The viscoelastic creep and relaxation functions are the ones in Eqs. (3.17a) and (3.17b). In those equations the subscript j is used for the layer j (from top to bottom) and the subscript $L+1 = 11$ or sub for the substrate. For all, layers and substrate, $\mu_{\infty j}/\mu_{0j} = 10$ $(j = 1, \cdots, L+1)$, and the substrate mechanical characteristics are always: $\mu_{\infty sub} = \mu_{\infty 11} = 3.86$ MPa and $\tau_{sub} = \tau_{11} = 10$ s. It comes obvious that the substrate which remains the same will serve as the reference. Thus, the contact considering no layer gives the useful Hertz parameters p_0 (the maximum contact pressure) and a_0 (the radius of the contact zone) in the

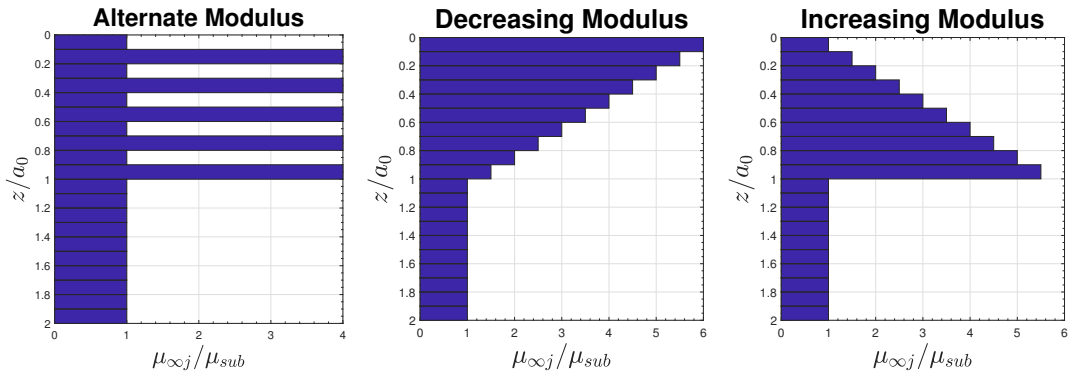

(a) (b) (c)

Figure 4.3: Different cases of variation of the instantaneous shear moduli of the layers.

elastic case.

The studies are performed by changing the instantaneous modulus of the layer $\mu_{\infty j}$ or/and its relaxation time τ_j $(j = 1, \cdots, 10)$. The instantaneous shear moduli will change following three main cases (see Fig.4.3):

- The "Alternate Modulus": the even index layers take the shear modulus value $4 \times \mu_{\infty sub}$ while the odd index layers take the shear modulus value $\mu_{\infty sub}$:

$$\mu_{\infty j} = \frac{\mu_{\infty j+1}}{4} = \mu_{\infty sub} \qquad (j = 1, 3, 5, 7, 9). \tag{4.20}$$

- The "Decreasing Modulus": the modulus decreases from $6 \times \mu_{\infty sub}$ with a constant step to reach the substrate modulus $\mu_{\infty sub}$:

$$\mu_{\infty j} = \left[6 - \frac{j-1}{2}\right] \times \mu_{\infty sub} \qquad (j = 1, \cdots, 10). \tag{4.21}$$

- The "Increasing Modulus": the modulus increases from $\mu_{\infty sub}$ to $5.5 \times \mu_{\infty sub}$ in the $10th$ layer:

$$\mu_{\infty j} = \left[1 + \frac{j-1}{2}\right] \times \mu_{\infty sub} \qquad (j = 1, \cdots, 10). \tag{4.22}$$

The above cases are replicated to have similar changes of the relaxation times. It comes, $\tau_j = \frac{\tau_{j+1}}{2} = \tau_{sub}$ (with $j = 1, 3, 5, 7, 9$) for the "Alternate Relaxation" time; $\tau_j = \left[3 - \frac{j-1}{5}\right] \times \tau_{sub}$ (with $j = 1, \cdots, 10$) for the "Decreasing Relaxation" time and $\tau_j = \left[1 + \frac{j-1}{5}\right] \times \tau_{sub}$ (with $j = 1, \cdots, 10$) for the "Increasing Relaxation" time.

4.3.2 Applied Normal Force

The analysis begins by applying a concentrate force $P = 1.48N$ on the sphere. The rolling velocity is given by $v\tau_{sub}/a_0 = 0.8$. Then, the computation is performed over a time domain $[0, 6\tau_{sub}]$ subdivided into 600 time steps. The contact surface is discretised with elements of size $0.2a_0 \times 0.2a_0$.

Figure 4.4 shows the evolution of the contact pressures along the rolling direction axis x. Results are plotted at (a) $t = 0$, (b) $t = \tau_{sub}/4$, (c) $t = \tau_{sub}$, (d) $t = 5 \times \tau_{sub}$ for the homogeneous half-space and the three non-homogeneous half-spaces where only the instantaneous shear moduli of the layers vary (see section 4.3.1).
The first remark on Fig. 4.4 is that at $t = 0$, the elastic response well correlates with the results of [YU 14] confirming that the present method for solving the matrix system in Eq. (4.18) works well. For the viscoelasticity, the method described in section 3.2.4.3 had been validated in [WAL 20]. In another hand, one can observe the significant decrease of the contact pressures at $t = \tau_{sub}/4$ but at the edge of the contact zones. At the $t = \tau_{sub}$, the pressures present the shape of a steady-state regime but will continue decreasing to reach the steady-state regime.
The calculations for an applied force is more time consuming as showed previously by [KOU 15b]. This, because there is a need for more time to reach the steady-state regime and also because the computation has to be performed over a greater surface. Thus, most of the parametric study will be made with a prescribed normal rigid body displacement: relaxation phenomenon.

4.3.3 Applied Normal Rigid Body Displacement

In this section, a normal displacement $\delta = 0.1a_0$ is prescribed and the time domain $[0, 2\tau_{sub}]$ with 80 time steps. The space domain is discretised with elements of size $0.2a_0 \times 0.2a_0 \times 0.05a_0$. The rigid sphere is rolling at a velocity given by $v\tau_{sub}/a_0 = 0.8$ over the half-space. Then, an analysis is performed to highlight the effects of the variation of the instantaneous shear moduli, the effects of the variation of the relaxation times, and the effects of both together.

4.3.3.1 Variation of the instantaneous shear moduli

Firstly, the focus is put on the effect of the change of the instantaneous shear moduli of the layers. For this purpose, the relaxation times are the same for all the layers $\tau_j = \tau_{sub}$ $(j = 1 \cdots, 10)$ and the instantaneous shear moduli are modified following the cases described in 4.3.1. Doing so, various outputs such as the contact pressure at different times, the apparent friction coefficient which expresses the resistance to the rolling, and the three-dimensional stresses are of interest.

Figure 4.5 shows the contact pressures along the rolling axis x at times (a) $t = 0$, (b) $t = \tau_{sub}/10$, (c) $t = \tau_{sub}/4$ and (d) $t = \tau_{sub}$. A comparison is made between a homogeneous viscoelastic half-space with the mechanical properties of the substrate, and three non-homogeneous half-spaces with 10 layers having the same relaxation

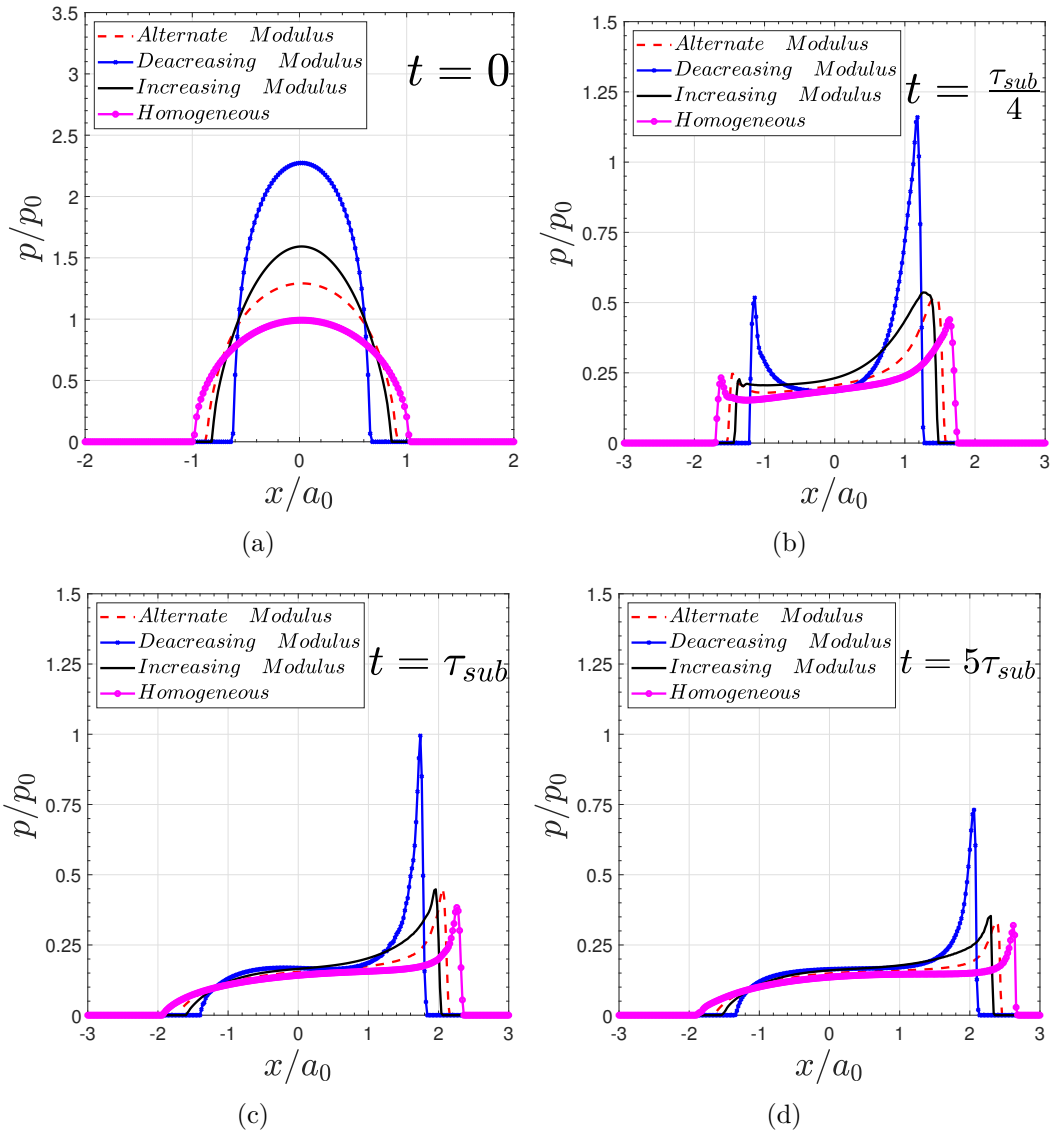

Figure 4.4: Normalised contact pressures along the rolling direction axis x, for a spherical contact on a multi-layered viscoelastic half-space with 10 layers with different instantaneous shear moduli; normal force $F_n = 1.48$ N prescribed and the dimensionless rolling velocity is $v\tau_{sub}/a_0 = 0.8$. The results are plotted at (a) $t = 0$, (b) $t = \tau_{sub}/4$, (c) $t = \tau_{sub}$, (d) $t = 5 \times \tau_{sub}$.

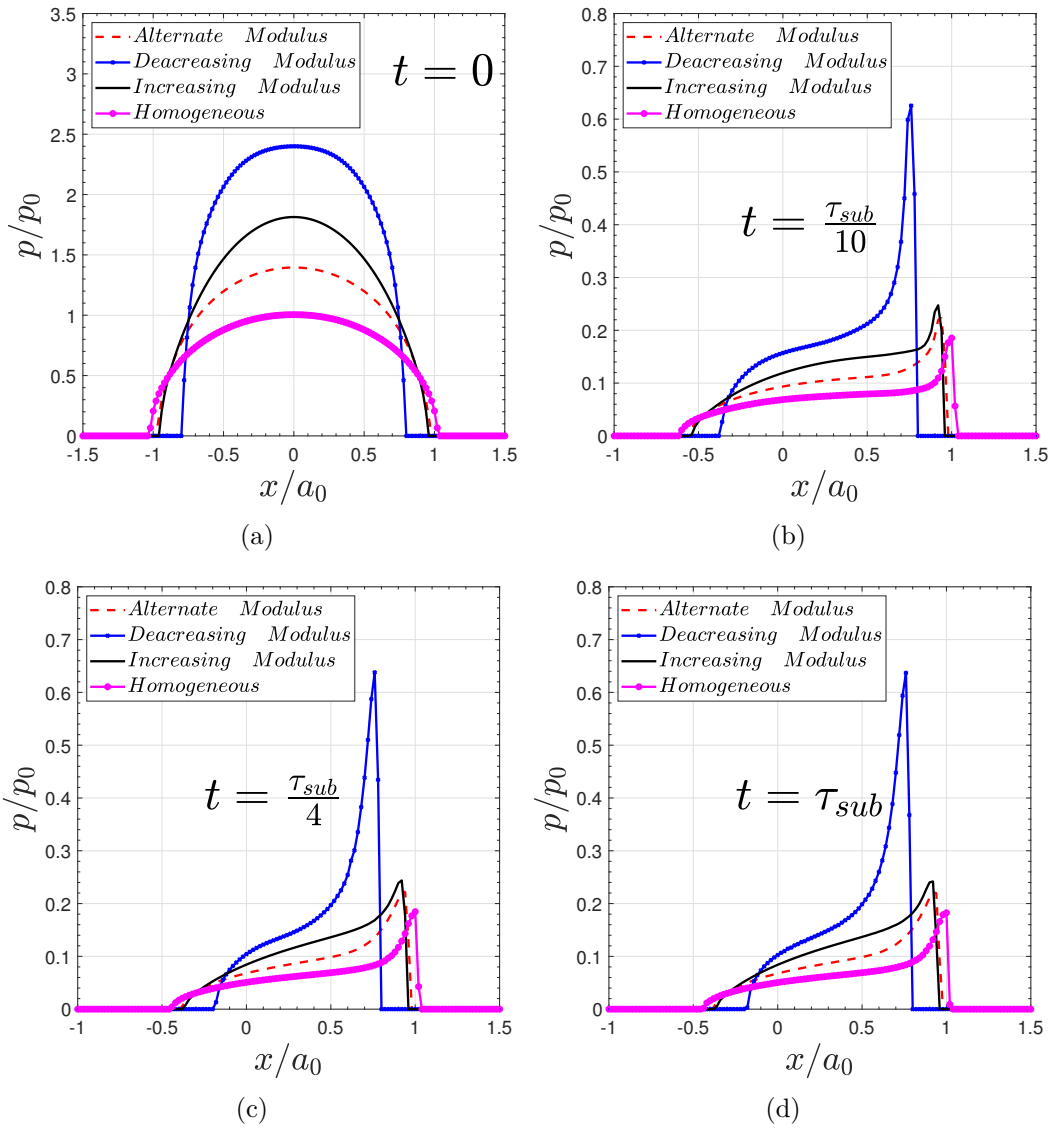

Figure 4.5: Normalised contact pressures along the rolling direction axis x, for a spherical contact on a multi-layered viscoelastic half-space with 10 layers with different instantaneous shear moduli; normal rigid displacement $\delta = 0.1a_0$ prescribed and the dimensionless rolling velocity is $v\tau/a_0 = 0.8$. The results are plottes at (a) $t = 0$, (b) $t = \tau_{sub}/10$, (c) $t = \tau_{sub}/4$, (d) $t = \tau_{sub}$.

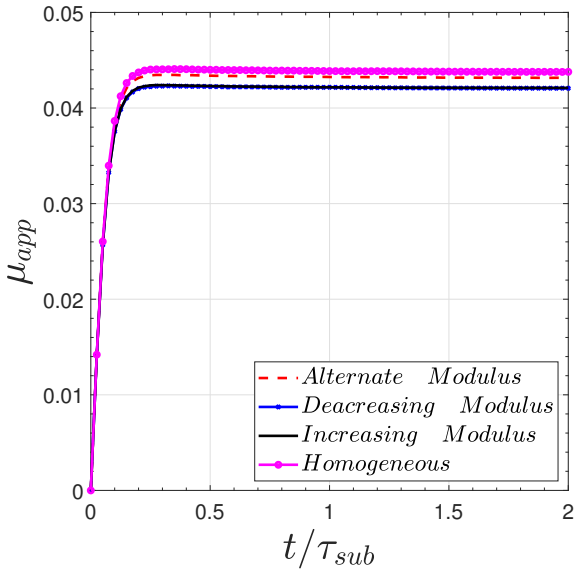

Figure 4.6: Apparent friction coefficient, for a spherical contact on a multi-layered viscoelastic half-space with 10 layers with different instantaneous shear moduli; normal rigid displacement $\delta = 0.1a_0$ prescribed and the dimensionless rolling velocity is given by $v\tau/a_0 = 0.8$

time but with either increasing modulus, decreasing modulus or alternate modulus (see Fig. 4.3).
In all the non-homogeneous cases, the overall stiffness of the layers is higher than the one of the substrate. This is the reason why the contact pressure of the homogeneous shows the lowest maximum with a wider profile. Moreover, among those cases, the top layer is stiffer for the decreasing modulus. Obviously, and as shown for a bilayer [O'S 88], [WAN 12], [WAL 20] the top surface has the greatest direct influence on the contact. Under this remark, it comes comprehensive that the decreasing modulus shows a higher maximum pressure with the smallest contact zone. For the alternate modulus case and the increasing modulus case, the top layer is the same. Thus, the results allow us to say that the overall stiffness of the alternate modulus case is lower than the one of the increasing modulus case.
Further, when the time increases, the trend will stay the same since all the layers have the same relaxation time. In addition, one can see the evolution through a transient regime to achieve what seems to be a steady-state regime in sub-figure (c) and (d) of Fig. 4.5. This transition from transient to steady-state regime is confirmed by the apparent friction coefficient in Fig. 4.6 which shows that the steady-state regime is achieved quite quickly; near $t = 0.2\tau_{sub}$. Furthermore, one can remark the small effect of the instantaneous shear moduli on the resistance to the rolling. This correlates with results found for only one layer on the half-space [WAL 20].

Beside the contact results, the sub-surface stresses are of undeniable interest. Figure 4.7 shows the dimensionless second invariant of the stress tensor $\sqrt{J_2}/p_0$,

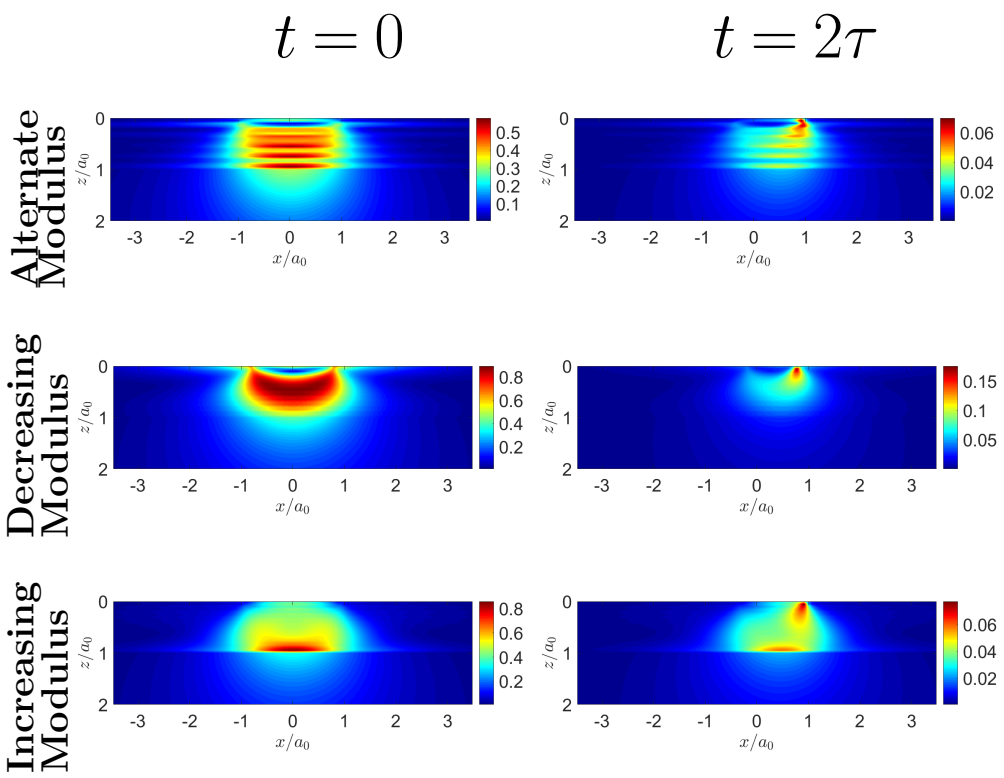

Figure 4.7: Normalised second invariant of the stress tensor $\sqrt{J_2}/p_0$ in the plane $y = 0$, for a spherical contact on a multi-layered viscoelastic half-space with 10 layers with different instantaneous shear moduli; normal rigid displacement $\delta = 0.1a_0$ prescribed and the dimensionless rolling velocity is $v\tau/a_0 = 0.8$. Results are plotted at $t = 0$(left) and $t = 2\tau$ (right)

at $t = 0$ (left) which corresponds to the elastic case, and $t = 2\tau_{sub}$ which is in the steady-state regime.

Again, the 3D-stress distribution well correlates with the results of [YU 14] at $t = 0$. One can clearly see that the effect of the alternate modulus induces a jump of the stress from a layer to another. The high stresses appear when we move (from top to bottom,) from a stiffer layer to a less stiffer one; the exception being near the surface where the modulus is low (the top layer has the modulus of the substrate). For the the increasing modulus and the decreasing modulus cases, there is no jump of stresses between the layers and in the decreasing modulus case, the stresses distribution is closer to a homogeneous modulus case distribution. This remark, can mean that for a decreasing modulus case, the overall half-space behaves like a homogeneous half-space with a greater instantaneous shear modulus. Otherwise, the increasing modulus case shows an increase of the stress from top to bottom in the layers, and reaches a maximum at the interface with the substrate. At that interface, there is a jump from a very high value (the maximum) to a very low value in the substrate.

At the steady-state regime, for the three plotted cases, the stresses relax and the maxima change location. For each, the maximum goes then under the leading edge of the contact and very close to the surface.

4.3.3.2 Variation of relaxation times

The interest is now put on the effect of the change of the relaxation times of the layers. For this purpose, the instantaneous shear moduli are kept the same for all the layers $\mu_{\infty j} = \mu_{\infty sub}$ $(j = 1 \cdots, 10)$ and modify the relaxation times change following the cases describe in section 4.3.1.

Figure 4.8 shows the contact pressures along the x axis at different time steps. The elastic response of the three cases is the same as expected since the instantaneous moduli are the same for all the layers and the substrate. For the alternate, increasing and homogeneous relaxation cases, the difference is not such significant. The reason lies in the fact that the top layer is the same for those three cases; and as said earlier, the top layer influences the most the contact. Otherwise, for the decreasing relaxation case, the result is different. The top layer in that case has a greater relaxation time. Thus, the contact pressure relaxes less rapidly. And, even when the steady-state regime is achieved, the profile is less wide and the maximum value is greater.

When a look is cast on the apparent friction coefficient (see Fig. 4.9), the similarity of the behaviour for all the cases is observed except for the decreasing relaxation time one. For the latter, not only the steady-state regime is achieved later (i.e. for $t/\tau = 2$), but also the apparent friction coefficient is greater. The 3D stresses are the same for all the cases at $t = 0$ as expected.
Recall that for the calculation of the stresses, a convolution of the actual contact pressure with the elastic influence coefficients has to be performed. This can explain that no significant change is observed between the alternate and increasing relaxation cases since the contact pressures also are close (see Fig. 4.10). The decreasing relaxation case shows again a less wide distribution with a greater maximum stress. However, in all the cases, there is a change of the distribution in the steady-state regime; the stresses relax and the maximum moves under the leading edge of the surface and closer to the surface.

4.3.3.3 Variation of both instantaneous shear moduli and relaxation times

Now consider a mixed framework: the increasing modulus case coupled with the decreasing relaxation time case. The goal is to show a more complex case, under an applied force or an applied body displacement. For both cases, the surface is discretised with elements of size $0.2a_0 \times 0.2a_0$; and, the computations performed in a time domain $[0, 6\tau_{sub}]$ for the applied force case, and in $[0, 2\tau_{sub}]$ for the applied body displacement.

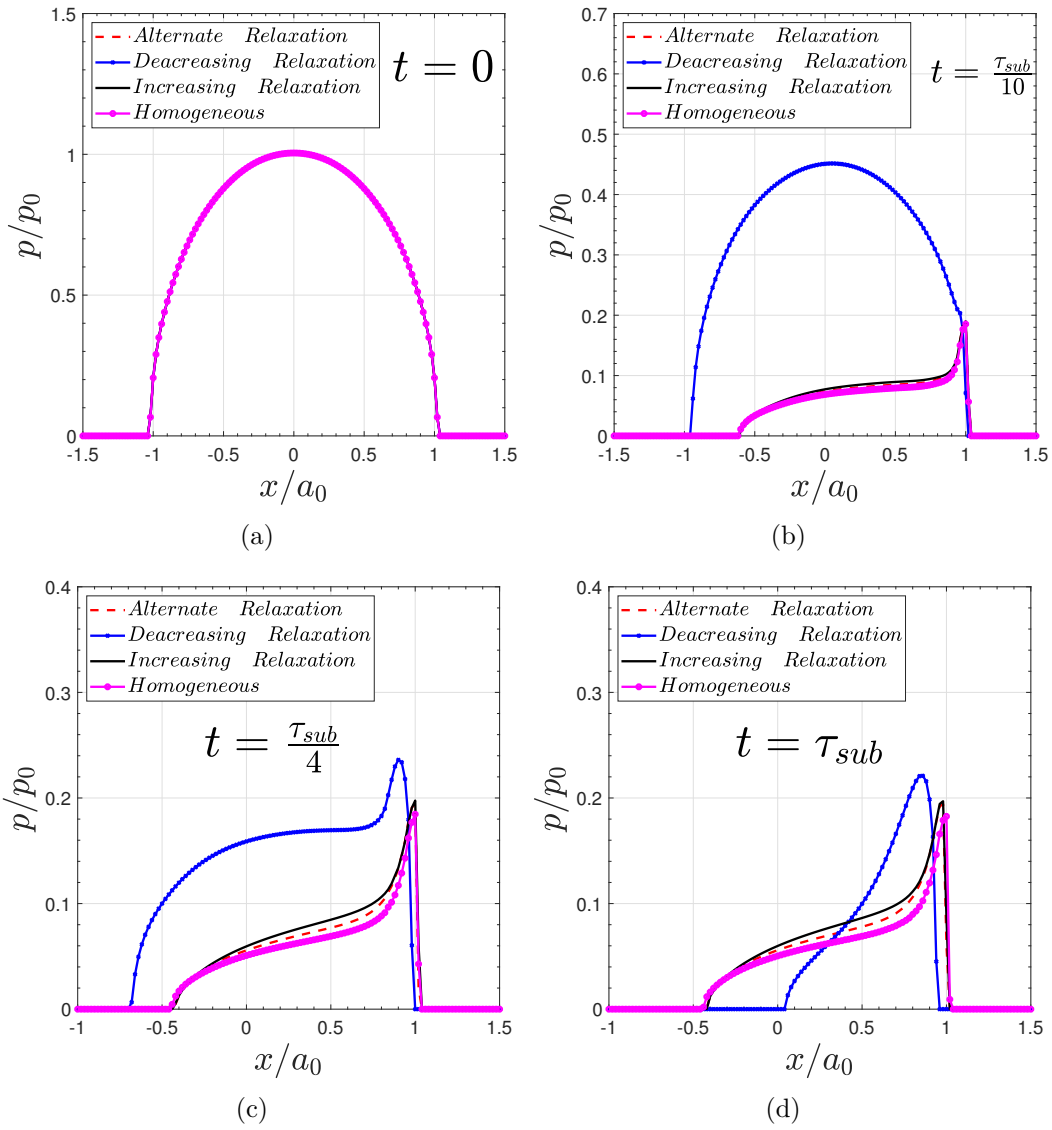

Figure 4.8: Normalised contact pressures along the rolling direction, for a spherical contact on a multi-layered viscoelastic half-space with 10 layers with different relaxation times; normal rigid displacement $\delta = 0.1a_0$ prescribed and the dimensionless rolling velocity is $v\tau/a_0 = 0.8$. The results are plottes at (a) $t = 0$, (b) $t = \tau_{sub}/10$, (c) $t = \tau_{sub}/4$, (d) $t = \tau_{sub}$.

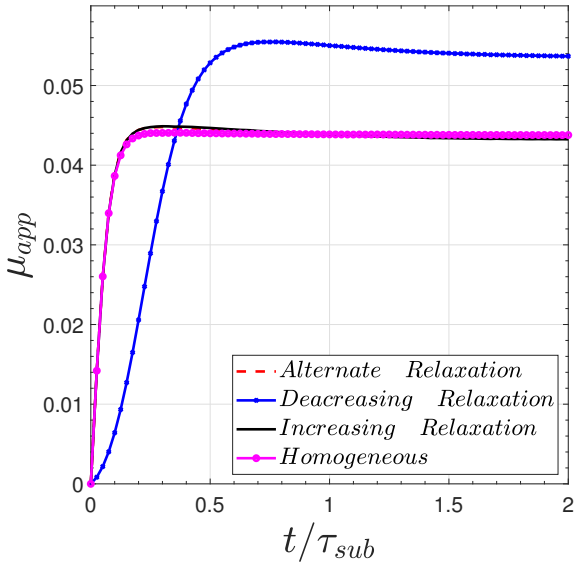

Figure 4.9: Apparent friction coefficient during time, for a spherical contact on a multi-layered viscoelastic half-space with 10 layers with different relaxation times; normal rigid displacement $\delta = 0.1a_0$ prescribed and the dimensionless rolling velocity is given by $v\tau/a_0 = 0.8$

Figure 4.11 shows the contact pressure profiles along the x axis at various time steps for an applied force and for an applied body displacement. One can immediately see the huge difference between the profiles in the transient and in the steady-state regime when there is an applied force or when it is an applied body displacement. Furthermore, one can once again remark that the steady-state regime is achieved earlier for an applied body displacement. Confirmation of this is given with the apparent friction coefficient in Fig. 4.12. The latter figure shows also that for an applied force, the resistance to rolling is higher than for an applied body displacement.

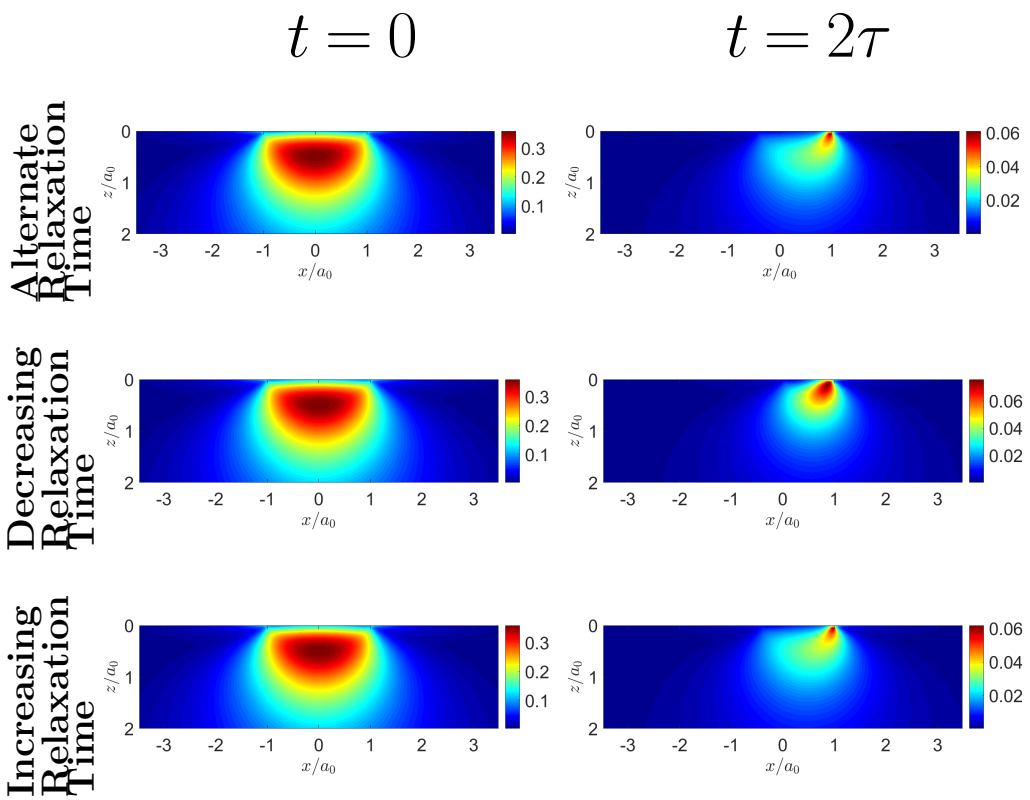

Figure 4.10: Normalised second invariant of the stress tensor $\sqrt{J_2}/p_0$ in the plane $y = 0$, for a spherical contact on a multi-layered viscoelastic half-space with 10 layers with different relaxation times; normal rigid displacement $\delta = 0.1a_0$ prescribed and the dimensionless rolling velocity is $v\tau/a_0 = 0.8$. Results are plotted at $t = 0$(left) and $t = 2\tau$ (right)

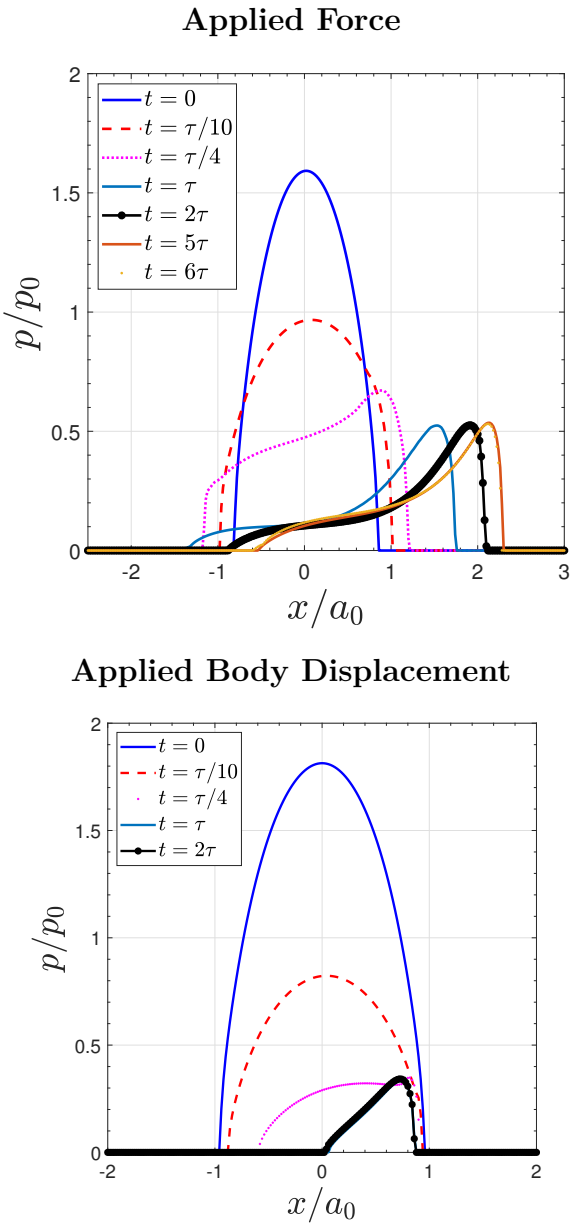

Figure 4.11: Normalised contact pressure along the rolling direction axis x, for a spherical contact on a multi-layered viscoelastic half-space with 10 layers in the increasing modulus case coupled with the decreasing relaxation time case; the dimensionless rolling velocity is $v\tau/a_0 = 0.8$. Results are plotted for an applied force and for an applied body displacement.

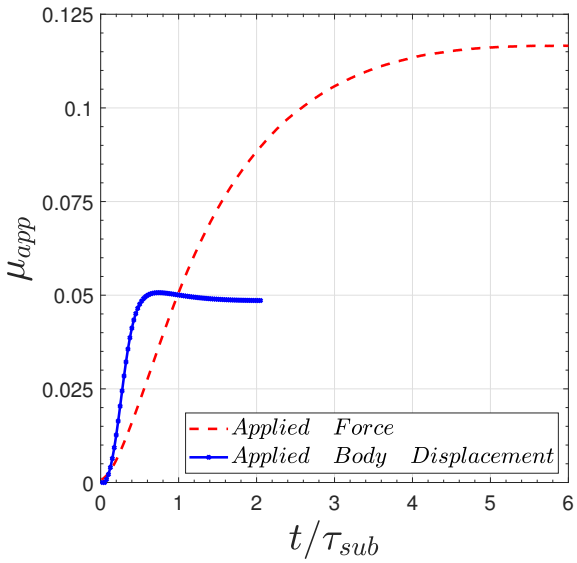

Figure 4.12: Apparent friction coefficient during time, for a spherical contact on a multi-layered viscoelastic half-space with 10 layers in the increasing modulus case coupled with the decreasing relaxation time case; the dimensionless rolling velocity is $v\tau/a_0 = 0.8$. Results are plotted for an applied force and for an applied body displacement.

4.4 Conclusion

Drawn from the viscoelastic studies on a single layered half-space, this work is an extension to the rolling contact on a multi-layered visco half-space. The model is developed using the multi-layered elastic solution coupled with an Elastic/viscoelastic correspondence. Using the numerical tools of semi-analytical methods (mainly CGM and FFT algorithms), a code to solve the problem efficiently has been developed. For example, a three-dimensional computation for $L = 10$ layers, for 80 time steps, takes 8017 s CPU ($\approx$ 2h15min).
Using the developed model, some effects of the variation of the instantaneous shear moduli and of the variation of the relaxation time have been highlighted. To do so, the Prony series representation of a generalised Maxwell viscoelastic model is used. Varying the parameters, it comes also some expected effects on the three-dimensional stresses which change greatly from $t = 0$ to the steady state regime.
However, this study has been voluntarily limited to the pure rolling case. As perspective, a coupling of this model with the tractive rolling algorithm, is to be done to cover the complete rolling contact in viscoelasticity for multi-layered bodies.

Chapter 5

Elastic Transient Tractive Rolling Contact

In this chapter, the tractive rolling contact is analysed. From the theory of Kalker for rolling bodies, a CGM algorithm is proposed to solve the transient tractive rolling contact between elastically dissimilar bodies, under tangential tractive forces and a spinning moment. The proposed algorithm is applied to multi-layered half-spaces.

Sommaire

5.1 Introduction

In the last two chapters, the contact has been considered frictionless i.e. with no Coulomb friction coefficient between the bodies in contact. This assumption makes sense when dealing with a pure rolling motion, even if it is not exact. The *pure rolling* motion is the rolling motion where no overall tangential force is imposed or induced by the contact conditions. In that case, when the bodies in contact are elastically dissimilar, shear tractions appear in the contact zone due to the fact that the two bodies deform differently in the tangent plane under the same normal load. On contrary, when the bodies in contact are elastically similar, the pure rolling contact does not induce shear tractions in the contact because the deformations of the two bodies are similar. Note that in a pure rolling motion, friction is considered between the two bodies unlike the *free rolling* where the contact is frictionless.

Furthermore, in a rolling contact where friction is considered at the contact interface, overall tangential forces can hold as well as a moment around the normal direction. This case is the general case of *tractive rolling*.

In practical applications the rolling motion is generally thought as a free rolling motion. This is the reason why in the pavement field, only the normal load is used for the design. However, some relatively obvious motions such as acceleration and braking can occur in the rolling motion. Theoretically, an acceleration motion is an increase of velocity of the rolling body during the rolling motion. In fact, an acceleration demands to impose an acceleration force to the system, especially when talking about a car. This force is parallel to the tangent plane of the contact and has an influence on the contact in presence of friction. The analysis of the effects of the tangential forces on the rolling contact, is the basement of the tractive rolling modelling.

In this chapter, the tractive rolling contact is solved in its more general form as possible. The formulation used here is drawn from the works of the pioneer Kalker [KAL 68a, KAL 90, KAL 91]. Since the construction of railways, the tractive rolling contact has been of high interest and many studies have been conducted toward its comprehension. Carter [CAR 26] has been the first to propose a two-dimensional plane strain solution to the tractive rolling problem between two cylinders. Among the studies which stand as reference, Bentall and Johnson [BEN 67], followed later by Nowell and Hills [NOW 88], have studied the tractive rolling contact between two elastically dissimilar rollers. Recently, semi-analytical methods have been proposed to solve the tractive rolling contact in steady-state regime by authors like Wang et al. [WAN 12] and Manyo [MAN 19b]. In those models the spin creepage is not taken into account. Xi et al. [XI 21] have added the contribution of the spin creepage to the model of Wang et al. [WAN 12].
The tractive rolling problem is a partial slip problem since the applied tangential forces allow the system to stay in a rolling motion, and not to slide. Methods such as Boundary Element Method (BEM) and Finite Element Method (FEM) have also been used in solving this tractive rolling problem (see for exam-

ple [ROD 10, ZHA 15]).

From all the previous works, one may retain that in a tractive rolling motion, when the bodies in contact are elastically similar, a stick zone holds in the leading zone while a slip zone stands in the trailing zone (see for instance [KAL 90]). When the bodies are elastically dissimilar, multiple slip zones can appear in the contact including close to the leading edge [BEN 67, NOW 88]. Other interesting results concern the effects of the friction coefficient and the applied tangential force: in summary, when the friction increases, the stick zone increases in the tractive rolling contact; when the applied tangential force increases, the slip zone increases. Many other analysis can be found in the above cited papers for various geometries of the bodies, modelling hypothesis, etc.

In what follows next, the tractive rolling problem is solved in both transient and steady-state regime. Note that the overall forces are used as input of the problem, unlike in [XI 21]. The elastic properties of the bodies is not imposed in the formulation so that the simulations can be performed for both elastically similar and elastically dissimilar bodies.

Firstly, the general formulation of the tractive rolling contact is given. Then an algorithm based on FFT and CGM algorithms is proposed for solving the problem. Further, a validation is performed by comparison with previous results from the literature. Finally, a parametric study highlights the effects of elastic similarity and dissimilarity on various combinations of the tangential loadings.

5.2 Formulation

The studied system consists of two elastic bodies in contact as defined earlier in this document. E_i and ν_i are respectively the elastic modulus and the Poisson's ratio of the body $i = 1, 2$. Here the focus is put on the rolling motion. The rolling motion is a relative angular motion between the two bodies in contact, about an axis parallel to the tangent plane of the contact zone. In term of kinematics, in a rolling motion, the relative velocity of the contact area is much greater than the velocity of the contacting particles.

The framework of the general tractive rolling contact studied in this work is presented in Fig. 5.1. It is a rolling body of revolution on a half-space under a normal force P and tangential forces F_x and F_y, and a spinning moment M_z. The rolling motion occurs along the direction x according to the axis system (xyz) displayed in the figure. The Coulomb's law is used to handle the friction at the contact interface where a friction coefficient f is considered.

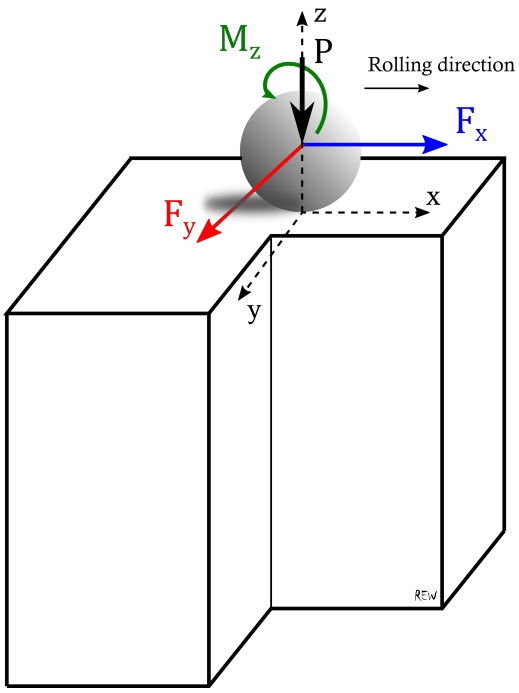

Figure 5.1: The problem being considered: a rolling body of revolution on a half-space under the normal force P and the tangential forces F_x and F_y, and the spinning moment M_z. The rolling motion occurs along the direction x.

This configuration of the tractive rolling contact problem involves a normal contact component and a tangential contact component. The two problems are usually uncoupled and solved successively using the modified Panagiotopoulos process which is recalled:

1. Shear tractions are put to zero. The normal contact problem is solved in the same way as in the case of the free rolling contact. The contact pressure p and the contact area Γ_c are obtained as output

2. The tangential contact problem is then solved by considering the results of the previous step for the normal contact as input. The contribution of the known pressure field on the tangential tractions q_x and q_y can be determined using the adequate influence coefficients

3. The normal contact problem is solved by taking into account the tangential shears found in the previous iteration for the tangential contact problem

The two last steps are repeated successively until the convergence is reached.

In fact, the effects of the tangential problem and the normal problem on each other depend on the properties of the materials in contact. When the bodies have the same elastic properties, they are said *elastically similar* and in that case there is no relative effect of the normal and the tangential problems. Otherwise they are said *elastically dissimilar* and a relative effect of two problems appears.
The parameter used to highlight the elastic similarity between the materials is the well-known Dundurs' parameter β[1].

The relative effect of the normal and tangential problems can be highlighted in the expressions of the displacements. Since the works of Boussinesq [BOU 85], Cerutti [CER 82] and Love [LOV 52] for the influence coefficients for a homogeneous half-space, it is well known that the surface displacements can be written as:

$$\begin{aligned}
\bar{u_x}(i,j) =& \sum_{l=1}^{N_x}\sum_{m=1}^{N_y} p(l,m)K_x^p(i-l,j-m) + \sum_{l=1}^{N_x}\sum_{m=1}^{N_y} q_x(l,m)K_x^{q_x}(i-l,j-m) \\
&+ \sum_{l=1}^{N_x}\sum_{m=1}^{N_y} q_y(l,m)K_x^{q_y}(i-l,j-m), \\
\bar{u_y}(i,j) =& \sum_{l=1}^{N_x}\sum_{m=1}^{N_y} p(l,m)K_y^p(i-l,j-m) + \sum_{l=1}^{N_x}\sum_{m=1}^{N_y} q_x(l,m)K_y^{q_x}(i-l,j-m) \\
&+ \sum_{l=1}^{N_x}\sum_{m=1}^{N_y} q_y(l,m)K_y^{q_y}(i-l,j-m), \\
\bar{u_z}(i,j) =& \sum_{l=1}^{N_x}\sum_{m=1}^{N_y} p(l,m)K_z^p(i-l,j-m) + \sum_{l=1}^{N_x}\sum_{m=1}^{N_y} q_x(l,m)K_z^{q_x}(i-l,j-m) \\
&+ \sum_{l=1}^{N_x}\sum_{m=1}^{N_y} q_y(l,m)K_z^{q_y}(i-l,j-m),
\end{aligned} \tag{5.1}$$

[1]The Dundurs' paramter is: $\beta = \frac{1}{2}\left[\frac{(1-2\nu_1)/G_1-(1-2\nu_2)/G_2}{(1-\nu_1)/G_1+(1-\nu_2)/G_2}\right]$

where the $K_\alpha^{p_\tau}$ are the influence coefficients corresponding to the effect of the load $p_\tau = p, q_x, q_y$ on the displacement u_α where $\alpha = x, y, z$. Those formula in Eq. (5.1) describe the fact that every component of the displacement vector is given by the superposition of the effects of the normal pressure and the contact shears in the two tangential directions.

In the case of elastically similar bodies, there is no need to calculate the contribution of the normal and tangential problems on each other since the bodies react the same way in every direction. Thus displacements can be evaluated using the forms:

$$\begin{aligned}
\bar{u_x}(i,j) &= \sum_{l=1}^{N_x}\sum_{m=1}^{N_y} q_x(l,m) K_x^{q_x}(i-l, j-m), \\
\bar{u_y}(i,j) &= \sum_{l=1}^{N_x}\sum_{m=1}^{N_y} q_y(l,m) K_y^{q_y}(i-l, j-m), \\
\bar{u_z}(i,j) &= \sum_{l=1}^{N_x}\sum_{m=1}^{N_y} p(l,m) K_z^{p}(i-l, j-m).
\end{aligned} \tag{5.2}$$

The above explanations are useful for the understanding of the distinction that will be made, further in this chapter, between the tractive rolling contact between elastically similar bodies and the tractive rolling contact between elastically dissimilar bodies. Moreover, in some contacts, one may want to neglect the effects of the tangential and the normal problems on each other, but keep the relative influences in the two directions for the tangential problem. In that case, the term with q_y is added to u_x and the term with q_x is added to u_y in the above equation.

Now, let's formulate mathematically the tractive rolling contact problem to solve and give its constitutive equations.

Firstly, the normal contact is supposed solved because there is not any novelty to add to the previous algorithm described in chapter 2. Thence, the focus is put on modelling the tangential contact problem for the tractive rolling contact. For this purpose, it is important to define the slip that occurs for the rolling motion. The formulation of this slip is found in the theory of Kalker (see his book [KAL 90]). It is briefly recalled below.

Consider a contact zone where two particles are located at the positions x_{i1} and x_{i2} respectively for body 1 and 2. Under the *small strain assumption*, the partial derivatives of the displacements with respect to x and y are negligible. From a previous time step t' to the actual time step t, the slip is defined as:

$$s_i^t = \dot{s}^t(t-t') = (\dot{x}_{1i}^t - \dot{x}_{2i}^t)(t-t') + \left[(\bar{u}_{1i}^t - \bar{u}_{2i}^t) - (\bar{u}_{1i}^{t'} - \bar{u}_{2i}^{t'})\right], \tag{5.3}$$

where the dot $\dot{.} = \frac{d}{dt}$ and the bar is the displacement at the contact surface $z = 0$. In the above description of the slip, the contribution of the rigid body displacements is contained in the term $(\dot{x}_{1i} - \dot{x}_{2i})$.

Those rigid body displacements also called the local creepages have a contribution that can be written as:

$$(\dot{x}_{1i} - \dot{x}_{2i})(t - t') = \begin{pmatrix} \xi_x - \varphi y \\ \xi_y + \varphi x \end{pmatrix} \tag{5.4}$$

where ξ_x ξ_y and φ are respectively the longitudinal, transversal and spin creepages. Then, using the symbol Δ for the variation between t' and t, the slip reads:

$$\begin{pmatrix} s_x^t \\ s_y^t \end{pmatrix} = \begin{pmatrix} \xi_x - \varphi y + \Delta \bar{u}_x^t \\ \xi_y + \varphi x + \Delta \bar{u}_y^t \end{pmatrix}. \tag{5.5}$$

In this formulation, the time is kept implicitly so that the transient part of the rolling contact can be modelled over a range of intended time steps. In order to solve this transient problem, the inputs at each time step are: an elementary covered distance in the rolling direction and the tractive loads applied.

Finally, solving this tangential contact problem implies to find the following unknowns:

- The shear tractions in the contact q_x and q_y;
- The slip zone Γ_{slip} and the stick zone Γ_{stick};
- The local creepages ξ_x, ξ_y and φ;

Since the normal contact is solved, the contact zone is supposed to be the same for the tangential problem. Thus, holds the relation: $\Gamma_c = \Gamma_{stick} \cup \Gamma_{slip}$. Adding the equilibrium equations, the following set of equations has to be verified:

$$\Gamma_c = \Gamma_{stick} \cup \Gamma_{slip}, \tag{5.6a}$$

$$F_x = \int\int_{\Gamma_c} q_x(x,y) dxdy \tag{5.6b}$$

$$F_y = \int\int_{\Gamma_c} q_y(x,y) dxdy \tag{5.6c}$$

$$M_z = \int\int_{\Gamma_c} (x q_y(x,y) - y q_x(x,y))\, dxdy \tag{5.6d}$$

With the constitutive equations of the problem (Eqs. (5.5) and (5.6)), the tractive rolling contact problem can be written in its variational formulation so that can be solved with a CGM algorithm. The general variational formulation of the contact problem is given by Kalker [KAL 90] as:

$$\min \int_{\Gamma_c} \left(h^* + \frac{1}{2}\bar{u}_z \right) p dxdy + \int_{\Gamma_c} \left(\mathbf{W}_\tau^* - \frac{1}{2}\bar{\mathbf{u}}_\tau \right) \mathbf{q} dxdy, \tag{5.7a}$$

$$p \geq 0, \tag{5.7b}$$

$$\|\mathbf{q}\| \leq fp. \tag{5.7c}$$

where h^* consists of the initial gap, the normal displacement induced by the shear tractions and eventually the rigid normal displacement. $\mathbf{W}_\tau^*$ embodies the contribution of the creepages and the tangential displacements due to the normal pressure.

As it has been said earlier in this document, the Conjugate Gradient Method is used here for solving minimisation formulations which are the variational forms of the contact problem.

5.3 Solver

With view to solve the variational formulation of the contact problem for the tractive rolling case, the Lagrangian method which is exposed in chapter 2 is used. The normal component is supposed already solved and then the tangential component of the contact problem has to be handled. CGM and FFT are used as numerical tools.

On the way to solve this tangential contact, two barriers have to be overcome:

1. The creepages ξ_x ξ_y and φ have to be updated at every step since they have to converge also for imposed tangential forces and spinning moment. To do so, the equilibrium equations with the Lagrangian formulation are used:

$$\xi_x - \varphi y_j - \Delta\bar{u}_{xij} + \lambda_{ij}\frac{q_{xij}}{fp_{ij}} = 0 \tag{5.8a}$$

$$\xi_y + \varphi x_i - \Delta\bar{u}_{yij} + \lambda_{ij}\frac{q_{xij}}{fp_{ij}} = 0 \tag{5.8b}$$

$$-y_j\left(\xi_x - \varphi y_j - \Delta\bar{u}_{xij} + \lambda_{ij}\frac{q_{xij}}{fp_{ij}}\right) + x_i\left(\xi_y + \varphi x_i - \Delta\bar{u}_{yij} + \lambda_{ij}\frac{q_{xij}}{fp_{ij}}\right) = 0 \tag{5.8c}$$

   where $\bar{u}_{xij} = \bar{u}_{x1ij} - \bar{u}_{x2ij}$ and λ_{ij} are the Lagrange multipliers.

2. The second issue concerns the equilibrium of the applied tractive forces and moment in Eq. (5.6) which has to be verified. This is done by adding values of shear in the stick zone as correction: $q_{xij} \leftarrow q_{xij} + a - c.y_j$ and $q_{yij} \leftarrow q_{yij} + b - c.y_j$. a, b and c are constants obtained by solving the equilibrium equations:

$$\begin{pmatrix} \sum_{\Gamma_{st}} 1 & 0 & -\sum_{\Gamma_{st}} y_j \\ 0 & \sum_{\Gamma_{st}} 1 & \sum_{\Gamma_{st}} x_i \\ -\sum_{\Gamma_{st}} y_j & \sum_{\Gamma_{st}} x_i & \sum_{\Gamma_{st}} \left(x_i^2 + y_j^2\right) \end{pmatrix} \begin{pmatrix} a \\ b \\ c \end{pmatrix} = \begin{pmatrix} F_x/S - \Sigma_{\Gamma_c} q_{xij} \\ F_y/S - \sum_{\Gamma_c} q_{yij} \\ M_z/S + \sum_{\Gamma_c} (y_j \cdot q_{xij} - x_i \cdot q_{yij}) \end{pmatrix} \tag{5.9}$$

   Those procedures are inspired by the methodology used by Gallego [GAL 07b].

The CGM algorithm that yields for solving the transient tractive rolling contact between elastic bodies is:

1. $\Gamma'_{stick} = \Gamma_c$, $\Gamma'_{slip} = \{0\}$. Thus, $\lambda_{ij} = 0$. The shear tractions are initialised in such a way that the equilibrium equations are verified.

2. The contact pressure and shears are moved along x with a δ_x which is the elementary covered distance. Then, DC-FFT is applied for the calculation of the surface tangential displacements $\bar{\mathbf{u}}_\tau = \bar{\mathbf{u}}_\tau^p + \bar{\mathbf{u}}_\tau^{q_x} + \bar{\mathbf{u}}_\tau^{q_y}$.

3. The creepages ξ_x ξ_y and φ are approximated using the Lagrangian formulation in Eq. (5.8). The matrix system is solved with a Gauss-Jordan algorithm.

4. The residue of the system is then calculated in the contact zone:
$$\begin{cases} r_{xij} = \Delta\bar{u}_{xij} + (\xi_x - \varphi y_j) \\ r_{yij} = \Delta\bar{u}_{yij} + (\xi_y + \varphi x_i) \end{cases}, \quad (i,j) \in \Gamma_c. \tag{5.10}$$

5. The Lagrange multipliers are calculated for the slip zone Γ'_{slip}
$$\lambda_{ij} = -\|\mathbf{r}_{ij}\| \times sign(\mathbf{r}_{ij}.\mathbf{q}_{ij}); \tag{5.11}$$

6. The complementary conditions are tested:
$$\text{If } \lambda_{ij} < 0, \text{ then } \Gamma'_{stick} \leftarrow \Gamma'_{stick} \cup (i,j) \text{ and } \zeta = 0. \tag{5.12}$$
and an error is evaluated with respect to the angle between the shear vectors and the slip in the slip zone:
$$\varepsilon^{slip} = \frac{\sum_{(i,j)\in\Gamma'_{slip}} \|\mathbf{r}_{ij} + \lambda_{ij}\frac{\mathbf{q}_{ij}}{fp_{ij}}\|}{\sum_{(i,j)\in\Gamma'_{slip}} \lambda_{ij}} \tag{5.13}$$

7. The descent direction is calculated in function of the residue and the previous descent direction
$$\mathbf{d}_{ij} \leftarrow \mathbf{r}_{ij} + \zeta\frac{G}{G_{old}}\mathbf{d}_{ij}, \quad (i,j) \in \Gamma'_{stick} \tag{5.14a}$$
$$\mathbf{d}_{ij} \leftarrow (\mathbf{r}_{ij} + \lambda_{ij}\mathbf{q}_{ij}) + \zeta\frac{G}{G_{old}}\mathbf{d}_{ij}, \quad (i,j) \in \Gamma'_{slip} \tag{5.14b}$$
with
$$G = \sum_{(i,j)\in\Gamma'_c} \left(\mathbf{r}_{ij} + \lambda_{ij}\frac{\mathbf{q}_{ij}}{fp_{ij}}\right).\left(\mathbf{r}_{ij} + \lambda_{ij}\frac{\mathbf{q}_{ij}}{fp_{ij}}\right) \tag{5.14c}$$
and finally $G_{old} \leftarrow G$ and $\zeta \leftarrow 1$.

8. The DC-FFT is applied to the descent direction

$$\mathbf{rt}_\tau^q = \mathbf{A}_\tau^q \mathbf{d} \tag{5.15}$$

and then,

$$\mathbf{rt}_\tau^q \leftarrow \mathbf{rt}_\tau^q + \frac{\lambda_{ij}\mathbf{d}_{ij}}{fp_{ij}}. \tag{5.16}$$

The descent step is

$$\alpha = \frac{\sum_{(i,j)\in\Gamma_c}\left(\mathbf{r}_{ij} + \lambda_{ij}\frac{\mathbf{q}_{ij}}{fp_{ij}}\right).\left(\mathbf{r}_{ij} + \lambda_{ij}\frac{\mathbf{q}_{ij}}{fp_{ij}}\right)}{\sum_{(i,j)\in\Gamma_c}\mathbf{d}_{ij}\mathbf{rt}_{ij}}; \tag{5.17}$$

9. The shears are updated

$$\mathbf{q}_{ij} \leftarrow \mathbf{q}_{ij} + \alpha\mathbf{d}_{ij} \quad (i,j) \in \Gamma_c \tag{5.18}$$

10. The complementary conditions are enforced:

$$\text{if } \|\mathbf{q}_{ij}\| > fp_{ij}, \quad (i,j) \in \Gamma'_{stick} \quad \text{then}, \quad \Gamma'_{slip} \leftarrow \Gamma'_{slip} \cup (i,j), \quad \zeta = 0, \quad \mathbf{q}_{ij} \leftarrow fp_{ij}\frac{\mathbf{q}_{ij}}{\|\mathbf{q}_{ij}\|}; \tag{5.19}$$

11. The equilibrium equations in Eq. (5.6) are enforced and then the convergence criteria is tested

$$\varepsilon = \frac{\sum_{(i,j)\in\Gamma_c}\sqrt{(q_{xij} - q_{xoldij})^2 + (q_{yij} - q_{yoldij})^2}}{\sum_{(i,j)\in\Gamma_c}\sqrt{q_{xij}^2 + q_{xij}^2}} \tag{5.20}$$

Finally, $\mathbf{q}_{old} \leftarrow \mathbf{q}$.

5.4 Validation

The validation of the above algorithm is done by comparison to results from the literature. Firstly, the tractive rolling contact between elastically similar bodies is simulated and compared to the works of Kalker [KAL 90] and Manyo [MAN 19b]. The model presented by Manyo is built with the same numerical tools used in this work (CGM and FFT). However, it solves only the steady-state regime of the tractive rolling contact. Meanwhile, the model of Kalker covers both the transient and the steady-state regimes. The model of Kalker has been developed with different numerical tools and his simulations have been performed on coarse meshed surface.

After the validation in a case involving elastically similar bodies, the tractive rolling contact will be simulated between dissimilar cylinders and compared to the results of Nowell and Hills [NOW 88].

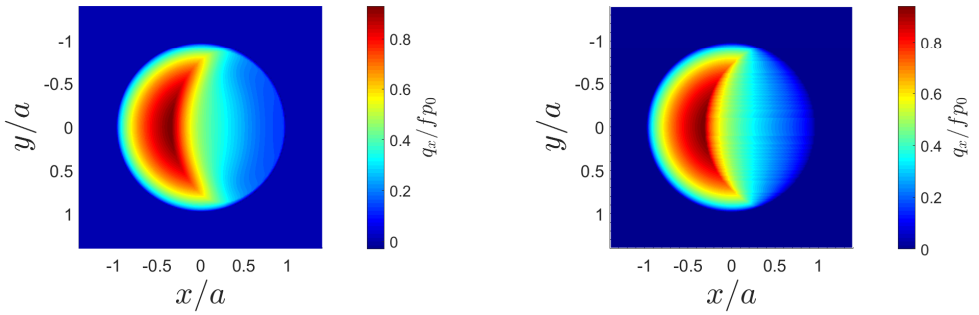

(a) (b)

Figure 5.2: Two dimensional longitudinal dimensionless shear q_x/p_0 for a tractive rolling contact between elastically similar spheres ($\beta = 0$) of radius $R_1 = R_2 = 337.5mm$ for a tangential force $F_x/fP = 0.657$ applied. The present model (left) is compared to the model of Manyo (right).

5.4.1 Validation of the tractive rolling contact between elastically similar bodies

For the first validation of the present tractive rolling contact algorithm, a simulation of the tractive rolling contact between two elastically similar ($\beta = 0$) and geometrically identical spheres ($R_1 = R_2$) is performed. The validation case used is taken from Manyo in his PhD thesis [MAN 19b] where he found a good agreement with the results of Kalker [KAL 90].

For the validation, the two elastic spheres have the same radius R and are put into contact under a normal force P and a tangential force F_x in the direction of the rolling. The potential contact area is divided into square elements of size $(5. \times 10^{-4}) \times (5. \times 10^{-4})$ mm^2.

Figure 5.2 shows the two-dimensional view of the dimensionless shear traction q_x/p_0 in the steady-state regime, p_0 being the Hertz maximum pressure. The results are for an applied tangential force $F_x/fP = 0.657$ and made dimensionless using the Hertz contact results (the maximum pressure p_0 and the width of the contact zone a). When the shear traction q_x/p_0 is plotted along the axis x in the plane $y = 0$, Fig.5.3 is obtained, where a perfect fit is observed except near the leading edge.

As said in the previous section, the simulation here is made from the transient to the steady-state regime. In the case of elastically similar bodies, when a constant tangential force is applied throughout the rolling, the contact goes from the Cattaneo shift (at the static state) to the steady-state regime shown above.

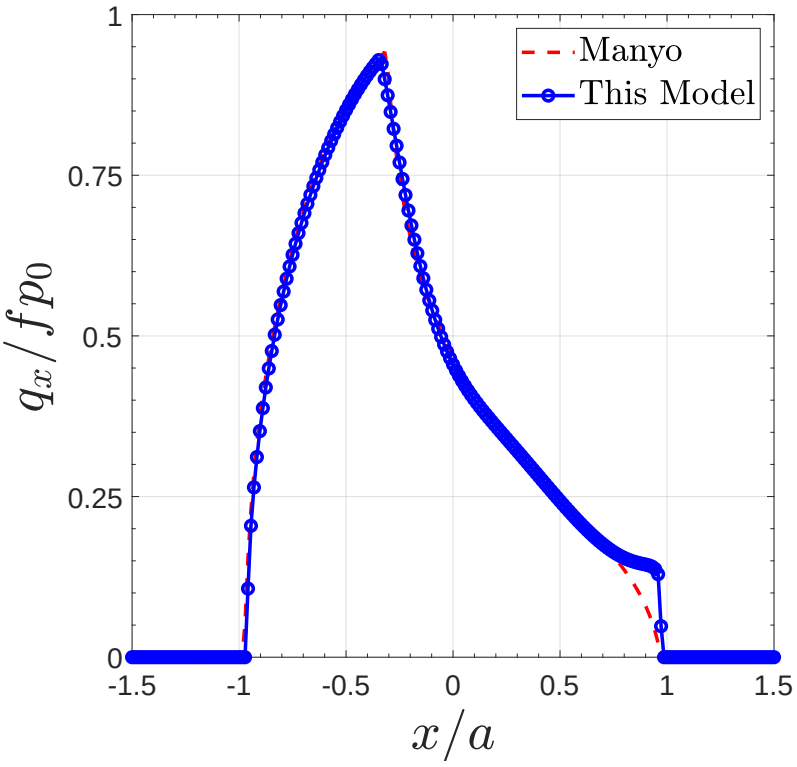

Figure 5.3: Longitudinal shear for a tractive rolling contact between geometrically identical and elastically similar ($\beta = 0$) spheres for an applied tangential force $F_x/fP = 0.657$ along the line x in the plane $y = 0$.

From the Cattaneo-Mindlin shift to the steady-state regime: The transition from the Cattaneo-Mindlin shift to the steady-state regime in the tractive rolling contact has been examined by Kalker [KAL 90]. It is presented here in Fig. 5.4. The simulation by Kalker has been performed on a zone discretised with few elements. *unit* on the figure represent the unit chosen for length in a coherent system of units. The top row shows the plots along the longitudinal axis x in the middle plane $y = 0$. Meanwhile, in the bottom row, one can observe the changes of the contact zone related to the distance V_t covered. The steady-state regime seems to be achieved for 5 *units* covered.

For the validation of the transient part, the same simulation has been performed with the present model. The simulation has been performed in 200 time steps. The tractive force $F_x/fP = 0.657$ is maintained constant throughout the simulation and at every time step, a distance $d = 5. \times 10^{-4}$ mm is covered. Note that this elementary distance d covered in one step had appeared to have an influence on what happens at the leading edge of the contact. In fact, for bigger values of d, the steady-state regime is achieved quicker, but some instabilities appear at the leading edge.

Let's call V_t the overall distance covered at a certain time *itime*. Figure 5.5 shows

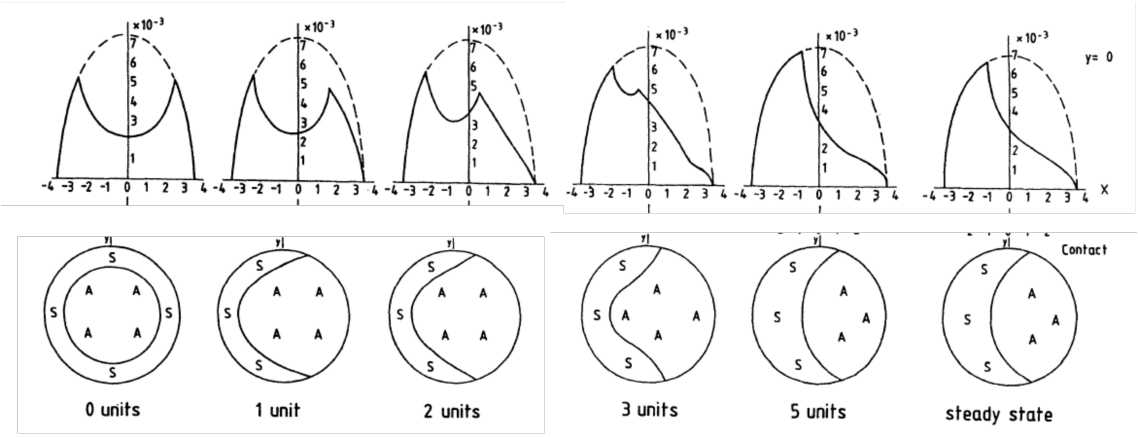

Figure 5.4: Results of Kalker for the tractive rolling contact between geometrically identical and elastically similar ($\beta = 0$) spheres for an applied tangential force $F_x/fP = 0.657$ along the line x in the plane $y = 0$.s. From the Cattaneo shift to the steady-state rolling motion, the evolution of the longitudinal shear q_x/p_0 is given until the steady-state regime.

the contact longitudinal dimensionless shear q_x/p_0 for a) $V_t/a = 0$; b) $V_t/a = 0.14$; c) $V_t/a = 0.35$; d) $V_t/a = 0.70$; e) $V_t/a = 1.40$ and f) $V_t/a = 2.81$. One can observe that $V_t/a = 0$ corresponds to the Cattaneo shift since the rolling has not begun yet but the tangential force is applied. Throughout the rolling motion, the adhesion zone in the leading edge grows until the steady-state regime is achieved.

Nota: An analysis of the time when the steady-state is achieved has shown that it is approximately at a moving distance $V_t/a \approx 1.5$.

When the results are plotted along the x axis in the plane $y = 0$, the profiles of dimensionless shear q_x/p_0 in Fig. 5.6 are obtained.

Finally, the results of the simulations with the present model show the same behaviour in transient regime as the model of Kalker. The constraint here is a need of performing the simulation into much time steps because of the influence of the elementary covered distance on the instabilities near at the leading edge. For instance, when the simulation is performed with an elementary covered distance divided by 10 $d = 5. \times 10^{-3}$, the simulation is performed into 20 time steps. The results, in Fig. 5.7 show some instabilities at the leading edge. However, the overall results remain good compared to the expected results.

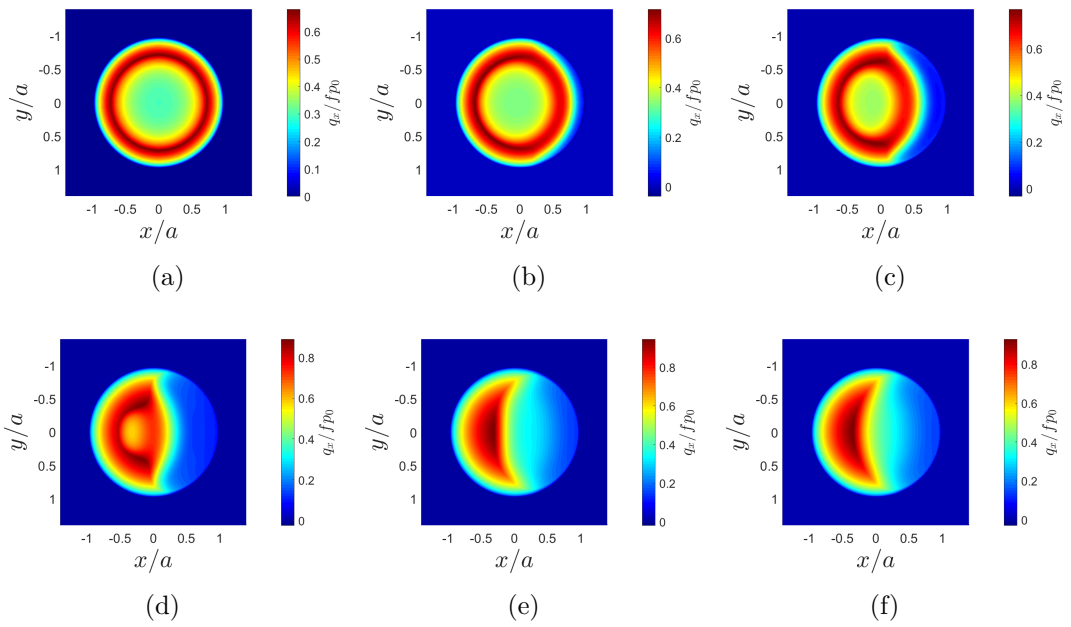

Figure 5.5: Results with the present model for the tractive rolling contact between geometrically identical and elastically similar ($\beta = 0$) spheres for an applied tangential force $F_x/fP = 0.657$ along the line x in the plane $y = 0$. From the Cattaneo shift to the steady-state rolling motion, the evolution of the longitudinal shear q_x/p_0 is given until the steady-state regime. a) $V_t/a = 0$; b) $V_t/a = 0.14$; c) $V_t/a = 0.35$; d) $V_t/a = 0.70$; e) $V_t/a = 1.40$ and f) $V_t/a = 2.81$.

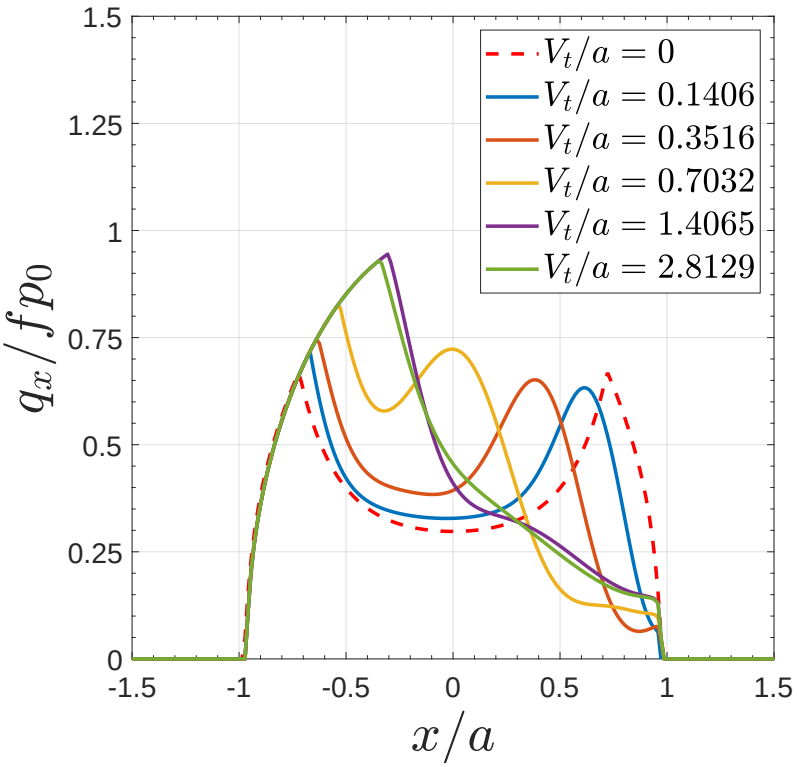

Figure 5.6: Evolution of the dimensionless shear q_x/fp_0 in a tractive rolling contact between elastically similar spheres along the x axis in the plane $y = 0$.

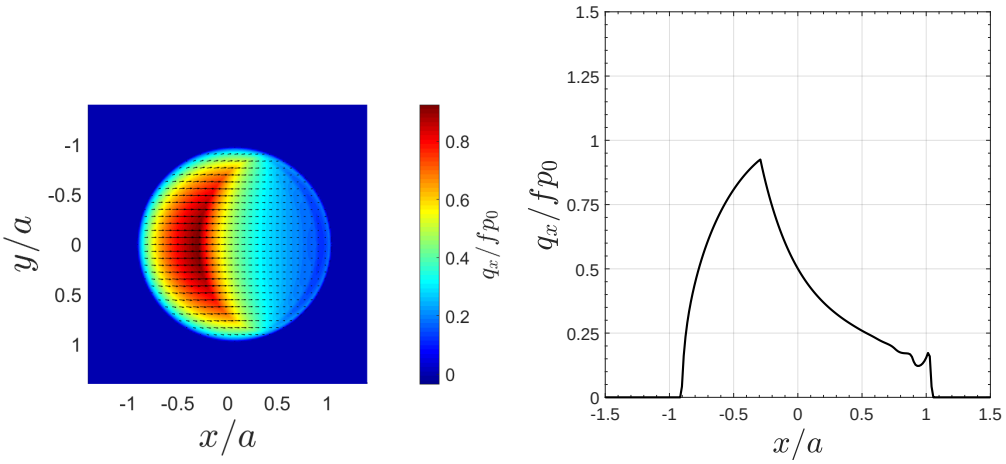

Figure 5.7: Perturbation at the leading edge of the tractive rolling contact when the rolling is performed within an insufficient number of time steps. Here the simulation is performed in 20 time steps.

5.4.2 Validation of the tractive rolling contact between dissimilar materials

For further validation, a simulation of the tractive rolling contact between dissimilar bodies is performed according to the framework in Nowell and Hills [NOW 88]. Their model is a two dimensional plane strain model. To perform the simulation, a Johns-Gohar logarithmic profile [JOH 81] is used to define the cylinder. The contact between a cylinder and a half-space where the materials are elastically dissimilar ($\beta/f = -2.88$) is simulated under a tractive force $F_x/fP = 0.83$. The simulation with the present model has been performed by using a finite cylinder of length $\approx 117 \times a$ (a being the contact radius). As results in Fig. 5.8 one can see the dimensionless shear q_x/p_0 where agreement between the two models is quite good but not perfect.

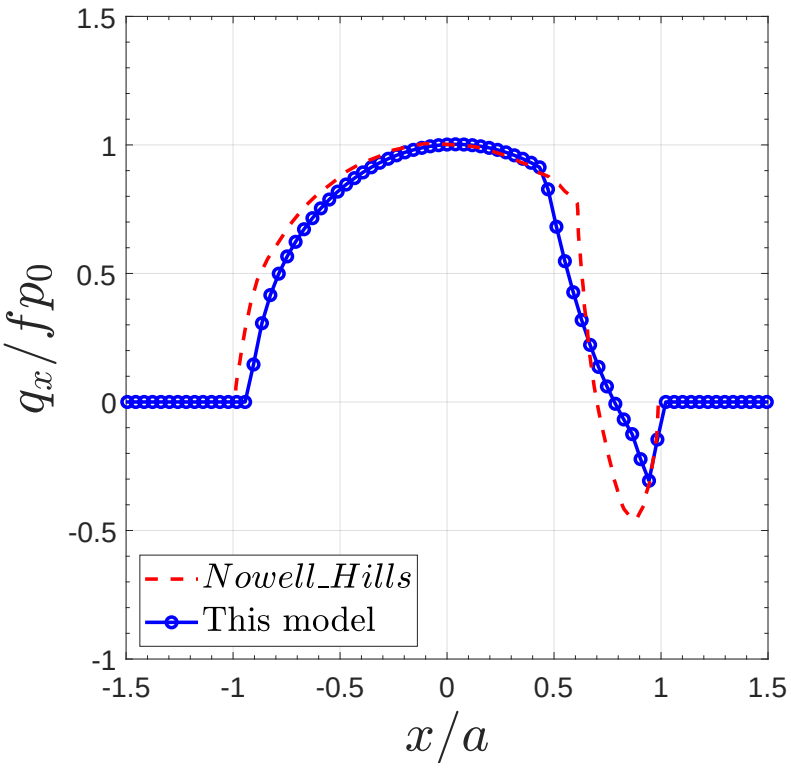

Figure 5.8: Longitudinal shear for a tractive rolling contact between dissimilar bodies ($\beta/f = -2.88$) for an applied tangential force $F_x/fP = 0.83$ along the line x in the plane $y = 0$.

In summary, the results given by the developed model are satisfactory. Apart from instabilities at the leading edge, a perfect fit is observed for the contact between elastically similar bodies. When compared to a plane strain model of tractive rolling contact between elastically dissimilar bodies, a good agreement is also ob-

served. Moreover, the model allows to model the transient regime and takes into account any kind of tangential loading.
In order to investigate the effects of the two tangential tractive forces and the spininng moment, various combinations of loading are examined. In a first part, the tractive rolling contact is analysed between elastically similar bodies; and in a second part elastically dissimilar bodies are considered.

5.5 Results

In the tractive rolling contact formulation, the three creepages ξ_x, ξ_y and φ influence the distribution of the shears in the contact zone. Figure 5.9 shows the expected shapes of the slip and adhesion areas in the contact zone with respect to the creepages activated.

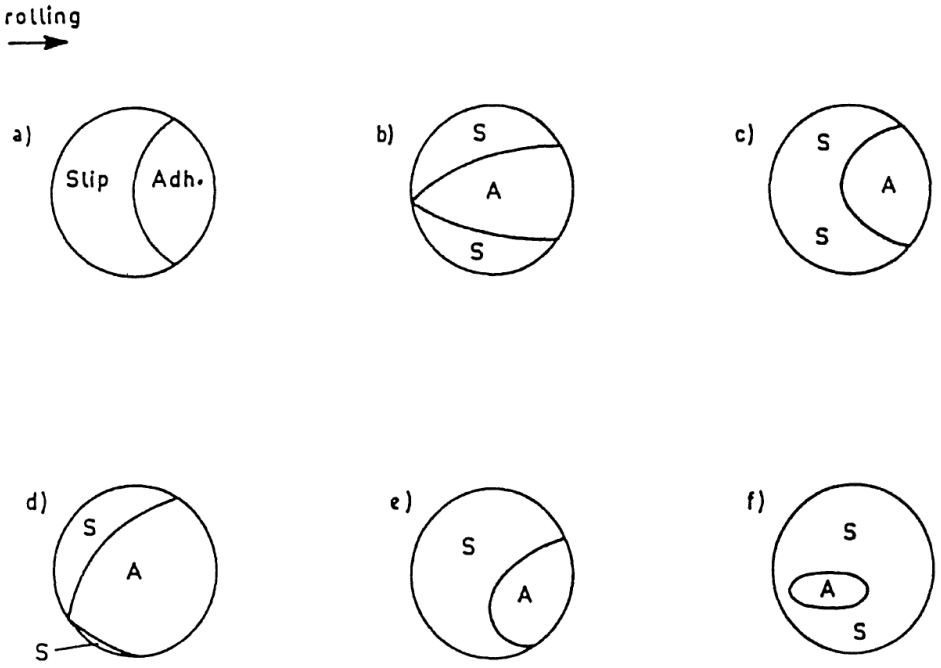

Figure 5.9: Slip and adhesion areas in the contact zone for a tractive rolling contact submitted to a) pure tangential creepages ($\varphi = 0$) ; b) pure spin ($\xi_x = \xi_y = 0$) ; c) spin and lateral creepages ($\xi_x = 0$) ; d) spin and longitudinal creepages ($\xi_y = 0$) ; e) General case ($\xi_x \neq 0$, $\xi_y \neq 0$ and $\varphi \neq 0$) and f) pure spin (large) [KAL 90].

In what follows next, a parametric study is performed with view to analyse the effects of each of the creepages. In the present work, the overall tractive forces are applied since it is the more realistic way to see the practical applications. Therefore, applying some tractive forces induces the activation of some creepages. Note that

in a further study, a simple modification of the algorithm can be done to directly impose the creepages.

For the first analysis, the framework is the one used for the validation in section 5.4.1. Geometrically identical spheres are submitted to the elastic rolling contact under forces F_x (longitudinal), F_y (transversal) and a spinning moment M_z. The spheres have the same radius $R_1 = R_2 = 337.5$ mm. The potential contact surface is discretised with square elements of size $(5. \times 10^{-4}) \times (5. \times 10^{-4})$ mm^2. The normal load is a constant force $P = 0.4705$ N throughout the simulation. The Coulomb's friction coefficient is $f = 0.4013$ and the simulations are performed in 200 time steps with an elementary covered distance $d = 5. \times 10^{-4}$ mm at ever time step. **Nota:** The *longitudinal* direction is the direction of the rolling (x here), *transversal* or *lateral* direction is the perpendicular direction to the rolling direction in the tangent plane (y here).

Let's begin the analysis by examining the tractive rolling contact between elastically similar spheres.

5.5.1 Solutions for elastically similar bodies

Here, the bodies are geometrically and elastically identical with Young modulus $E_1 = E_2 = 2560000$ MPa and Poisson's ratio $\nu_1 = \nu_2 = 0.28$. In this case where $\beta = 0$, the coupling between the normal and the tangential problems is negligible. Various simulations are performed by combining the tangential longitudinal tractive force F_x, the tangential transversal tractive force F_y and the spinning moment around the z axis M_z.

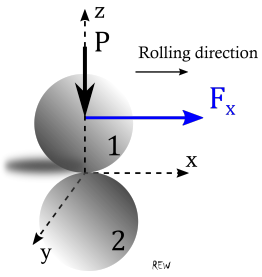

5.5.1.1 Pure longitudinal tractive force

For this case, the tangential loading consists only in a tangential force $F_x/fP = 0.657$ while $F_y = 0$ and $M_z = 0$. This loading implies the appearance of the longitudinal creepage ξ_x only. Note that the tractive force is applied from the very first step to the last. This is the reason why, the first time step corresponds to the Cattaneo-Mindlin shift. It is exactly the same case of the validation case presented in section 5.4.

Figure 5.10 shows the two dimensional view of the norm of the shear vector in the contact surface for a covered distance equal to a) $V_t/a = 0$; b) $V_t/a = 0.14$; c) $V_t/a = 0.35$; d) $V_t/a = 0.70$; e) $V_t/a = 1.40$ and f) $V_t/a = 2.81$. The quantity plotted

is the $\|q_\tau\| = \sqrt{q_x^2 + q_y^2}$ made dimensionless by division by the friction coefficient f and by the Hertz contact maximum pressure p_0.

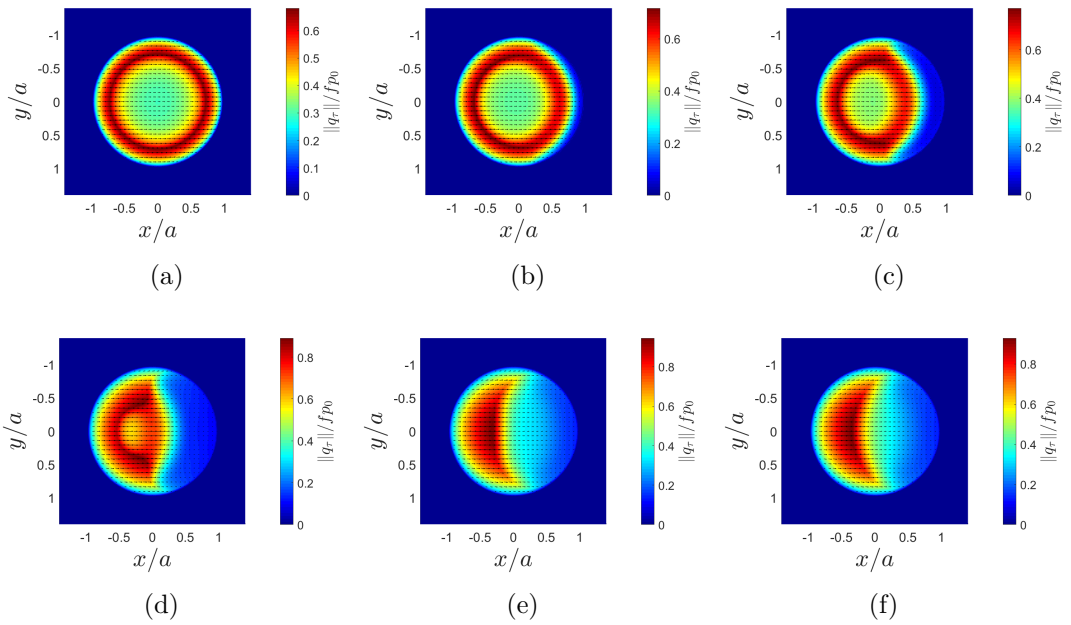

Figure 5.10: Two dimensional view of the dimensionless norm of the shear vector q_τ in the contact surface for a covered distance a) $V_t/a = 0$; b) $V_t/a = 0.14$; c) $V_t/a = 0.35$; d) $V_t/a = 0.70$; e) $V_t/a = 1.40$ and f) $V_t/a = 2.81$ for the contact between geometrical and elastically identical spheres ($\beta = 0$) and an applied pure longitudinal tractive force $F_x/fP = 0.657$.

The shear vectors are plotted on the surface with small arrows, showing the directions of the streamlines of the shear in the surface. For the pure longitudinal tractive force, the streamlines are following the longitudinal direction throughout the motion. This makes sense since the applied tractive force is following the rolling direction. This configuration where only a longitudinal tractive force is applied can be seen as imposing an acceleration or deceleration force (negative tractive F_x should then be applied) to the system.

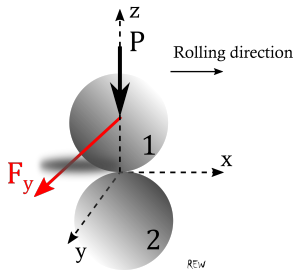

5.5.1.2 Pure transversal tractive force

The loading is only the transversal tractive force $F_y/fP = 0.657$ while $F_x = 0$ and $M_z = 0$. This case is of great interest since the application of such loading surprisingly induces not only a transversal creepage ξ_y, but also a spin creepage φ. This has been already observed by Johnson [JOH 85] and further by Kalker [KAL 90].

When one imagines the situation, it may come clearer. Consider a rolling sphere on a plane; for an applied transversal force to that rolling sphere, a perturbation is brought to the rolling motion. Coupling the rolling with the transversal, it comes a spinning trend. This phenomenon induces the apparition of the spin creepage. The contribution of the spin creepage can be observed in Fig. 5.11 where the two dimensional norm of the shear vector is plotted in the contact zone for a covered distance a) $V_t/a = 0$; b) $V_t/a = 0.14$; c) $V_t/a = 0.35$; d) $V_t/a = 0.70$; e) $V_t/a = 1.40$ and f) $V_t/a = 2.81$.

By observing closer the shear vectors in the contact, one can make two remarks:

- ✧ firstly, the streamlines are globally following the transversal direction;
- ✧ secondly, when the transient regime advances, the vectors in the adhesion zone are undergoing a twisting from the transversal directions due to the spin creepage.

To exemplify this case for the tire-pavement contact, consider a rolling car on an inclined plane perpendicularly to its rolling direction, the force induced in the transverse direction can be seen as this lateral force applied here.

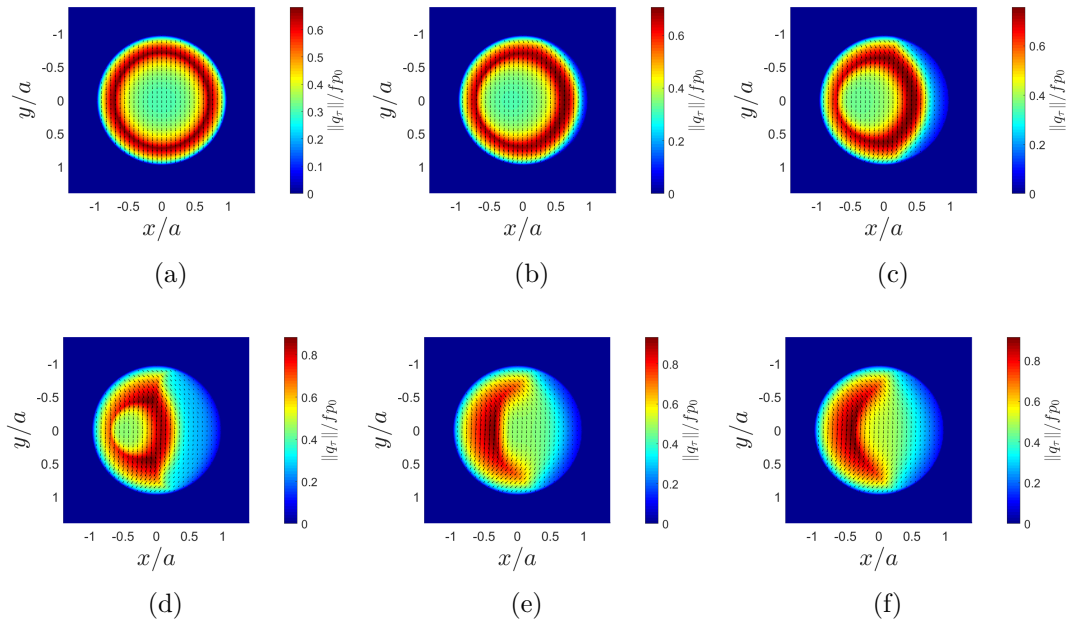

Figure 5.11: Two dimensional view of the dimensionless norm of the shear vector q_τ in the contact surface for a covered distance a) $V_t/a = 0$; b) $V_t/a = 0.14$; c) $V_t/a = 0.35$; d) $V_t/a = 0.70$; e) $V_t/a = 1.40$ and f) $V_t/a = 2.81$; for the contact between quasi-identical bodies ($\beta = 0$) and an applied pure transversal tractive force $F_y/fP = 0.657$.

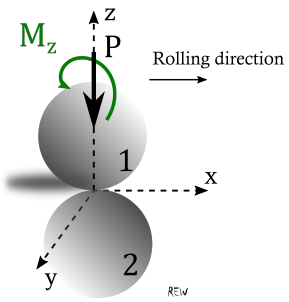

5.5.1.3 Pure spinning moment

Here, only a spinning moment around the normal z axis is applied: $M_z/fPa = 0.3$, $F_x = 0$ and $F_y = 0$. In a similar way as for the pure transversal tractive force applied, applying only a spinning moment gives rise not only to a spin creepage but also to a transversal creepage. This can be observed in Fig. 5.12 where the two dimensional norm of the shear vector in the contact zone is plotted for a covered distance a) $V_t/a = 0$; b) $V_t/a = 0.14$; c) $V_t/a = 0.35$; d) $V_t/a = 0.70$; e) $V_t/a = 1.40$ and f) $V_t/a = 2.81$.

Two interesting remarks have to be made. The first one concerns the apparition of the transversal creepage in an analogue way to the previous case in section 5.5.1.2.

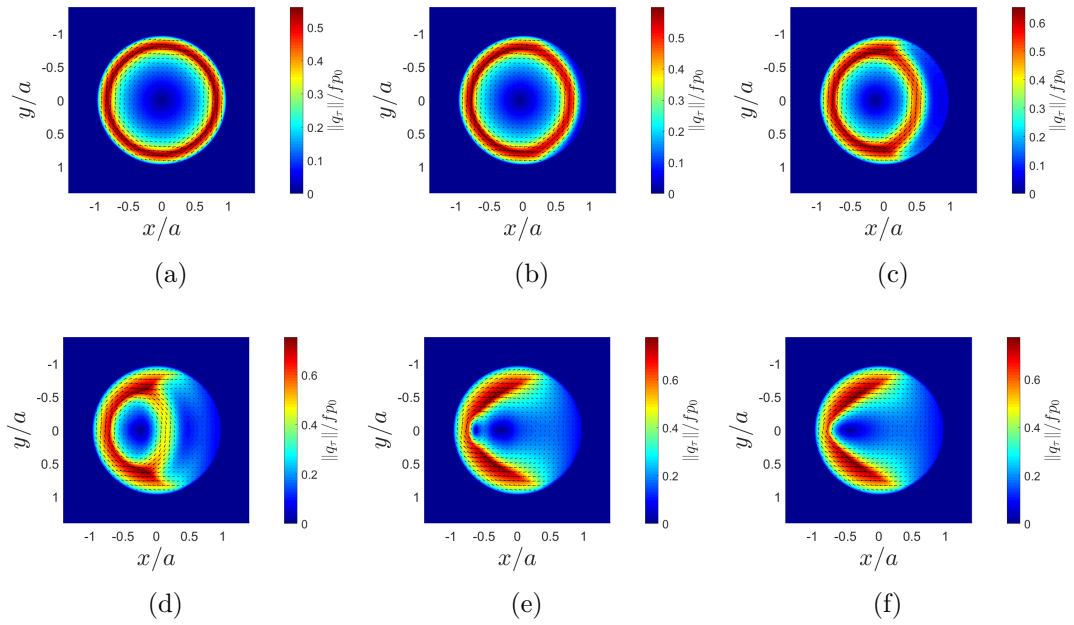

Figure 5.12: Two dimensional view of the dimensionless norm of the shear vector q_τ in the contact surface for a covered distance a) $V_t/a = 0$; b) $V_t/a = 0.14$; c) $V_t/a = 0.35$; d) $V_t/a = 0.70$; e) $V_t/a = 1.40$ and f) $V_t/a = 2.81$; for the contact between quasi-identical bodies ($\beta = 0$) and an applied pure spinning moment $M_z/fPa = 0.3$.

The second is about the center of the streamlines. Note that for $V_t/a = 0$, the streamlines are circumferential around the center of the contact. When moving toward the steady-state regime, the streamlines are no more circumferential, surely due to the transversal creepage and the fact that the center of the shears has moved.

As summary of the analysis of the effect of each of the single loading on the rolling contact between elastically similar bodies, one can retain that:

- applying a longitudinal tractive force F_x gives rise to the longitudinal creepage ξ_x;

- while applying a transversal tractive force F_y or a spinning moment M_z, gives rise to both transversal creepage ξ_y and spin creepage φ.

In order to continue the investigation, combinations of the tractive forces and with the spinning moment are set in the next cases.

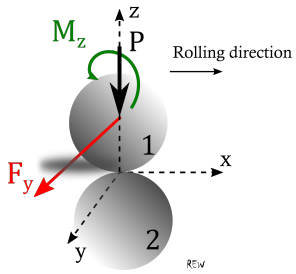

5.5.1.4 Transversal force + Spinning moment

A transversal tractive force and a spinning moment are applied simultaneously. Based on the observations made in the previous sections, this configuration should imply the apparition of a transversal creepage and a spin creepage. Thus the overall behaviour is expected to be similar to the pure transversal tractive force case (see 5.5.1.2) but for different levels of impact on the creepages involved. For the

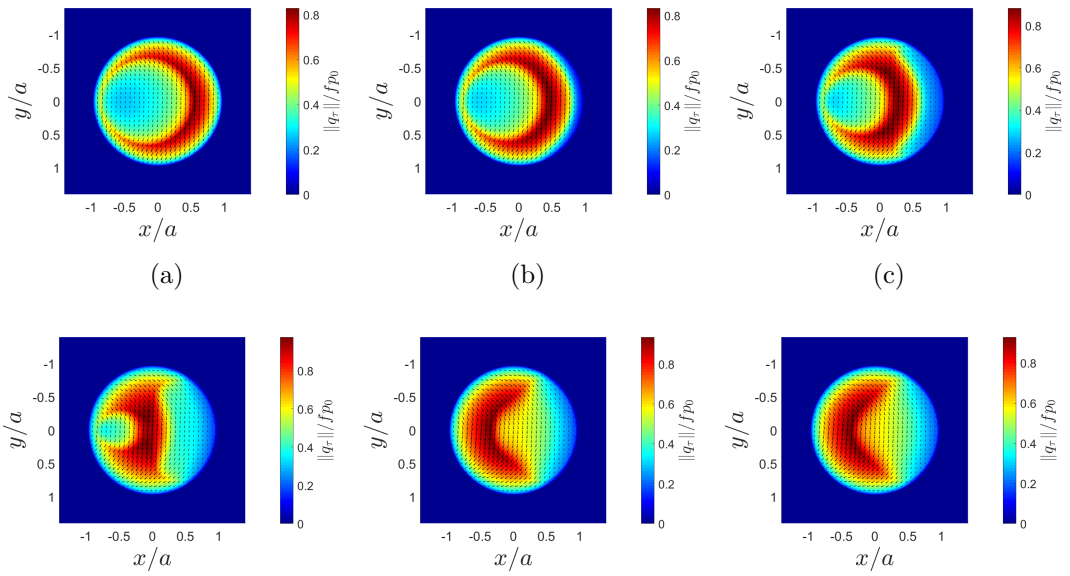

Figure 5.13: Two dimensional view of the dimensionless norm of the shear vector q_τ in the contact surface for a covered distance a) $V_t/a = 0$; b) $V_t/a = 0.14$; c) $V_t/a = 0.35$; d) $V_t/a = 0.70$; e) $V_t/a = 1.40$ and f) $V_t/a = 2.81$; for the contact between quasi-identical bodies ($\beta = 0$) and an applied transversal tractive force $F_y/fP = 0.657$ and a spinning moment $M_z/fPa = 0.15$.

simulation, the loading is: $F_x = 0$, $F_y/fP = 0.657$ and $M_z/fPa = 0.15$. Then the resulting contact shear is presented in Fig. 5.13 where one can see the two dimensional view of the norm of the shear vector in the contact zone for a covered distance a) $V_t/a = 0$; b) $V_t/a = 0.14$; c) $V_t/a = 0.35$; d) $V_t/a = 0.70$; e) $V_t/a = 1.40$ and f) $V_t/a = 2.81$.

At the first time step, the shear is asymmetric. The slip zone appears near the leading edge at the beginning; and throughout the motion, the adhesion takes place in the leading edge while the slip zone is near the trailing edge. The general shape of the norm of the shear vector as well as the streamlines in steady-state regime are similar to the case of the pure transversal tractive force applied.

This loading configuration for the tire-pavement topic can be viewed as a turnaround. The centrifugal force is the lateral force; and the turning motion imposed to the wheel is represented by the moment.

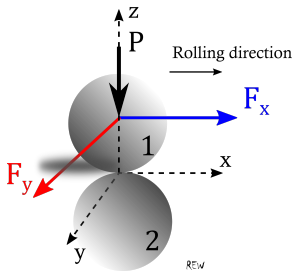

5.5.1.5 Longitudinal + Transversal tractive forces

The configuration considered is the combination of the longitudinal tractive force and the transversal one, while the spinning moment goes to zero. The values are: $F_x/fP = 0.35$, $F_y/fP = 0.35$ and $M_z/fPa = 0$. In this framework, all the three creepages hold.

The results of the simulation are shown in Fig. 5.14 where the two-dimensional view of the dimensionless norm of the shear vector is plotted for a covered distance a) $V_t/a = 0$; b) $V_t/a = 0.14$; c) $V_t/a = 0.35$; d) $V_t/a = 0.70$; e) $V_t/a = 1.40$ and f) $V_t/a = 2.81$. The first step corresponds to the Cattaneo-Mindlin shift. While moving, the adhesion zone takes place at the leading edge but the field becomes asymmetric due to the spin creepage.
With the model of Manyo [MAN 19b] where the spin creepage is not considered, the results of a tractive rolling contact where both longitudinal and transversal forces are imposed, do not show this turning type of shear field.

This loading is, for example, the acceleration of a car which is rolling on an inclined plane perpendicularly to its rolling direction.

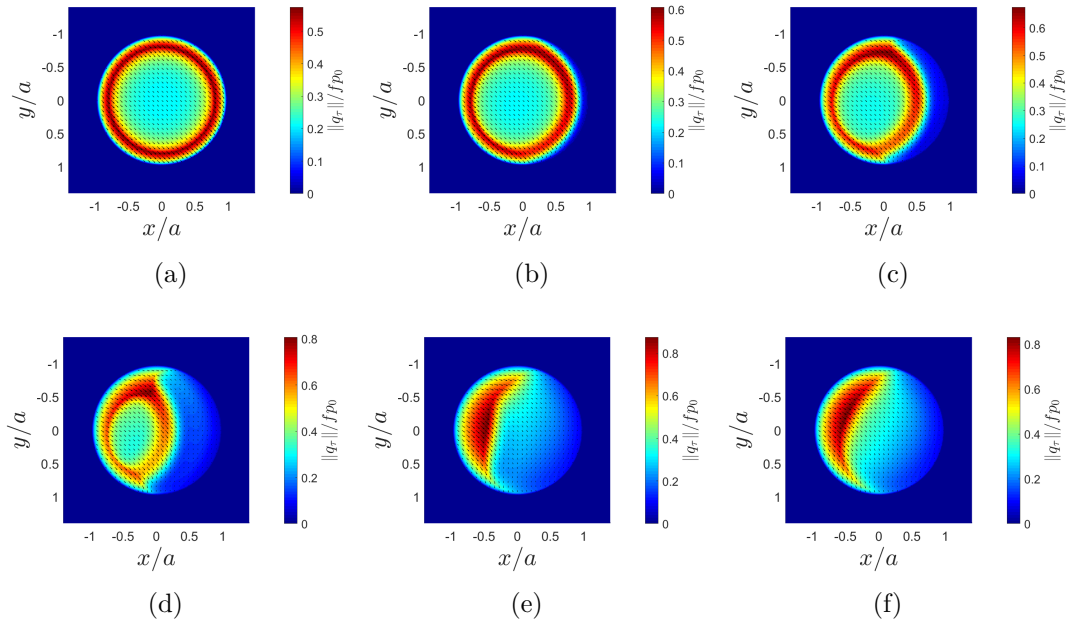

Figure 5.14: Two dimensional view of the dimensionless norm of the shear vector q_τ in the contact surface at time steps for a covered distance a) $V_t/a = 0$; b) $V_t/a = 0.14$; c) $V_t/a = 0.35$; d) $V_t/a = 0.70$; e) $V_t/a = 1.40$ and f) $V_t/a = 2.81$; for the contact between quasi-identical bodies ($\beta = 0$) and an applied longitudinal tractive force $F_x/fP = 0.35$ and a transversal tractive force $F_y/fP = 0.35$.

5.5.1.6 Longitudinal force + Spinning moment

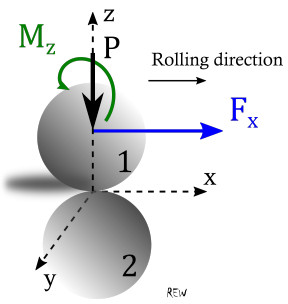

The combination of the longitudinal tractive force and the spinning moment is studied: $F_x/fP = 0.35$, $F_y/fP = 0$ and $M_z/fPa = 0.15$. As in the previous case, all the three creepages are expected.

The results of the simulation are displayed in Fig. 5.15 where the two dimensional view of the dimensionless norm of the shear vector corresponds to a covered distance a) $V_t/a = 0$; b) $V_t/a = 0.14$; c) $V_t/a = 0.35$; d) $V_t/a = 0.70$; e) $V_t/a = 1.40$ and f) $V_t/a = 2.81$. For the first step, the results combines the Cattaneo-Mindlin shift to the results for an applied moment only. The resulting shear field is asymmetric. Throughout the steps the contact shape becomes similar to the one of the previous

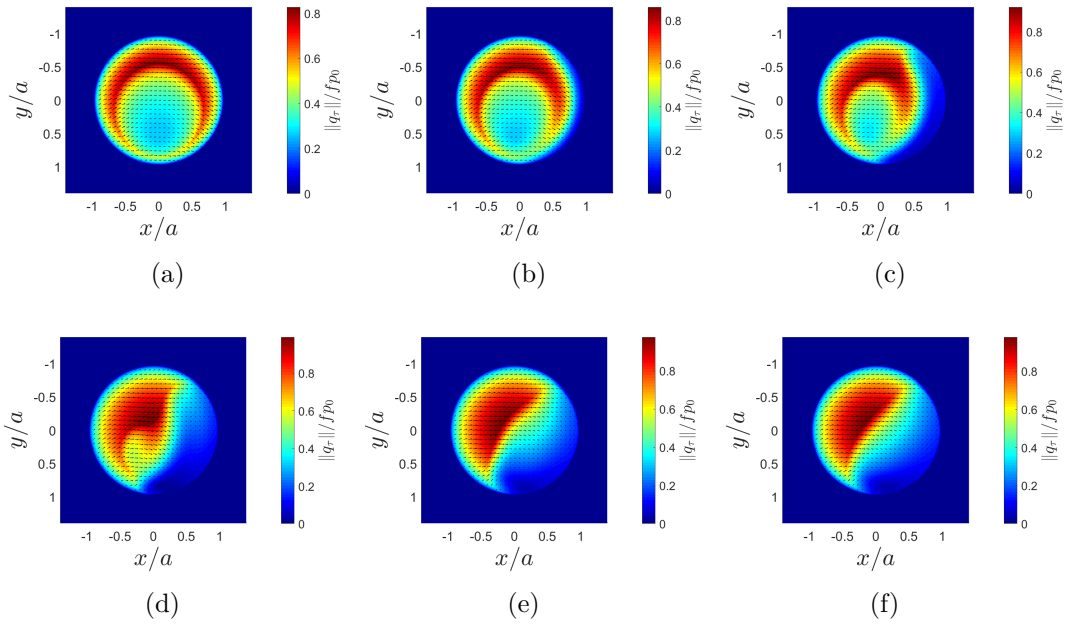

Figure 5.15: Two dimensional view of the dimensionless norm of the shear vector q_τ in the contact surface at time steps for a covered distance a) $V_t/a = 0$; b) $V_t/a = 0.14$; c) $V_t/a = 0.35$; d) $V_t/a = 0.70$; e) $V_t/a = 1.40$ and f) $V_t/a = 2.81$; for the contact between quasi-identical bodies ($\beta = 0$) and an applied longitudinal tractive force $F_x/fP = 0.657$ and a spinning moment $M_z/fPa = 0.15$.

section. This is understandable since, the behaviour induced by the application of a transversal tractive force is somehow similar to the one induced by the application of a spinning moment (both imply lateral and spin creepages), especially in steady-state regime.

For the tire-pavement contact, this configuration can be seen as an acceleration in the turnaround where the centrifugal force can be negligible.

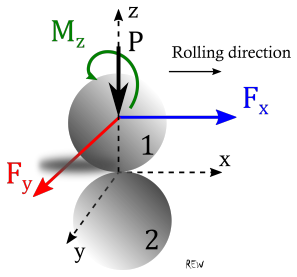

5.5.1.7 General case

Finally, the general case, where all the input loads take non zero values, is studied. For the purpose, the following values are taken: $F_x/fP = 0.35$, $F_y/fP = 0.35$ and $M_z/fPa = 0.15$. The three creepages ξ_x, ξ_y and φ hold.

The results of the simulation are presented in Fig. 5.16. The dimensionless norm of the shear vector is plotted in the contact zone at different time steps corresponding to covered distances a) $V_t/a = 0$; b) $V_t/a = 0.14$; c) $V_t/a = 0.35$; d) $V_t/a = 0.70$; e) $V_t/a = 1.40$ and f) $V_t/a = 2.81$. To exemplify this general case in the context

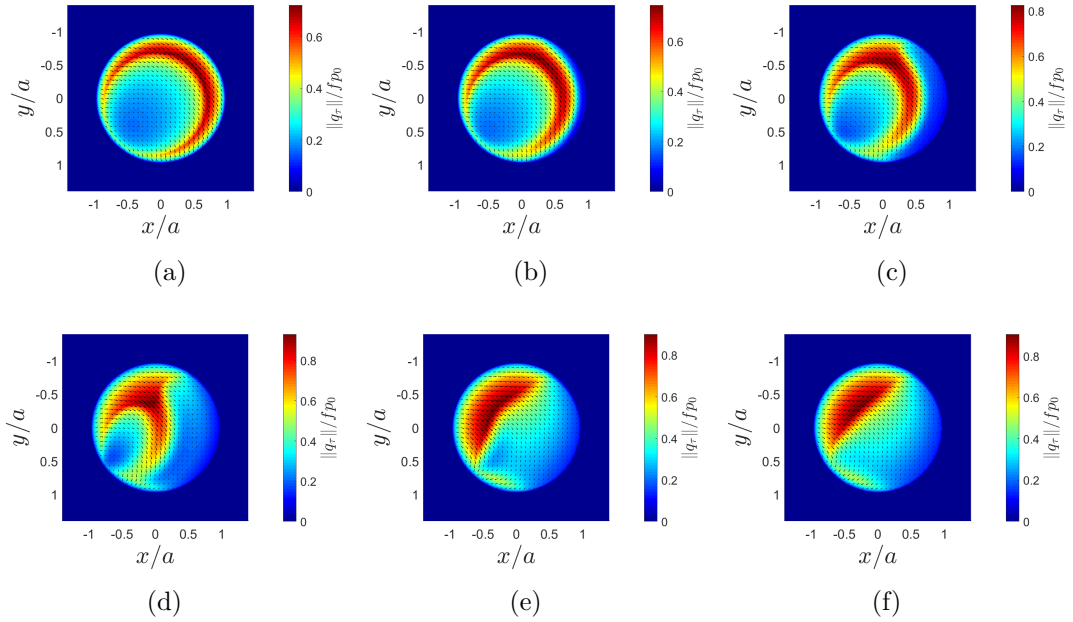

Figure 5.16: Two dimensional view of the dimensionless norm of the shear vector q_τ in the contact surface for a covered distance a) $V_t/a = 0$; b) $V_t/a = 0.14$; c) $V_t/a = 0.35$; d) $V_t/a = 0.70$; e) $V_t/a = 1.40$ and f) $V_t/a = 2.81$; for the contact between quasi-identical bodies ($\beta = 0$) and an applied longitudinal tractive force $F_x/fP = 0.35$, a transversal tractive force $F_y/fP = 0.35$ and a spinning moment $M_z/fPa = 0.15$.

of tire-pavement contact, consider an acceleration in turnaround. The acceleration force represents the longitudinal tractive force; the centrifugal force related is the transversal force and the turning motion imposed to the wheels is the moment.

In summary, various combinations of the input in terms of tractive force applied have been analysed. In function of the forces involved, corresponding local creepages appear. This parametric study has been done by considering that the bodies in contact are elastically similar. Since the present study regards the tire-pavement contact (tire and pavement are made of clearly different materials), it is interesting now to investigate what happens for elastically dissimilar bodies.

5.5.2 Solutions for elastically dissimilar bodies

In the previous section, the complete analysis of the transient tractive rolling has been performed for elastically similar bodies. For those cases where the bodies are the same, the response is the same for each body since they react to the same forces. When the Dundurs' parameter is not nil, the deformations are no more the same at the contact surface. The dissimilarity is supposed to induce additional slip zones because of the difference of elastic displacements under the same forces. In what follows next, the analysis of the transient tractive rolling is performed for all the loading configurations as in the previous section by only changing the materials of the bodies in contact. For the purpose, the rolling body 1 becomes rigid: $E_1 = 10E20MPa$ and $\nu_1 = 0.5$. The body 2 has the elastic properties: $E_2 = 2560000MPa$ and $\nu_2 = 0.28$. This configuration gives a Dundurs' parameter $\beta = -0.3056$.

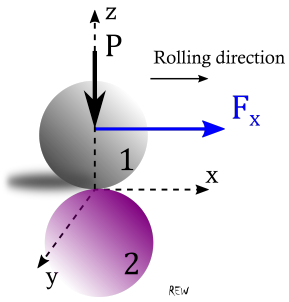

5.5.2.1 Pure longitudinal tractive force

The contact between the dissimilar bodies where $\beta = -0.3056$ is simulated under an applied longitudinal tractive force only: $F_x/fP = 0.657$ while $F_y/fP = 0$ and $M_z/fPa = 0$. In the case of a pure longitudinal tractive force applied, only the creepage ξ_x appears.
Note that the discretisation for both space and time domains remain the same as for elastically similar case.
Figure 5.17 shows the norm of the shear vector in the contact zone for a covered distance a) $V_t/a = 0$; b) $V_t/a = 0.14$; c) $V_t/a = 0.35$; d) $V_t/a = 0.70$; e) $V_t/a = 1.40$ and f) $V_t/a = 2.81$.

For $V_t/a = 0$, the results corresponds to the case of Cattaneo-Mindlin case but for elastically dissimilar bodies. The asymmetry of the shear distribution at the surface is due to that dissimilarity which induces unequal displacements for two particles facing each other. Throughout the steps, the adhesion and the slip zones evolve to reach the steady-state regime where the adhesion zone is near the leading edge and the slip zone behind at the trailing edge of the rolling.

When the profile of only the shear q_x/p_0 is plotted along the axis x in the plane $y = 0$, Fig. 5.18 is obtained. One can observe that it can take negative values particularly in the adhesion zone. This result joins in a way the results of Nowell and Hills for dissimilar finite cylinders in section 5.4.

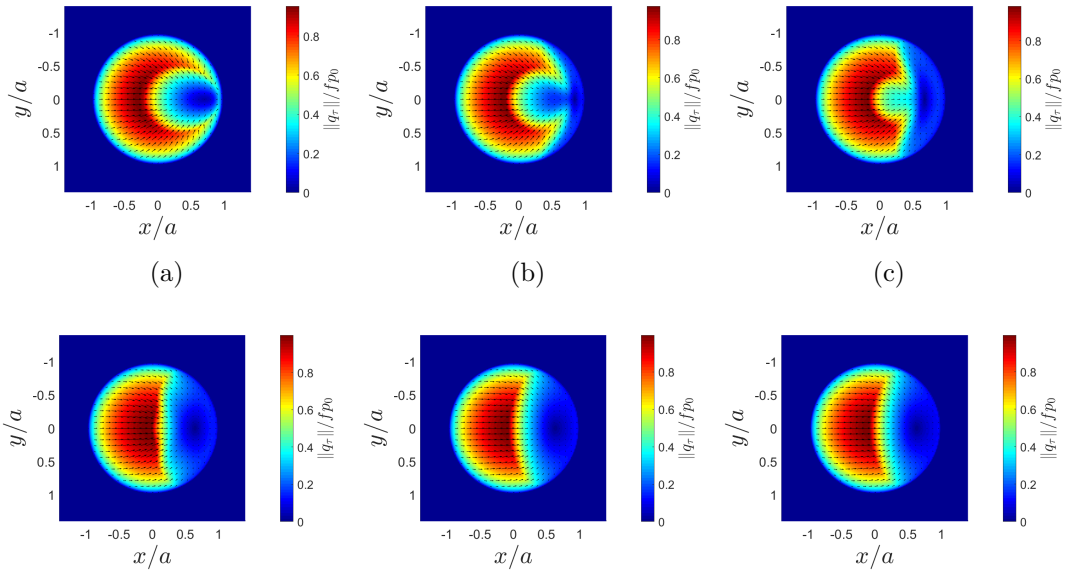

Figure 5.17: Two dimensional view of the dimensionless norm of the shear vector q_τ in the contact surface for a covered distance a) $V_t/a = 0$; b) $V_t/a = 0.14$; c) $V_t/a = 0.35$; d) $V_t/a = 0.70$; e) $V_t/a = 1.40$ and f) $V_t/a = 2.81$; for the contact between dissimilar bodies ($\beta = -0.3056$) and an applied pure longitudinal tractive force $F_x/fP = 0.657$.

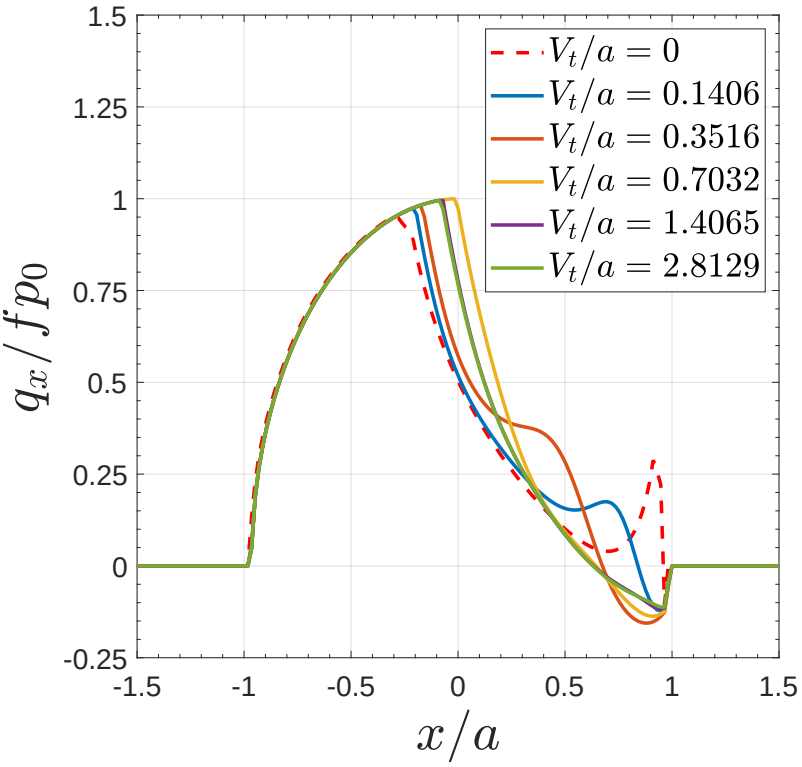
1.5
1.25
1
0.75
0.5
0.25
0
-0.25
-1.5
-1
-0.5
0
0.5
1
1.5
$q_x / f p_0$
x/a
$V_t/a = 0$
$V_t/a = 0.1406$
$V_t/a = 0.3516$
$V_t/a = 0.7032$
$V_t/a = 1.4065$
$V_t/a = 2.8129$

Figure 5.18:

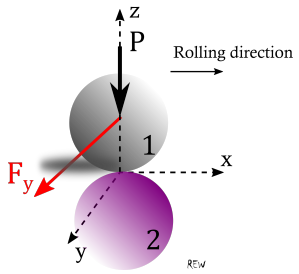

5.5.2.2 Pure transversal tractive force

Here the loading is only the transversal tractive force $F_y/fP = 0.657$ while $F_x = 0$ and $M_z = 0$. In this case, creepages ξ_y and φ appear as explained for the elastically similar case (see section 5.5.1.2).
Figure 5.19 shows the two dimensional norm of the shear vector in the contact zone for a covered distance a) $V_t/a = 0$; b) $V_t/a = 0.14$; c) $V_t/a = 0.35$; d) $V_t/a = 0.70$; e) $V_t/a = 1.40$ and f) $V_t/a = 2.81$.

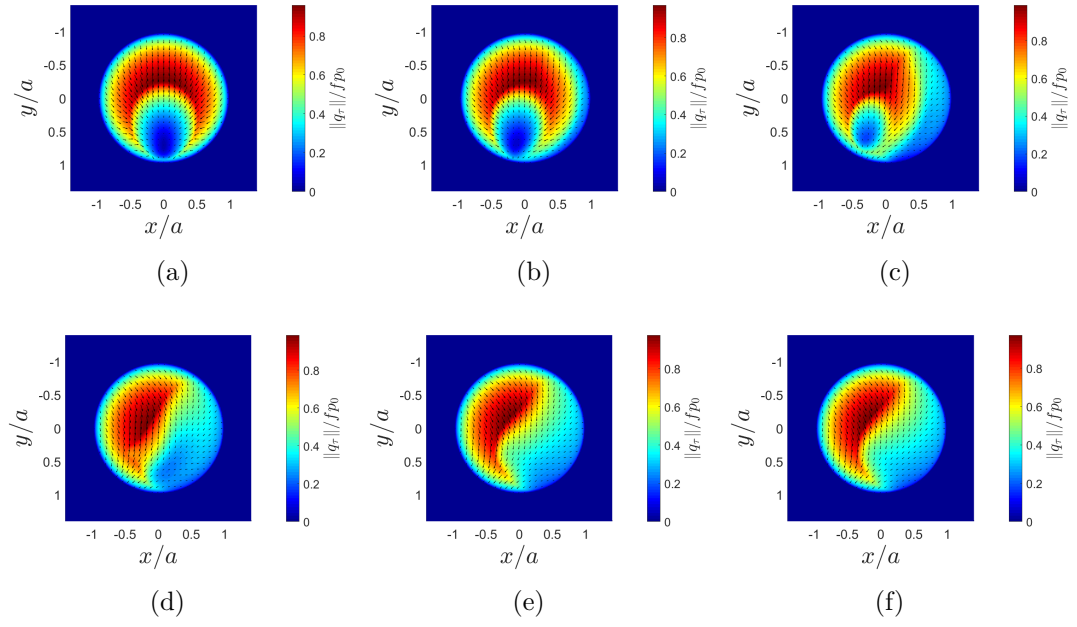

Figure 5.19: Two dimensional view of the dimensionless norm of the shear vector q_τ in the contact surface for a covered distance a) $V_t/a = 0$; b) $V_t/a = 0.14$; c) $V_t/a = 0.35$; d) $V_t/a = 0.70$; e) $V_t/a = 1.40$ and f) $V_t/a = 2.81$; for the contact between dissimilar bodies ($\beta = -0.3056$) and an applied pure transversal tractive force $F_y/fP = 0.657$.

One can observe the orientation of the streamlines of the shear in the transversal direction for the first step. Unlike for elastically similar bodies, it seems that the effect of the spin creepage is higher. It would be the reason why in steady-state regime, the shear is not symmetric with respect to the x axis as in the case of

elastically similar bodies.

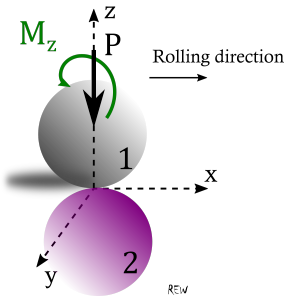

5.5.2.3 Pure spinning moment

Only a spinning moment around the normal z axis is applied: $M_z/fPa = 0.3$, $F_x = 0$ and $F_y = 0$. In the same way as for the pure transversal tractive force applied, applying only a spinning moment gives rise to the creepages ξ_y and φ. Figure 5.20 shows the two dimensional norm of the shear vector in the contact zone for a covered distance a) $V_t/a = 0$; b) $V_t/a = 0.14$; c) $V_t/a = 0.35$; d) $V_t/a = 0.70$; e) $V_t/a = 1.40$ and f) $V_t/a = 2.81$.

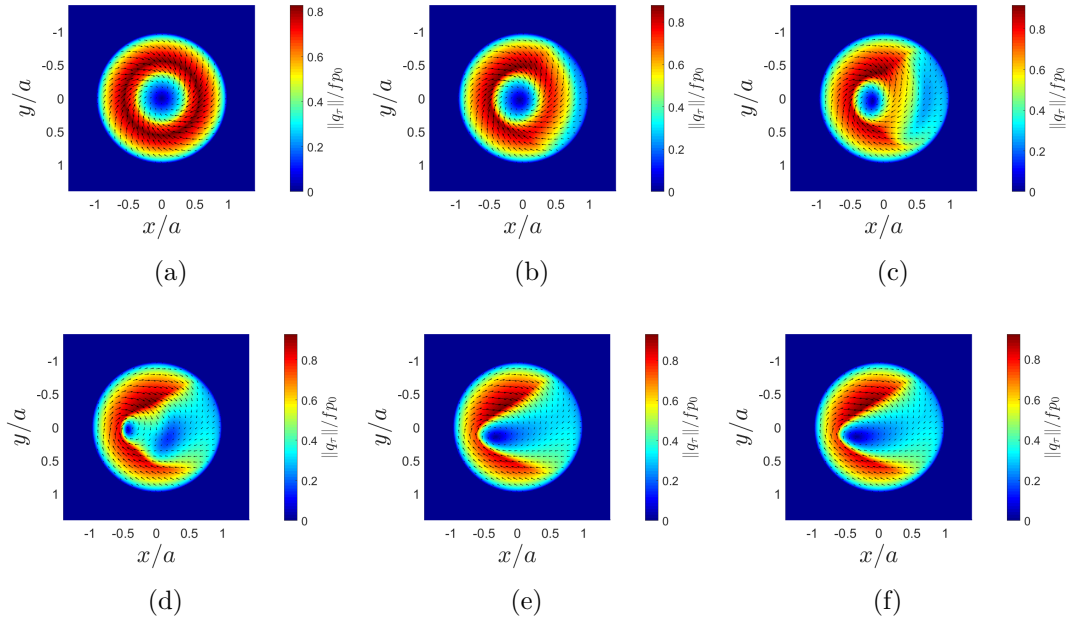

Figure 5.20: Two dimensional view of the dimensionless norm of the shear vector q_τ in the contact surface for a covered distance a) $V_t/a = 0$; b) $V_t/a = 0.14$; c) $V_t/a = 0.35$; d) $V_t/a = 0.70$; e) $V_t/a = 1.40$ and f) $V_t/a = 2.81$; for the contact between dissimilar bodies ($\beta = -0.3056$) and an applied pure spinning moment $M_z/fPa = 0.3$.

The results for this case of loading show the same behaviour as for the case of

elastically similar bodies. However, in steady-state regime, a slight asymmetry of the profile is observed with respect to the x axis. Note that for the same value of loading, the shears are higher in these case than in the cases of elastically similar bodies in section 5.5.1.

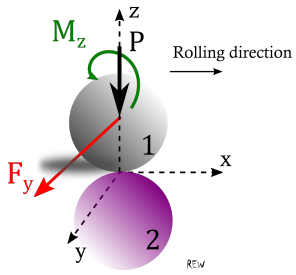

5.5.2.4 Transversal force + Spinning moment

Here a transversal tractive force and a spinning moment are applied simultaneously. It implies a transversal creepage and spin creepage. Thus the overall behaviour is expected to be similar to the pure transversal tractive force case (see 5.5.1.2) but for different levels of impact on the creepages involved. The loading is: $F_x = 0$, $F_y/fP = 0.657$ and $M_z/fPa = 0.15$.
Then, the results in term of contact shear are presented in Fig. 5.24 where one can see the two dimensional view of the norm of the shear vector in the contact zone for a covered distance a) $V_t/a = 0$; b) $V_t/a = 0.14$; c) $V_t/a = 0.35$; d) $V_t/a = 0.70$; e) $V_t/a = 1.40$ and f) $V_t/a = 2.81$. As expected, the behaviour in the contact is very close the one for an applied transversal tractive force.

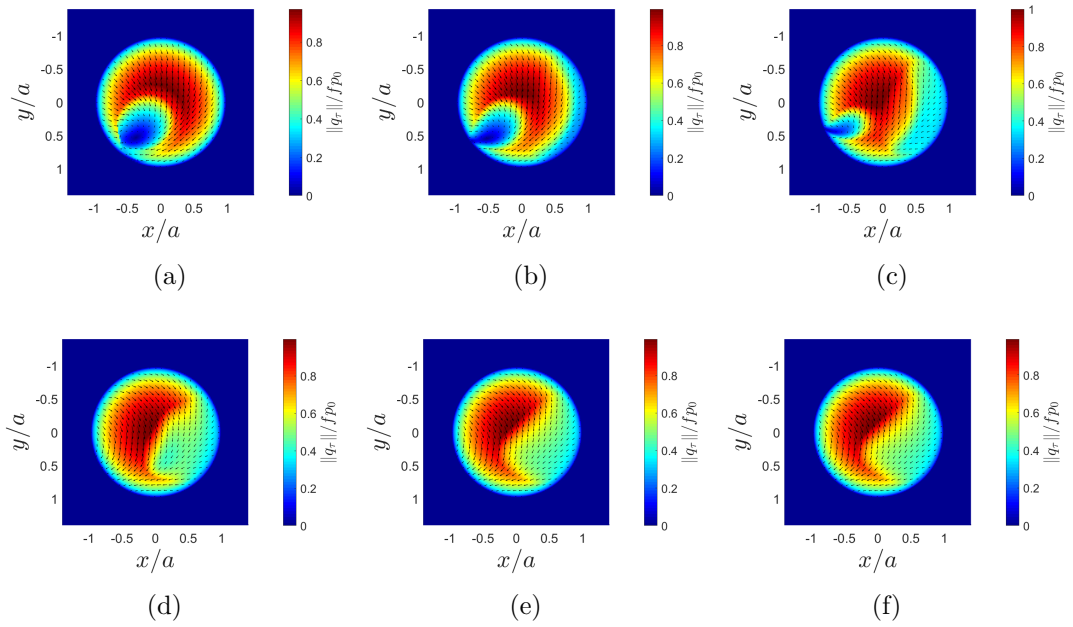

Figure 5.21: Two dimensional view of the dimensionless norm of the shear vector q_τ in the contact surface at time steps for a covered distance a) $V_t/a = 0$; b) $V_t/a = 0.14$; c) $V_t/a = 0.35$; d) $V_t/a = 0.70$; e) $V_t/a = 1.40$ and f) $V_t/a = 2.81$; for the contact between dissimilar bodies ($\beta = -0.3056$) and an applied transversal tractive force $F_y/fP = 0.657$ and a spinning moment $M_z/fPa = 0.15$.

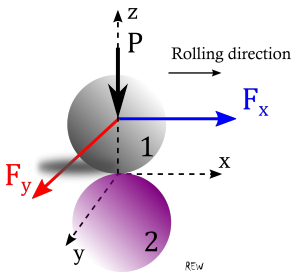

5.5.2.5 Longitudinal + Transversal tractive forces

The configuration is the combination of the longitudinal tractive force and the transversal one, while the spinning moment goes to zero. The values are: $F_x/fP = 0.35$, $F_y/fP = 0.35$ and $M_z/fPa = 0$. In this framework, all the creepages are expected to be present.

The results of the simulation are shown in Fig. 5.22 where the two-dimensional view of the dimensionless norm of the shear vector is plotted for a covered distance a) $V_t/a = 0$; b) $V_t/a = 0.14$; c) $V_t/a = 0.35$; d) $V_t/a = 0.70$; e) $V_t/a = 1.40$ and f) $V_t/a = 2.81$.

The first step corresponds to the Cattaneo-Mindlin shift for elastically dissimilar bodies. Unlike the case of elastically similar bodies, the shear is asymmetric.

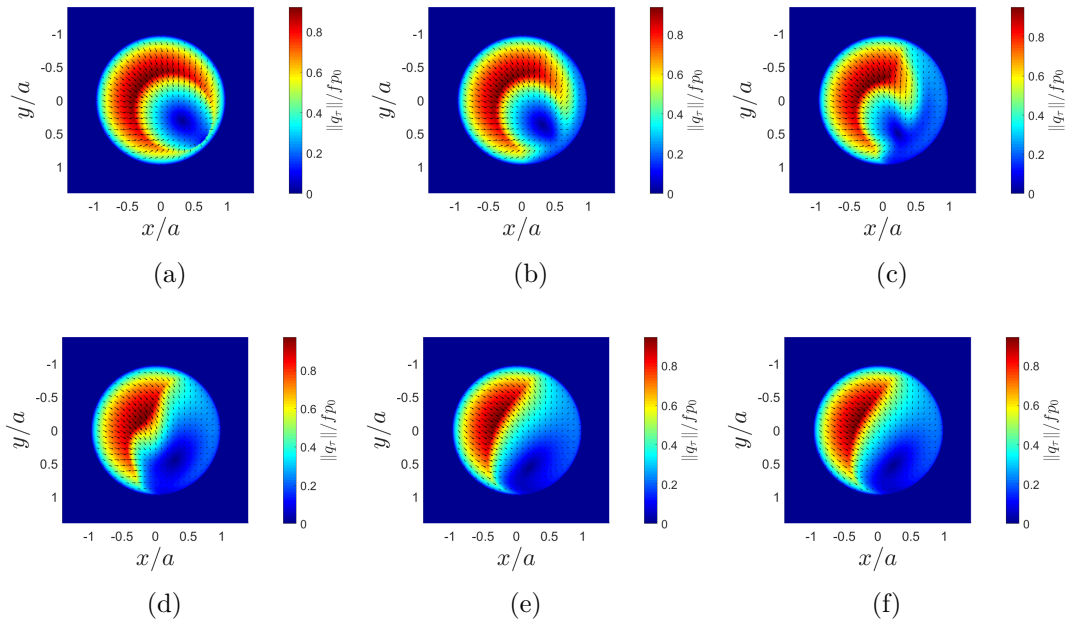

Figure 5.22: Two dimensional view of the dimensionless norm of the shear vector q_τ in the contact surface at time steps for a covered distance a) $V_t/a = 0$; b) $V_t/a = 0.14$; c) $V_t/a = 0.35$; d) $V_t/a = 0.70$; e) $V_t/a = 1.40$ and f) $V_t/a = 2.81$; for the contact between dissimilar bodies ($\beta = -0.3056$) and an applied longitudinal tractive force $F_x/fP = 0.35$ and a transversal tractive force $F_y/fP = 0.35$.

Moreover, one can observe that at the first step, the behaviours seems to be a result of the cases of pure longitudinal and pure transversal tractive forces applied. While moving, the adhesion zone takes place at the leading edge but not in the middle axis. It is interesting to remark that the point, where the adhesion is stronger, is clearly located off-center.

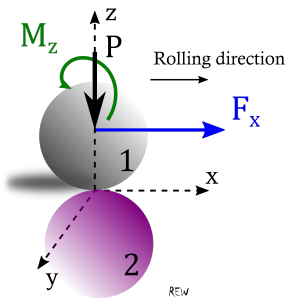

5.5.2.6 Longitudinal force + Spinning moment

Here the loading consists of a longitudinal tractive force and a spinning moment: $F_x/fP = 0.35$, $F_y/fP = 0$ and $M_z/fPa = 0.15$. As in the previous case, all the three creepages are expected.

The results of the simulation are displayed in Fig. 5.23. As previously the dimensionless norm of the shear vector is plotted at different time steps corresponding to a covered distance a) $V_t/a = 0$; b) $V_t/a = 0.14$; c) $V_t/a = 0.35$; d) $V_t/a = 0.70$; e) $V_t/a = 1.40$ and f) $V_t/a = 2.81$

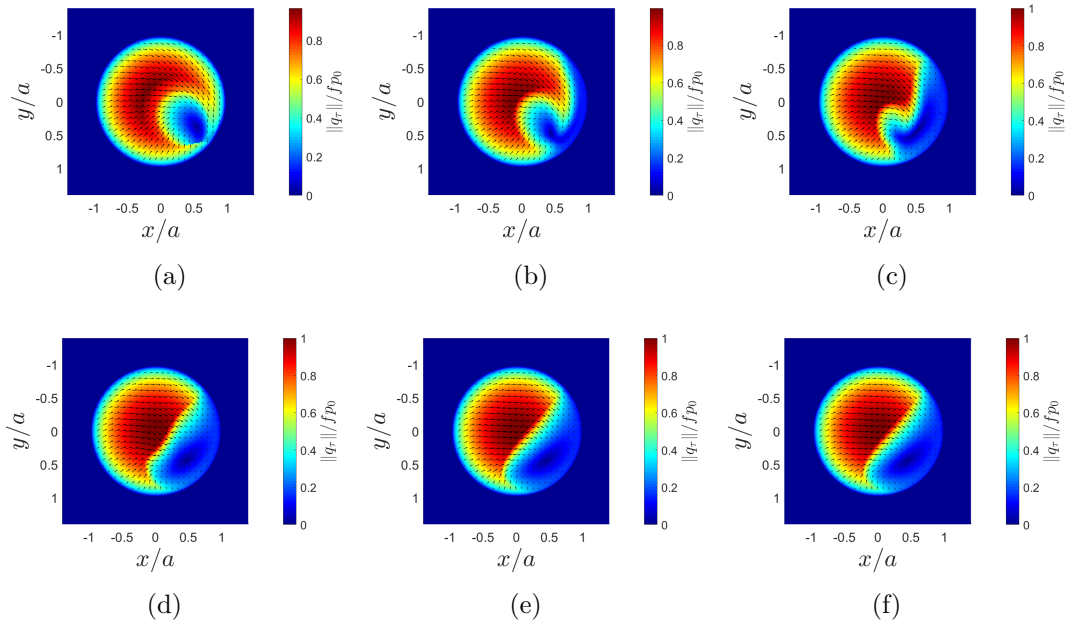

Figure 5.23: Two dimensional view of the dimensionless norm of the shear vector q_τ in the contact surface for a covered distance a) $V_t/a = 0$; b) $V_t/a = 0.14$; c) $V_t/a = 0.35$; d) $V_t/a = 0.70$; e) $V_t/a = 1.40$ and f) $V_t/a = 2.81$; for the contact between dissimilar bodies ($\beta = -0.3056$) and an applied longitudinal tractive force $F_x/fP = 0.657$ and a spinning moment $M_z/fPa = 0.15$.

One can observe that these results seem to be a rotation of the results of the case of a pure longitudinal tractive force applied. Adding the spinning moment may then be considered as rotating the shear field around the z axis. It is the effect of the spin creepage.

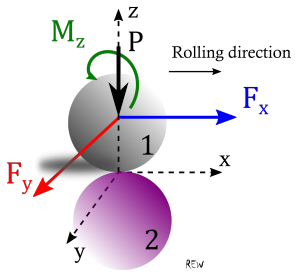

5.5.2.7 General case

Finally, the general case, where all the input loads take non zero values, is studied. For the purpose, the following values are taken: $F_x/fP = 0.35$, $F_y/fP = 0.35$ and $M_z/fPa = 0.15$. The three creepages ξ_x, ξ_y and φ appear.
The results of the simulation are presented in Fig. 5.24. The dimensionless norm of the shear vector is plotted in the contact zone at different time steps corresponding to covered distances a) $V_t/a = 0$; b) $V_t/a = 0.14$; c) $V_t/a = 0.35$; d) $V_t/a = 0.70$; e) $V_t/a = 1.40$ and f) $V_t/a = 2.81$.

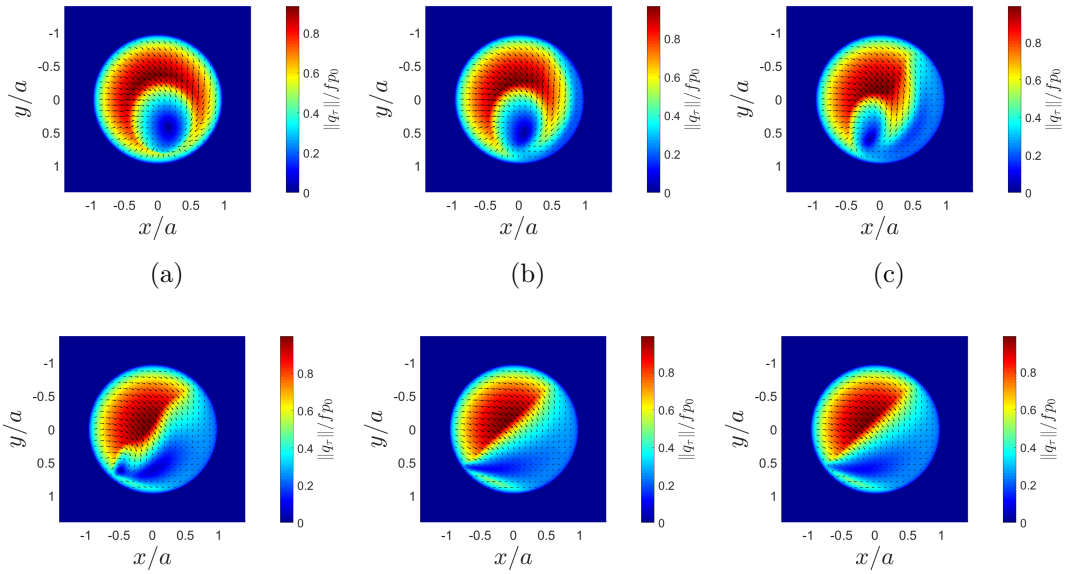

Figure 5.24: Two dimensional view of the dimensionless norm of the shear vector q_τ in the contact surface for a covered distance a) $V_t/a = 0$; b) $V_t/a = 0.14$; c) $V_t/a = 0.35$; d) $V_t/a = 0.70$; e) $V_t/a = 1.40$ and f) $V_t/a = 2.81$; for the contact between dissimilar bodies ($\beta = -0.3056$) and an applied longitudinal tractive force $F_x/fP = 0.35$, a transversal tractive force $F_y/fP = 0.35$ and a spinning moment $M_z/fPa = 0.15$.

The general behaviour of this case resembles the one of the general case for elastically similar bodies. The shears are higher due to the dissimilarity.

5.5.3 Three-dimensional stresses: Elastic Tractive rolling on a Multi-layered half-space

Once the contact field i.e. pressure and shear fields are found, the calculation of the three-dimensional quantities can be performed. The contact field is used as source to be convoluted with the influence coefficients corresponding to the wanted 3D stresses and displacements.

For illustration, several simulations have been performed on a multi-layered half-space. The multi-layered formulation of chapter 4 is used. In the calculations, the elastic moduli of the layers are set in four configurations:

- The "Homogeneous modulus"
- The "Alternate Modulus"
- The "Increasing Modulus"
- The "Decreasing Modulus"

For the calculations, a circular contact is considered between a sphere and a flat surface. The sphere takes a very high elastic modulus so that it can be viewed as a rigid body; and the elastic modulus of the multi-layered half-space is given above. The loading is the one of a general case: $F_x/fP = 0.35$, $F_y/fP = 0.35$ and $M_z/fPa = 0.15$.
The discretisation is performed with hexahedral elements of size $0.02a \times 0.02a \times 0.05a$. The dimensionless second invariant J_2/p_0 is plotted in Fig. 5.25 at different time steps corresponding to a covered distance $V_t/a = 0$; $V_t/a = 0.5$; $V_t/a = 1.$; $V_t/a = 4.$ and in the middle plane $y = 0$.

At the surface of the contact what happens is similar to the general case of loading between dissimilar materials (see section 5.5.2.7). From those previous observations, it comes that the asymmetry of the shear field induces an asymmetry of the stresses. In Fig. 5.25, only the qualitative trends of what happens in the various configurations of variation of modulus in the half-space is commented. It comes that for all the cases, the higher stress is close to the surface. This is a very interesting remark in the context of tire/pavement contact, for the explanation of the surface degradations. Further, when the steady-state regime is achieved, the higher stresses are located close the trailing zone of the contact.
For the alternate modulus, one can observe that the stress takes higher value at every interface due to the jump of modulus. The other cases (homogeneous modulus, increasing modulus and decreasing modulus) show a more homogeneous distribution of the stress. The increasing modulus case shows an increase of stress at the last interface due to the significant jump of the modulus there.

Note that for a quantitative analysis, it would have been more relevant to plot the stresses in a plane tilted with respect to the chosen plane $y = 0$. The angle of the rotation is to be found by well regarding the contact shear distribution so that it allows to observe the maximum stress needed in the case a of dimensioning.

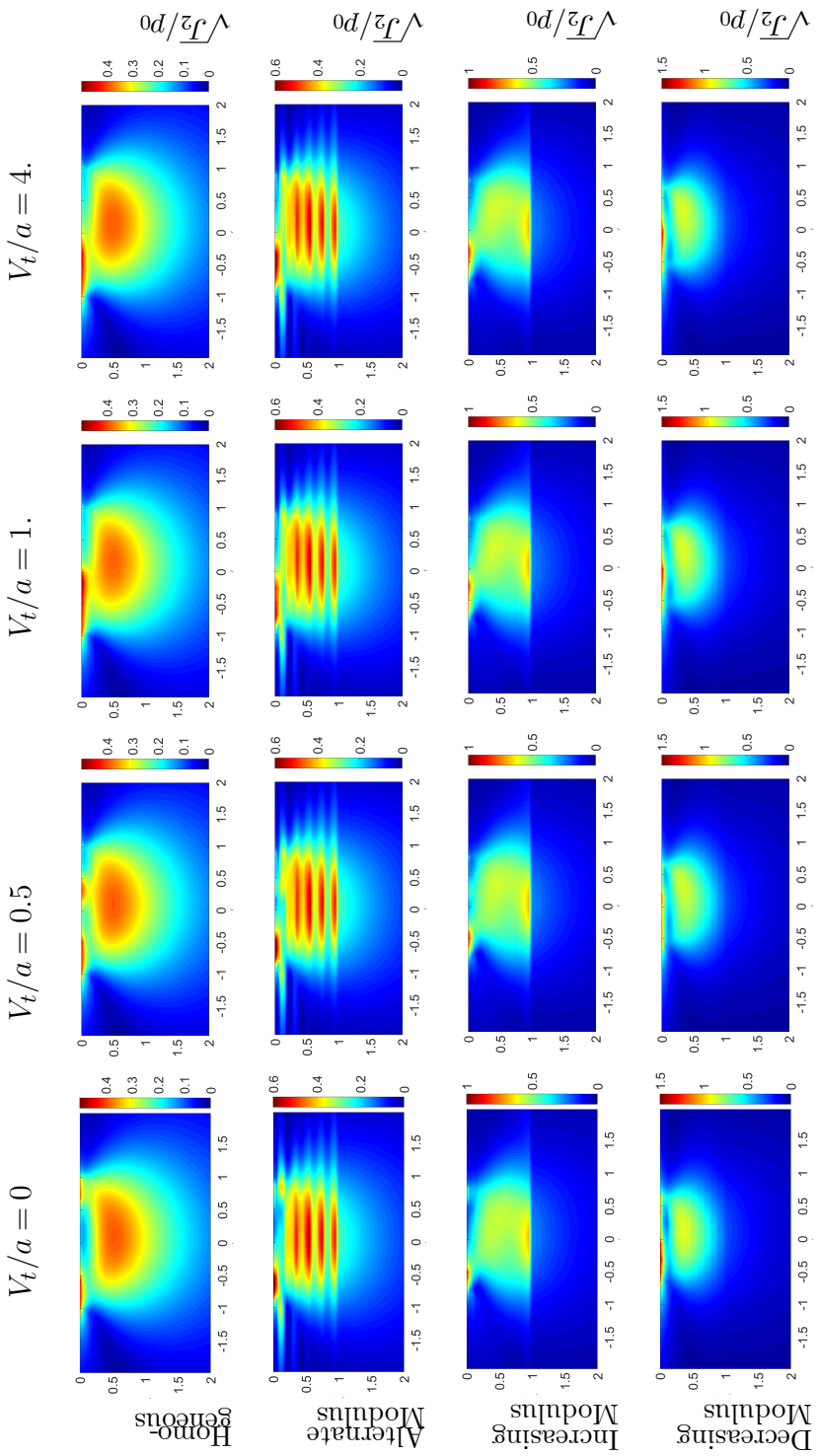

Figure 5.25: The dimensionless second invariant J_2/p_0 in the middle plane $y = 0$ at different time steps corresponding to a covered distance $V_t/a = 0$; $V_t/a = 0.5$; $V_t/a = 1.$; $V_t/a = 4.$ for different configurations of variation of elastic modulus in a multi-layered half-space.

5.6 Conclusion

In this chapter, the tractive rolling contact has been studied. Drawn from the theory of Kalker, the problem has been formulated first with the definition of the slip during a rolling motion. Then an algorithm for solving the variational formulation that yields has been proposed. A highlight of the algorithm is the imposition of an elementary covered at every time step so that the transient aspect of the problem can be solved. Moreover, the model takes as input the tangential tractive forces in the two directions in the tangent plane and a spinning moment around the normal direction.
The proposed model has been validated by comparison with the previous algorithms of Manyo [MAN 19b] and Kalker [KAL 90] for the contact between elastically similar bodies. Further, it has been compared to the plane strain model of Nowell and Hills [NOW 88] for the tractive rolling contact between elastically dissimilar bodies. After the validation of the model a parametric study has been performed. Various combinations of the tractive forces have been analysed for the contact between elastically similar bodies in one hand, and between elastically dissimilar bodies in the other hand. Finally, a brief analysis of the tractive rolling contact in a general case has been done on different multi-layered half-spaces.

The takeaways of this chapter in term of results can be summarised in the following forms:

- Applying longitudinal tractive force implies the apparition of the local longitudinal creepages
- Applying a transversal tractive force or a spinning moment, implies the apparition of both the local transversal creepage and the local spin creepage
- When the bodies are elastically dissimilar, the shears are higher for the same applied force compared to when the bodies are elastically similar
- The effect of tractive rolling contact is very significant on the Von Mises stress, especially in a zone close to the surface.

The two last remarks are interesting for the pavement field where we need to understand the origin of the degradations close to the surface.

Chapter 6

Elastic Fretting Contact on Multi-layered half-space

The fretting problem is tackled for multi-layered bodies. Using the present semi-analytical model coupled with the influence coefficients for the multi-layered half-space, the Cattaneo and the Spence shifts are analysed. A fretting loop is also simulated for the analysis of the contact field as well as the stresses in the subsurface.

Sommaire

6.1 Introduction

The general contact problem is a coupled normal - tangential problem. The normal problem has been extensively discussed earlier in this document and in the literature for various kind of loadings, geometries, materials, etc. So has it been for the tangential problem under two main conditions: the *partial slip* and the *full slip*.

While in the full slip conditions the whole contact zone is sliding, the partial slip conditions consider that the contact is in equilibrium from a general point of view. Using the Coulomb's law for friction, it means that the overall applied tangential force is less than the normal force times the friction coefficient. In these conditions, the general contact is in equilibrium but in the contact zone some points are undergoing a local slip. The partial slip is what happens for example in the tractive rolling contact studied in the previous chapter.

In this chapter, a problem where the partial slip and the full slip can occur is studied: the *fretting contact*. The fretting contact is characterised by an oscillating loading. A body submitted to small oscillating tangential displacements, is the typical example of fretting contact. In this fretting contact, in function of the loading and the material, one can even observe a transition from partial slip conditions to full slip [KOU 15a].

Fretting is generally studied under three different modes as presented in Fig.6.1: mode I, mode II and mode III.

- Mode I: In this mode, the bodies are in contact under a constant normal load. Then, a small oscillating tangential load is imposed. The contact shear vector induced, show a transversal orientation of the subsequent slip.

- Mode II: Here, an oscillating normal load is applied. As said previously, when friction is considered at the contact interface, a normal load induces tangential shears. In this respect, shear is generated in the contact zone and a radial slip is observed.

- Mode III: In this mode, a constant normal load is maintained during the contact. The oscillating loading here is a moment around the normal direction. It gives rise to a circumferential slip in the contact zone.

For examples of works on the fretting contact within the literature, the reader is referred to the following works [GAL 06, GAL 10b, WAN 15, NOW 98, DIN 04, WAN 11b, KES 16, GAL 07a, GAL 10a, SPI 20, SPI 15]. The fretting contact has been studied earlier by Wang et al. for layered bodies [WAN 11b] and for multi-layered and functionally graded materials [WAN 15].

The goal in this part of the work is to reproduce the fretting contact on a multi-layered half-space. In the following lines, the formulation is recalled briefly. Then, several results are presented on a single layered half-space and on a multi-layered half-space. The Spence and the Cattaneo-Mindlin problems are also simulated for

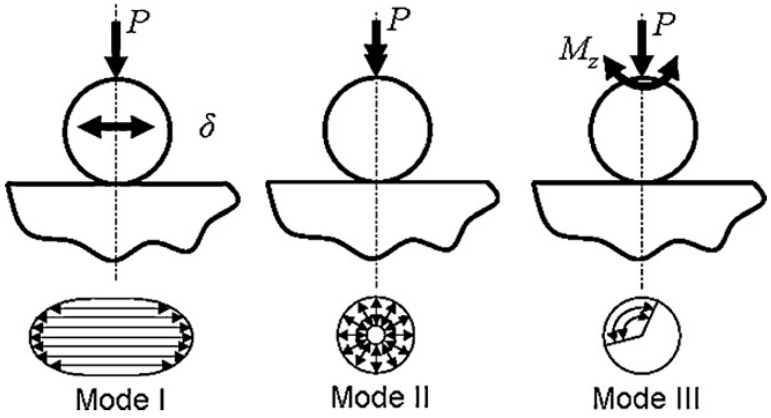

Figure 6.1: The three different fretting modes depending on the forces and moments in transmitted through the contact. Slip are transversal in mode I; slips are radial in fretting mode II, slips are circumferential in fretting mode III. [GAL 10b]

those half-spaces. Finally, a single loop of fretting in mode I is studied in order to highlight the evolution of the slip in those cases.

6.2 Formulation

The formulation used in this chapter is the same as the one of chapter 2. The main points are recalled.
Consider a non conforming contact between two bodies submitted to both normal and tangential loads. The resulting contact gives rise to pressure field $p(x,y)$ and shear fields $q_x(x,y)$ and $q_y(x,y)$. The bodies are modelled under the half-space assumption which means that at the infinity the elastic field vanishes, and that the contact size is small compared to the size of the bodies in contact. The initial separation between the bodies is defined by the profile of the surfaces of the bodies. The surfaces can be of any type in a discretised form. Moreover, the small strain assumption is considered. Then, the general contact problem consists of a normal contact problem and a tangential contact problem.

The normal contact problem The normal contact problem is the contact problem considering an applied normal force or an applied normal displacement. To solve this problem, the actual gap is used. It is classically defined as:

$$g(x,y) = \bar{u}_z^p(x,y) + h^*(x,y) \tag{6.1}$$

where the term $h^*(x,y)$ is the sum of the initial gap -function of the surface profiles-, the rigid normal body displacement and the elastic displacements due to the contact shears. $\bar{u}_z^p$ is the elastic displacement at the surface due to the pressure field p. From the definition of the gap, the contact is activated in a point (x,y) and added to the contact zone Γ_c when $g(x,y) = 0$, where the pressure is always positive $p(x,y) > 0$. Outside of the contact zone, the gap is strictly positive $g(x,y) > 0$ and the pressure field goes to zero $p(x,y) = 0$.

The tangential contact problem The tangential contact problem is to be considered when there is friction between the surfaces. In that case, shear tractions appear in the contact zone even for no tangential global force applied [SPE 75]. In term of kinematics, the moving contact between bodies is formulated through the definition of the slip in the contact zone. The definition of the slip is well exposed by Kalker for the rolling contact (see chapter 5). It comes that, for two particles in contact, located at the positions $\mathbf{x_1}$ and $\mathbf{x_2}$ respectively for body 1 and 2, the slip velocity can be written as:

$$\dot{s}_i = (\dot{x}_{1i} - \dot{x}_{2i}) + \frac{1}{2}(\dot{x}_{1j} + \dot{x}_{2j})(\bar{u}_{1i,j} - \bar{u}_{2i,j}) + \partial(\bar{u}_{1i} - \bar{u}_{2i})/\partial t, \tag{6.2}$$

where the dot $\dot{}$ represents the derivative with respect to time; the bar is for the displacements at the contact surface.
Thus, one can identify two particular motions: the *shift* and the *rolling motion*. When the velocity of the contact zone is much greater than the velocity of the

particles in the contact, it is the *rolling motion*. Otherwise, when the velocity particles is comparable to the velocity of the contact zone, it is a *shift motion*. In the present chapter, the interest is put on the shift motion where the term $\frac{1}{2}(\dot{x}_{1j}+\dot{x}_{2j})(\bar{u}_{1i,j}-\bar{u}_{2i,j})$ may be neglected with respect to $(\dot{x}_{1i}-\dot{x}_{2i})$. Thus the slip velocity can be defined as:

$$\dot{s}_i = (\dot{x}_{1i}-\dot{x}_{2i})+\partial(\bar{u}_{1i}-\bar{u}_{2i})/\partial t. \tag{6.3}$$

The term $(\dot{x}_{1i}-\dot{x}_{2i})$ embodies the contribution of the rigid body displacements δ_x, δ_y and ϕ_z. With some developments the slip vector is found as:

$$\dot{s}_i = \begin{pmatrix} \Delta\bar{u}_x - \Delta\delta_x + y.\Delta\phi_z \\ \Delta\bar{u}_y - \Delta\delta_y - x.\Delta\phi_z \end{pmatrix} \tag{6.4}$$

where $\Delta\bar{u}_i$ is the variation of surface tangential displacement, $\Delta\delta_i$ and $\Delta\phi_z$ the variation of the rigid body displacements (2 translations and one rotation).

In theory, the general contact problem has to be solved in a single procedure for the normal and tangential parts so that the coupling effects are kept. Because this would be tedious, a modified procedure of Panagiotopoulos process is used to solve successively the problems. In this spirit, at every step the normal problem is solved by taking into account the effect of the contact shears from the previously solved tangential problem. Then the tangential problem is solved by taking into account the effect of the previous contact pressure. Then, we iterate between the normal and the tangential problems until convergence.

The above formulations are a summary of the formulation described in chapter 2 where the reader may find the detailed general formulation and algorithms for solving the contact problem.

Note that in the definition of the contact, the elastic displacements are found by using the influence coefficients. The are used in this work to link the applied pressure and shears to the corresponding elastic field induced. The influence coefficients for multi-layered half-space will be used.

Influence Coefficients for a multi-layered half-space The influence coefficients for a layered half-space are found using the Papkovich-Neuber potential to formulate the elastic field. Then, an integral transform allows to linearise the equations and apply the boundary conditions. Finally, the solutions are found in a frequency domain and a numerical inverse transform is applied.
A method inspired by the works of Yu et al. [YU 14] has been used earlier in chapter 4.

Using the numerical tools and the developed algorithms, the fretting contact can be simulated between both elastic and viscoelastic multi-layered bodies. Here are presented some results for only elastic bodies.

6.3 Results: Single layered half-space

The parametric study is performed in two parts:

- ❖ Results are presented for a single layer on a half-space. The contact, as well as the interface between the coating and the substrate are analysed. Three cases of tangential shifts are considered:
  - → The Spence shift: Only a normal force is applied.
  - → The Cattaneo-Mindlin shift: A normal and a tangential loads are applied simultaneously in such a way that the system is in equilibrium from an overall point of view.
  - → A loop of fretting in mode I is simulated.
- ❖ Results are presented for a multi-layered half-space with 10 layers. A loop of fretting in mode I for an applied tangential force is studied for *Alternate modulus*, *Decreasing modulus* and *Increasing modulus*. The 3D stresses are analysed in this case.

6.3.1 Framework

For the analysis, consider an elastic sphere of radius $R = 10$ mm in contact with a plane. The sphere has the elastic properties defined with a Young modulus E_1 and a Poisson's ratio ν_1 while the second body has the elastic properties (E_s, ν_s) and (E_c, ν_c) for substrate and coating respectively. The coating has a thickness h. A Coulomb's friction coefficient f is considered at the contact interface.
A force $P = 200$ N is applied and the following parameters are found using the theory of Hertz:

$$a = \left(\frac{3PR}{4E^*}\right)^{1/3}, \tag{6.5a}$$

$$p_0 = \left(\frac{6PE^{*2}}{\pi^3 R^2}\right)^{1/3}, \tag{6.5b}$$

where $E^* = \frac{1-\nu_1^2}{E_1} + \frac{1-\nu_s^2}{E_s}$ is the equivalent Young modulus. a is the contact radius and p_0 is the maximum pressure.

The first simulation is the Spence shift which takes as input only a normal load. Then the general contact problem is solved and a shear field is found at the contact surface in addition to the pressure field.

6.3.2 The Spence shift

Consider two elastic bodies defined by the elastic properties (E_1, ν_1) and (E_2, ν_2), the Dundurs' parameter β [1] is introduced to described the level of similarity of the

[1] $\beta = \frac{1}{2}\left[\frac{(1-2\nu_1)/G_1 - (1-2\nu_2)/G_2}{(1-\nu_1)/G_1 + (1-\nu_2)/G_2}\right]$

bodies. The bodies are elastically similar when $\beta = 0$.
In the case of elastically similar bodies in contact under only a normal load, there is no shear in the contact surface. On contrary, when the bodies are dissimilar, applying only a normal force, in presence of friction, induces shear tractions at the contact surface (see Fig. 6.2). Spence [SPE 75] has been the first to treat the question.
In this section, the purpose is to extend the Spence shift to the case of a single layered half-space. To this end, the set up considers a friction coefficient $f = 0.1$ at the contact interface. As reference, the contact of Hertz is solved for the elastic properties given in Tab. 6.1.

Body 1		Body 2			
-		Substrate		Coating	
E_1[MPa]	ν_1	E_s[MPa]	ν_s	E_c[MPa]	ν_c
10E20	0.285	114600	0.285	-	-

Table 6.1: General elastic properties of the bodies in the contact studied in section 6.3.2.

To compute the elastic Spence shift, a normal load ramp is imposed from $P =$ 200 N to $P = 400$ N divided into 10 time steps.

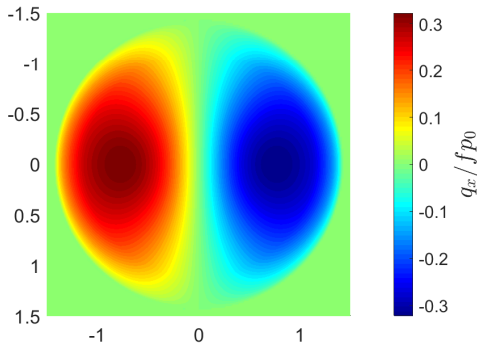

Figure 6.2: Example of two dimensional view of the dimensionless surface shear traction q_x/fp_0 for the Spence shift in a circular contact.

The elastic properties for the materials chosen for the simulation correspond to a Dundurs' parameter $\beta = -0.3007$. Due to the dissimilarity of the materials, the applied normal force induces shear tractions in the contact zone as shown in Fig. 6.2. The x axis the horizontal while the vertical is the y axis.

In the next two subsections, an analysis of the Spence shift is performed for a layered half-space. The effects of the variation of the Young modulus of the coating and its thickness are highlighted.

6.3.2.1 Influence of the ratio of Young modulus

The Spence shift is simulated in the same conditions as above by only modifying the Young modulus of a coating ($E_c = \cdots E_s$) which has a thickness $h = a$.
Figure 6.3 shows the dimensionless q_x/fp_0 along the x axis in the plane $y = 0$. In a) the maximum pressure p_0 and the width a of the contact zone for the case $E_c = E_s$ are used for the normalisation, while in b) p_0 and a for each case are used for the normalisation. The shears are accompanied by the dimensionless contact pressure p/p_0 in dashed line. According to the shear traction bound defined with the Coulomb's law, one can distinguish the slip zone where the shear line confounds with the pressure line, from the stick zone close to the center. These observations are classically known since the works of Spence [SPE 75]. The addition of coating to the half-space has the following consequences:

- When the coating is more compliant, the overall shears decrease and spread as does the contact pressure.
- On contrary, when the coating is stiffer, the contact zone shrinks and so both pressure and shears take greater values on a smaller zone.

Those results are expected since the contact is influenced by the coating with regard to what has been observed for the normal contact in chapter 3. Note that the thickness of the coating has been chosen so that it can have a marked effect.

The original result here is plotted in Fig. 6.3(b) where one can observe that the size of the slip zone decreases when the coating becomes less stiffer than the substrate.

6.3.2.2 Influence of the coating thickness

Here the elastic modulus of the coating is set to $E_c = E_s/4$ in the above framework and then the thickness of the coating changes in function of the Hertz parameter a ($h = \cdots a$).
Figure 6.4 shows the dimensionless shear q_x/fp_0 along the x axis in the plane $y = 0$ for different values of the thickness of the coating. In a) the maximum pressure p_0 and the width a of the contact zone for the case $E_c = E_s$ are used for the normalisation, while in b) p_0 and a for each case are used for the normalisation.
The coating here is four time less stiffer than the substrate. The consequence is that the contact zone extends and the contact pressure and shears take low overall values. This behaviour accentuates when the thickness of the coating increases. However, it seems that the change starts to become less significant when $h > a$. This kind

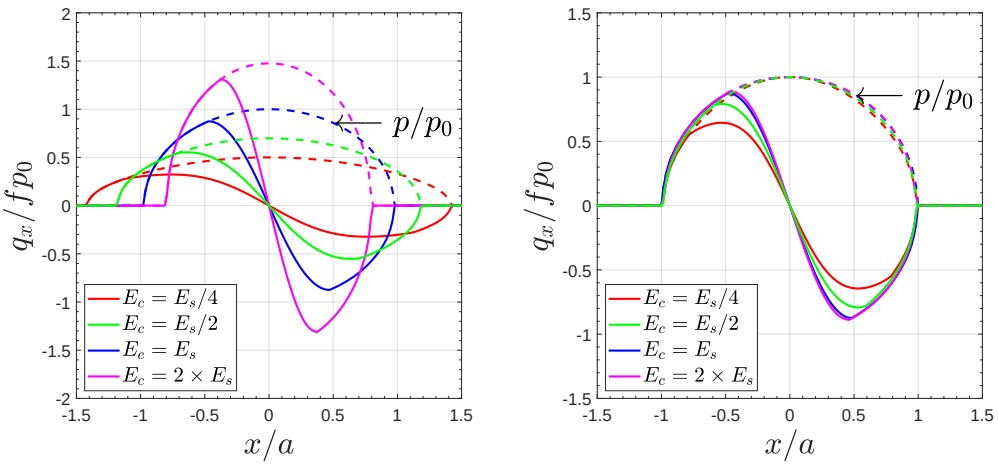

Figure 6.3: Dimensionless shear q_x/fp_0 along the x axis in the plane $y = 0$ for the Spence shift on coated bodies where $E_c = E_s/4$; $E_c = E_s/2$; $E_c = E_s$ and $E_c = 2 \times E_s$. In a) the maximum pressure p_0 and the width of the contact zone a for the case $E_c = E_s$ are used for the normalisation, while in b) p_0 and a for each case are used for the normalisation.

of observation is interesting and can be helpful in an industrial context where the coating material can have a non negligible cost.

In Fig. 6.4(b), one can observe that the size of the slip zone decreases with the thickness before $h = a$. For $h = 2 \times a$ the behaviour of the contact tends to be the one of an homogeneous half-space with the properties of the coating. Therefore, the size of the slip zone in that case tends toward the one for the $h = 0$ case.

Another classical shift that is worth understanding in the case of layered bodies is the Cattaneo-Mindlin shift. It consists in applying a normal and a tangential loads simultaneously.

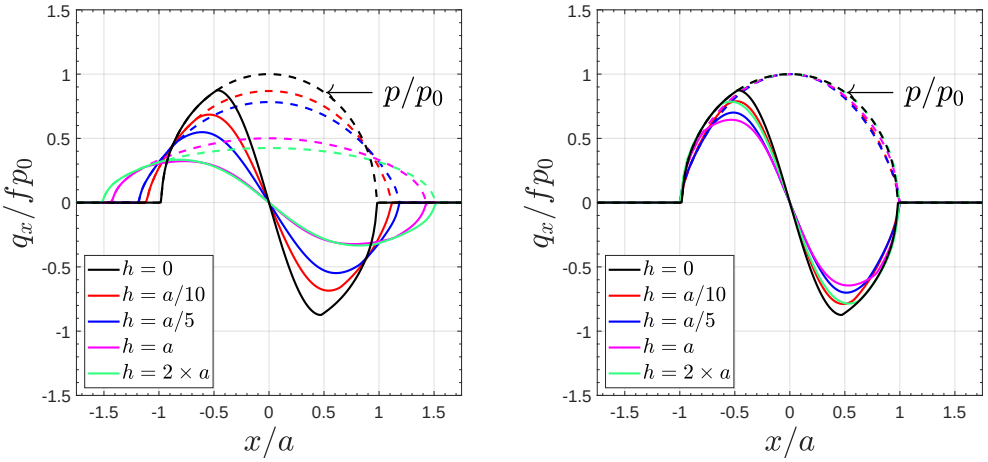

(a) (b)

Figure 6.4: Dimensionless shear q_x/fp_0 along the x axis in the plane $y = 0$ for the Spence shift on coated bodies where $E_c = E_s/4$ for different values of coating thickness. In a) the maximum pressure p_0 and the width of the contact zone a for the case $E_c = E_s$ are used for the normalisation, while in b) p_0 and a for each case are used for the normalisation.

6.3.3 The Cattaneo-Mindlin shift

The Cattaneo-Mindlin shift originally concerns elastically similar bodies in contact under a normal force $P = 200$ N and a tangential force Q so that $Q < fP$, where f is the friction coefficient. According to the Coulomb's friction law, the system is in an equilibrium state from a general point of view. Cattaneo [CAT 38] and Mindlin [MIN 49] have shown that in this type of contact configuration, slip zones appear beside stick zones. In the case of a spherical contact for example, it has been shown that slip appears in an crown bounded to the edges of the contact zone.
When coatings of different elastic properties are set, one can expect that the similarity of the bodies are disturbed. Thus, the purpose here is to reproduce the Cattaneo-Mindlin shift for coated bodies.
The simulations are performed for a friction coefficient $f = 0.25$ and the fixed elastic properties of Tab. 6.2. A tangential force $Q_x/fP = 0.5$ is applied only in the x

Body 1		Body 2			
-		Substrate		Coating	
E_1[MPa]	ν_1	E_s[MPa]	ν_s	E_c[MPa]	ν_c
114600	0.285	114600	0.285	-	-

Table 6.2: General elastic properties of the bodies in the contact studied in section 6.3.3.

direction in 4 time steps. As for the Spence shift, the effect of the ratio of Young modulus is analysed as well as the effect of the thickness of the coating.

6.3.3.1 Influence of the ratio of Young modulus

The above framework is used and the thickness is set to $h = a$ while the ratio of Young modulus between the coating and the substrate varies ($E_c = \cdots E_s$).
The results of the computations are plotted in Fig. 6.5, where the dimensionless contact shears q_x/fp_0 is plotted for a) $E_c = E_s/4$; b) $E_c = E_s$ and c) $E_c = 2 \times E_s$. One may remark that the case b) well correlates with the classical results. For the two other cases, the disturbance brought by the coating is visible on the shear field. In fact, adding the coating induces a change of the Dundurs' parameter. The contact is directly influenced by the properties of the layer. Thus the simulation shows that the behaviour expected for the Cattaneo-Mindlin shift for dissimilar materials which has been studied by Gallego [GAL 07b].
As one can expect, the shears take greater values for a stiffer coating. The most surprising phenomena is the asymmetry observed for the cases a) and c). It comes that for a more compliant coating, the greater values of shears are in the negative side with respect to the direction of the applied tangential force. Meanwhile, for stiffer coating, the greater values of shears are found in the positive side with respect to the direction of the applied tangential force.
These phenomena can be explained by the fact that the difference of elastic tangential displacements of the bodies in contact are the origin of slip. And according to this difference of displacement between the bodies, it seems that the more compliant body drives the slip. Note that the load imposed in the direction x on the body 1 has its resultants in the x opposite direction on the body 2. Thence, for $E_c = E_s/4$, the slip is driven by body 2 and the slip is predominant in the opposite direction to x while the slip is predominant in the x direction when body 1 is more compliant.

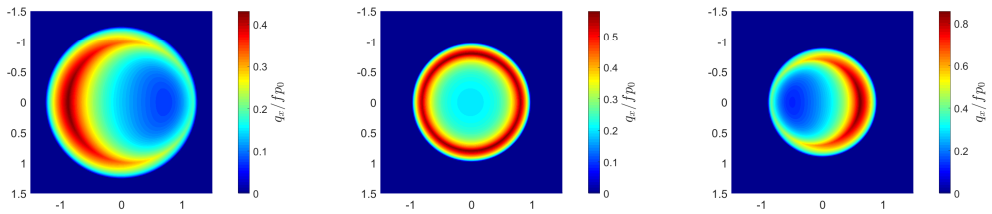

(a) (b) (c)

Figure 6.5: Two dimensional view of the dimensionless shear q_x/f_0 for the Cattaneo-Mindlin shift for an applied tangential force $Q_x/fP = 0.5$ for coated half-space where a)$E_c = E_s/4$; b)$E_c = E_s$ and c)$E_c = 2 \times E_s$.

The same considerations remain when the dimensionless shear q_x/fp_0 is plotted along the x axis in the plane $y = 0$ (see Fig. 6.6).

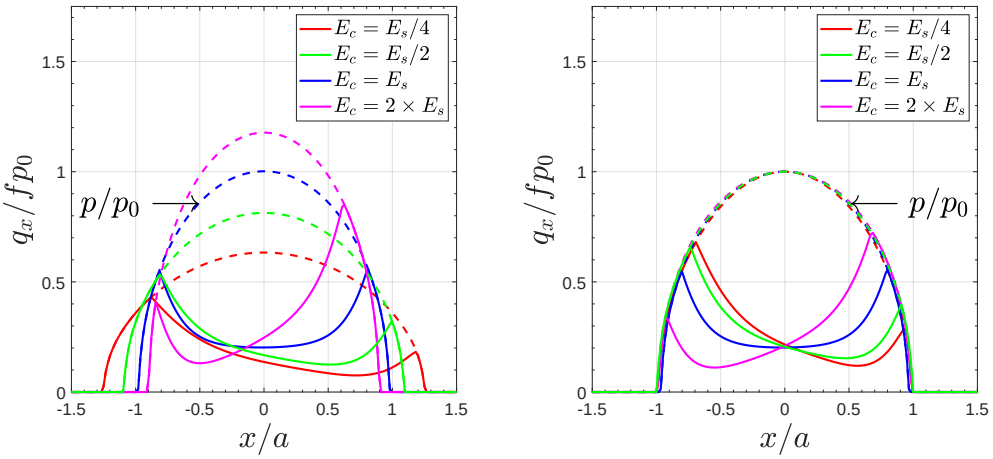

Figure 6.6: Dimensionless shear q_x/fp_0 along the x axis in the plane $y = 0$ for the Cattaneo-Mindlin shift on coated bodies where $E_c = E_s/4$; $E_c = E_s/2$; $E_c = E_s$ and $E_c = 2 \times E_s$. In a) the maximum pressure p_0 and the width of the contact zone a for the case $E_c = E_s$ are used for the normalisation, while in b) p_0 and a for each case are used for the normalisation.

6.3.3.2 Influence of the coating thickness

For this study, the framework of the previous section is used with the elastic modulus of the coating set to $E_c = E_s/4$ i.e. less stiffer than the substrate. The value of the thickness changes ($h = \cdots a$).

Figure 6.7 shows the dimensionless shear q_x/fp_0 along the x axis in the plane $y = 0$ for various values of coating thickness. In a) the maximum pressure p_0 and the width a of the contact zone for the case $E_c = E_s$ are used for the normalisation, while in b) p_0 and a for each case are used for the normalisation. The asymmetry of the profile of the shear is observed and explained previously. One can observe that this asymmetry of the slip zone accentuates with the coating thickness. Moreover, the profile for $h = 2 \times a$ shows that there is no restriction on the sign of the shear traction.

Evidently, when the thickness takes a very high value, the system will behave as if it was a contact on a homogeneous half-space with the elastic properties of the coating. Unlike the Spence shift, the difference between the cases $h = a$ and $h = 2 \times a$ is relatively significant.

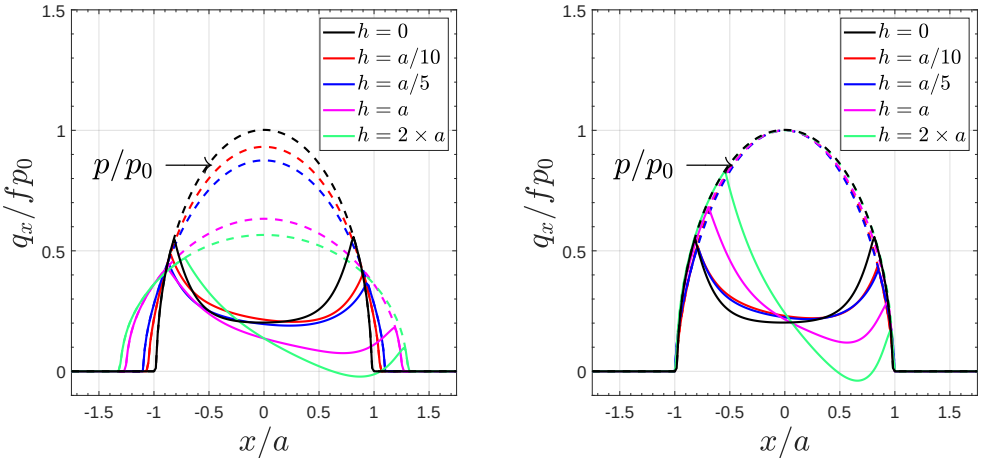

Figure 6.7: Dimensionless shear q_x/fp_0 along the x axis in the plane $y = 0$ for the Cattaneo-Mindlin shift on coated bodies where $E_c = E_s/4$ for different values of coating thickness. In a) the maximum pressure p_0 and the width of the contact zone a for the case $E_c = E_s$ are used for the normalisation, while in b) p_0 and a for each case are used for the normalisation.

6.3.4 Example of Fretting loop: Mode I

In this part, a loop of fretting in mode I is simulated since it is the most common in industrial applications. For this purpose, the framework for the Cattaneo-Mindlin shift is used (see section 6.3.3), but this time for the contact between dissimilar materials. The general elastic properties chosen for the simulation are presented in Tab. 6.3. For this simulation a single loop is considered for an applied tangential

Body 1		Body 2			
-		Substrate		Coating	
E_1[MPa]	ν_1	E_s[MPa]	ν_s	E_c[MPa]	ν_c
114600	0.1	114600	0.5	-	0.5

Table 6.3: General elastic properties of the bodies in the contact studied in section 6.3.4.

force Q_x. The loading path for the tangential force is given in Fig. 6.8. It consists of a ramp load from an initial small tangential force (where $Q_x = 10\%fP$) to the maximum imposed force at the point A where $Q_x = 90\%fP$. Then, it decreases linearly to reach the lowest value at the point C where $Q_x = -90\%fP$. Finally, it linearly goes again to the maximum at the point E where $Q_x = 90\%fP$. Throughout the simulation, the normal force is constant.

In the same way as previously, the effects of the ratio of Young modulus and

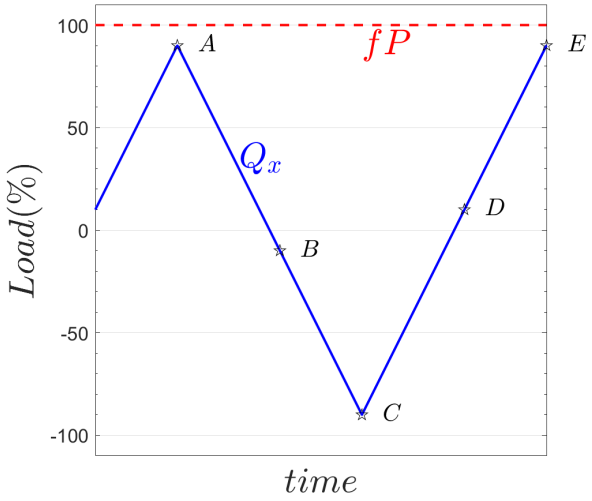

Figure 6.8: Fretting path for the tangential load. The maximum applied tangential force is fP. At the point A the applied tangential force is $Q_x = 90\%fP$; at B the applied force is $Q_x = -10\%fP$; at C $Q_x = -90\%fP$; at D $Q_x = 10\%fP$ and at E $Q_x = 90\%fP$.

the effects of the coating's thickness are analysed. Since failures mainly come from interfaces in industrial components, a particular look is cast on them.

6.3.4.1 Influence of the ratio of Young moduli

For the study of the influence of the ratio of Young modulus, the thickness of the coating is fixed to $h = a$ and the elastic properties of substrate are given in Tab. 6.3. Only the ratio of Young modulus changes ($E_c = \cdots E_s$).
Figure 6.9 shows the dimensionless shear traction q_x/fp_0 along the x axis in the plane $y = 0$ for various ratios of Young modulus and at different points of the loading path in Fig. 6.8: a) at the point A where $Q_x = 90\%fP$; b) at the point B where $Q_x = -10\%fP$; c) at the point C where $Q_x = -90\%fP$; d) at the point D where $Q_x = 10\%fP$ and e) at the point E where $Q_x = 90\%fP$.

Firstly, one can remark that the slip zone of the contact increases with the norm of the applied tangential force applied. The slip grows from the edge of the contact to the center. Moreover, the sign of the shear tractions are influenced by the sign of the overall force.
Secondly, the transient behaviour of the contact can be observed. Although we are treating an elastic contact, the behaviour of the structure depends on the history of the loading. This is confirmed by comparing the subplots in Figs. 6.9(a) and 6.9(e) where the loading is the same. The behaviours of those two cases differ due to the influence of the history of the loading. The history effect is contained in the definition of the slip which is based on the variation between two consecutive time

steps.
According to the influence of the ratio of Young moduli between the substrate and the coating, the overall observations as in section 6.3.3 remain available. Adding a more compliant coating to the half-space allows to relax the tractions while they increase when the coating is stiffer. Finally, observing the contact shears normalised by their own parameters a and p_0 in Fig. 6.10, no significant dependence is highlighted with respect to the ratio of elastic moduli E_c/E_s.

An analysis of the interface between the coating and the substrate is done with the second invariant J_2 of the stress tensor. Figure 6.11 shows the dimensionless second invariant $\sqrt{J_2}/p_0$ of the stress tensor at the coating/substrate interface along the x axis in the plane $y = 0$ for various ratio of Young modulus and at different points of the loading path in Fig. 6.8: a) at the point A where $Q_x = 90\%fP$; b) at the point B where $Q_x = -10\%fP$; c) at the point C where $Q_x = -90\%fP$; d) at the point D where $Q_x = 10\%fP$ and e) at the point E where $Q_x = 90\%fP$.
As expected, the higher the contact pressure and shears are, the higher are the stresses. By comparing Figs. 6.11(a) and 6.11(e), the differences between the two are not as significant as for the contact shear. It means that the effect of this particular fretting for one loop is low. No generalisation cannot, however, been done since those slight differences can accumulate for a high number of fretting loops.

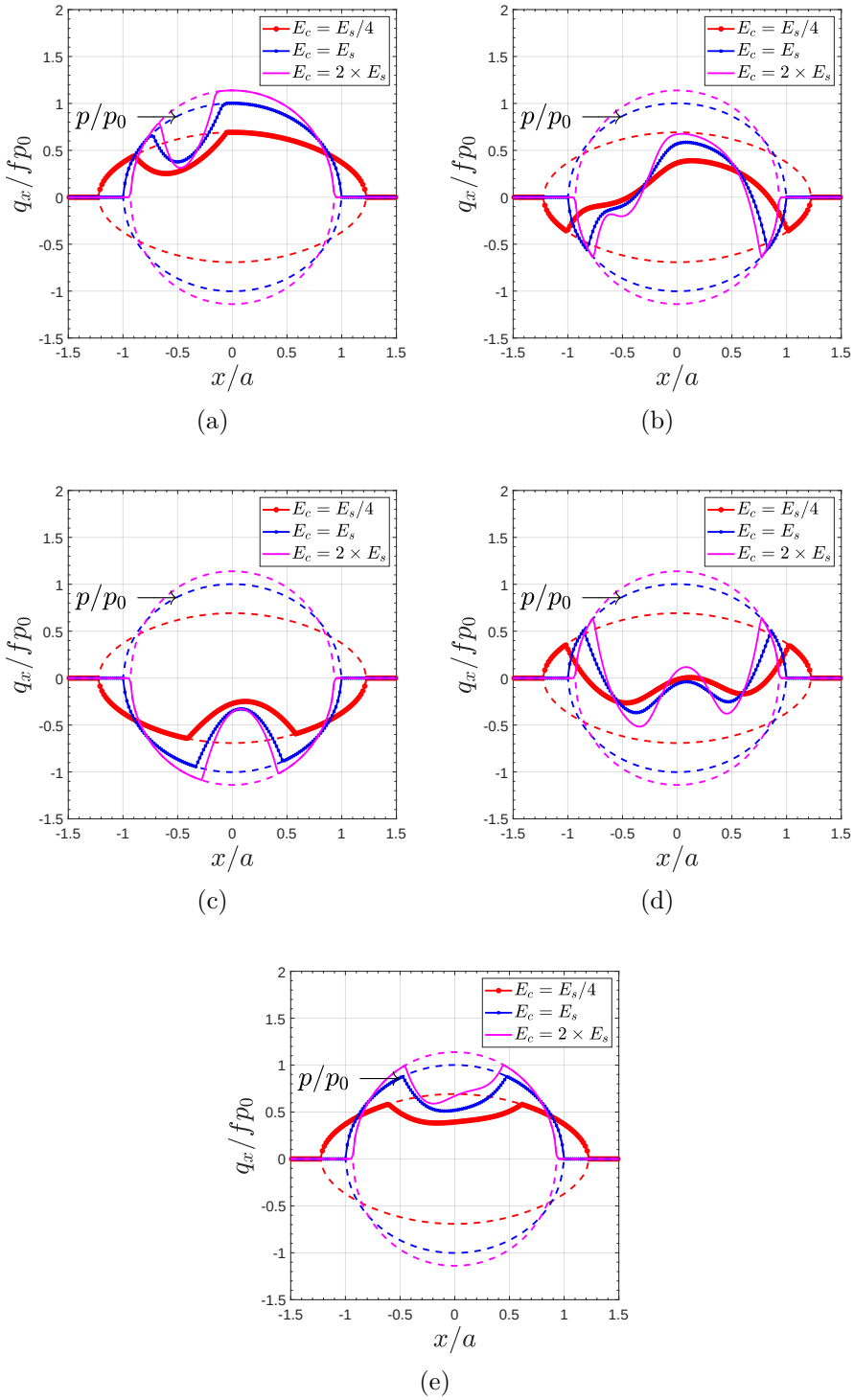

Figure 6.9: Dimensionless contact shear q_x/fp_0 along the x axis in the plane $y = 0$ for the fretting loop in Fig. 6.8. It is plotted for $E_c = E_s/4$, $E_c = E_s$ and $E_c = 2 \times E_s$ at the point a) A; b) B; c) C; d) D and e) E of the loading path in Fig. 6.8.

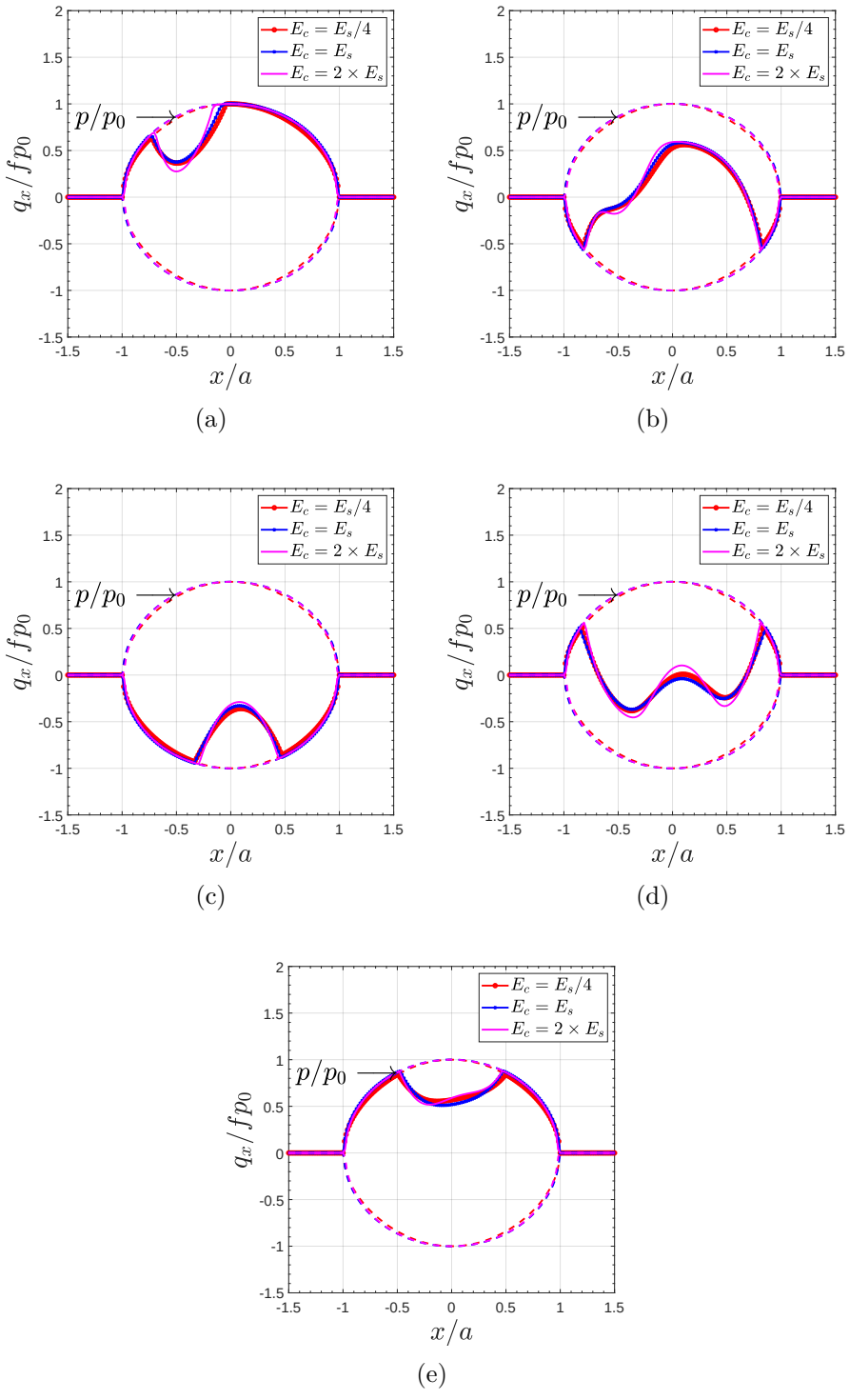

Figure 6.10: Dimensionless contact shear q_x/fp_0 along the x axis in the plane $y = 0$ for the fretting loop in Fig. 6.8. It is plotted for $E_c = E_s/4$, $E_c = E_s$ and $E_c = 2 \times E_s$ at the point a) A; b) B; c) C; d) D and e) E of the loading path in Fig. 6.8. Here a p_0 for each case are used for the normalisation.

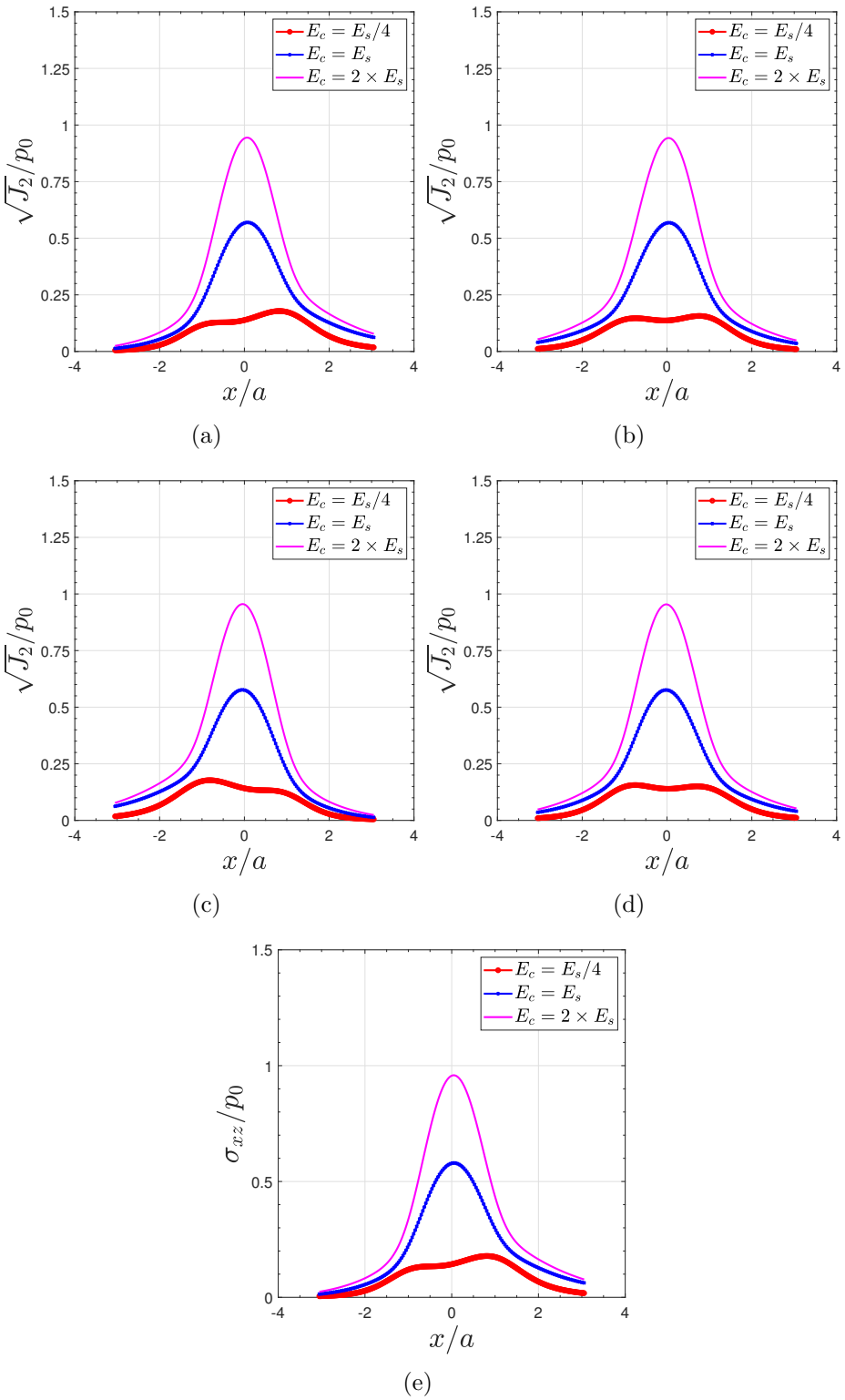

Figure 6.11: Dimensionless second invariant $\sqrt{J_2}/p_0$ of the stress tensor, at the coating/substrate interface along the x axis in the plane $y = 0$ for the fretting loop in Fig. 6.8. It is plotted for $E_c = E_s/4$, $E_c = E_s$ and $E_c = 2 \times E_s$ at the point a) A; b) B; c) C; d) D and e) E of the loading path in Fig. 6.8.

6.3.4.2 Influence of the coating thickness

Here, we keep the values of Tab. 6.3 with a Young modulus of the coating fixed to $E_c = E_s/4$. Then, the thickness h of the coating changes ($h = \cdots a$).

Figure 6.12 shows the dimensionless shear traction q_x/fp_0 along the x axis in the plane $y = 0$ for various coating thickness and at different points of the loading path in Fig. 6.8: a) at the point A where $Q_x = 90\%fP$; b) at the point B where $Q_x = -10\%fP$; c) at the point C where $Q_x = -90\%fP$; d) at the point D where $Q_x = 10\%fP$ and e) at the point E where $Q_x = 90\%fP$.

The general trends are the same as in the section 6.3.3.2. For an industrial application, if one wants to use a coating which behaviour is important for the structure the right thickness may be near the parameter a. For greater values, the difference might not worth the cost while for lower values, the behaviour of the substrate is dominant. These remarks are relevant when the coating aims to act on pressure and stresses distribution. It is not true when the coating is used for other purposes. For instance, coatings are also used to modify the friction at the contact interface. In that case, the study is to be done around the friction coefficient and eventually the wearing and delamination effects. It is known that for greater friction at the contact interface, the stick zone is greater and inversely. But for high friction at the contact interface wearing effects tend to increase also. Thus, a balance is to be found, and the use of coatings is certainly a good alternative so that the frictional and wearing effects can be controlled independently to the structure dimensioning. Finally, as for the ratio of elastic moduli, no significant dependence is highlighted with respect to the coating thickness (see Fig. 6.13).

Furthermore, the use of coatings induces other questions. For example, the delamination effects have to be studied when using coatings since they are not perfectly bounded in practice. In this spirit, here is presented the dimensionless second invariant $\sqrt{J_2}/p_0$ of the stress tensor at the coating/substrate interface along the x axis in the plane $y = 0$ for various ratio of coating thickness and at different points of the loading path in Fig. 6.8: a) at the point A where $Q_x = 90\%fP$; b) at the point B where $Q_x = -10\%fP$; c) at the point C where $Q_x = -90\%fP$; d) at the point D where $Q_x = 10\%fP$ and e) at the point E where $Q_x = 90\%fP$.

One can observe that the asymmetry is more pronounced due to the ratio $E_c/E_s = 0.25$ chosen. Moreover, it is accentuated when the coating thickness decreases. The overall stress decreases when the thickness is greater because the body tends to behave like the coating which is less stiffer. It is also interesting to remark that the peak of the stress is located in the direction of the applied force and takes higher values for higher of imposed tangential force. This means that the tangential force has a significant effect on the risk of delamination at the coating/substrate interface. The last remark concerns Figs. 6.14(a) and 6.14(e). For the two figures the loading state is the same but the stresses show a slight decrease especially for the case $h = a/5$. This might mean that a more compliant coating might induce a relaxation of stresses at the coating/substrate interface during the fretting motion.

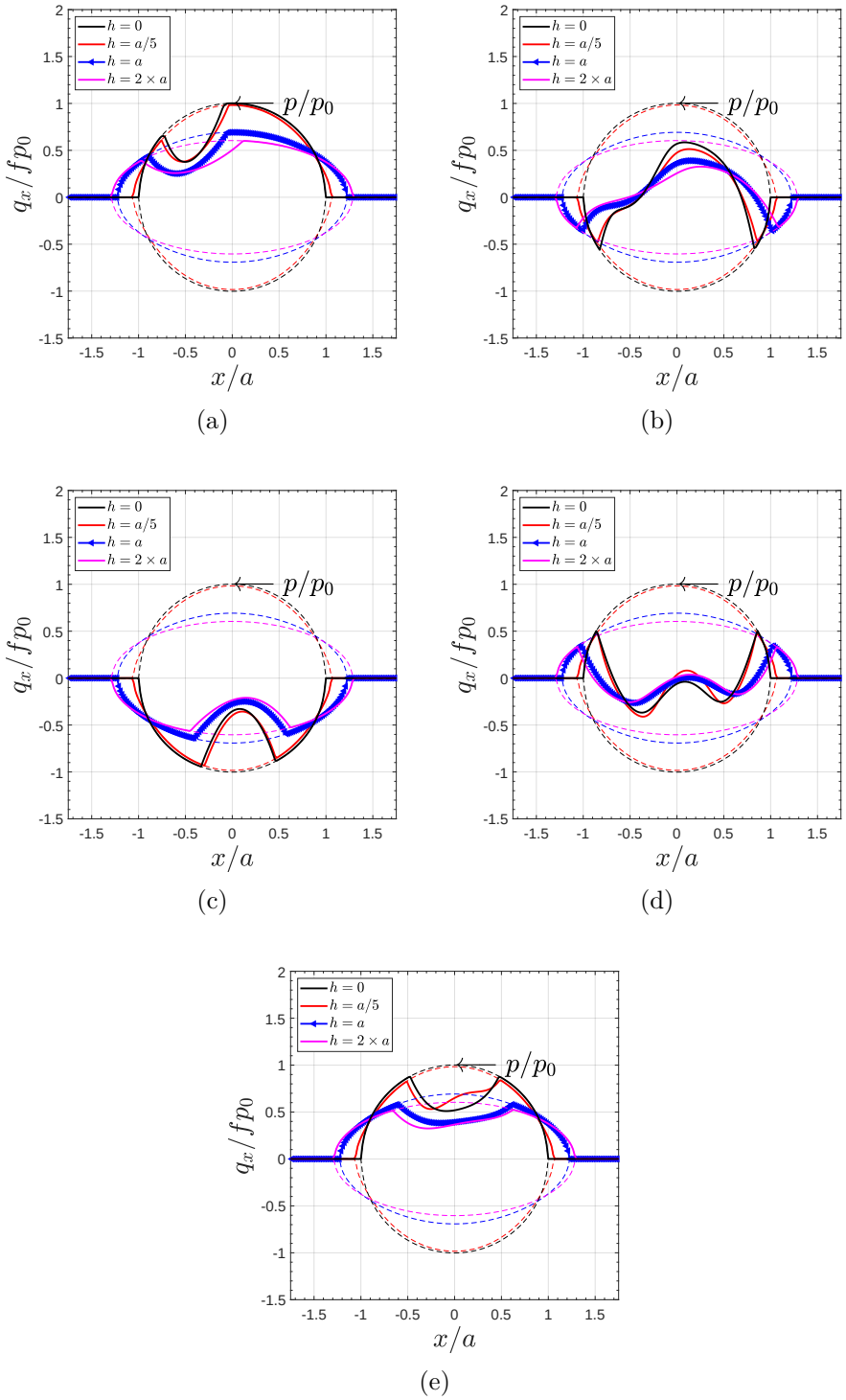

Figure 6.12: Dimensionless contact shear q_x/fp_0 along the x axis in the plane $y = 0$ for the fretting loop in Fig. 6.8. It is plotted for $E_c = E_s/4$ and $h = 0, a/5, a, 2a$ at the point a) A; b) B; c) C; d) D and e) E of the loading path in Fig. 6.8.

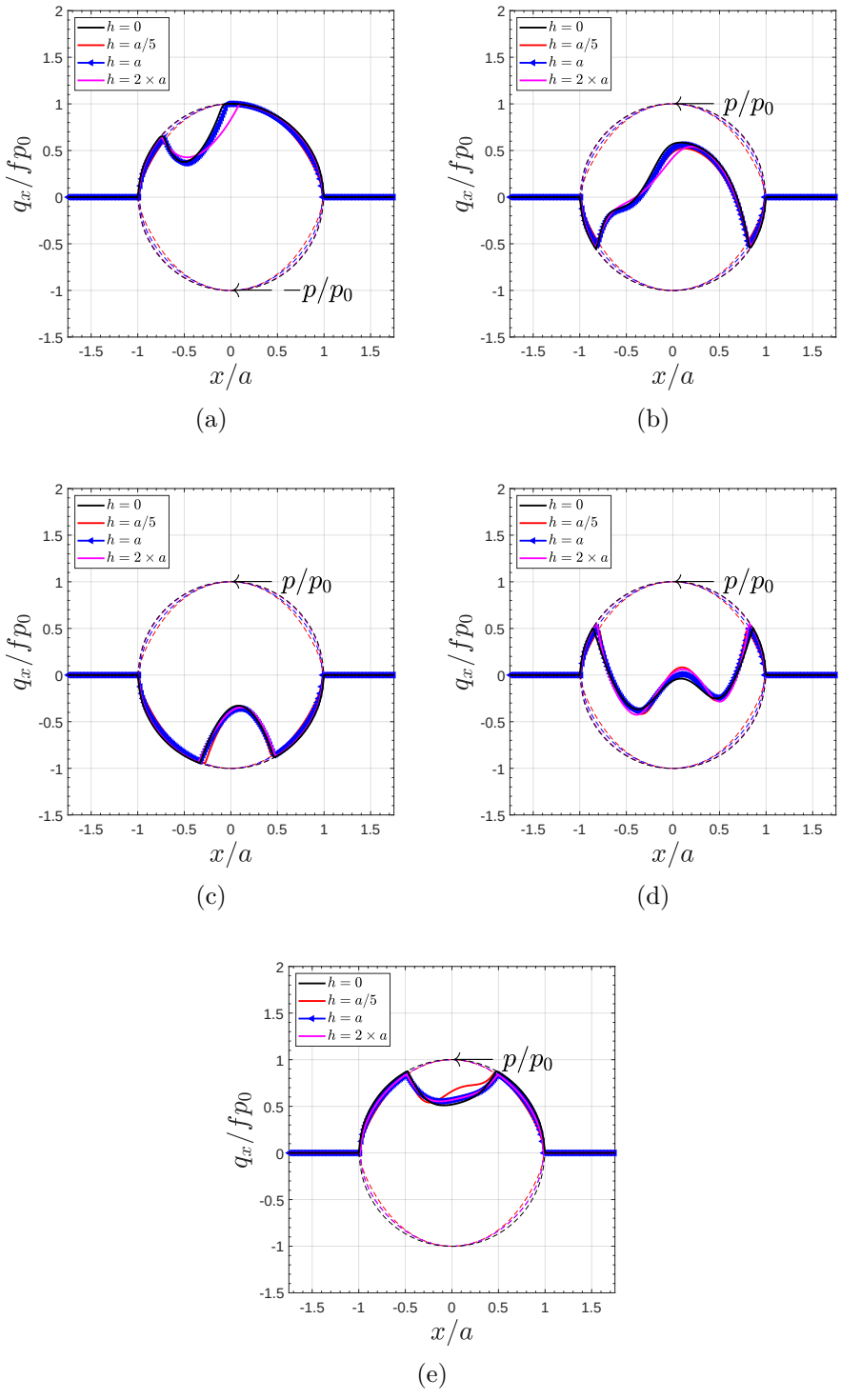

Figure 6.13: Dimensionless contact shear q_x/fp_0 along the x axis in the plane $y = 0$ for the fretting loop in Fig. 6.8. It is plotted for $E_c = E_s/4$ and $h = 0, a/5, a, 2a$ at the point a) A; b) B; c) C; d) D and e) E of the loading path in Fig. 6.8. Here a p_0 for each case are used for the normalisation.

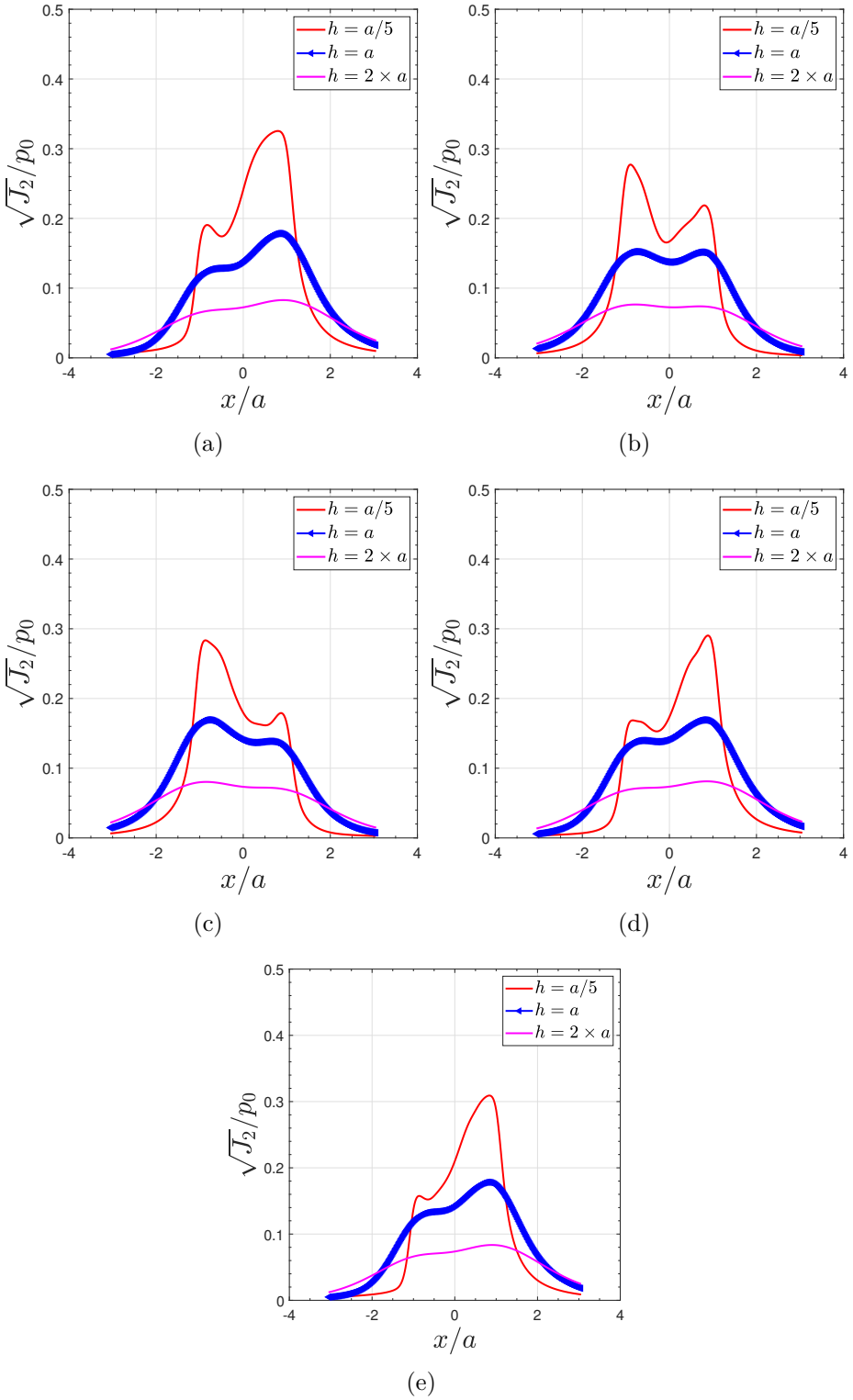

Figure 6.14: Dimensionless second invariant $\sqrt{J_2}/p_0$ of the stress tensor, at the coating/substrate interface along the x axis in the plane $y = 0$ for the fretting loop in Fig. 6.8. It is plotted for $E_c = E_s/4$ and $h = a/5, a, 2a$ at the point a) A; b) B; c) C; d) D and e) E of the loading path in Fig. 6.8.

Apart from single layered bodies, many multi-layered are used in the industry in various forms (multi-layered, graded, etc). Especially, the pavement structure which is the topic of this thesis is not single layered but multi-layered. Thus, it is important to give a view of the fretting contact on a multi-layered half-space.

6.4 Results: Multi-layered half-space

6.4.1 Framework

The algorithm for the tangential shift motion can be applied for any half-space if the corresponding influence coefficients are known. Since the influence coefficients of a multi-layered half-space have been found in chapter 4, the elastic fretting contact can be simulated for multi-layered bodies.

For illustration, several simulations have been performed on a multi-layered half-space with 10 layers by using these configurations for the elastic moduli of the layers:

- The "*Alternate Modulus*": the even index layers take the elastic modulus value $4 \times E_{sub}$ while the odd index layers take the shear modulus value E_{sub} :
- The "*Increasing Modulus*": the modulus increases from E_{sub} to $5.5 \times E_{sub}$ in the $10th$ layer:
- The "*Decreasing Modulus*": the modulus decreases from $6 \times E_{sub}$ with a constant step to reach the substrate modulus E_{sub}:

Figure 6.15 shows the three cases of variation of elastic modulus in the half-space described above.

For the following simulations, a sphere comes into contact with a flat multi-layered half-space. The general elastic parameters used in the simulation are presented in Tab. 6.4.

Body 1		Body 2			
-		Subtrate		Layers	
E_1[MPa]	ν_1	E_{sub}[MPa]	ν_{sub}	E_j[MPa]	ν_j
10E20	0.3	210000	0.3	-	0.3

Table 6.4: Elastic properties of the bodies for the reference Hertz which will gives the hertz parameters for finding the dimensionless results for the study of the multi-layered half-space.

Two cases are analysed for the above configurations: the Spence shift and an example of fretting mode I loop.

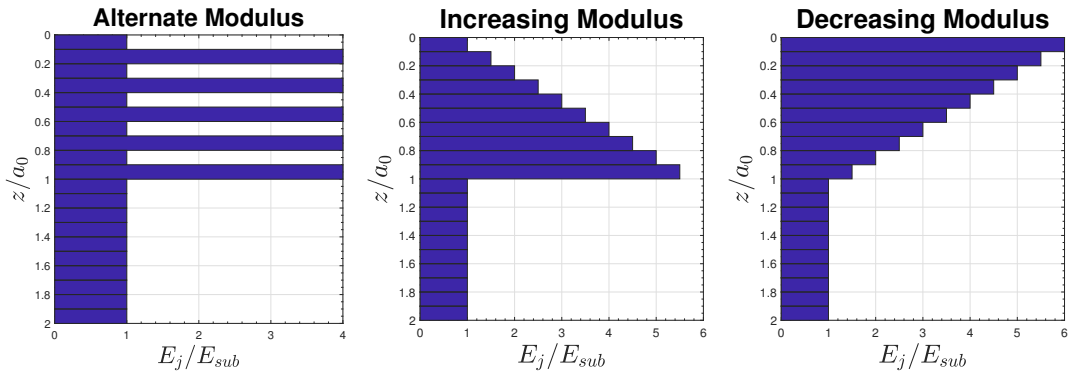

(a) (b) (c)

Figure 6.15: Different cases of variation of elastic moduli of the layers for the multi-layered half-space.

6.4.2 The Spence shift

In this part, the Spence shift is simulated on multi-layered half-spaces with the previously described alternate modulus, increasing modulus and decreasing modulus. A normal force ramp is imposed from $P = 1000$ N to $P = 10000$ N in 10 time steps. The friction coefficient at the contact interface is set to $f = 0.5$.

Figure 6.16 shows the dimensionless shear traction q_x/fp_0 along the x axis in the middle plane $y = 0$. The dimensionless pressures p/p_0 are drawn in dashed line to show the extent of the slip zone where the shear $q_x = fp_0$ and the stick zone where $q_x < fp_0$. The general behaviour of the contact is similar to the cases of homogeneous and single layered-half spaces: the slip zone is located in a crown at the bound of the contact. The extent of the slip zone depends on the parameter β/f, where β is the Dundurs parameter and f the friction coefficient. When $\beta/f = 0$, there is no slip zone in the contact area. This case happens for very high friction coefficient or when the materials in contact are elastically similar. When $|\beta/f|$ takes higher value, the slip zone increases because whether the dissimilarity is higher and/or the friction coefficient is lower.

For the analysis of the three-dimensional stresses, the z direction is discretised over a depth $z = 2 \times a$. Then, Fig. 6.17 shows the dimensionless second invariant $\sqrt{J_2}/p_0$ of the stress tensor for the three configurations of variation of Young modulus in the multi-layer: a) Alternate modulus; b) Increasing modulus and c) Decreasing modulus.
One can observe that each configuration of variation of Young modulus influences the distribution of stress as observed in chapter 4. In addition to the observations in the case of an applied normal load only, the shear at the surface has an effect close to the surface. For each configuration, an increase of the stress can be observed close to the surface, corresponding to the crown of the slip.
The takeaway for these observations, is that in function of the dissimilarity and

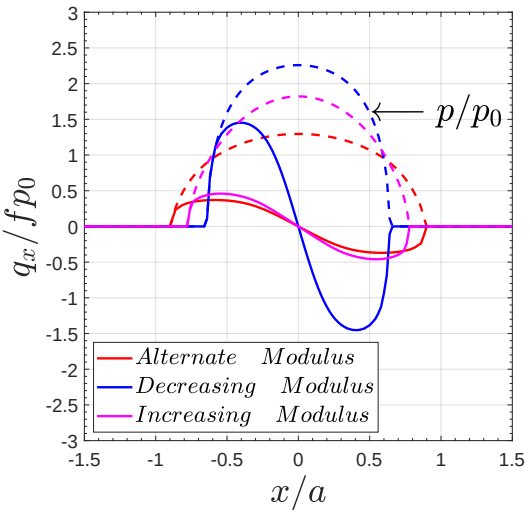

Figure 6.16: Dimensionless shear q_x/fp_0 along the x axis in the plane $y = 0$ for the Spence shift on multi-layered bodies with *Alternate modulus*, *Increasing modulus* and *Decreasing modulus*.

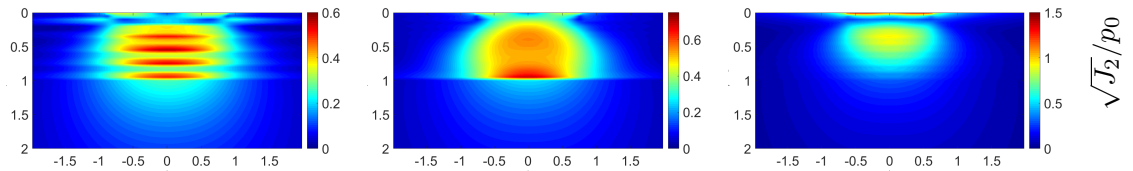

(a) Alternate modulus (b) Increasing modulus (c) Decreasing modulus

Figure 6.17: 2D dimensionless second invariant $\sqrt{J_2}/p_0$ of the stress tensor in the plane $y = 0$ for the Spence shift on multi-layered bodies with *Alternate modulus*, *Increasing modulus* and *Decreasing modulus*.

the friction at the contact interface, the elastic field that yields from the contact changes. Thus, in the context of tire/pavement modelling, it might be interesting to consider the friction at the interface even when there is no tractive force imposed.

In order to continue the investigation, it is worth doing an example of fretting loop in mode I, in order to highlight the impact not only in the contact zone but also in the subsurface.

6.4.3 Example of Fretting loop: Mode I

This section aims at analysing a fretting loop on the elastic field in a multi-layered body. For this purpose, the three configurations of variation of Young modulus in the multi-layered half-space are used (see section 6.15). The friction coefficient is set to $f = 0.5$; a constant normal force $P = 10000$ N is imposed throughout the

steps. The tangential load is applied in the x direction following the loading path in Fig.6.8.

Figure 6.18 shows the dimensionless shear traction q_x/fp_0 along the x axis in the plane $y = 0$ for alternate modulus, increasing modulus and decrease modulus; and at different points of the loading path in Fig. 6.8: a) at the point A where $Q_x = 90\%fP$; b) at the point B where $Q_x = -10\%fP$; c) at the point C where $Q_x = -90\%fP$; d) at the point D where $Q_x = 10\%fP$ and e) at the point E where $Q_x = 90\%fP$.
Firstly, one may observe the difference between the profiles at the points A and E. For these two points of the loading path, the tangential load is the same. This is due to the history that is contained in the formulation. The same observation goes for the points B and D which are points of opposite tangential loading. In this respect, the obtain shear without taking into account the history of the loading would have been simply the symmetric with respect to the x axis without the history effect.

Further, an analysis of the three dimensional stresses for the three cases of variation of Young modulus in the multi-layered half-space is performed. The dimensionless second invariant $\sqrt{J_2}/p_0$ of the stress is plotted at different points of the loading path in Fig. 6.8. For each column, corresponding to the variation of elastic modulus, one can observe that near the surface, the overall stress undergoes an increase compared to the frictionless case due to the shear contribution. In the volume, the changes are also marked depending on the tangential loading. They are definitely undeniable in the case of increasing modulus where the stress distribution clearly follows the fretting motion.

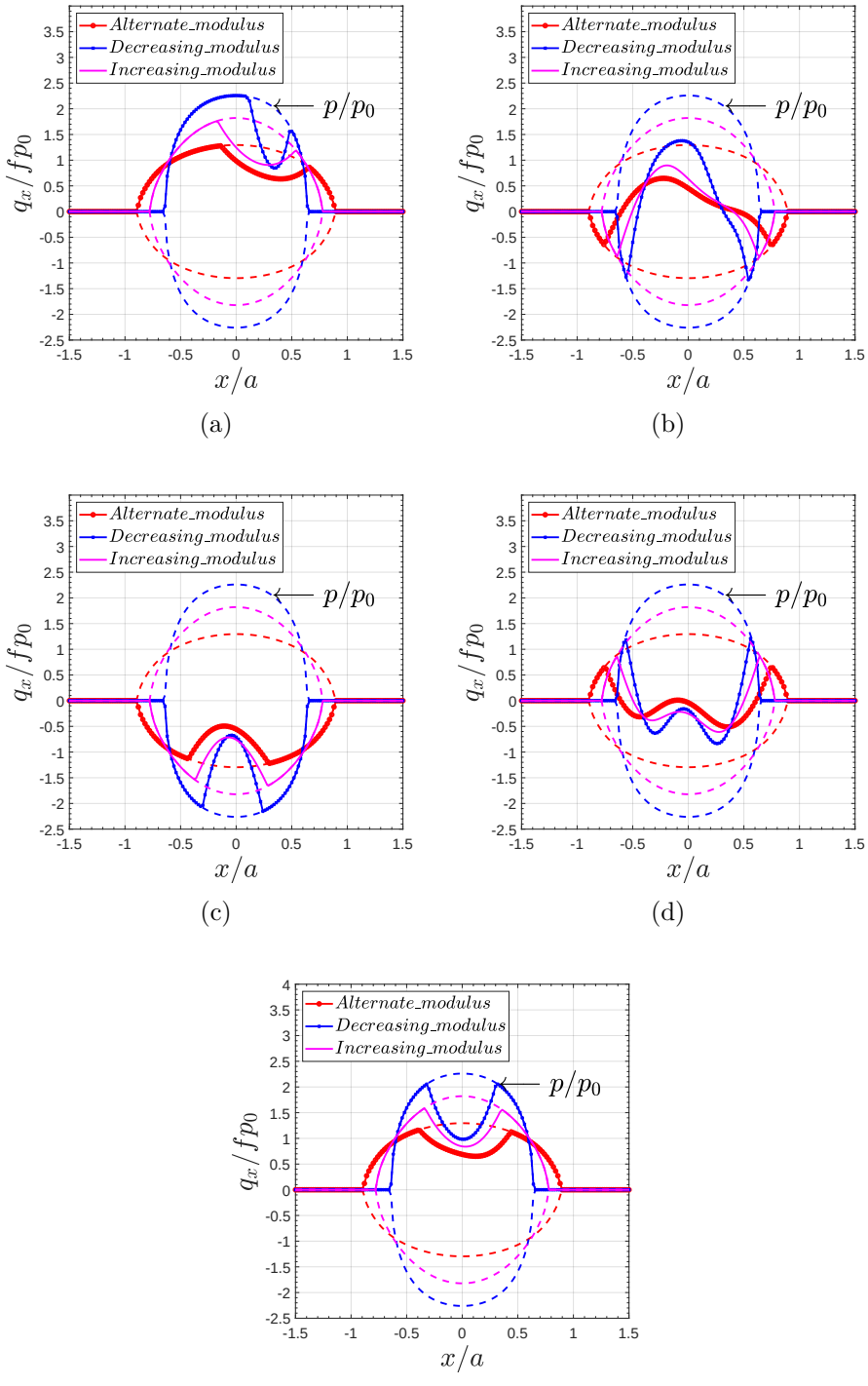

Figure 6.18: Dimensionless contact shear q_x/fp_0 along the x axis in the plane $y=0$ for the fretting loop in Fig. 6.8 on multi-layered bodies. It is plotted for *Alternate modulus*, *Increasing modulus* and *Decreasing modulus* at the point a) A; b) B; c) C; d) D and e) E of the loading path in Fig. 6.8.

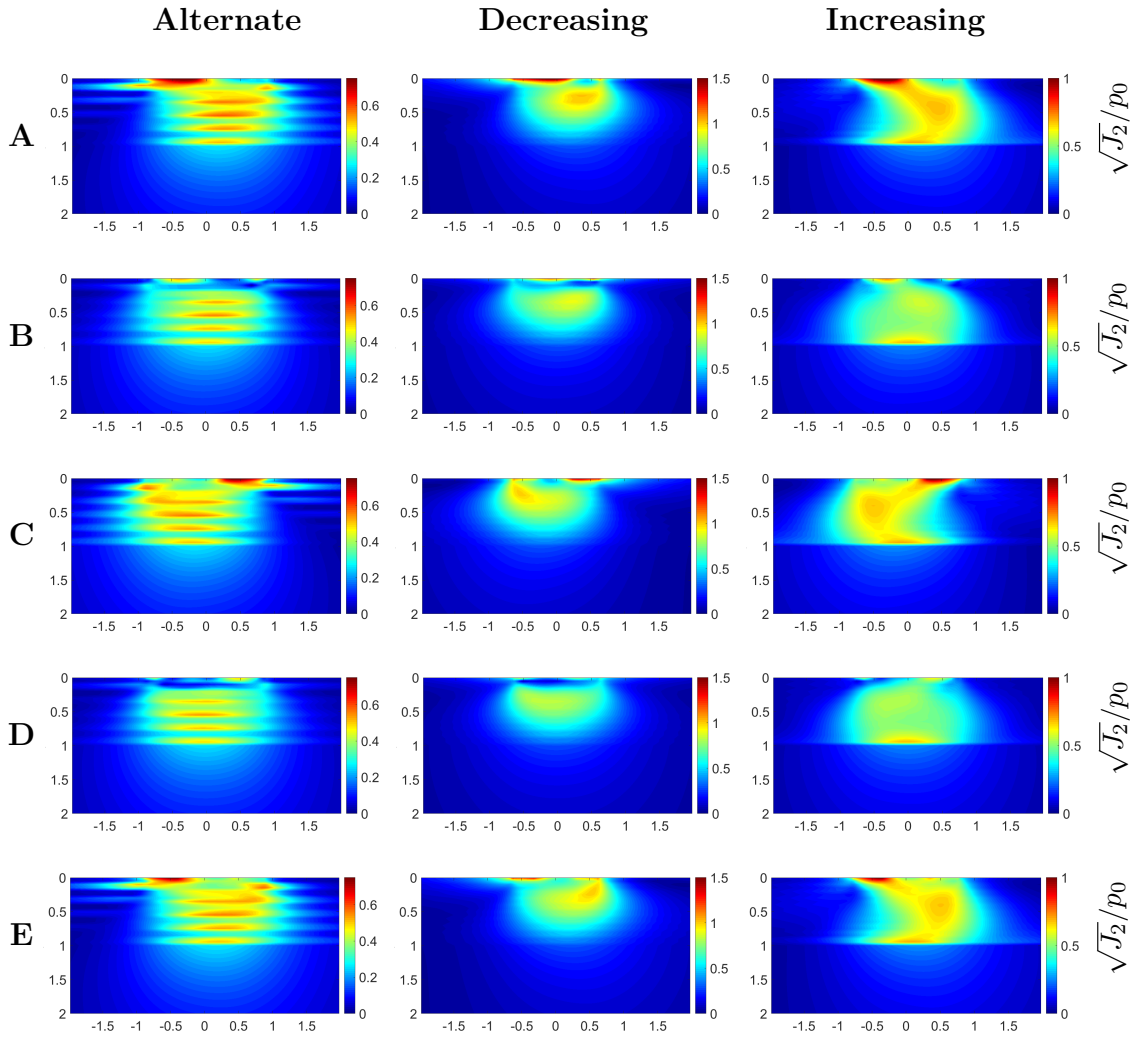

Figure 6.19: Dimensionless second invariant $\sqrt{J_2}/p_0$ of the stress tensor in the plane $y = 0$ for the fretting loop in Fig. 6.8 on multi-layered bodies. It is plotted for *Alternate modulus*, *Increasing modulus* and *Decreasing modulus* at the points A, B, C, D and E of the loading path in Fig. 6.8.

6.5 Conclusion

In summary, the fretting contact has been studied with the present semi-analytical model. After a brief recall of the formulation of the contact problem, results have been presented.

In a first part, the single layered half-space has been considered. The Spence shift, the Cattaneo-Mindlin shift and an example of fretting loop in mode I have been simulated. The effects of the ratio of elastic moduli between the coating and the substrate have been investigated, as well as the effect of the thickness of the coating. The main conclusions of the study are:

- For the Spence shift, the slip zone increases with the ratio of elastic moduli E_c/E_s. For a coating more compliant that the substrate, the slip zone decreases with the coating thickness before $h = a$ (where a is the contact radius given by the same contact condition with $E_c = E_s$); and when the coating thickness becomes bigger than a, the slip zone tend toward the homogeneous case (i.e. $E_c = E_s$).

- For the Cattaneo-Mindlin shift, it has come that the more compliant of the materials in contact drives the direction of the higher shear. In this respect, when the coating on body 2 is stiffer than the other body 1 in contact, the slip is predominant in the direction of the applied tangential force. Instead, when the coating on body 2 is more compliant than the other body 1 in contact, the slip is predominant in the opposite direction of the applied tangential force. Note that the force is applied here on body 1. When normalised, there is no significant change of the extent of the size of the slip zone in this case.

- For a single loop of fretting, the history effect has been marked in the contact. Its effect on the stresses at the coating/substrate interface is significant for relatively small thickness only. Moreover, a relaxation effect has been observed: the overall stresses tend to slightly decrease for the same loading in the fretting motion.

In a second part, the Spence shift and an example of fretting loop in mode I have been tackled for a multi-layered half-space. Alternate modulus, increasing modulus and decreasing modulus cases have been taken for this purpose. Then, the contact field and the three-dimensional stresses have been analysed. It has come that:

- For the Spence shift, apart from the general behaviour in the contact which are similar to the single layered half-space case; close to the surface, the overall stress show an increase due to the fact that a Coulomb friction coefficient is taken into account.

- For the fretting loop in mode I, an increase of the stresses is also observed close to the surface. Moreover, the stress distribution clearly follows the tangential applied load.

Chapter 7

Application: Advanced tire/road contact modelling

This chapter is dedicated to the application of the developed model to the tire-pavement contact. The profile of a real tire is acquired by image reconstruction techniques. Then, simulations are performed and results compared to the reference model of ViscoRoute. Further, the effect of the tractive rolling on the stresses in the pavement structure are investigated through some realistic cases of tangential loadings. Finally, an experimental validation of the work is made.

Sommaire

7.1 Introduction

Throughout the previous chapters, the modelling of various phenomena have been performed with view to improve the design of pavements. The numerical tools developed allow to bring some novelty in the modelling of the tire-pavement contact. To perform the analysis by using the contact modelling, several parameters have to be well defined here:

- The geometry: In the dimensioning methods, idealised footprints are used to define the tire-pavement contact. In this work a real tire profile obtained by image reconstitution is used. For the pavement a flat surface is used.
- The materials: The tire is considered here as an homogeneous elastic isotropic and incompressible body. Its elastic modulus is given by the inflation pressure. The road pavement is an elastic multi-layered half-space where known elastic parameters are used for the simulations. The viscoelasticity has not been computed in the present work.
- The loading: A same normal force is applied for all the cases. For the computation of the tractive rolling effects, arbitrary values of tangential forces and moment have been taken but with view to represent the reality.
- The contact conditions: Both frictional and frictionless contacts have been simulated. A general rolling contact case is simulated as in chapter 5.

In this chapter, an attempt of answer is given to several questions by the use of the modelling. Firstly, the influence of the use of a real tire profile instead of an idealised footprint, is investigated. A recent work of Manyo [MAN 19b] have shown an undeniable qualitative effect of the use of a striated tire profile in the modelling rather than a smooth idealised profile. Here the investigations will be pursued by adding a quantitative point of view since the present model is able to model all the layers of the pavement structure unlike the homogeneous half-space model of Manyo.
Secondly, the influence of the roughness of the road is analysed by using a generated randomly rough surface as surface of the pavement.
Thirdly, the tractive effects are investigated by the simulation of several cases where the tangential effects should not be neglected.
Finally, an experimental validation is presented. Full scale tests have allowed to measure strains in pavement. Those strains are compared to results from the modelling.

7.2 An idealised or a real tire profile?

In the french method for the dimensioning of the pavements, the classical software used is *Alizé-Lcpc* [LCP 10]. In Alizé, normalised and idealised footprints are used to represent the contact zone which yields from the tire-pavement contact. In the context of new generation of European trucks, another software named *ViscoRoute* has been developed with view to take into account the viscoelastic behaviour of the pavements, especially in the rolling course. In those two softwares, which stand as reference for the design of pavement in France, the contact is not solved but a distributed load is applied over normalised chosen footprints. Those footprints are usually rectangular, circular or elliptical. For instance, Fig. 7.1 shows the normalised dual circular footprint used to represent the dual tire in the framework of Alizé and ViscoRoute.

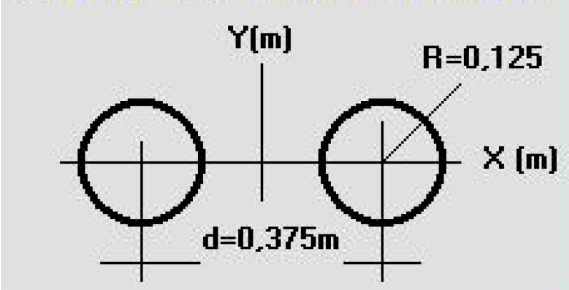

Figure 7.1: The reference normalised circular tire profiles in Alizé and ViscoRoute.

Before any further application of the model developed in the present work, it is important to investigate the impact of using idealised profiles to represent the tire. For this purpose, results obtained with a real tire profile are compared to the results for idealised footprints. As explained in chapter 2, the present model allows to use any kind of surface profile in its discretised form. Therefore, the prior step to the analysis is to obtain the real tire profile.

7.2.1 How to obtain the real profile of the tire?

The tire profile used in this work has been obtained by Manyo [MAN 19b] in his PhD thesis works. The tire is a trailer tire *Michelin 315/80R22.5*, inflated at 820 kPa. The procedure for obtaining the profile combines two image reconstruction methods: *Fringe Projection Method* (FPM) and *photogrammetry*. The goal is to extract a regularly meshed file that can be used by the present model. The two methods are briefly described below.

Fringe Projection Method (FPM): This method allows to obtain the three-dimensional profile of an object by analysing the changes of a projected fringe pattern on the object. The method generally consists of four main steps:

- *Projection and acquisition:* A structured pattern of fringe is projected onto the surface of the object. For the present tire profile, a sinusoidal fringe pattern has been used.
- *Fringe analysis:* The image of the fringe pattern, which is modulated by the object height distribution, is recorded. For the present tire, a Charged Coupled Device (CCD) camera has been used for recording the images. The phase modulation is calculated by analysing the image with a fringe analysis technique. A FFT method has been used here to get the phase distribution of the fringe images.
- *Phase unwrapping:* A continuous phase distribution has to be found from the wrapped phase map. A grey-scale color code coupled with a phase shift has been used to do so.
- *Calibration:* This final step is to make a correspondence between the phase distribution and the real 3D coordinates.

The FPM for a tire 5.2S10 has allowed to obtain the profile in Fig. 7.2. The FPM

Figure 7.2: The profile obtained by using the Fringe Projection Method (FPM) on a trailer tire 5.2S10 [MAN 19b].

method has been coupled with the *photogrammetry* method for obtaining the desired meshed profile of the tire.

The photogrammetry method: Also called *stereophotogrammetry*, it consists in using two-dimensional images to generate a three dimensional single one. Many photographs are taken of a fix object under various angles and then a reconstitution is performed by using a special software.
From the different photographs of the object, common points are identified. A line

of sight (or line of ray) can be constructed from the camera location to the point on the object. It is the intersection of these rays (triangulation) that determines the three-dimensional location of the point. This photogrammetry process has been performed for this trailer tire *Michelin 315/80R22.5* by Manyo [MAN 19b] with the help of the software *Capture Reality*. It has allowed to generate a mesh made of triangular elements.
Figure 7.3 shows the a) meshed; b) textured; c) meshed and textured surface of the tire obtained by this photogrammetry method.

(a) Meshed (b) Textured (c) Meshed and Textured

Figure 7.3: The profile obtained using the Fringe Projection Method (FPM) on a trailer tire *Michelin 315/80R22.5* [MAN 19b].

Finally, an image reconstitution has to be made to find the good data table for the present model. The reader is recalled that the actual SAM uses a regular mesh with rectangular elements imposed, among other things, by the use of FFT. Thus, the reconstitution model developed by d'Errico [D'E 16] is used to extract a surface meshed regularly with rectangular elements from the obtained data. Figure 7.4 shows a three dimensional surface of the obtained data in the form of a dual tire. Note that this dual tire is a simple duplication of the obtained single tire. This tire will be used throughout this chapter for the calculation every time that the real tire will be called upon.

Before deeper analysis, let's evaluate the impact of using this real tire profile, on the design of the pavement. For the purpose, a comparative study is performed in what follows next.

7.2.2 Influence of the real tire profile on the stresses in the road pavement

To perform the simulations, the tire is taken as an elastic homogeneous isotropic body of Young modulus $E_{tire} = 3.649$ MPa and Poisson's ratio $\nu_{tire} = 0.5$. The pavement is a multi-layered half-space with the characteristics given in Tab. 7.1. It has come that the very first step of the analysis should be the analysis of a pure normal contact case. This configuration is the elastic frictionless rolling contact of the tire on the pavement. Only a normal force $P = 65000$ N is applied on the

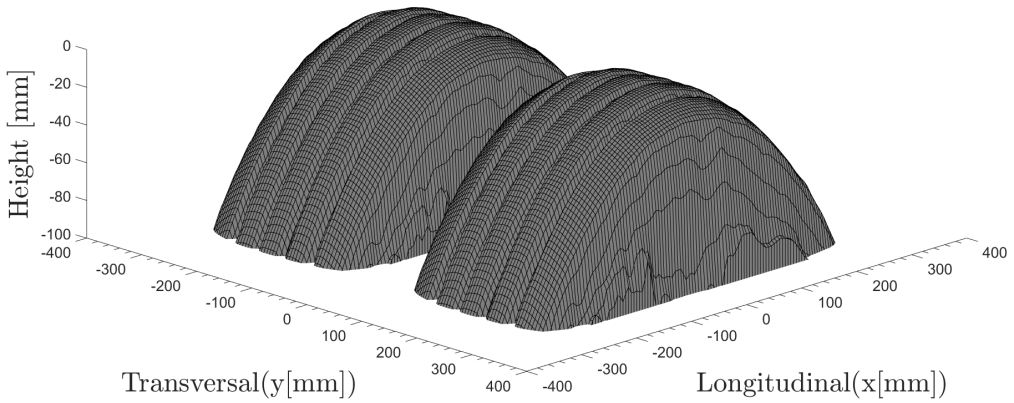

Figure 7.4: Three dimensional view of the final dual tire obtained by the FPM and the photogrammetry methods.

dual tire. The contact is supposed frictionless i.e the friction coefficient $f = 0$. The surface as well as the tire are discretised with square elements of size 5×5 mm^2.

With view to make a comparison, the same simulation has been performed by using in one hand the real tire profile, and in the other hand two spheres of radius $R = 125$ mm with a distance $d = 375$ mm between their center. In fact, it should be a footprint where a constant pressure is set on the dual footprint according to the framework in Fig. 7.1. For solving the contact the spheres have been chosen and the out-coming results in the zones of interest have shown a good agreement with the results which are based on footprints.

	Thickness [mm]	**Young modulus E [MPa]**	**Poisson's ratio**
1	50	5400	0.35
2	80	9300	0.35
3	850	83	0.35
4	770	16	0.35
5	200	500	0.35
6	∞	100000	0.35

Table 7.1: Set of elastic properties for the layers of the pavement structure.

Figure 7.5 shows the two dimensional contact pressure distribution for a) the two spheres and b) the real tire profile. Both the calculations have been performed with the present model. The differences in the contact are expected and so do not worth further discussions. The only relevant observation one can make is the realistic form of the pressure distribution given by the real profile showing not only the ability of

this contact model to handle the tire-pavement contact.

In order to find out if it is worth using the real tire for the dimensioning of the road pavement, it is important to pay a close attention to the three dimensional stresses. In this spirit, Fig. 7.6 shows a three dimensional view of the second invariant of the stress tensor $\sqrt{J_2}$ for both cases. The differences between the two profiles do not seem very significant in the subsurface.

	Thickness [mm]	**Young modulus E [MPa]**	**Poisson's ratio**
1	60	2054	0.35
2	80	2763	0.35
3	850	83	0.35
4	770	16	0.35
5	200	500	0.35
6	∞	10000	0.35

Table 7.2: Set of elastic properties for the layers of the pavement structure for comparison with ViscoRoute.

Moreover, in Fig. 7.7 a comparison is made between the results from the present SAM and from the software ViscoRoute [CHA 10]. The previously described framework has been taken for the simulation in ViscoRoute in elasticity and viscoelasticity; but with elastic properties of Tab. 7.2. Then, the components a) σ_{xx}, b)σ_{yy} c)σ_{zz} and d)σ_{xz} of the stress tensor are plotted at the first interface i.e. for $z = 60$ mm in the middle plane $y = 0$ along the x. The four cases are: the two cases presented here i.e. the dual sphere profile and the real profile, and the elastic and viscoelastic cases from ViscoRoute. One can highlight that, in elasticity, a good agreement is found between the two models. In addition, the use of the real tire profile does not seem to have a significant effect on the stresses at that interface.

It is important at this step to recall that generally, the design of pavement is performed at the interfaces and in particular at that first interface ($z = 60$ mm in this comparison). Therefore, if the only parameter was the stress at that first interface, the conclusion would be that it is not necessary to use the real tire profile for the dimensioning of the interfaces.

In summary, the analysis of the effect of the real tire profile shows that close to the surface the impact of the real profile is undeniable. However, at the first interface, the effects are not significant. This conclusion is valid for a framework where only the frictionless rolling contact has been considered.

Apart from the real tire profile, one can ask what is the impact of textures on the road on the stresses. The present model allows to take into account any surface profile for both bodies in contact. It means that not only the real tire profile can be modelled but also the real surface profile of the road. Before putting efforts in obtaining the real surface profile of the road, it is possible with the present model to investigate numerically its eventual impact.

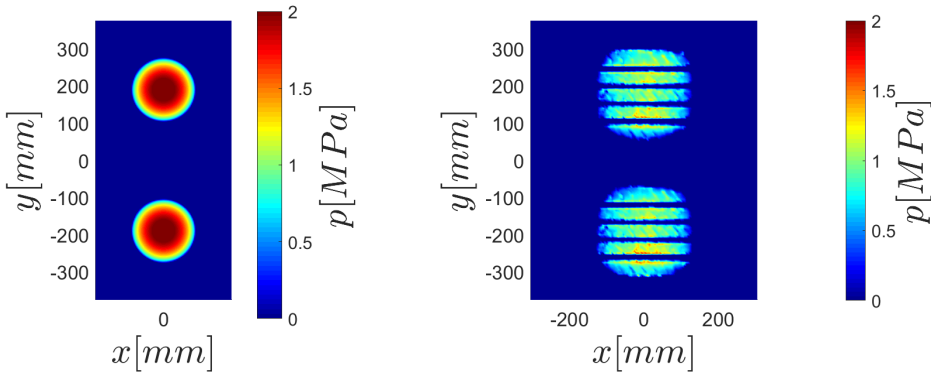

Figure 7.5: tire-pavement contact simulation for a) the dual sphere as tire profile versus b) the real dual tire profile obtained by image reconstitution.

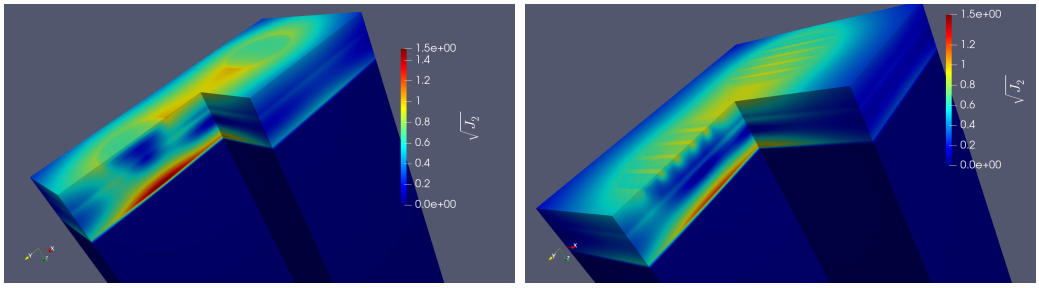

(a) Dual sphere (b) Real tire profile

Figure 7.6: Three dimensional second invariant $\sqrt{J_2}$ of the stress tensor for tire-pavement contact simulation for a) the dual sphere as tire profile versus b) the real dual tire profile obtained by image reconstitution.

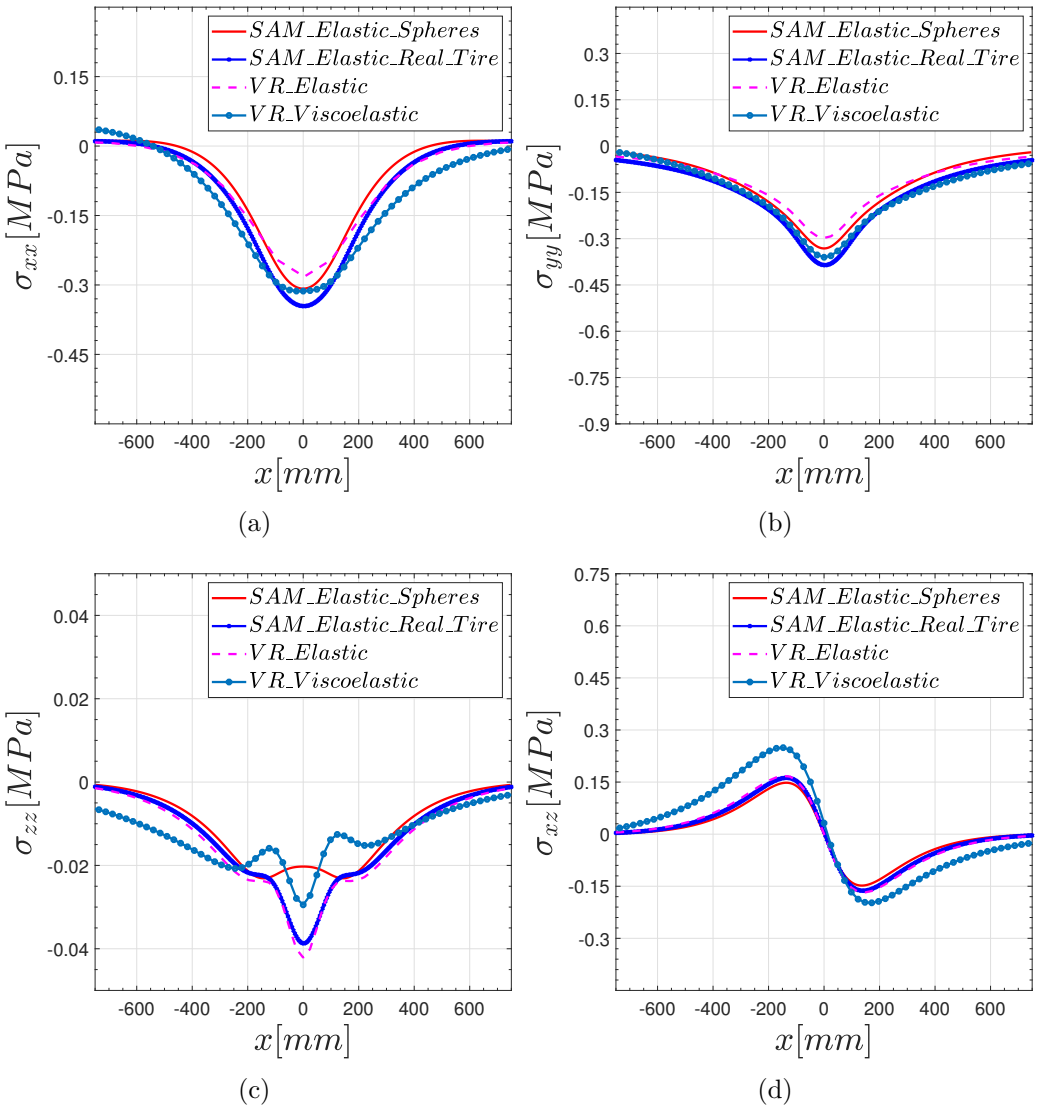

Figure 7.7: Comparison between the present semi-analytical model (SAM) and the software ViscoRoute. Stresses at the first interface ($z = 50$ mm) of the elastic multi-layered pavement structure are plotted. The components a) σ_{xx} ; b) σ_{yy} ; c) σ_{zz} and d) σ_{xz} of the stress tensor are plotted along the x axis in the middle plane $y = 0$.

7.3 A smooth road or a real road?

For the analysis of the effect of a rough road on the tire-pavement contact, the real tire profile is used. A rough road surface is generated randomly with the Root Mean Square (RMS) method. The surface has a Gaussian height distribution and exponential autocovariance (in both directions). The RMS height is 2.5 mm and the correlation lengths are chosen the same in the two directions with a value 10 mm. Figure 7.8 shows the textured surface generated surface obtained.

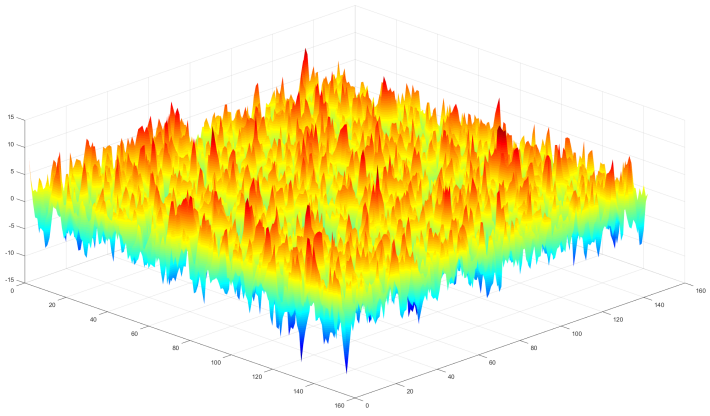

Figure 7.8: Random rough surface generated with a Gaussian height distribution and exponential autocovariance (in both directions).The RMS height is 2.5 mm and the correlation lengths are chosen the same in the two direction with a value 10 mm.

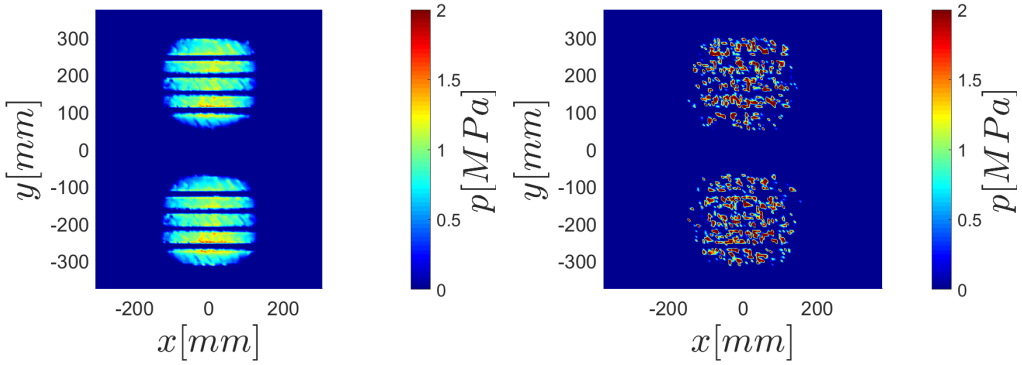

(a) Smooth surface (b) Rough surface

Figure 7.9: Pressure field for tire-pavement contact simulation with a) a smooth surface for the pavement versus b) a rough surface generated randomly with a RMS height of 2.5 mm.

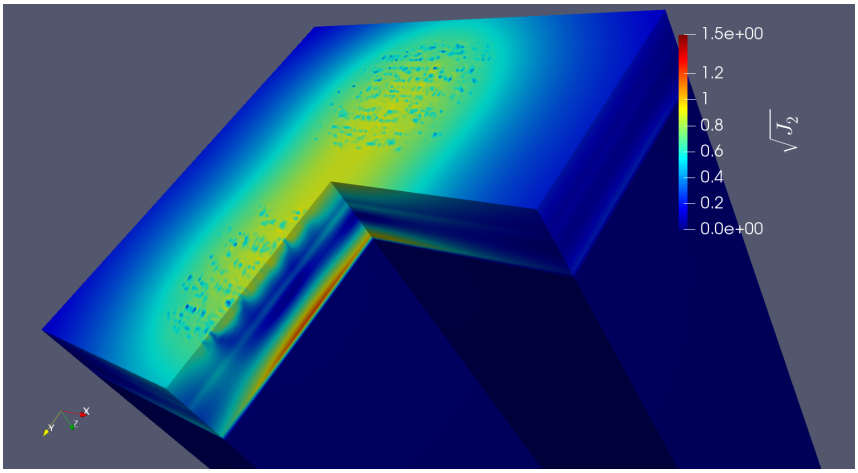

Figure 7.10: Three dimensional second invariant $\sqrt{J_2}$ of the stress tensor for tire-pavement contact simulation for a rough surface of the pavement generated randomly.

The set of parameters in Tab. 7.1 are used for the elastic properties of the pavement.
The surface pressure rendered from the contact simulation is compared to the one from a smooth pavement (see Fig. 7.5). One can observe that the maximum pressure is higher for the textured surface. This is due to the fact that, by using the use of a rough generated surface, the contact surface is reduced. In order to respect the equilibrium equation $P = \int_{\Gamma_c} p d\Gamma_c$, the pressures increase. This observation, even if it is expected, allows to say that the dimensioning method might ignore the fact that a very rough surface induces higher stresses in a zone close to the surface. Consequently, the aggression of the rolling course might be underestimated. This can partially explain the degradation to the zone very close to the surface on some very rough roads.
When plotting the second invariant $\sqrt{J_2}$ of the stress tensor in the pavement structure, Fig. 7.10 is obtained. The observation of the maximum stress for this case, compared to the case of smooth road in Fig. 7.6(b), shows the same maximum with very slight differences in general. Further investigation is done by plotting the components a) σ_{xx} ; b) σ_{yy} ; c) σ_{zz} and d) σ_{xz} of the stress tensor at the first interface i.e. $z = 50$ mm, along the x axis in the middle plane $y = 0$ in Fig. 7.11. The changes on the stresses at that interface are not significant. This indicates that the effect of the roughness of the road is limited to a zone close to the surface.

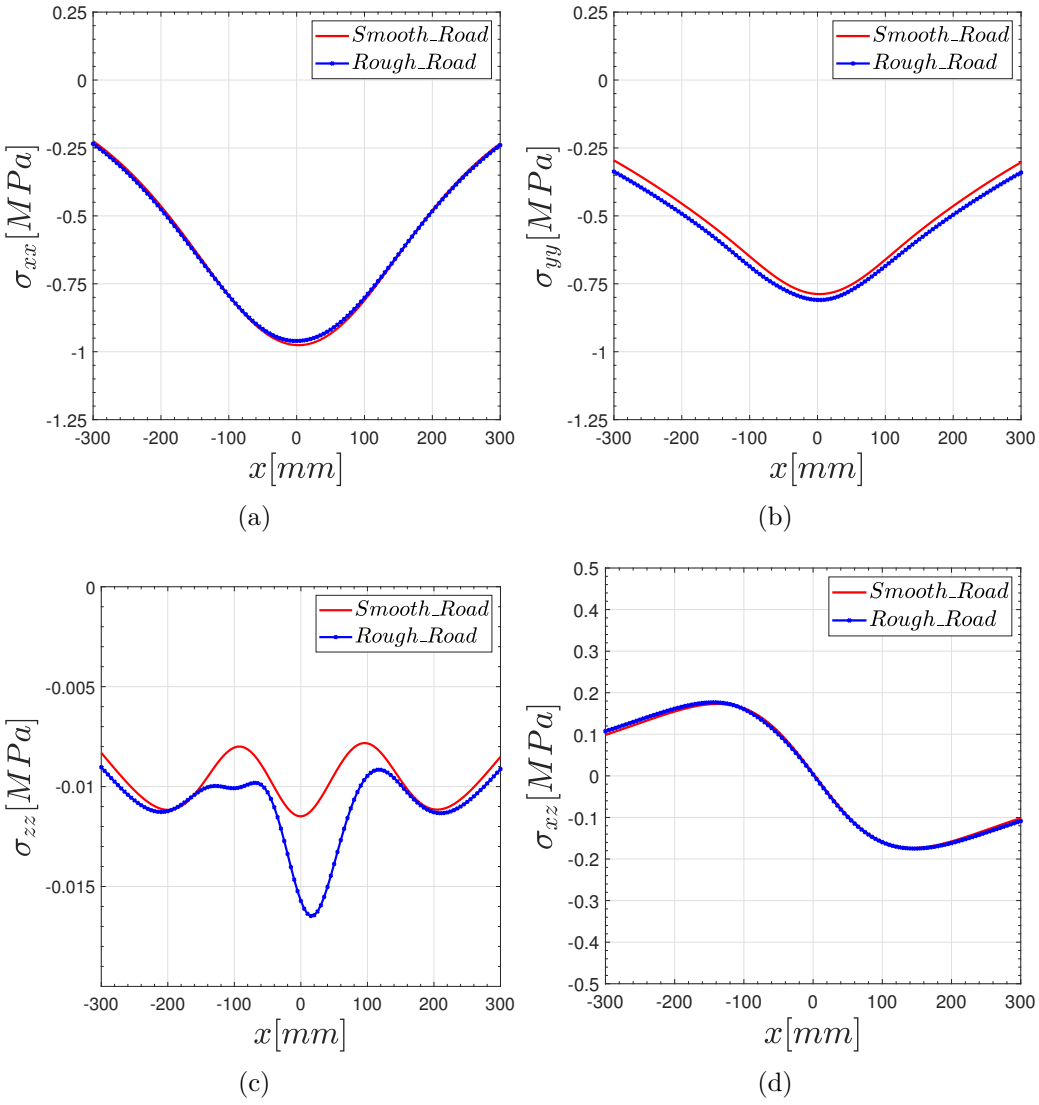

Figure 7.11: Influence of the roughness of the surface of the road pavement on the stresses at the first interface ($z = 50$ mm) of the elastic multi-layered pavement structure. The components a) σ_{xx} ; b) σ_{yy} ; c) σ_{zz} and d) σ_{xz} of the stress tensor are plotted along the x axis in the middle plane $y = 0$.

Ultimately, the frictionless rolling contact has been analysed using the developed semi-analytical model. In this configuration, the investigations have brought out that the tire profile has an impact in a zone very close to the surface but not at the first interface. The roughness surface profile of the road is expected to have an impact also limited to a region very close to the rolling surface but not at the first critical interface.

In those results, the friction at the contact interface has not been considered. In practice, there is friction between the tire and the pavement. Thus, the elastic tractive rolling contact should be studied instead.

7.4 Elastic tractive rolling contact between tire and pavement

The transient tractive rolling contact has been exposed in detail in the previous chapter 5. Briefly, it is the rolling motion where an overall tangential force and/or moment are applied on the rolling body. Forces and/or moment are applied so that the body does not go into a full sliding motion (also called gross slip). With the Coulomb's friction law, it means that the overall tangential forces are $< fP$, where f is the friction coefficient and P is the normal force applied. The developed algorithm in chapter 5 can operate here for the grasp of the influence of the friction on the elastic rolling motion between tire and pavement.

For the study, a friction coefficient $f = 0.7$ is considered at the contact interface between the tire and the pavement. The elastic properties of Tab. 7.1 are used for the pavement structure; and the tire remains incompressible $\nu_1 = 0.5$ with a Young modulus $E_1 = 3.649$ MPa.

The general tractive rolling loading for the tire pavement contact is presented in Fig. 7.12 where longitudinal and tractive forces are applied as well as a spinning moment around the z axis. The tire is rolling in the x direction. By combining the tangential forces and the moment, several real cases can be simulated. Some of those cases are studied in what follows next.

For all the simulations below, the real tire profile is used. The surface is taken smooth and discretised with square elements of size 5×5 mm^2. A normal force $P = 65000$ N is applied. The rolling motion is simulated in 200 time steps with an elementary displacement at each step set to 5 mm.

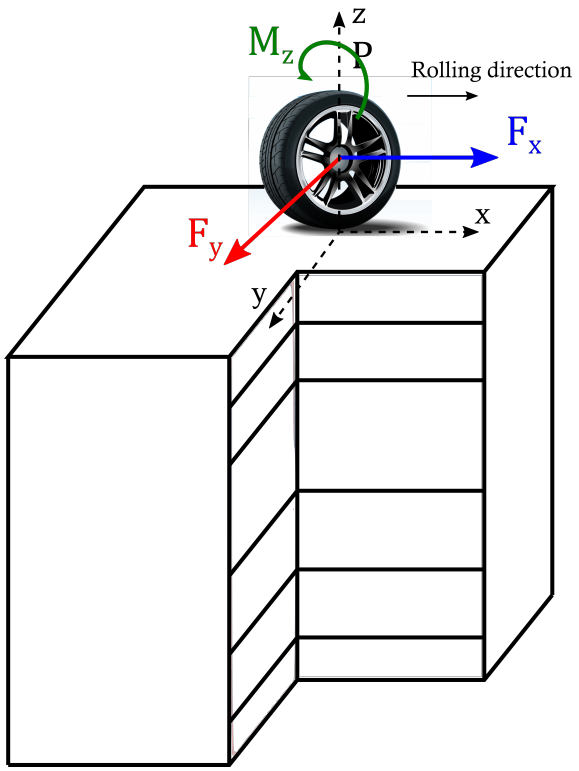

Figure 7.12: General case of tractive rolling contact of a tire on a multilayered pavement structure. Tangential forces F_x, F_y and a spinning moment M_z are applied on the tire in addition to the normal force P.

7.4.1 Pure Rolling

The pure rolling case studied here is the rolling case where only a normal force is applied on the system. If there was no friction at the contact interface, this contact case would be exactly the same as the one studied in sections 7.2 and 7.3 i.e. a frictionless rolling. Due to the friction, even when no tangential force is applied, shear tractions appears in the contact zone. This remark is based on the works of Spence [SPE 75] in contact mechanics as explained earlier in this document.

The goal here is to highlight the influence of the normal contact pressure on the shears in the tire-pavement contact. For this purpose, the rolling contact has been simulated in the same conditions as in section 7.2 but with a friction $f = 0.7$ at the contact interface. The results in terms of normal pressure remain the same as in section 7.2, but this time shear tractions are obtained in the contact zone. The two dimensional view of the contact shear vector norm is plotted in Fig. 7.13 for a covered distance a)$V_t = 0$, b) $V_t = 50$ mm, c) $V_t = 100$ mm, d)$V_t = 150$ mm , e)$V_t = 250$ mm and f) $V_t = 1000$ mm.

From a qualitative point of view, the shear are higher at the first step and decrease throughout the steps. However, in general, one can highlight that the

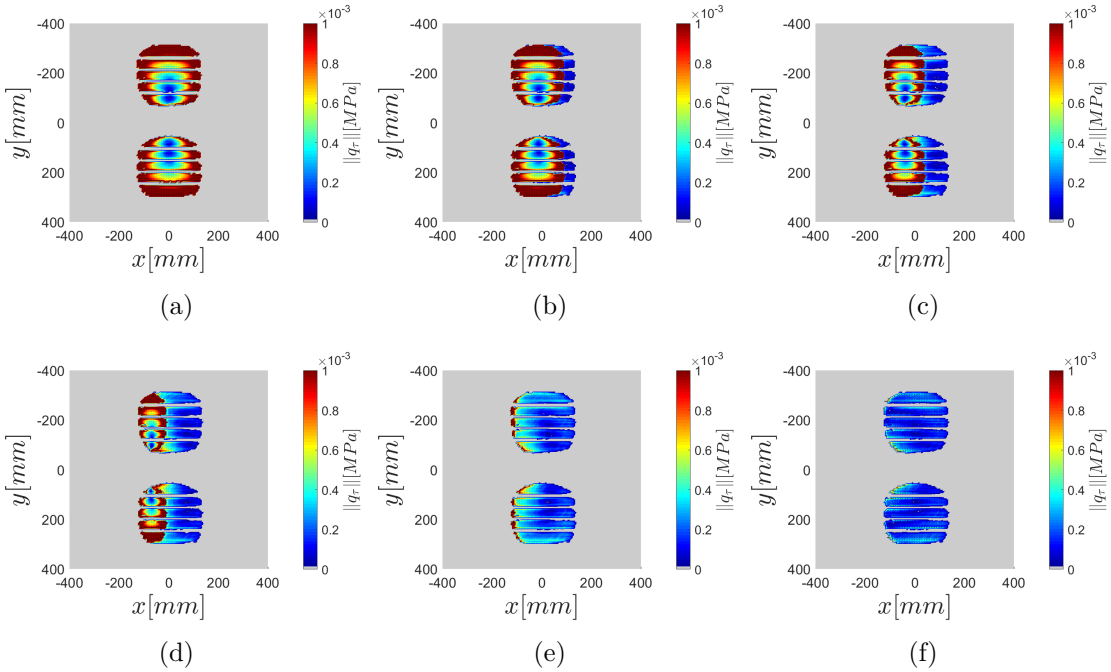

Figure 7.13: Evolution of the norm of the shear vector in the contact zone in a pure rolling tire-pavement contact for a friction coefficient $f = 0.7$.

shear is takes very low values. Therefore, it would make sense not to take them into account in a design process.

The above analysis, allows to neglect the effect of the normal contact on the tangential shears in the rolling motion. Thence, in the following simulations, the tractive rolling will be studied with no coupling between the normal and the tangential problems so that the calculations can process faster. The coupling between the tangential components x and y remains. Three cases of tractive rolling have been chosen with view to represent what can happen in reality: *acceleration*, *turnaround* and *drift* situations.

7.4.2 Acceleration

For the acceleration of a car during a rolling motion, a tangential longitudinal force has to be prescribed in the direction of the rolling. This driving force represents a longitudinal tractive force applied on the wheels. It implies the opposite force on the road. In the modelling, a tractive force $F_x/fP = -0.75$ is applied on the pavement in the direction of the rolling, while $F_y = 0$ and $M_z = 0$.

The two dimensional view of the norm of the contact shear vector is plotted in Fig. 7.14 for a covered distance a) $V_t = 0$, b) $V_t = 50$ mm, c) $V_t = 100$ mm, d) $V_t = 150$ mm , e) $V_t = 250$ mm and f) $V_t = 1000$ mm.
Firstly, the overall values of the shear tractions are high and of the same order as

the pressure (see Fig. 7.5). Secondly, one can observe the evolution of the shears from the transient regime to the steady state regime where a slip zone stand at the trailing edge while an adhesion zone lies in the leading edge of the contact.
From the first remark, the effects of shears on what happens in the subsurface cannot be expected negligible. The plot the second invariant $\sqrt{J_2}$ of the stress tensor in the pavement shows in Fig. 7.15 that in the zone close to the surface the stresses are very high. Thence the aggression of the top layer becomes significant and may explain the degradations of pavements from the top.

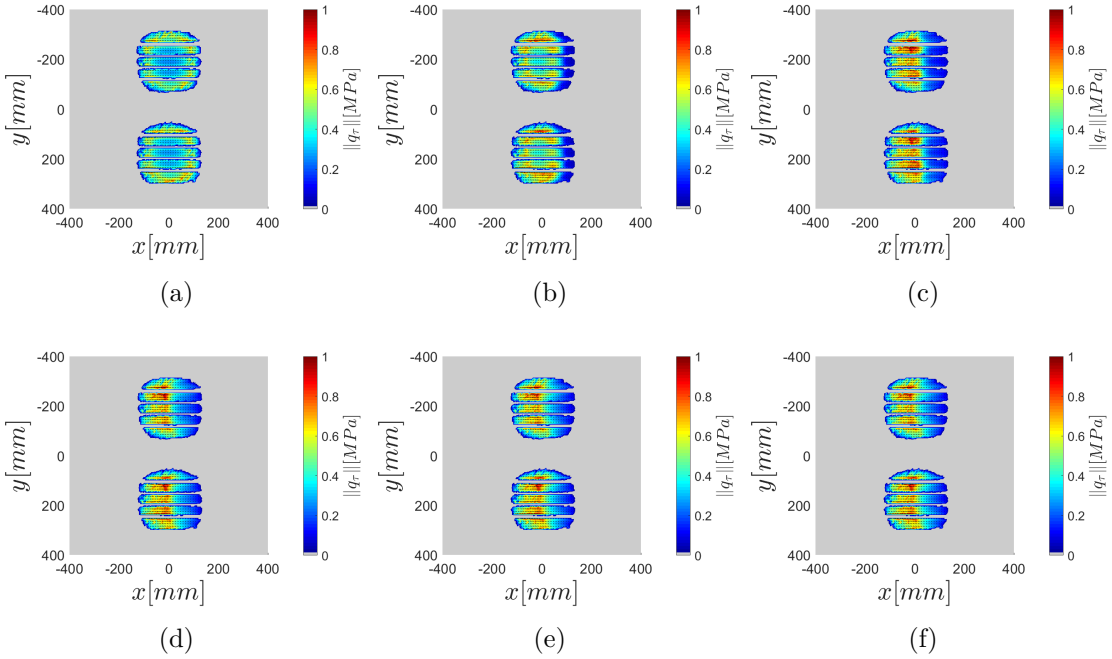

Figure 7.14: Two dimensional view of the norm of the contact shear vector for a covered distance a) $V_t = 0$, b) $V_t = 50$ mm, c) $V_t = 100$ mm, d) $V_t = 150$ mm , e) $V_t = 250$ mm and f) $V_t = 1000$ mm. An "acceleration" motion is analysed where only a tractive force $F_x/fP = -0.75$ is applied on the pavement.

In the acceleration motion, only the longitudinal tractive force is applied. It implies that the component q_x of the contact shear vector is the dominant one as shown in Fig. 7.16 where the components a) q_x and b) q_y of the shear vector are plotted.

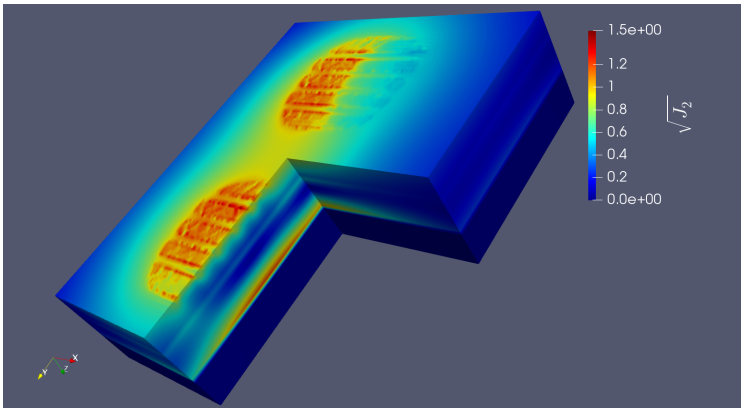

Figure 7.15: Three dimensional view of the second invariant $\sqrt{J_2}$ of the stress tensor in steady state regime for an "acceleration" motion where only a tractive force $F_x/fP = -0.75$ is applied on the pavement.

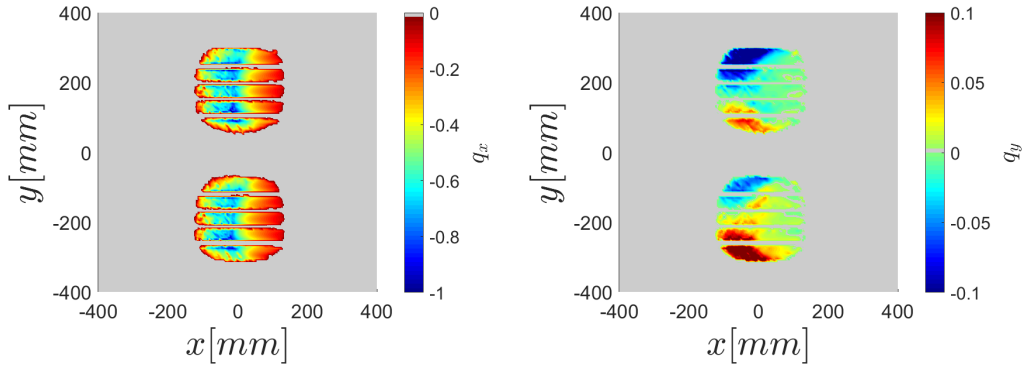

(a) (b)

Figure 7.16: Two dimensional view of the components a) q_x and b) q_y of the contact shear vector in steady state regime for an "acceleration" motion where only a tractive force $F_x/fP = 0.75$ is applied on the pavement.

7.4.3 Turnaround

For the simulation of a car or a truck in a turnaround situation, a transversal tractive force is applied to represent the centrifugal force in the turnaround, $F_y/fP = 0.45$. Besides, a moment around the z axis is set to represent the turning motion imposed to the wheels, $M_z = 7000$ N.m.
Note that even if the titling of the tire has been shown recently to have some effects on the distribution of the shears in the contact zone [OUB 21], it is not taken into account in here.

The results of the simulation of the turnaround are given in Fig.7.17. In a) a three dimensional view of the second invariant $\sqrt{J_2}$ of the stress tensor is plotted, showing a very significant increase of the stresses close to the surface in comparison with the free rolling case studied in section 7.2. In steady state regime, the 2D view of the components q_x (Fig. 7.17(b)) and q_y (Fig. 7.17(c)) of the shear vector are given. Finally, a two dimensional view of the norm of the contact shear vector is plotted in steady state regime in Fig. 7.17(d).
From the norm of the shear vector, one can see that in the turnaround case, in steady state regime, the slip zone is located at the trailing edge as for the acceleration. Moreover in this case, it seems that the shears are higher close to the exterior edges of the tires.

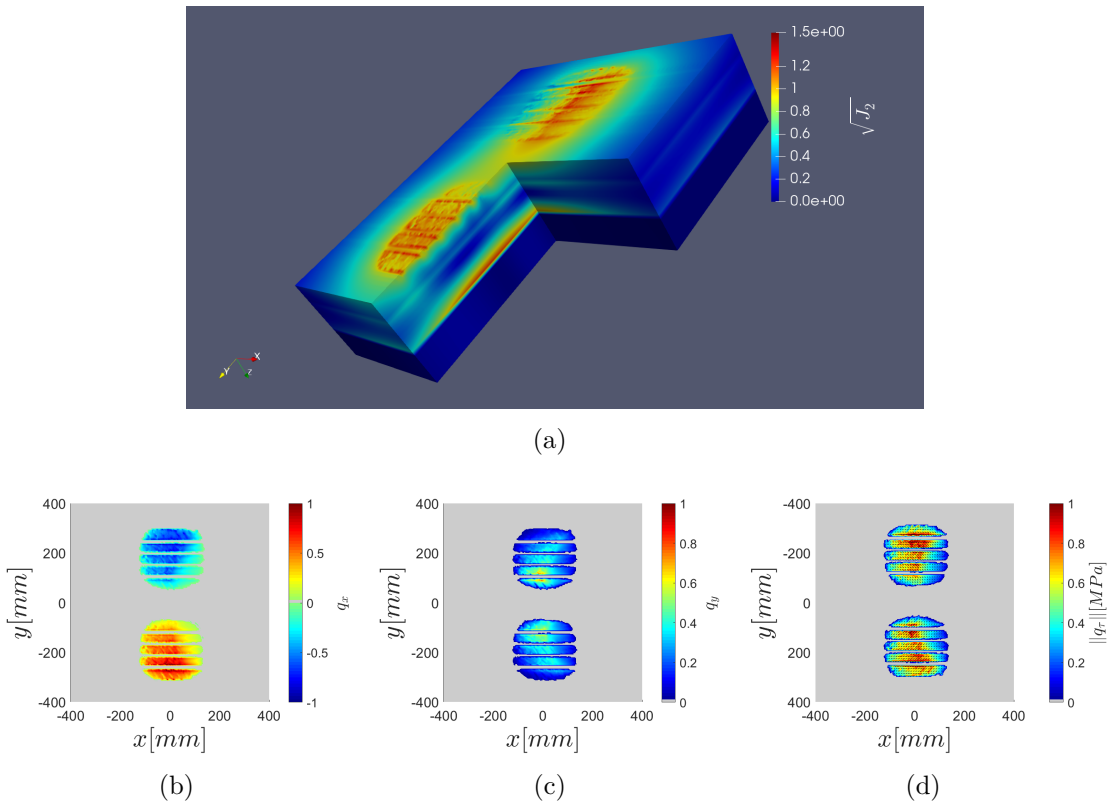

Figure 7.17: Tire-pavement contact results in a turnaround motion where a transversal tractive force $f_y/fP = 0.45$ and a spinning moment $M_z = 7000$ N.m are applied on the tire. In a) a three dimensional view of the second invariant $\sqrt{J_2}$ of the stress tensor is plotted. The components b) q_x and c) q_y of the contact shear vector and its norm in d) are also given.

7.4.4 Drift

The drift is thought here as a motion where the driver is simultaneously braking, and turning the wheels. Therefore, the simulation is performed by applying a negative longitudinal tractive force on the wheels. This implies a positive longitudinal force $F_x/fP = 0.4$ which represents the braking force; a transversal tractive force is applied for the lateral effects due to the centrifugal force $F_y/fP = -0.25$; and a moment is applied $M_z = -3500$ N.m as the turning force.

The results of the simulation of this drift are given in Fig.7.18. In a) a three dimensional view of the second invariant $\sqrt{J_2}$ of the stress tensor is plotted, showing as for the other cases of tractive rolling a significant increase of the stresses close to the surface in comparison with the free rolling case studied in section 7.2. In steady state regime two dimensional views of the components q_x (Fig. 7.18(b)) and q_y (Fig. 7.18(c)) of the shear vector are given. Finally, a two dimensional view of the norm of the contact shear vector is plotted in steady state regime in Fig. 7.18(d).

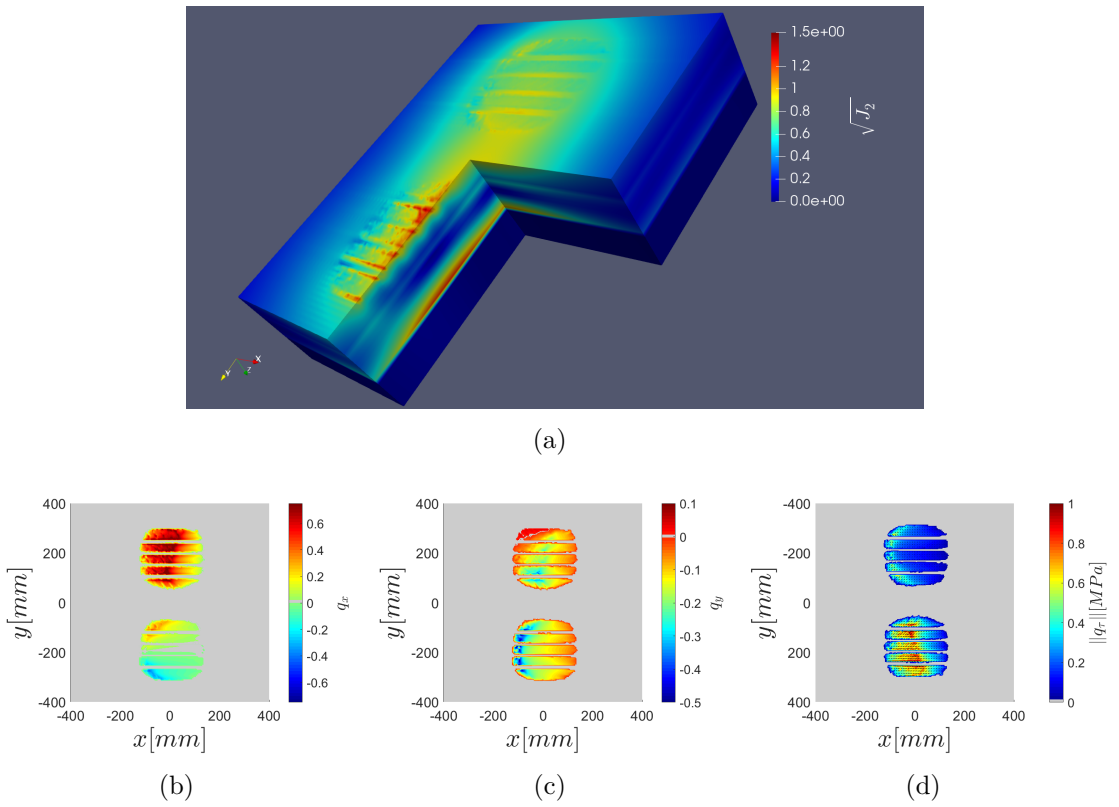

Figure 7.18: Tire-pavement contact results in a drift motion where a braking force in the longitudinal direction $F_x/fP = 0.4$, a transversal tractive force $f_y/fP = -0.25$ and a spinning moment $M_z = -3500$ N.m are applied on the tire. In a) a three dimensional view of the second invariant $\sqrt{J_2}$ of the stress tensor is plotted. The components b) q_x and c) q_y of the contact shear vector and its norm in d) are also given.

It is interesting to remark that in this case of drift, the shears are dominant under one tire of the dual tire. It means that, while one of the tire is having a good adhesion on the road, the other shows significant slip areas in its contact zone.

Furthermore, the plot of the stresses a) σ_{xx} ; b) σ_{yy} ; c) σ_{zz}; d) σ_{xz}; e) σ_{xy} and f) σ_{yz} of the stress tensor along the x axis in the middle plane $y = 0$ gives Fig. 7.19. The plot of the same stresses is given in Fig. 7.20 but in the plane $y = 90$ mm (interior edge of one of the tires).

The analysis of Figs. 7.19 and 7.20 allow to say that clear changes are observed at the interface $z = 50$ mm when the tractive effects are taken into account the calculation of the stresses in the pavement. For instance, the shear stress σ_{xy} is higher in the turnaround and drift cases where a lateral tractive force and a spinning moment are involved. Note that the higher overall tractive force has been applied in the acceleration case. This is the reason why this case shows the higher stresses in general.

As consequence of the increase of the stresses for those cases of tractive rolling, the strains also increase. In this respect, the stresses a) ε_{xx} and b) ε_{yy} in Fig. 7.22 show great increase in tractive rolling cases compared to the pure rolling case.

It is interesting to highlight the asymmetry of the strains. This asymmetry has been observed by Petitjean et al. [PET 02] in asphalt pavements. It has been explained by authors such as Chabot et al. [CHA 10, CHA] as a result of the viscoelastic behaviour of the asphalt pavements. It is clear that viscoelasticity is not negligible when dealing with asphalt material in pavement structures. However, for very low temperatures (9.7° C in [CHA 10]), even for low frequencies (0.33Hz in [CHA 10]), viscoelasticity might not be the only reason why this asymmetry is observed. The results in Fig. 7.22 provides new information and ideas on the physics involved.

In summary, the observations in this analysis allow to question the fact of ignoring the tractive effect in the design process. The above results clearly show that the effects of the tractive forces are very significant close to the contact surface; and those effects are seen at the first interface also.

Furthermore, in order to link the modelling works to the application, experimental tests have been performed for the measurement of strains in the pavement structure. A comparison between the results from the model and a real rolling case is performed in the next section.

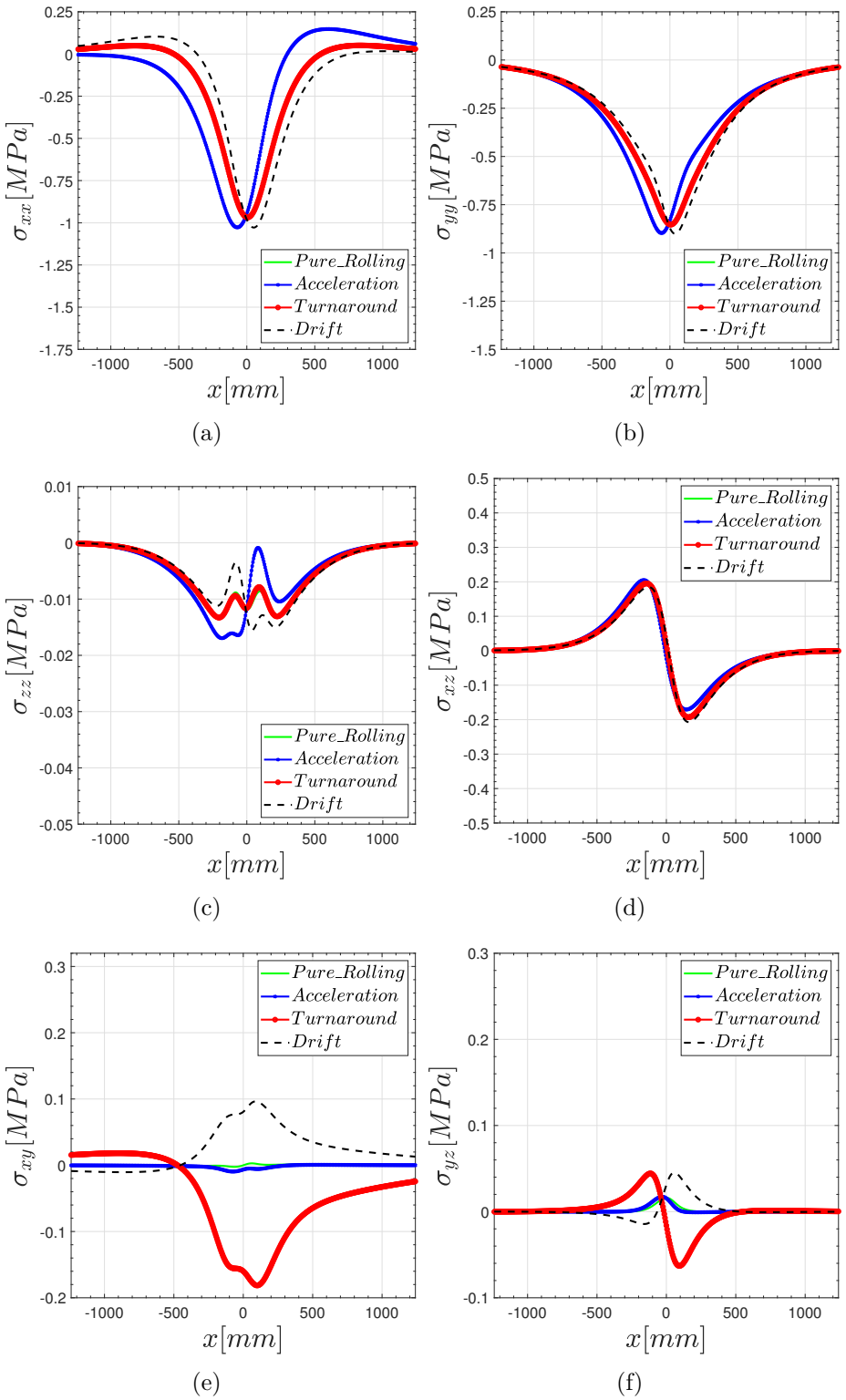

Figure 7.19: The components a) σ_{xx} ; b) σ_{yy} ; c) σ_{zz}; d) σ_{xz}; e) σ_{xy} and f) σ_{yz} of the stress tensor along the x axis in the middle plane $y = 0$. A comparison is made in tractive rolling between a pure rolling, an acceleration motion, a turnaround motion and a drift motion.

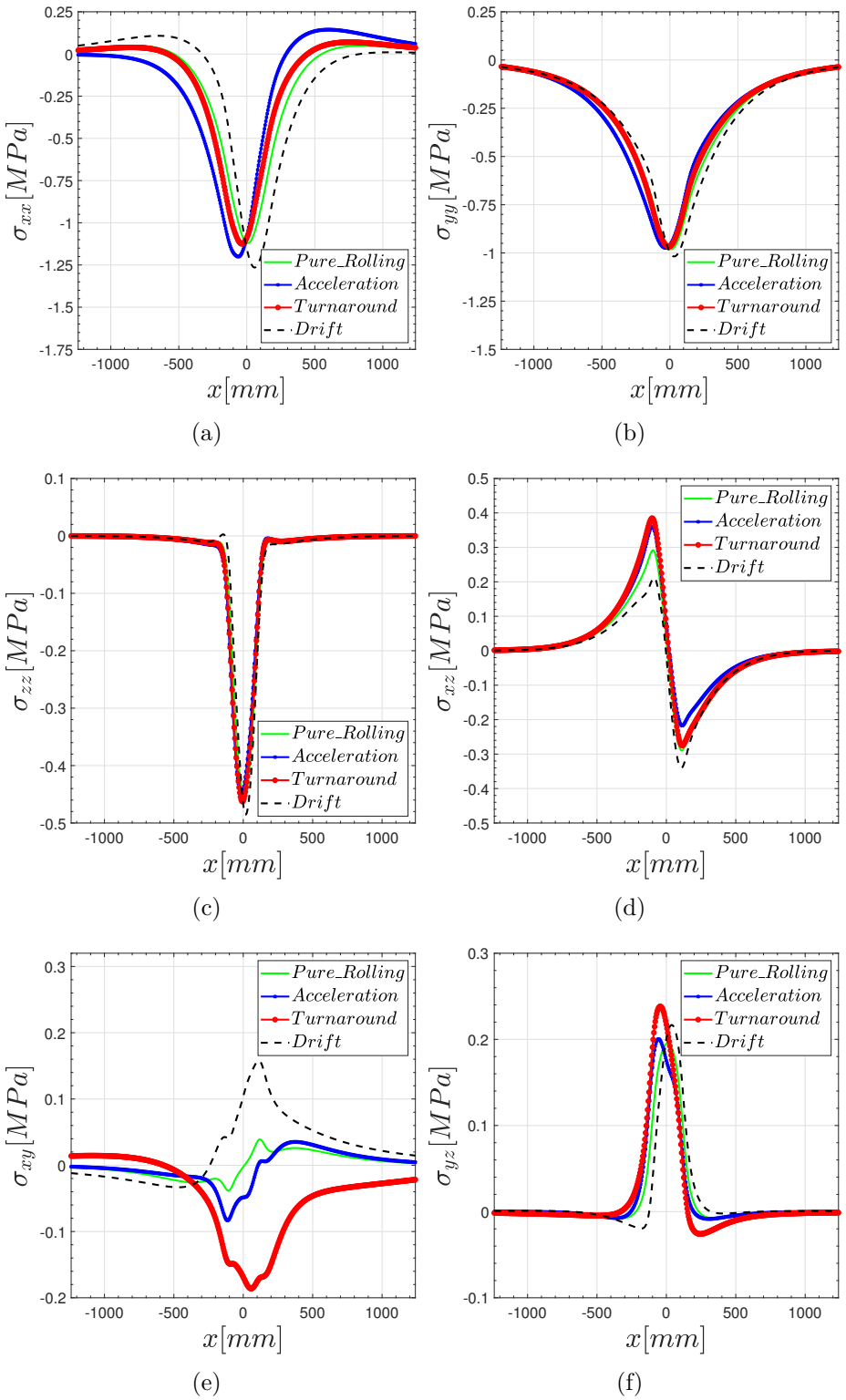

Figure 7.20: The components a) σ_{xx} ; b) σ_{yy} ; c) σ_{zz}; d) σ_{xz}; e) σ_{xy} and f) σ_{yz} of the stress tensor along the x axis in the plane $y = 90$ mm (below the interior edge of one of the tires). A comparison is made in tractive rolling between a pure rolling, an acceleration motion, a turnaround motion and a drift motion.

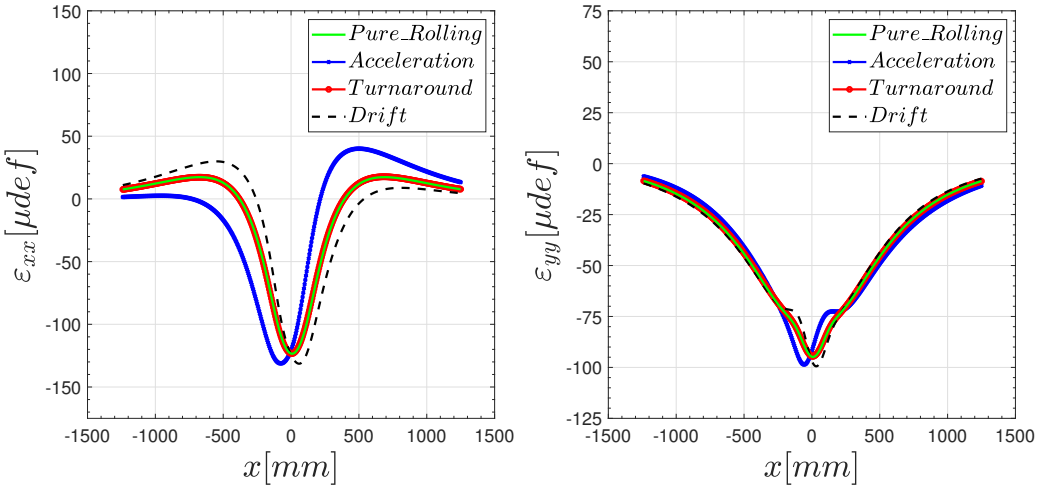

Figure 7.21: The components a) ε_{xx} and b) ε_{yy} of the strain tensor are given along the x axis in the middle plane $y = 0$. A comparison is made in tractive rolling between a pure rolling, an acceleration motion, a turnaround motion and a drift motion.

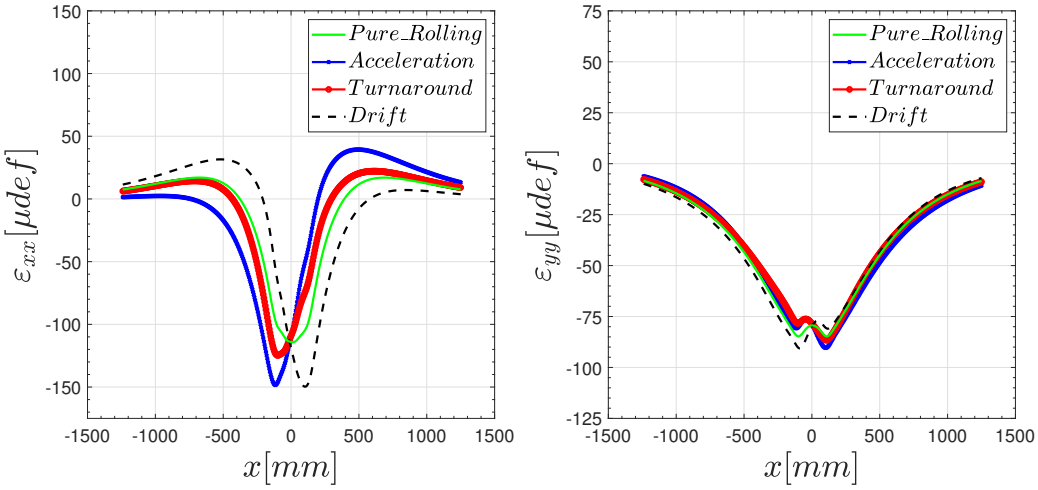

Figure 7.22: The components a) ε_{xx} and b) ε_{yy} of the strain tensor are given along the x axis in the plane $y = 90$ mm (below the interior edge of one of the tires). A comparison is made in tractive rolling between a pure rolling, an acceleration motion, a turnaround motion and a drift motion.

7.5 Toward an Experimental Validation

The modelling work has been conducted in parallel with experimental studies in collaboration with the pavement team in the laboratory GC2D[1] . The goal of the experimentations is to reproduce the life cycle of the pavement under a controlled environment. Observations mainly concern the strains in the pavement (surface and interfaces) and surface rutting. For the purpose, a full scale testing in laboratory has been build to test new generations of pavement structures.

An experimental pavement has been constructed over a rectangular area of dimension $3 \times 8\,\mathrm{m}^2$ (see Figs. 7.25 and 7.24). Its structure in terms of elastic properties is given in Tab. 7.3 for a temperature of 15°C and frequency 1Hz (order of the frequencies of the solicitations). For the measurements of the results presented here, strain gauges have been placed at the first interface i.e. $z = 50$ mm. Classical strain gauges (specifications are given in Fig. 7.23) have been stuck between the first and the second layers in the longitudinal and the transversal directions. Their positions in the horizontal plane are precisely given in Fig. 7.24. The gauges are connected to an acquisition system (here HBM Spider-8) which allows to convert the changes of resistance of the gauges into micro-deformations i.e. strains.

Besides, the traffic simulator MLS10 in Fig. 7.26 has been used. The MLS10 has been constructed in Cape Town (South Africa) in 2006 for laboratory tests on pavement. It possesses four bogies, each supporting two tires (reference 295/65 R22.5, diameter 940 mm). The tires roll successively on the pavement structure and so simulate a regular traffic. A maximum normal charge $P = 65000$ N can be applied and a maximum velocity $v = 6.11$ m/s prescribed.

The simulation of the life cycle of a pavement structure, allows to study the various phenomena which occur in the life cycle of a real pavement in laboratory. In this work, few informations are given in order to directly tackle the measurements that fall into the present topic. The only informations concern the measurement of the strains at the interface $z = 50$ mm in a pure rolling motion of the tire over the pavement.

	Thickness [mm]	**Young modulus E [MPa]**	**Poisson's ratio**
1	50	2200	0.35
2	80	6900	0.35
3	850	83	0.35
4	770	16	0.35
5	200	500	0.35
6	∞	10000	0.35

Table 7.3: Set of elastic properties for the layers of the pavement structure for the experimental validation.

[1]GC2D is the "Laboratoire de Génie Civil, Diagnostic et Durabilité ", a civil engineering laboratory specialised in the pavement topic. It is based in the region of Limoges, France.

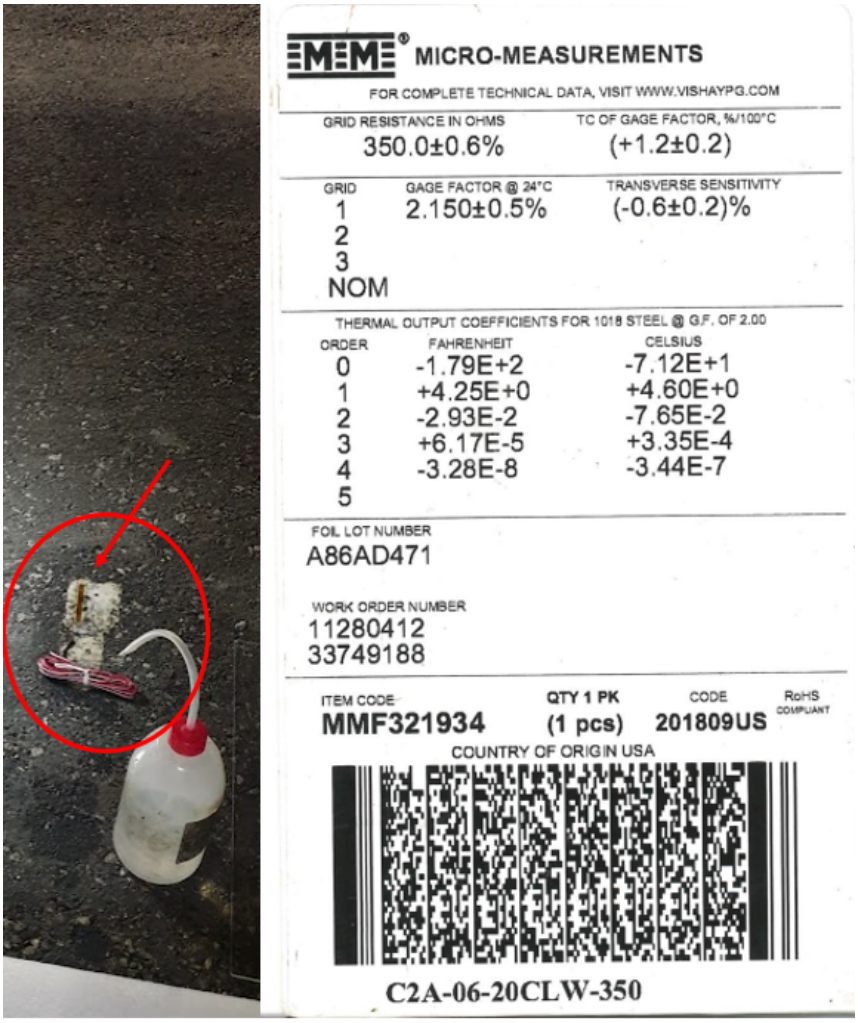

Figure 7.23: Specifications of the strain gauges placed at the interface $z = 50$ mm during the full scale experiments with the traffic simulator MLS10.

For the present validation, the normal load applied is $P = 65000$ N and the rolling velocity is $v = 1.94$ m/s. The temperature of the experiment is around 15°C. Then, the strains a) ε_{xx} in the middle plane $y = 0$ and b) ε_{yy} in the plane $y = 90$ mm (under the edge of the tire) are measured as showed in Fig. 7.24. In the experiments, the acquisition of strains is done with respect to time. Since the tire is moving along the x direction, those strains correspond to the strains along this x axis.
Note that for data gathered the motion is supposed to be a pure rolling motion. This because, in one hand there is no apply tangential load, and in the other hand the zone of measurements is not in the landing nor the take-off zones where an eventual transient regime can hold.

A comparison between the results of the experimentations and the modelling is performed in Fig. 7.27 where the strains a) ε_{xx} in the middle plane $y = 0$ and b)

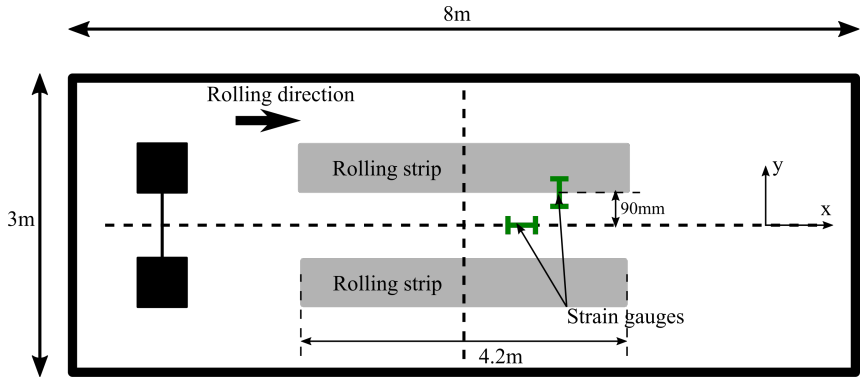

Figure 7.24: Position of the strain gauges at the interface $z = 50$ mm during the full scale experiments with the traffic simulator MLS10.

ε_{yy} in the plane $y = 90$ mm (under the edge of the tire) are plotted at the interface $z = 50$ mm along the x axis. One can say that the agreement found between the modelling and the experiments is satisfactory. The small differences may come from measurement uncertainties from the experimental point of view; while from the modelling, they may come from the fact that the formulation of the multi-layered half-space here hypothesizes perfectly bounded layers. However, in general a quite good correlation is found between the experiments and the modelling.

On the component ε_{xx} plotted in Fig. 7.27, one can see that the experimental data show a slight asymmetry. This asymmetry might be due to viscoelasticity or from the servo system which, with view to maintain the rolling velocity, has to regulate by applying slight tangential forces.

Figure 7.25: Building the pavement structure for the experimental investigations in GC2D.

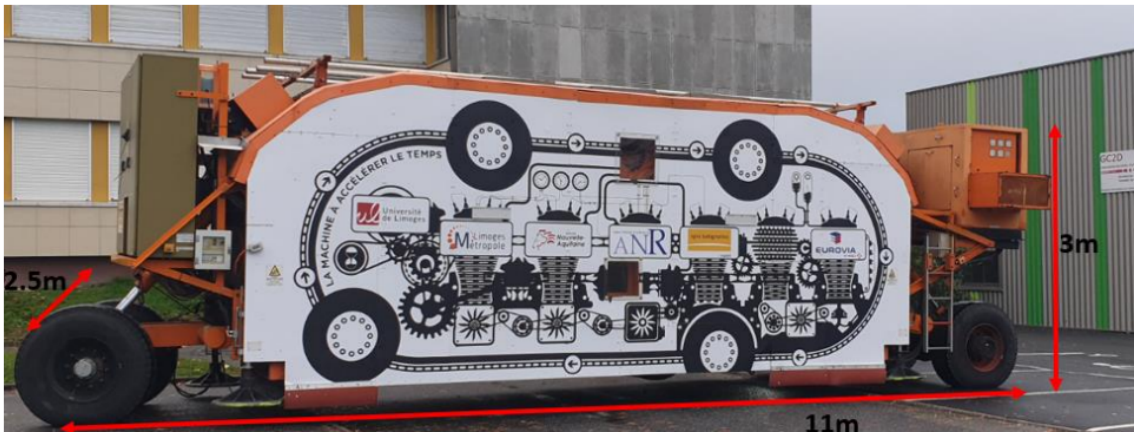

Figure 7.26: Traffic simulator MLS10 used for the full scale tests in laboratory.

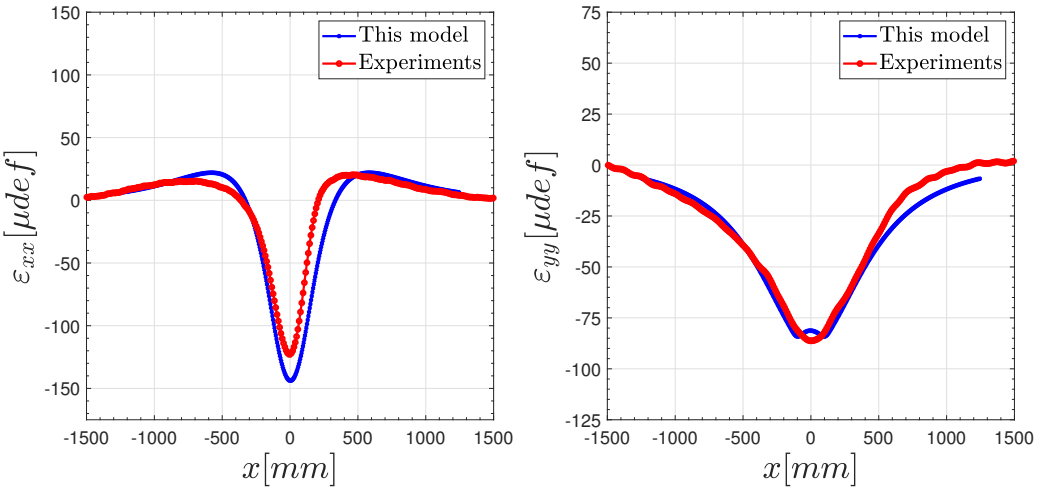

Figure 7.27: Comparison between the results from the experiments and the modelling. The strains a) ε_{xx} in the middle plane $y = 0$ and b) ε_{yy} in the plane $y = 90$ mm (under the edge of the tire) are plotted along the x axis at the interface $z = 50$ mm.

7.6 Conclusion

In this chapter, the rolling contact between a tire and a pavement structure has been analysed. With the model developed in this PhD work, the tire-pavement contact has been simulated with various loading conditions.

In a first part, the effects of the real tire profile and the effects of a rough generated road have been investigated. It comes that for both cases, the effects are marked in a zone close to the surface but less significant in the subsurface (from the first interface). Those effects have been analysed in a free rolling case.

In a second part, the tractive rolling contact has been simulated. Introducing friction at the contact interface has induced higher stresses in the pavement for acceleration, turnaround and drift cases in general. Moreover, according to the set of applied overall tangential forces, corresponding components of the stress tensor are modified.

Finally, an experimental comparison have been made using full scale tests. Strains at the first interface have been compared, showing a very good agreement between the experiments and the modelling in a free rolling case.

The reader may take from this study that the modelling proposed here allows to simulate real rolling cases. The results from the investigations of the tractive rolling allow to say that the design methods should take into account tangential effects. For example, a relatively simple acceleration case might integrate the dimensioning procedure in order to make sure that those tangential effects are not neglected.

Conclusions and prospects

Due to the under-dimensioning of road pavements, cracking and rutting are still observed at the top surface of the road pavements. In this work, it has been shown that for a better grasp of the origin of those degradations, the modelling has to be improved. Indeed, it has been shown that a real tire profile is to be used in the dimensioning; and the tractive effects during the rolling have to be taken into account.

After the generalities and the state of the art presented in the first chapter for both the tire-pavement topic and contact mechanics, a semi-analytical model has been developed. In fact, several aspects have been added to a home made Isaac code developed in LaMCoS, for solving efficiently the contact problem.

Isaac is based on a semi-analytical method which is presented in chapter 2. The method uses influence coefficients for the calculation of elastic fields. To reduce the computation time, Fast Fourier Transform (FFT) and Conjugate Gradient Method (CGM) algorithms are used.

The viscoelastic multi-layer aspect of the bodies in contact has been added in chapters 3 and 4. For this purpose, the influence coefficients have been calculated in the Fourier frequency domain and a numerical inverse transform has been performed. Then an Elastic/Viscoelastic correspondence has been proposed to turn the elastic solutions into their viscoelastic equivalent. The proposed correspondence is an exact solution is some cases (especially in steady state regime) and in the other cases, it is an approximation with a marginal error as shown by comparison with other methods. Moreover, the proposed model is 800 time faster than a Finite Element model computed in Abaqus. Using a generalised Maxwell model, parametric studies have been carried for a pure rolling contact. They have allowed to highlight the transition from transient to steady state regime; and the relaxation effects in a viscoelastic contact.

Further, the tangential effects have been analysed in the chapters 5 and 6. In chapter 5, the transient tractive rolling contact has been solved between elastically dissimilar and multi-layered bodies. Tangential forces and a spinning moment have been applied on the system. One of the highlights of the parametric study is that, when a transversal tangential force is imposed, it gives rise not only to a transversal creepage but also to a spin creepage. In a similar way, a moment gives rise to a transversal creepage. For the first time, the actual numerical method has been used for solving the transient tractive rolling. The results found well correlates

with the results of Kalker in the case of elastically similar and homogeneous bodies. Furthermore, the model solves efficiently the problem between elastically dissimilar and multi-layered bodies.
The chapter 6 focuses on the fretting contact on a multi-layered half-space. The classical problems of Spence and Cattaneo-Mindlin have been simulated on a single and a multi-layered half-spaces. Variations of the slip zone due to the coating have been highlighted.

Finally, the tractive rolling contact model has been applied to the tire-pavement contact. It has been shown that close to the rolling surface, it is important to take into account the real profile of the tire in the modelling. Further, several realistic cases of tractive rolling contact have been computed. Acceleration, turnaround and drift cases have shown that it is mandatory to take into account the tangential effects in the conception of roads in order to avoid an under-dimensioning, especially close to the surface. The results from the modelling are in good agreement with experiments for a pure rolling case.

The model has been developed in this work for the tire-pavement application. However, it can be applied to a very wide range of contact cases. To get higher efficiency, several improvements can be thought. For instance, from a numerical point of view, a parallelisation can be introduced in the recalculation of the influence coefficients. Indeed, in the proposed Elastic/Viscoelastic correspondence, the increase of calculation of time is due to the recalculation of the influence coefficients at every time step on one single CPU. Therefore, a parallelisation would allow to reduce this time by using the other CPUs of the computer. The same remark goes for the calculation of the influence coefficients in the case of a multi-layered half-space. In fact, the time needed for the calculations depends on the number of layers considered. Thence, a parallelisation can be imagined for a high number of layers.

Besides, it would be certainly of interest to use the developed algorithm for the transient tractive rolling for viscoelastic multi-layered bodies. It would be equivalent to using the developed algorithm and adding the relaxation terms to the displacements used in the CGM algorithm.

Furthermore, for the modelling of non-linearities observed at the contact surface, it would be interesting to integrate inhomogeneities in the layered (and further to the multi-layered) half-space. In this way, plasticity (i.e. rutting) will be modelled, as well as cracking which are the main non-linearities observed at the surface of roads.

Appendix A

Influence coefficients

Influence coefficients for a homogeneous elastic half-space

The contact problem has been solve firstly by Hertz. In his theory, the bodies in contact are supposed elastic, semi-infinite, homogeneous and isotropic. He then found the solution of the contact problem for ellipsoidal contact areas. As presented in this work, the half-space or semi-infinite hypothesis is kept and the influence coefficients are calculated. Influence coefficients correspond to the response of the half-space under an applied unit force. For the numerical implementations, there is a need of finding those influence coefficients over a rectangular zone which corresponds to an element from the discretization of the contact surface. Love [LOV 52] has found those influence coefficients for an applied normal pressure on a rectangular element. Further, Vergne [VER 85] has extended the solutions to tangential shears imposed on the rectangular element. The two solutions are recalled here.

To this aim, a rectangular zone of size $\Delta x_1 \times \Delta x_2$ with center O, is submitted to a constant pressure or a constant shear q_x or q_y distribution. The displacements induced at a point $\bar{M}(x_1, x_2)$ of the surface; and the stresses at a point $M(x_1, x_2, x_3)$ in the subsurface are searched.
Note that $\rho = \sqrt{x_1^2 + x_2^2 + x_3^2}$ and the subscripts I and J are referring to the components x_1, x_2 or x_3.

The stresses in the subsurface induced by a constant pressure p applied on the rectangular zone, are given by:

$$\begin{aligned}\frac{\sigma_{IJ}}{p} =& C_{IJ}^{p}\left(x_1,x_2,x_3,E,\nu\right) = S_{IJ}^{p}\left(x_1+\frac{\Delta_{x1}}{2},x_2+\frac{\Delta_{x2}}{2},x_3,E,\nu\right)\\ &+S_{IJ}^{p}\left(x_1-\frac{\Delta_{x1}}{2},x_2-\frac{\Delta_{x2}}{2},x_3,E,\nu\right)+S_{IJ}^{p}\left(x_1+\frac{\Delta_{x1}}{2},x_2-\frac{\Delta_{x2}}{2},x_3,E,\nu\right)\\ &+S_{IJ}^{p}\left(x_1-\frac{\Delta_{x1}}{2},x_2+\frac{\Delta_{x2}}{2},x_3,E,\nu\right),\end{aligned} \tag{A.1}$$

with

$$\begin{aligned}S_{x_1x_1}^{p}\left(x_1,x_2,x_3,E,\nu\right) &= \frac{\nu}{\pi}\arctan\left(\frac{x_3^2+x_2^2-x_2\rho}{x_3x_1}\right)+\frac{1-2\nu}{\pi}\arctan\left(\frac{\rho-x_2+x_3}{x_1}\right)+\frac{x_3}{2\pi}\frac{x_1x_2}{\left(x_1^2+x_3^2\right)\rho},\\ S_{x_2x_2}^{p}\left(x_1,x_2,x_3,E,\nu\right) &= \frac{\nu}{\pi}\arctan\left(\frac{x_3^2+x_2^2-x_2\rho}{x_3x_1}\right)+\frac{1-2\nu}{\pi}\arctan\left(\frac{\rho-x_1+x_3}{x_2}\right)+\frac{x_3}{2\pi}\frac{x_1x_2}{\left(x_2^2+x_3^2\right)\rho},\\ S_{x_3x_3}^{p}\left(x_1,x_2,x_3,E,\nu\right) &= \frac{1}{2\pi}\arctan\left(\frac{x_3^2+x_2^2-x_2\rho}{x_3x_1}\right)-\frac{x_3}{2\pi}\frac{x_1x_2}{\rho}\left(\frac{1}{x_1^2+x_3^2}+\frac{1}{x_2^2+x_3^2}\right),\\ S_{x_1x_2}^{p}\left(x_1,x_2,x_3,E,\nu\right) &= -\frac{x_3}{2\pi}\frac{1}{\rho}-\frac{1-2\nu}{2\pi}\ln\left(\rho+x_3\right),\\ S_{x_2x_3}^{p}\left(x_1,x_2,x_3,E,\nu\right) &= \frac{x_3^2}{2\pi}\frac{x_1}{\left(x_2^2+x_3^2\right)\rho},\\ S_{x_1x_3}^{p}\left(x_1,x_2,x_3,E,\nu\right) &= \frac{x_3^2}{2\pi}\frac{x_2}{\left(x_1^2+x_3^2\right)\rho}.\end{aligned} \tag{A.2}$$

The stresses induced in the subsurface by a constant shear distribution q_{x_1} over the rectangular surface, are given by:

$$\begin{aligned}\frac{\sigma_{IJ}}{q_{x1}} &= C_{IJ}^{q_{x1}}\left(x_1,x_2,x_3,E,\nu\right) = S_{IJ}^{q_{x1}}\left(x_1+\frac{\Delta_{x1}}{2},x_2+\frac{\Delta_{x2}}{2},x_3,E,\nu\right)\\ &+S_{IJ}^{q_{x1}}\left(x_1-\frac{\Delta_{x1}}{2},x_2-\frac{\Delta_{x2}}{2},x_3,E,\nu\right)+S_{IJ}^{q_{x1}}\left(x_1+\frac{\Delta_{x1}}{2},x_2-\frac{\Delta_{x2}}{2},x_3,E,\nu\right)\\ &+S_{IJ}^{q_{x1}}\left(x_1-\frac{\Delta_{x1}}{2},x_2+\frac{\Delta_{x2}}{2},x_3,E,\nu\right),\end{aligned} \tag{A.3}$$

with

$$
\begin{aligned}
S^{q_{x1}}_{x_1x_1}(x_1,x_2,x_3,E,\nu) &= -\frac{x_3}{2\pi}\frac{1}{\rho}\left(1+\frac{-x_1^2+x_3x_2}{(\rho+x_3)(\rho-x_2)}\right)+\frac{\nu}{\pi}\frac{x_2}{\rho+x_3}-\frac{1}{\pi}\ln(\rho-x_2)\\
S^{q_{x1}}_{x_2x_2}(x_1,x_2,x_3,E,\nu) &= -\frac{x_3}{2\pi}\frac{x_2}{\rho(\rho+x_3)}-\frac{\nu}{\pi}\left(\frac{x_2}{\rho+x_3}+\ln(\rho-x_2)\right)\\
S^{q_{x1}}_{x_3x_3}(x_1,x_2,x_3,E,\nu) &= \frac{x_3^2}{2\pi}\frac{x_2}{\rho\left(x_1^2+x_3^2\right)},\\
S^{q_{x1}}_{x_1x_2}(x_1,x_2,x_3,E,\nu) &= -\frac{x_3}{2\pi}\frac{x_1}{\rho(\rho+x_3)}-\frac{\nu}{\pi}\frac{x_1}{\rho+x_3}-\frac{1}{2\pi}\ln(\rho-x_1),\\
S^{q_{x1}}_{x_2x_3}(x_1,x_2,x_3,E,\nu) &= -\frac{x_3}{2\pi}\frac{1}{\rho},\\
S^{q_{x1}}_{x_1x_3}(x_1,x_2,x_3,E,\nu) &= \frac{x_3}{2\pi}\frac{x_1x_2}{\rho\left(x_1^2+x_3^2\right)}+\frac{1}{2\pi}\arctan\left(\frac{x_3^2+x_2^2-x_2\rho}{x_3x_1}\right).
\end{aligned}
\tag{A.4}
$$

The stresses induced in the subsurface by a constant shear distribution q_{x_2} over the rectangular surface, are given by:

$$
\begin{aligned}
\frac{\sigma_{IJ}}{q_{x2}} = C^{q_{x2}}_{IJ}(x_1,x_2,x_3,E,\nu) &= S^{q_{x2}}_{IJ}\left(x_1+\frac{\Delta_{x1}}{2},x_2+\frac{\Delta_{x2}}{2},x_3,E,\nu\right)\\
&+S^{q_{x2}}_{IJ}\left(x_1-\frac{\Delta_{x1}}{2},x_2-\frac{\Delta_{x2}}{2},x_3,E,\nu\right)+S^{q_{x}2}_{IJ}\left(x_1+\frac{\Delta_{x1}}{2},x_2-\frac{\Delta_{x2}}{2},x_3,E,\nu\right)\\
&+S^{q_{x2}}_{IJ}\left(x_1-\frac{\Delta_{x1}}{2},x_2+\frac{\Delta_{x2}}{2},x_3,E,\nu\right),
\end{aligned}
\tag{A.5}
$$

with

$$
\begin{aligned}
S^{q_{x2}}_{x_1x_1}(x_1,x_2,x_3,E,\nu) &= -\frac{x_3}{2\pi}\frac{x_1}{\rho(\rho+x_3)}-\frac{\nu}{\pi}\left(\frac{x_1}{\rho+x_3}+\ln(\rho-x_1)\right),\\
S^{q_{x}2}_{x_2x_2}(x_1,x_2,x_3,E,\nu) &= \frac{x_3}{2\pi}\frac{1}{\rho}\left(1+\frac{-x_2^2+x_3x_1}{(\rho+x_3)(\rho-x_1)}\right)+\frac{\nu}{\pi}\frac{x_1}{\rho+x_3}-\frac{1}{\pi}\ln(\rho-x_1),\\
S^{q_{x}2}_{x_3x_3}(x_1,x_2,x_3,E,\nu) &= \frac{x_3^2}{2\pi}\frac{x_1}{\rho\left(x_2^2+x_3^2\right)},\\
S^{q_{x2}2}_{x_2x_3}(x_1,x_2,x_3,E,\nu) &= \frac{x_3}{2\pi}\frac{x_2x_1}{\rho\left(x_2^2+x_3^2\right)}+\frac{1}{2\pi}\arctan\left(\frac{x_3^2+x_1^2-x_1\rho}{x_3x_2}\right),\\
S^{q_{x}2}_{x_1x_3}(x_1,x_2,x_3,E,\nu) &= -\frac{x_3}{2\pi}\frac{1}{\rho}.
\end{aligned}
\tag{A.6}
$$

In the same way, for $\bar{\rho}=\sqrt{x_1^2+x_2^2}$, the elastic displacements induced at the surface are found. The displacements induced at the surface by a constant pressure

p field applied over the rectangular zone, are given by:

$$\begin{aligned}\frac{\bar{u}_J}{p} =& K_J^p(x_1,x_2,E,\nu) = U_J^p\left(x_1+\frac{\Delta_{x1}}{2},x_2+\frac{\Delta_{x2}}{2},E,\nu\right)+U_J^p\left(x_1-\frac{\Delta_{x1}}{2},x_2-\frac{\Delta_{x2}}{2},E,\nu\right)\\ &+U_J^p\left(x_1+\frac{\Delta_{x1}}{2},x_2-\frac{\Delta_{x2}}{2},E,\nu\right)+U_J^p\left(x_1-\frac{\Delta_{x1}}{2},x_2+\frac{\Delta_{x2}}{2},E,\nu\right),\end{aligned} \tag{A.7}$$

with

$$\begin{aligned}U_{x_1}^p(x_1,x_2,E,\nu) &= -\frac{(1+\nu)(1-2\nu)}{2\pi E}\left(2x_1\arctan\left(\frac{\bar{\rho}-x_2}{x_1}\right)-x_2\ln\bar{\rho}\right)\\ U_{x_2}^p(x_1,x_2,E,\nu) &= -\frac{(1+\nu)(1-2\nu)}{2\pi E}\left(2x_2\arctan\left(\frac{\bar{\rho}-x_1}{x_2}\right)-x_1\ln\bar{\rho}\right)\\ U_{x_3}^p(x_1,x_2,E,\nu) &= -\frac{\left(1-\nu^2\right)}{\pi E}\left(x_2\ln(\bar{\rho}-x_1)+x_1\ln(\bar{\rho}-x_2)\right)\end{aligned} \tag{A.8}$$

The displacements induced at the surface by a constant shear field q_{x_1} applied over the rectangular zone, are given by:

$$\begin{aligned}\frac{\bar{u}_J}{q_{x1}} =& K_J^{q_{x1}}(x_1,x_2,E,\nu) = U_J^{q_{x1}}\left(x_1+\frac{\Delta_{x1}}{2},x_2+\frac{\Delta_{x2}}{2},E,\nu\right)+U_J^{q_{x1}}\left(x_1-\frac{\Delta_{x1}}{2},x_2-\frac{\Delta_{x2}}{2},E,\nu\right)\\ &+U_J^{q_{x1}}\left(x_1+\frac{\Delta_{x1}}{2},x_2-\frac{\Delta_{x2}}{2},E,\nu\right)+U_J^{q_{x1}}\left(x_1-\frac{\Delta_{x1}}{2},x_2+\frac{\Delta_{x2}}{2},E,\nu\right),\end{aligned} \tag{A.9}$$

with

$$\begin{aligned}U_x^{q_{x1}}(x_1,x_2,E,\nu) &= -\frac{1-\nu^2}{\pi E}x_1\ln(\bar{\rho}-x_2)-\frac{1+\nu}{\pi E}\ln(\bar{\rho}-x_1),\\ U_x^{q_{x1}}2(x_1,x_2,E,\nu) &= -\frac{\nu(1+\nu)}{\pi E}\bar{\rho},\\ U_{x_3}^{q_{x1}}(x_1,x_2,E,\nu) &= \frac{(1+\nu)(1-2\nu)}{2\pi E}\left(-2x_1\arctan\left(\frac{\bar{\rho}-x_2}{x_1}\right)+x_2\ln\bar{\rho}\right).\end{aligned} \tag{A.10}$$

The displacements induced at the surface by a constant shear field q_{x_2} applied over the rectangular zone, are given by:

$$\begin{aligned}\frac{\bar{u}_J}{q_{x2}} = K_J^{q_{x2}}(x_1,x_2,E,\nu) =& U_J^{q_{x2}}\left(x_1+\frac{\Delta_{x1}}{2},x_2+\frac{\Delta_{x2}}{2},E,\nu\right)+U_J^{q_{x2}}\left(x_1-\frac{\Delta_{x1}}{2},x_2-\frac{\Delta_{x2}}{2},E,\nu\right)\\ &+U_J^{q_{x2}}\left(x_1+\frac{\Delta_{x1}}{2},x_2-\frac{\Delta_{x2}}{2},E,\nu\right)+U_J^{q_{x2}}\left(x_1-\frac{\Delta_{x1}}{2},x_2+\frac{\Delta_{x2}}{2},E,\nu\right),\end{aligned} \tag{A.11}$$

with

$$
\begin{aligned}
U_x^{q_{x2}}(x_1,x_2,E,\nu) &= -\frac{\nu(1+\nu)}{\pi E}\bar{\rho},\\
U_x^{q_{x2}}(x_1,x_2,E,\nu) &= -\frac{1-\nu^2}{\pi E}x_2\ln(\bar{\rho}-x_1)-\frac{1+\nu}{\pi E}\ln(\bar{\rho}-x_2),\\
U_{x_3}^{q_{x2}}(x_1,x_2,E,\nu) &= \frac{(1+\nu)(1-2\nu)}{2\pi E}\left(-2x_2\arctan\left(\frac{\bar{\rho}-x_1}{x_2}\right)+x_1\ln\bar{\rho}\right).
\end{aligned}
\tag{A.12}
$$

Influence coefficients for a single layered elastic half-space

For the displacements and stresses for an elastic layered half-space, the influence are found in the Fourier frequency domain and numerically conversed. The forms of those displacements and stresses in the frequency domain are exposed in chapter 3. From the Papkovich-Neuber potentials, after solving the boundary conditions, the influence coefficients are found. The solutions are exposed in this appendix.
Let's define the following parameters: $\theta^- = e^{-\alpha h}$, $\theta = e^{\alpha h}$, $\overline{\mu} = \mu_c/\mu_s$, $\overline{\nu} = (1-\nu_s)/(1-\nu_c)$. Then by doing the appropriate combinations,

$$B^c = \beta_1(\overline{\mu}+1) \tag{A.13a}$$

$$\overline{B}^c = \beta_1(\overline{\mu}-1)\theta^{-2} \tag{A.13b}$$

$$B^s = 2\beta_1\theta^{-1}/\overline{\nu} \tag{A.13c}$$

where $\beta_1 = -\tilde{\tilde{s}}/\left\{2\alpha(1-\nu_1)\left[(1+\bar{\mu})+(1-\bar{\mu})\theta^{-2}\right]\right\}$.
Further, with the same surface and interface boundary conditions, the other coefficients can be extracted as:

$$C^c = \zeta_3\theta^{-2}\left(1-k\theta^{-2}-2\alpha hk\right)-2\zeta_2+\lambda_2-\lambda_1 \tag{A.14}$$

$$\overline{C}^c = \zeta_3\theta^{-2}k\left(\lambda_0\theta^{-2}+2\alpha h\theta^{-2}-1\right) \tag{A.15}$$

$$C^s = \theta^{-1}\left[C^c(1-\lambda_0)+(1-\bar{\mu})\zeta_1\right] \tag{A.16}$$

$$D^c = \left[\lambda_1+\lambda_2-(3-4\nu_1)C^c+\overline{C}^c\right]/(2\alpha) \tag{A.17}$$

$$\overline{D}^c = \left[\lambda_2-\lambda_1-C^c+(3-4\nu_c)\overline{C}^c\right]/(2\alpha) \tag{A.18}$$

$$D^s = -\theta^{-1}\left[C^c\left(3-4\nu_s\right)\left(1-\lambda_0\right)+\zeta_3\left(\lambda_0\theta^{-2}+2\alpha h\theta^{-2}-1\right)\times\left(k-1\right)+4\left(1-\nu_s\right)\left(\beta_2+\zeta_1\right)\right]/(2\alpha) \tag{A.19}$$

where,

$$k = \frac{\bar{\mu}-1}{\bar{\mu}+\left(3-4\nu_c\right)}$$

$$\lambda_0 = 1-\frac{4\left(1-\nu_c\right)}{1+\bar{\mu}\left(3-4\nu_s\right)}$$

$$\lambda_1 = -im\alpha^{-1}\left(B^c-\bar{B}^c\right)$$

$$\lambda_2 = \left[-\tilde{\tilde{p}}-2im\left(1-\nu_c\right)\left(B^c+\bar{B}^c\right)\right]/\alpha$$

$$\lambda_3 = 2im\beta_1[(1-\bar{\nu})/(\bar{\nu}\alpha)+h\bar{\mu}]$$

$$\lambda_4 = 2im\beta_1\left[2\left(1-\nu_s\right)\left(1-\bar{\mu}\right)/(\bar{\nu}\alpha)+h\right]$$

$$\lambda_5 = 2im\beta_1 h$$

$$\lambda_6 = 2im\beta_1[(\bar{\mu}-\bar{\nu})/(\bar{\nu}\alpha)+h\bar{\mu}]$$

$$\beta_2 = imB^s\theta\alpha^{-1} = 2im\beta_1/(\overline{\nu\alpha})$$

$$\zeta_1 = \frac{\lambda_3-\lambda_4+\lambda_5-\lambda_6}{\left[1+\left(3-4\nu_s\right)\mu\right]\left(1-\mu\right)} = \frac{\left(2\nu_s-1\right)\beta_2}{1+\left(3-4\nu_s\right)\mu}$$

$$\zeta_2 = \frac{\left[\left(\lambda_2-\lambda_1\right)\left(\lambda_0+2\alpha h\right)+\lambda_1+\lambda_2-2\lambda_4+4\left(1-\nu_s\right)\left(\bar{\mu}\zeta_1+\beta_2\right)\right]\theta^{-2}}{2\left(\lambda_0\theta^{-2}-1+2\alpha h\theta^{-2}\right)}$$

$$\zeta_3 = \frac{\lambda_4+\lambda_3-\lambda_2-\lambda_1-\left(3-2\nu_s\right)\beta_2+2\alpha h\left(2\zeta_2-\lambda_2+\lambda_1\right)}{1+\lambda_0 k\theta^{-4}-\left(\lambda_0+k+4\alpha^2h^2k\right)\theta^{-2}}$$

Influence coefficients for a multi-layered elastic half-space

In the same way as for a single layered half-space, the influence coefficients are found in the Fourier frequency domain for multi-layered half-space. The same Papkovich-Neuber potentials are used to write the displacements and stresses. Then, with the appropriate combinations, matrix systems are found (see chapter 4). The analytical solution of Eq. (4.17) is derived from the steps below. First let's use the following notations:

$$t_0^{(L+1)} = 1 \tag{A.20a}$$

$$t_0^{(j)} = \mu^{(j,j+1)} \frac{t_0^{(j+1)} + 1 + \left[t_0^{(j+1)} - 1\right] \left(\theta_-^{j+1}\right)^2}{t_0^{(j+1)} + 1 - \left[t_0^{j+1)} - 1\right] \left(\theta_-^{j+1}\right)^2} \qquad (j = L, \cdots, 1) \tag{A.20b}$$

Then the B functions can be written as:

$$\overline{B}^1 = \frac{\left(\theta_-^1\right)^2}{t_0^{(1)} + 1 - \left[t_0^{(1)} - 1\right] \left(\theta_-^1\right)^2} \frac{-1}{2\alpha\left(1 - v_1\right)} \left[t_0^{(1)} - 1\right] \tag{A.21}$$

$$B^1 = \overline{B}^1 - \frac{1}{2\alpha(1 - \nu_1)} \tag{A.22}$$

$$\overline{B}^j = \frac{1 - v_{j-1}}{1 - v_j} \frac{\left[t_0^{(j)} - 1\right] \left(\theta_-^j\right)^2}{t_0^{(j)} + 1 - \left[t_0^{(j)} - 1\right] \left(\theta_-^j\right)^2} \left[B^{j-1}\theta_-^{j-1} - \overline{B}^{j-1}\theta_+^{j-1}\right] \qquad (j = 2, \cdots, L) \tag{A.23}$$

$$B^j = \frac{1 - v_{j-1}}{1 - v_j} \frac{t_0^{(j)} + 1}{t_0^{(j)} + 1 - \left[t_0^{(j)} - 1\right] \left(\theta_-^j\right)^2} \left[B^{j-1}\theta_-^{j-1} - \overline{B}^{j-1}\theta_+^{j-1}\right] \qquad (j = 2, \cdots, L) \tag{A.24}$$

$$B^{L+1} = \frac{1 - v_L}{1 - v_{L+1}} \left[B^L \theta_-^L - \overline{B}^L \theta_+^L\right] \tag{A.25}$$

To write the second members of Eq. (4.18), one need the derivatives of the above functions. These derivatives about m are:

$$t_{0,m}^{(L)} = 0 \tag{A.26a}$$

$$t_{0,m}^{(j-1)} = 4\mu^{(j-1,j)} (\theta_-^j)^2 \frac{t_{0,m}^{(j)} - \left[t_0^{(j)} + 1\right] \left[t_0^{(j)} - 1\right] \frac{m h_j}{\alpha}}{\left\{t_0^{(j)} + 1 - \left[t_0^{(j)} - 1\right] (\theta_-^j)^2\right\}^2} \qquad (j = L, \cdots, 2) \tag{A.26b}$$

$$\overline{B}^1_{,m} = \frac{(\theta^1_-)^2}{t_0^{(1)}+1-\left(t_0^{(1)}-1\right)(\theta^1_-)^2}\frac{-1}{2\alpha\,(1-v_1)}\left\{\left[\frac{2t^{(1)}_{0,m}-(\frac{2mh_1}{\alpha})\left(t_0^{(1)}+1\right)\left(t_0^{(1)}-1\right)}{\left(t_0^{(1)}+1\right)-\left(t_0^{(1)}-1\right)(\theta^1_-)^2}\right]-\frac{m}{\alpha^2}\right\} \tag{A.27}$$

$$B^1_{,m} = \overline{B}^1_{,m} + \frac{m}{2\alpha^3(1-\nu_1)} \tag{A.28}$$

$$\begin{aligned}\overline{B}^j_{,m} =& \frac{1-v_{j-1}}{1-v_j}\frac{\left[t_0^{(j)}-1\right](\theta^j_-)^2}{t_0^{(j)}+1-\left[t_0^{(j)}-1\right](\theta^j_-)^2}\left\{\frac{\frac{-2mh_j}{\alpha}\left[t_0^{(j)}+1\right]+\frac{2t^{(j)}_{0m}}{t_0^{(j)}-1}}{t_0^{(j)}+1-\left[t_0^{(j)}-1\right](\theta^j_-)^2}\left[B^{j-1}\theta^{j-1}_- - \overline{B}^{j-1}\theta^{j-1}_+\right]\right.\\ &\left.+B^{j-1}_{,m}\theta^{j-1}_- - \overline{B}^{j-1}_{,m}\theta^{j-1}_+ - \frac{mh_{j-1}}{\alpha}\left[B^{j-1}\theta^{j-1}_- + \overline{B}^{j-1}\theta^{j-1}_+\right]\right\} \qquad (j=2,\cdots,L)\end{aligned} \tag{A.29}$$

$$\begin{aligned}B^j_{,m} =& \frac{1-v_{j-1}}{1-v_j}\frac{t_0^{(j)}+1}{t_0^{(j)}+1-\left[t_0^{(j)}-1\right](\theta^j_-)^2}\left\{\frac{\frac{2t^{(j)}_{0,m}}{t_0^{(j)}+1}(\theta^j_-)^2+\left[t_0^{(j)}-1\right]\frac{-2mh_j}{\alpha}(\theta^j_-)^2}{t_0^{(j)}+1-\left[t_0^{(j)}-1\right](\theta^j_-)^2}\left[B^{j-1}\theta^{j-1}_- - \overline{B}^{j-1}\theta^{j-1}_+\right]\right.\\ &\left.+B^{(j-1)}_{,m}\theta^{j-1}_- - \overline{B}^{j-1}_{,m}\theta^{j-1}_+ - \frac{mh_{j-1}}{\alpha}\left[B^{j-1}\theta^{j-1}_- + \overline{B}^{j-1}\theta^{j-1}_+\right]\right\} \qquad (j=2,\cdots,L)\end{aligned} \tag{A.30}$$

$$B^{L+1}_{,m} = \frac{1-v_L}{1-v_{L+1}}\left[B^L_{,m}\theta^L_- - \frac{mh_L}{\alpha}\theta^L_- B^L - \overline{B}^L_{,m}\theta^L_+ - \frac{mh_L}{\alpha}\theta^L_+\overline{B}^L\right] \tag{A.31}$$

Here, the functions of the second member of Eq. (4.18) can be expressed as:

$$S^{(0)}_1 = -\alpha^{-1} - 2im\alpha^{-1}(1-v_1)\left[B^1+\overline{B}^1\right] - i\alpha\left[B^1_{,m}+\overline{B}^1_{,m}\right], \tag{A.32}$$

$$S^{(0)}_2 = -i\left\{m\alpha^{-1}\left[B^1-\overline{B}^1\right]+\alpha\left[B^1_{,m}-\overline{B}^1_{,m}\right]\right\} = 0 \tag{A.33}$$

and for $j=1,\cdots,L$:

$$S^{(j)}_1 = \alpha i\left\{\mu^{(j,j+1)}\left[B^{j+1}_{,m}\theta^j_+ + \overline{B}^{j+1}_{,m}\theta^j_+\right]+\frac{1}{\alpha}mh_j\left[B^j-\overline{B}^j(\theta^j_+)^2\right]-B^j_{,m}-\overline{B}^j_{,m}(\theta^j_+)^2\right\}, \tag{A.34}$$

$$\begin{aligned}S^{(j)}_2 =& i\left\{\frac{\mu^{(j,j+1)}m}{\alpha}\left[B^{j+1}\theta^j_+ - \overline{B}^{j+1}\theta^j_+\right]+\mu^{(j,j+1)}\alpha\left[B^{j+1}_{,m}\theta^j_+ - \overline{B}^{j+1}_{,m}\theta^j_+\right]\right.\\ &\left.+mh_j\left[B^j+\overline{B}^j(\theta^j_+)^2\right]-\frac{m}{\alpha}\left[B^j-\overline{B}^j(\theta^j_+)^2\right]-\alpha\left[B^j_{,m}-\overline{B}^j_{,m}(\theta^j_+)^2\right]\right\},\end{aligned} \tag{A.35}$$

$$
\begin{aligned}
S_3^{(j)} = i\Big\{&\alpha^{-1} m\left[B^{j+1}\theta_+^j - \overline{B}^{j+1}\theta_+^j\right] + \alpha\left[B_{,m}^{j+1}\theta_+^j - \overline{B}_{,m}^{j+1}\theta_+^j\right] \\
&-\left(\alpha^{-1} - h_j\right) m B^j + \left(\alpha^{-1} + h_j\right) m(\theta_+^j)^2\overline{B}^j - \alpha\left[B_{,m}^j - \overline{B}_{,m}^j(\theta_+^j)^2\right]\Big\},
\end{aligned}
\tag{A.36}
$$

$$
\begin{aligned}
S_4^{(j)} =& i\Big\{2m\alpha^{-1}(1-v_{j+1})\left[B^{j+1}\theta_+^j + \overline{B}^{j+1}\theta_+^j\right] + \alpha\left[B_{,m}^{j+1}\theta_+^j + \overline{B}_{,m}^{j+1}\theta_+^j\right] \\
&-2m\alpha^{-1}(1-v_j)\left[B^j + \overline{B}^j(\theta_+^j)^2\right] + m h_j\left[B^j - \overline{B}^j(\theta_+^j)^2\right] - \alpha\left[B_{,m}^j + \overline{B}_{,m}^j(\theta_+^j)^2\right]\Big\}.
\end{aligned}
\tag{A.37}
$$

In this way the matrix system in Eq. (4.17) is solved analytically and the matrix system in Eq. (4.18) is constructed and can be solved numerically. Further, a numerical inversion is performed to find the influence coefficients in the space domain.

Appendix B

Validations

Viscoelastic single layered half-space

Contact on a homogeneous viscoelastic half-space

Apart from the validation of the elastic influence coefficients of the single layered, it is important to validate the Elastic/viscoelastic correspondence.
The simplest way to begin the validation of the contact on viscoelastic layered half-space, is comparison to the homogeneous case when taking the same viscoelastic properties for both substrate and coating. For this aim, the results of the present works are compared to the Semi-Analytical Model of Koumi et al. [KOU 15b] and to the model of Carbone and Putignano [CAR 13] which is based on the Boundary Element Method (BEM).
While the model of Carbone gives the solutions for steady-state regime, the model of Koumi is able to solve every kind of pressure history and every geometry. The present model is based on the model of Koumi, and so, allows solving the transient problems, taking into account various kind of loads and geometries. For the validation, consider numerical parameters presented in [KOU 15b] and [CAR 13]. An elastic sphere of radius $R = 10$ mm and of very high elastic modulus so that it can be assimilated to a rigid sphere, is taken. This sphere moves at constant velocity on a viscoelastic half-space. In the present work, the substrate and the coating take the same viscoelastic properties. The creep and relaxation functions used are in the forms:

$$J(t) = \left[\frac{1}{\mu_0} - \frac{1}{\mu_1}\exp\left(-\frac{t}{\tau}\right)\right] = \left[\frac{1}{\mu_\infty} + \frac{1}{\mu_1}\left(1 - \exp\left(-\frac{t}{\tau}\right)\right)\right] \tag{B.1}$$

$$R(t) = \left[\mu_0 + (\mu_\infty - \mu_0)\exp\left(-\frac{t}{\frac{\mu_0}{\mu_\infty}\tau}\right)\right] \tag{B.2}$$

where μ is the spring stiffness with $\mu_\infty = 3.086$ MPa, $\mu_\infty/\mu_0 = 10$ and τ the relaxation time.
The Poisson's ratio of both coating and substrate is $\nu_c = \nu_s = 0.3$.

Figure B.1 shows the pressure distribution for the three models for a prescribed normal body displacement $\delta = 0.1 \times a$, while the dimensionless velocity of the sphere is $v\tau/a = 0.8$ where a is the elastic contact radius and τ the relaxation time.
One can observe a very good agreement between the three methods.

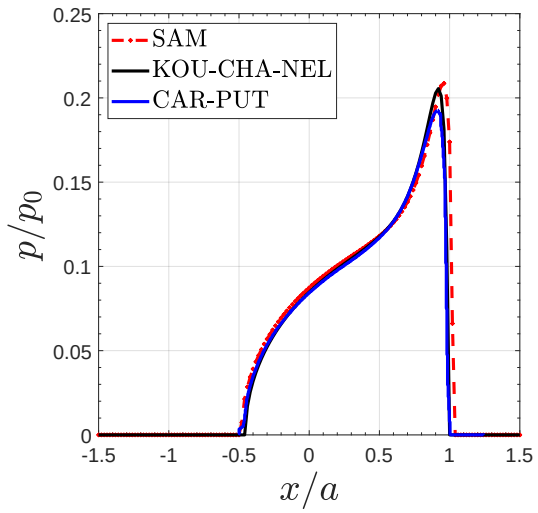

Figure B.1: Comparison of the normalized contact pressure between the present Semi-Analytical Method (SAM), the semi-analytical method of Koumi and the Boundary Element Method of Carbone, in steady-state regime with constant rolling velocity $v\tau/a = 0.8$; and for a constant penetration $\delta = 0.1 \times a$ of a rigid sphere.

Contact on a viscoelastic layer bonded by a rigid base: Stepanov

Stepanov and Torskaya [STE 18] studied the contact interactions for a viscoelastic layer bonded to a rigid half-space. The problem has been solved for an indenter under a constant load and moving at a constant velocity using Boundary Element Method. The results in term of contact pressure are found in the steady-state regime. The model of Stepanov uses the creep kernel $J(t) = k \times exp(-t/w)$, where w is the retardation time and k is the reciprocal of the relaxation time.
For the validation the parameter for Fig. 4b in [STE 18] are used. The comparison between the two results is plotted in Fig. B.2. One can also see a good agreement between the two dimensionless contact pressures.

These validations allow to trust the proposed Elastic/viscoelastic correspondence proposed.

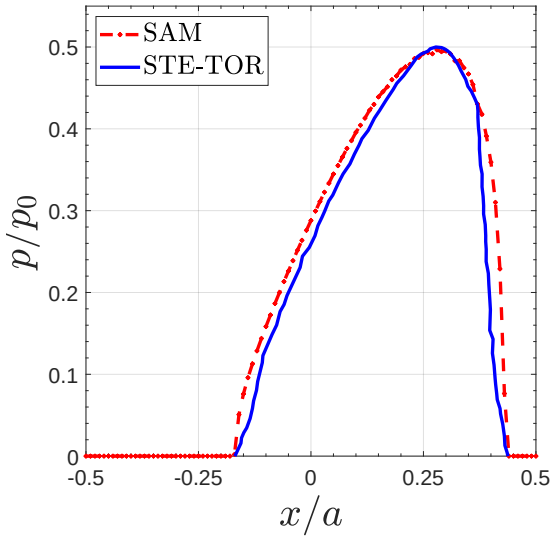

Figure B.2: Validation of the model with the results of Stepanov and Torskaya [STE 18] for a contact on a viscoelastic layer bonded by a rigid base

Multi-layered half-space

For validating the influence coefficients for the multi-layered half-space. Several computations are performed and compared to the results of Yu et al. [YU 14]. Figure B.3 shows the dimensionless second invariant $\sqrt{J_2}/p_0$ of the stress tensor in the middle plane $y = 0$ for the contact between a spherical rigid indenter and a tri-layered elastic half-space. A pure sliding motion is considered for different values of friction coefficient ($f = 0$, 0.25 and 0.5) and for the tri-layers $\mu_1 = 2\mu_2 = 4\mu_{sub}$ and $\mu_1 = \mu_2/2 = \mu_{sub}/4$.

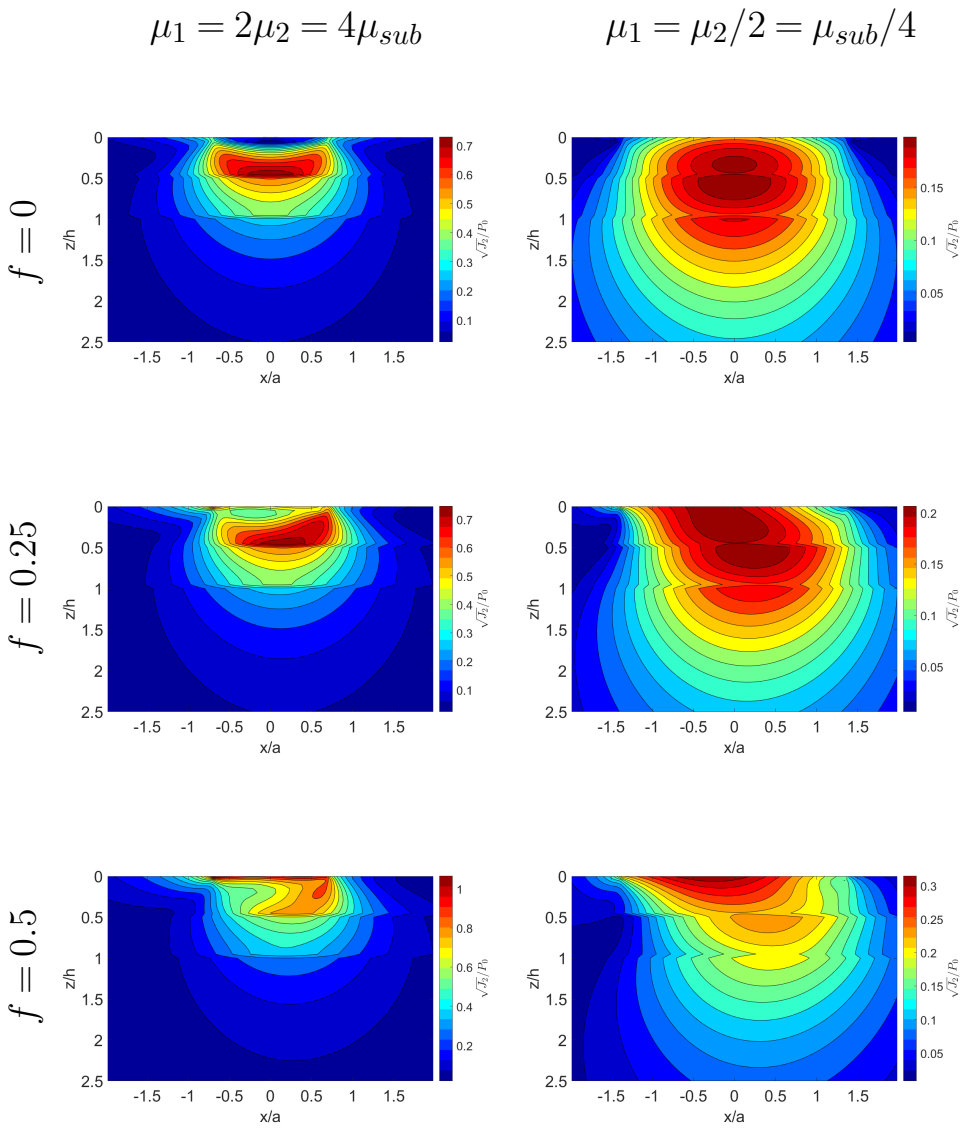

Figure B.3: Dimensionless second invariant $\sqrt{J_2}/p_0$ of the stress tensor in the middle plane $y = 0$ for the contact between a spherical rigid indenter and a tri-layered elastic half-space. A pure sliding motion is considered for different values of friction coefficients ($f = 0$, 0.25 and 0.5) and for the tri-layers $\mu_1 = 2\mu_2 = 4\mu_{sub}$ (left) and $\mu_1 = \mu_2/2 = \mu_{sub}/4$ (right).

Appendix C

On the Elastic/viscoelastic correspondence

Discussion on the Elastic/Viscoelastic correspondence

Due to the form of the elastic displacement found in chapter 3, the viscoelastic displacement u_z at the surface of a layered body can be written as:

$$u_z(x,y,t) = FT^{-1}\{\hat{u}_z(x,y,\omega)\} = FT^{-1}\{\hat{J}^1(\omega)\hat{\bar{G}}(x,y,\omega)i\omega\hat{p}(\omega)\} \tag{C.1}$$

$$= \int G(x,y,t-\xi)\frac{\partial p(\xi)}{\partial \xi}d\xi. \tag{C.2}$$

$$= \int J^1(t-\xi)F(x,y,\xi)d\xi \tag{C.3}$$

where

$$F(x,y,t) = FT^{-1}\{\hat{\bar{G}}(x,y,\omega)i\omega\hat{p}(\omega)\} \tag{C.4}$$

and

$$G(x,y,t) = FT^{-1}\{\hat{J}^1(\omega)\hat{\bar{G}}(x,y,\omega)\} = \int J^1(t-\eta)\bar{G}(x,y,\eta)d\eta. \tag{C.5}$$

Finding the exact solution by inverting the FT of the influence coefficient with respect to time would demand a significant amount of ressources. An alternative is proposed below.

Basically, there is a need to find the function $F(x,y,t)$ which can be written as:

$$F(x,y,t) = \int \hat{\bar{G}}(x,y,\omega)i\omega\hat{p}(\omega)\exp(i\omega t)\,d\omega \tag{C.6}$$

In the present work, the hypothesis is:

$$F(x,y,t) = FT^{-1}\{\hat{\bar{G}}(x,y,\frac{\hat{J}^k(\omega)}{\hat{J}^{k+1}(\omega)})i\omega\hat{p}(\omega)\} \approx \bar{G}\left(x,y,\frac{J^k(t)}{J^{k+1}(t)}\right)\frac{\partial}{\partial t}p(t). \tag{C.7}$$

This assumption is not mathematically correct. However, it is exact under some conditions and is a good approximation in the other cases. In particular, it is exact if the term $\hat{\bar{G}}(x,y,\frac{\hat{J}^k(\omega)}{\hat{J}^{k+1}(\omega)})$ does not depend on ω, with regard to Eq. (C.6). In what follows next, details are given to justify this assumption.

Recall that the Maxwell generalised model is used and its creep function for the layer k can be written as:

$$J^k(t) = j_0^k - \sum_{l=1}^{N_k} j_l^k \exp\left(-t/\tau_l^k\right), \qquad t > 0. \tag{C.8}$$

The Fourier transform of this function is given by:

$$\hat{J}^k(\omega) = j_0^k \delta(\omega) - \sum_{l=1}^{N_k} \frac{j_l^k \tau_l^k}{1 + i\omega\tau_l^k}. \tag{C.9}$$

If one plots the norm of the ratio $\frac{\hat{J}^k(\omega)}{\hat{J}^{k+1}(\omega)}$, it can be seen that for the times where we want to observe viscoelasticity, the ratio takes a constant value apart from the frequencies close to $\omega = 0$.
This phenomenon is explained by the behaviour of the Fourier transform: *"Generally speaking, the more concentrated $f(x)$ is, the more spread out its Fourier transform $\hat{f}(\xi)$ must be. In particular, the scaling property of the Fourier transform may be seen as saying: if we squeeze a function in x, its Fourier transform stretches out in ξ. It is not possible to arbitrarily concentrate both a function and its Fourier transform."*

In order to observe viscoelasticity, the regions where the creep functions spread are of interest. Therefore, their transforms are concentrated around the frequency 0. On the basis of this observation, the following equation can be inferred:

$$\begin{aligned} F(t) &= \int_0^\beta \hat{\bar{G}}(x,y,\omega) i\omega \hat{p}(\omega) \exp(i\omega t)\, d\omega \\ &= \int_0^\varepsilon \hat{\bar{G}}(x,y,\omega) i\omega \hat{p}(\omega) \exp(i\omega t)\, d\omega + \int_\varepsilon^\beta \hat{\bar{G}}(x,y,\omega) i\omega \hat{p}(\omega) \exp(i\omega t)\, d\omega \end{aligned} \tag{C.10}$$

where β is the equivalent of t in the frequency domain; and ε is a small frequency which indicates the frequencies over which the ratio $\frac{\hat{J}^k(\omega)}{\hat{J}^{k+1}(\omega)}$ is not constant.
Over $[\varepsilon;\beta]$, the ratio $\frac{\hat{J}^k(\omega)}{\hat{J}^{k+1}(\omega)}$ is constant. Thus, it makes sense to write:

$$F(t) = \int_0^\varepsilon \hat{\bar{G}}(x,y,\omega) i\omega \hat{p}(\omega) \exp(i\omega t)\, d\omega + \bar{G}\left(x,y,\frac{J^k(t)}{j^{k+1}(t)}\right) \int_\varepsilon^\beta i\omega \hat{p}(\omega) \exp(i\omega t)\, d\omega. \tag{C.11}$$

It comes that the error in the calculation of $F(x,y,t)$ lies in the term $\int_0^\varepsilon \hat{J}^1(\omega)\hat{\bar{G}}(x,y,\omega)\exp(i\omega t)\,d\omega$. This term corresponds to very low frequencies where the viscoelastic effects can physically assumed negligible. Thus, those low frequencies are not expected to bring a significant effect on the viscoelastic response of the structure. In addition, the ignored points are in an area so small in the frequency domain that in a discretised form they might be missed without significant loss of informations. This explained the fact that the present approximation allows to get good results when compared to FEM as shown in chapter 3.

Conclusion: In summary, the areas of validity of the approximation are:

1. In steady state regime, the approximation meets the exact solution. Indeed, in the steady state regime, the behaviour in $\hat{\bar{G}}(x,y,\omega)$ is constant; and according to Eq. (C.6), it is the exact solution to write Eq. (C.7). Therefore, since all the final steps of our results are given for the steady state regime, they are exact.

2. When the ratio of creep functions is a constant, the ratio of their FT gives a constant. Thence, the term $\int_0^\varepsilon \hat{J}^1(\omega)\hat{\bar{G}}(x,y,\omega)\exp(i\omega t)\,d\omega$ is equal to 0. Consequently, the applied solution is exact in the study of the effect of "Variation of the instantaneous shear moduli" in the paper (section 4.3.3.1).

3. For the other cases, the error made is contained in the term $\int_0^\varepsilon \hat{J}^1(\omega)\hat{\bar{G}}(x,y,\omega)\exp(i\omega t)\,d\omega$. This term involves very low frequencies where the viscoleastic behaviour is not physically very significant. Thus, ignoring it implies an error which is not expected to by high.

Bibliography

[AAS 08] AASHTO
Mechanistic-Empirical Pavement Design Guide - A Manual of Practice (Interim Edition). American Association of State Highway and Transportation Officials (AASHTO), Place of publication not identified, 2008. OCLC: 746484666.

[ABD 86] Abdul-Mihsein M., Bakr A., Parker A.
A boundary integral equation method for axisymmetric elastic contact problems. *Computers & Structures*, vol. 23, n° 6, 1986, p. 787–793.

[ABU 12] Abu Al-Rub R. K., Darabi M. K., Huang C.-W., Masad E. A., Little D. N.
Comparing finite element and constitutive modelling techniques for predicting rutting of asphalt pavements. *International Journal of Pavement Engineering*, vol. 13, n° 4, 2012, p. 322–338.

[AGE 06] Agency H.
Design Manual for Roads and Bridges, vol. 7. 2006.

[AI 99] Ai X., Sawamiphakdi K.
Solving Elastic Contact Between Rough Surfaces as an Unconstrained Strain Energy Minimization by Using CGM and FFT Techniques. vol. 121, n° 4, 1999, p. 639–647.

[AKB 05] Akbulut H., Aslantas K.
Finite element analysis of stress distribution on bituminous pavement and failure mechanism. *Materials & Design*, vol. 26, n° 4, 2005, p. 383–387.

[ALE 01] Alexandrov V. M., Pozharskii D. A.
Three-Dimensional Contact Problems, vol. 93 of *Solid Mechanics and Its Applications*. Springer Netherlands, Dordrecht, 2001.

[ALQ 08] Al-Qadi I. L., Wang H., Yoo P. J., Dessouky S. H.
Dynamic Analysis and in Situ Validation of Perpetual Pavement Response to Vehicular Loading. *Transportation Research Record: Journal of the Transportation Research Board*, vol. 2087, n° 1, 2008, p. 29–39.

[AMU 16a] Amuzuga K.
Damage mechanism related to plasticity around heterogeneous under rolling contact loading in hybrid bearings ceramic/steel. Thèse de doctorat, INSA Lyon, Lyon, 2016.

[AMU 16b] Amuzuga K. V., Chaise T., Duval A., Nélias D.
Fully Coupled Resolution of Heterogeneous Elastic–Plastic Contact Problem. *Journal of Tribology*, vol. 138, n° 2, 2016, Page 021403.

[AND 81] Andersson T.
The Boundary Element Method applied to Two-Dimensional Contact Problems with Friction. Brebbia C. A., Ed., *Boundary Element Methods*, p. 239–258 Springer Berlin Heidelberg, Berlin, Heidelberg, 1981.

[ANS 19] Ansys I.
. « Ansys », 2019.

[ANT 06] Antoine J.-F., Visa C., Sauvey C., Abba G.
Approximate Analytical Model for Hertzian Elliptical Contact Problems. *Journal of Tribology*, vol. 128, n° 3, 2006, p. 660–664.

[ASS 20a] Assogba O. C., Sun Z., Tan Y., Nonde L., Bin Z.
Finite-Element Simulation of Instrumented Asphalt Pavement Response under Moving Vehicular Load. *International Journal of Geomechanics*, vol. 20, n° 3, 2020, p. 1–19.

[ASS 20b] Assogba O. C., Tan Y., Zhou X., Zhang C., Anato J. N.
Numerical investigation of the mechanical response of semi-rigid base asphalt pavement under traffic load and nonlinear temperature gradient effect. *Construction and Building Materials*, vol. 235, 2020, p. 117406 1–25.

[BAG 12] Bagault C., Nélias D., Baietto M.-C.
Contact Analyses for Anisotropic Half Space: Effect of the Anisotropy on the Pressure Distribution and Contact Area. *Journal of Tribology*, vol. 134, n° 3, 2012, Page 031401.

[BAG 13] Bagault C., Nélias D., Baietto M., Ovaert T.
Contact analyses for anisotropic half-space coated with an anisotropic layer: Effect of the anisotropy on the pressure distribution and contact area. *International Journal of Solids and Structures*, vol. 50, n° 5, 2013, p. 743–754.

[BAS 87] Bass J. M.
Three-dimensional finite deformation, rolling contact of a hyperelastic cylinder: Formulation of the problem and computational results. *Computers & Structures*, vol. 26, n° 6, 1987, p. 991–1004.

[BAZ 20] Bazi G., Hajj E. Y., Ulloa-Calderon A., Ullidtz P.
Finite element modelling of the rolling resistance due to pavement deformation. *International Journal of Pavement Engineering*, vol. 21, n° 3, 2020, p. 365–375.

[BEC 97] Becker A., Seifert B.
Simulation Of Wear With A FE Tyre Model Using A Steady State Rolling Formulation. *Transactions on Engineering Sciences*, vol. 14, 1997, p. 119–128.

[BEE 96] de Beer M.
Measurement of tyre/pavement interface stresses under moving wheel loads. *International Journal of Vehicle Design*, vol. 3, n° 1-4, 1996, p. 97–115.

[BEN 67] Bentall R., Johnson K.
Slip in the rolling contact of two dissimilar elastic rollers. *International Journal of Mechanical Sciences*, vol. 9, n° 6, 1967, p. 389–404.

[BEN 68] Bentall R., Johnson K.
An elastic strip in plane rolling contact. *International Journal of Mechanical Sciences*, vol. 10, n° 8, 1968, p. 637–663.

[BER 09] Berthier J.
Dimensionnement des chaussées routières. *Construction et travaux publics / Travaux publics et infrastructures*, , 2009, Page 27.

[BLA 02] Blab R., Harvey J.
Modeling Measured 3D Tire Contact Stresses in a Viscoelastic FE Pavement Model. vol. 2, n° 3, 2002, Page 19.

[BLA 16] Blanco-Lorenzo J., Santamaria J., Vadillo E. G., Correa N.
On the influence of conformity on wheel–rail rolling contact mechanics. *Tribology International*, vol. 103, 2016, p. 647–667.

[BLA 18] Blanco-Lorenzo J., Santamaria J., Vadillo E. G., Correa N.
A contact mechanics study of 3D frictional conformal contact. *Tribology International*, vol. 119, 2018, p. 143–156.

[BOA 62] Board H. R.
The AASHO Road Test - Report 5 Pavement Research. National academy of sciences - national research council edition, 1962.

[BOF 12] Boffy H., Baietto M.-C., Sainsot P., Lubrecht A. A.
An Efficient 3D Model of Heterogeneous Materials for Elastic Contact Applications Using Multigrid Methods. *Journal of Tribology*, vol. 134, n° 2, 2012, p. 021401 1–8.

[BOF 14] Boffy H., Venner C. H.
Multigrid solution of the 3D stress field in strongly heterogeneous materials. *Tribology International*, vol. 74, 2014, p. 121–129.

[BOR 93] Borodich F.
The Hertz frictional contact between nonlinear elastic anisotropic bodies (the similarity approach). *International Journal of Solids and Structures*, vol. 30, n° 11, 1993, p. 1513–1526.

[BOU 85] Boussinesq M. J.
Application des potentiels a l'étude des mouvement des solides élastiques. Paris, gauthier-villars edition, 1885.

[BOU 08] Boucly V.
Semi-Analytical Modeling of the Transient Thermal-Elastic-Plastic Contact and its Application to Asperity Collision, Wear and Running-in of Surfaces. Thèse de doctorat, INSA Lyon, Lyon, 2008.

[BRO 92] Brown E. R., Cross S. A.
A national study of rutting in hot mix (HMA) pavements. Report n° 92-05, february 1992.

[BRO 02] Brown E. R., Jr L. A. C., Hanson D., Lynn C., Powell B., Prowell B., Watson D.
NCAT test track design, construction and performance. Report n° 0.-12, november 2002.

[BUF 71] Bufler H.
Theory of elasticity of a multilayered medium. *Journal of Elasticity*, vol. 1, n° 2, 1971, p. 125–143.

[BUR 45a] Burmister D. M.
The General Theory of Stresses and Displacements in Layered Soil Systems. II. *Journal of Applied Physics*, vol. 16, n° 3, 1945, p. 126–127.

[BUR 45b] Burmister D. M.
The General Theory of Stresses and Displacements in Layered Soil Systems. III. *Journal of Applied Physics*, vol. 16, n° 5, 1945, p. 296–302.

[BUR 45c] Burmister D. M.
The General Theory of Stresses and Displacements in Layered Systems. I. *Journal of Applied Physics*, vol. 16, n° 2, 1945, p. 89–94.

[BUS 75] Bush A., Gibson R., Thomas T.
The elastic contact of a rough surface. *Wear*, vol. 35, n° 1, 1975, p. 87–111.

[CAR 26] Carter F. W.
On the action of a locomotive driving wheel. *Proceedings of the Royal Society of London. Series A, Containing Papers of a Mathematical and Physical Character*, vol. 112, n° 760, 1926, p. 151–157.

[CAR 13] Carbone G., Putignano C.
A novel methodology to predict sliding and rolling friction of viscoelastic materials: Theory and experiments. *Journal of the Mechanics and Physics of Solids*, vol. 61, n° 8, 2013, p. 1822–1834.

[CAT 38] Cattaneo C.
Sul contatto di due corpi elastici : distribuzione locale degli sforzi. *Rendiconti dell'Accademia Nazionale dei Lincei*, vol. 27, n° 6, 1938, p. 342–348, 434–436, 474–478.

[CER 82] Cerruti V.
Ricerche intorno all'equilibrio de' corpi elastici isotropi. *Atti della R. Accademia dei Lincei*, vol. 13, n° 3, 1882, p. 81–123.

[CHA] Chabot A., Tamagny P., Poché D., Duhamel D.
Visco-elastic modelling for asphalt pavements - Software ViscoRoute. Page 10.

[CHA 09] Chazallon C., Koval G., Hornych P., Allou F., Mouhoubi S.
Modelling of rutting of two flexible pavements with the shakedown theory and the finite element method. *Computers and Geotechnics*, vol. 36, n° 5, 2009, p. 798–809.

[CHA 10] Chabot A., Chupin O., Deloffre L., Duhamel D.
ViscoRoute 2.0: A Tool for the Simulation of Moving Load Effects on Asphalt Pavement. *Road Materials and Pavement Design*, vol. 11, n° 2, 2010, p. 227–250.

[CHA 11a] Chaise T.
Mechanical simulation using a semi analytical method: from elasto-plastic rolling contact to multiple impacts. Thèse de doctorat, 2011.

[CHA 11b] Chaise T., Nélias D.
Contact Pressure and Residual Strain in 3D Elasto-Plastic Rolling Contact for a Circular or Elliptical Point Contact. *Journal of Tribology*, vol. 133, n° 4, 2011, Page 041402.

[CHE 71] Chen W.
Computation of stresses and displacements in a layered elastic medium. *International Journal of Engineering Science*, vol. 9, n° 9, 1971, p. 775–800.

[CHE 72] Chen W., Engel P.
Impact and contact stress analysis in multilayer media. *International Journal of Solids and Structures*, vol. 8, n° 11, 1972, p. 1257–1281.

[CHE 09] Chen J., Bull S.
Finite element analysis of contact induced adhesion failure in multilayer coatings with weak interfaces. *Thin Solid Films*, vol. 517, n° 13, 2009, p. 3704–3711.

[CHE 11] Chen W. W., Wang J. Q., Huan Z., Luo X.
Semi-Analytical Viscoelastic Contact Modeling of Polymer-Based Materials. *Journal of Tribology*, vol. 133, n° 4, 2011, Page 041404.

[CHO 69] Chou Y. T., Larew H. G.
Stresses and Displacements in Viscoelastic Pavement Systems Under a Moving Load. *Highway Research Record*, , 1969, Page 16.

[COO 65] Cooley J. W., Tukey J. W.
An Algorithm for the Machine Calculation of Complex Fourier Series. *Mathematics of computation*, vol. 19, 1965, p. 297–301.

[COR 13] Coran A.
Vulcanization. *The Science and Technology of Rubber*, p. 337–381 Elsevier, 2013.

[COU 85] Coulomb M.
Théorie des machines simples, en ayant égard au frottement de leurs parties. Et à la roideur des cordages. *Mémoires de mathématique et de physique*, p. 161–342 Paris, 1785.

[D'E 16] D'Errico J.
Surface Fitting using gridfit. *MATLAB Central File Exchange*, , 2016.

[DEA 02] Deacon J. A., Harvey J. T., Guada I., Popescu L., Monismith C. L.
Analytically Based Approach to Rutting Prediction. *Transportation Research Record*, vol. 1806, n° 1, 2002, p. 9–18.

[DIN 04] Dini D., Nowell D.
Flat and rounded fretting contact problems incorporating elastic layers. *International Journal of Mechanical Sciences*, vol. 46, n° 11, 2004, p. 1635–1657.

[DJA 94] Djabella H., Arnell R.
Finite element analysis of elastic stresses in multilayered systems. *Thin Solid Films*, vol. 245, n° 1-2, 1994, p. 27–33.

[DRA 01] Drakos C. A., Roque R., Birgisson B.
Effect of Measured Tire Contact Stresses on Near-Surface Rutting. *Transportation Research Record*, vol. 1764, n° 01-3243, 2001, p. 59–69.

[DUB 12] Dubois G., Cesbron J., Yin H., Anfosso-Ledee F.
Numerical evaluation of tyre/road contact pressures using a multi-asperity approach. *International Journal of Mechanical Sciences*, vol. 54, n° 1, 2012, p. 84–94.

[DUN 49] Dunlop K. E.
The history of the Dunlop rubber Co., Ltd., 1888-1939. Thèse de doctorat, University of Illinois, URBANA, ILLINOIS, 1949.

[DUV 72] Duvaut G., Lions J.-L.
Les inequations en mecanique et en physique, vol. 1. Dunod, Paris, 1972.

[ELL 71] Elliott J. F., Moavenzadeh F.
Analysis of stresses and displacements in three-layer viscoelastic systems. *Highway Research Record*, , 1971, p. 45–57.

[ELS 18] Elseifi M. A., Baek J., Dhakal N.
Review of modelling crack initiation and propagation in flexible pavements using the finite element method. *International Journal of Pavement Engineering*, vol. 19, n° 3, 2018, p. 251–263.

[FAR 72] Farrell W. E.
Deformation of the Earth by surface loads. *Reviews of Geophysics*, vol. 10, n° 3, 1972, Page 761.

[FAR 92] Faria L. O., Oden J. T., Yavari B., Tworzydlo W. W., Bass J. M., Becker E. B.
Tire Modeling by Finite Elements. *Tire Science and Technology*, vol. 20, n° 1, 1992, p. 33–56.

[FRO 27] Fromm H.
Berechnung des Schlupfes beim Rollen deformierbarer Scheiben. *ZAMM - Zeitschrift für Angewandte Mathematik und Mechanik*, vol. 7, n° 1, 1927, p. 27–58.

[FUL 11] Fulleringer B.
Semi-analytical modeling of complex mechanical contacts: Application to inclusions and wear of coated surfaces. Thèse de doctorat, INSA Lyon, Lyon, 2011.

[GAL 06] Gallego L., Nélias D., Jacq C.
A Comprehensive Method to Predict Wear and to Define the Optimum Geometry of Fretting Surfaces. *Journal of Tribology*, vol. 128, n° 3, 2006, p. 476–485.

[GAL 07a] Gallego L., Nélias D.
Modeling of Fretting Wear Under Gross Slip and Partial Slip Conditions. *Journal of Tribology*, vol. 129, n° 3, 2007, p. 528–535.

[GAL 07b] Gallego L.
Fretting et usure des contacts mecaniques : modelisation numerique. Thèse de doctorat, INSA Lyon, Lyon, 2007.

[GAL 10a] Gallego L., Fulleringer B., Deyber S., Nélias D.
Multiscale computation of fretting wear at the blade/disk interface. *Tribology International*, vol. 43, n° 4, 2010, p. 708–718.

[GAL 10b] Gallego L., Nélias D., Deyber S.
A fast and efficient contact algorithm for fretting problems applied to fretting modes I, II and III. *Wear*, vol. 268, n° 1-2, 2010, p. 208–222.

[GIL 92] Gillespie T. D., Karamihas S. M., Cebon D., Sayers M. W., Nasim M. A., Hansen W., Ehsan N.
National Cooperative Highway Research Program Transportation Research Board National Research Council. *The University of Michigan Transportation Research Institute*, , 1992, Page 266.

[GLA 08] Gladwell G. M. L., Galin L. A.
Contact problems: the legacy of L. A. Galin. N° 155 Solid mechanics and its applications Springer, Dordrecht, Netherlands, 2008. OCLC: ocn267150554.

[GOO 65] Goodman L. E., Keer L. M.
The contact stress problem for an elastic sphere indenting an elastic cavity. *International Journal of Solids and Structures*, vol. 1, n° 407, 1965.

[GOO 19] Goodyear
The Goodyear AERO-A Concept Tire for Autonomous, Flying Cars. *https://news.goodyear.eu/aero/*, , 2019.

[GOR 95] Goryacheva I., Goryachev A., Sadegi F.
Contact of elastic bodies with thin visco-elastic coatings under conditions of rolling or sliding friction. *Journal of Applied Mathematics and Mechanics*, vol. 59, n° 4, 1995, p. 607–614.

[GOR 03] Gorishnyy T. Z., Olson L. G., Oden M., Aouadi S. M., Rohde S. L.
Optimization of wear-resistant coating architectures using finite element analysis. *Journal of Vacuum Science & Technology A: Vacuum, Surfaces, and Films*, vol. 21, n° 1, 2003, p. 332–339.

[GOR 19] Goryacheva I., Miftakhova A.
Modelling of the viscoelastic layer effect in rolling contact. *Wear*, vol. 430-431, 2019, p. 256–262.

[GRE 66] Greenwood J. A., Williamson J. B. P.
Contact of nominally flat surfaces. *Proceedings of the Royal Society of London. Series A. Mathematical and Physical Sciences*, vol. 295, n° 1442, 1966, p. 300–319.

[GRE 70] Greenwood J. A., Tripp J. H.
The Contact of Two Nominally Flat Rough Surfaces. *Proceedings of the Institution of Mechanical Engineers*, vol. 185, n° 1, 1970, p. 625–633.

[HAI 63] Haines D. J., Ollerton E.
Contact Stress Distributions on Elliptical Contact Surfaces Subjected to Radial and Tangential Forces. *Proceedings of the Institution of Mechanical Engineers*, vol. 177, n° 1, 1963, p. 95–114.

[HAJ 05] Hajj E. Y., Sebaaly P. E., Weitzel D.
Fatigue Characteristics of Superpave and Hveem Mixtures. *Journal of Transportation Engineering*, vol. 131, n° 4, 2005, p. 302–310.

[HAN 18] Hankook
Hankook Tire présente de nouveaux concepts de pneumatiques futuristes lors du salon automobile Essen 2018. *https://www.hankooktire-mediacenter.com/fr/communique-de-presse/news/hankook-tire-presente-de-nouveaux-concepts-de-pneumatiques-futuristes-lors-du-salon-automobile-essen/?flt=1&tx_news_pi1%5Bcontroller%5D=News&tx_news_pi1%5Baction%5D=detail&cHash=*
, 2018.

[HAR 79] Hartnett M. J.
The Analysis of Contact Stresses in Rolling Element Bearings. *Journal of Lubrication Technology*, vol. 101, n° 1, 1979, p. 105–109.

[HAR 93] Hardy M., Cebon D.
Response of Continuous Pavements to Moving Dynamic Loads. *Journal of Engineering Mechanics*, vol. 119, n° 9, 1993, p. 1762–1780.

[HER 82] Hertz H.
Ueber die Beruhrung fester elastischer Korper. *Journal fur die reine und angewandte Mathematik*, , 1882, p. 156–171.

[HER 17] Hernandez J. A., Al-Qadi I. L.
Tire–pavement interaction modelling: hyperelastic tire and elastic pavement. *Road Materials and Pavement Design*, vol. 18, n° 5, 2017, p. 1067–1083.

[HES 80] Hestenes M. R.
Conjugate Direction Methods in Optimization. Springer New York, New York, NY, 1980.

[HOG 38] Hogg A.
Equilibrium of a thin plate, symmetrically loaded, resting on an elastic foundation of infinite depth. *The London, Edinburgh, and Dublin Philosophical Magazine and Journal of Science*, vol. 25, n° 168, 1938, p. 576–582.

[HOG 44] Hogg A.
Equilibrium of a thin slab on an elastic foundation of finite depth. *The London, Edinburgh, and Dublin Philosophical Magazine and Journal of Science*, vol. 35, n° 243, 1944, p. 265–276.

[HOP] Hopman P. C.
VEROAD: A Viscoelastic Multilayer Computer Program. *Transportation Research Record*, vol. 1539, n° 1, p. 72–80.

[HOW 86] Howell W. E., Perez S. E., Vogler W. A.
Aircraft tire Hfootprint forces. *The Tire Pavement Interface*, n° 929 ASTM Special Technical Publication, p. 110–124 American Society for Testing and Materials, 1986.

[HOW 09] Howard I. L., Warren K. A.
Finite-Element Modeling of Instrumented Flexible Pavements under Stationary Transient Loading. *Journal of Transportation Engineering*, vol. 135, n° 2, 2009, p. 53–61.

[HU 99] Hu Y.-Z., Barber G. C., Zhu D.
Numerical analysis for the elastic contact of real rough surfaces. *Tribology Transactions*, vol. 42, n° 3, 1999, p. 443–452.

[HUA 04] Huang Y. H.
Pavement analysis and design. Pearson/Prentice Hall, Upper Saddle River, NJ, 2nd edition, 2004.

[HUG 85] Hugo F., Kennedy T. W.
SURFACE CRACKING OF ASPHALT MIXTURES IN SOUTHERN AFRICA (WITH DISCUSSION). *Association of Asphalt Paving Technologists Proc*, vol. 54, 1985, p. 454–501.

[HWU 98] Hwu C., Fan C. W.
Contact Problems of Two Dissimilar Anisotropic Elastic Bodies. *Journal of Applied Mechanics*, vol. 65, n° 3, 1998, p. 580–587.

[ISH 62] Ishihara K.
The General Theory of Stresses and Displacements in Two-Layer Viscoelastic Systems. *Soils and Foundations*, vol. 2, n° 2, 1962, p. 51–68.

[JAC 01] Jacq C.
Limite d'endurance et durée de vie en fatigue de roulement du 32CrMoV13 nitruré en présence d'indentations. Thèse de doctorat, INSA Lyon, Lyon, 2001.

[JAC 02] Jacq C., Nélias D., Lormand G., Girodin D.
Development of a Three-Dimensional Semi-Analytical Elastic-Plastic Contact Code. *Journal of Tribology*, vol. 124, n° 4, 2002, p. 653–667.

[JEU 62] Jeuffroy G., Bachelez J.
Note on a Method of Analysis for Pavements. *Proc. Ann Arbor Conf.*, , 1962.

[JOH 81] Johns P. M., Gohar R.
Roller bearings under radial and eccentric loads. *Tribology International*, vol. 14, n° 3, 1981, p. 131–136.

[JOH 85] Johnson K. L.
Contact mechanics. Cambridge University Press, Cambridge [Cambridgeshire] ; New York, 1985.

[JU 96] Ju Y., Farris T. N.
Spectral Analysis of Two-Dimensional Contact Problems. *Journal of Tribology*, vol. 118, n° 2, 1996, p. 320–329.

[KAL 68a] Kalker J.
On the rolling contact of two elastic bodies in the presence of dry friction. *Wear*, vol. 11, n° 4, 1968, p. 1–303.

[KAL 68b] Kalker J. J.
The tangential force transmitted by two elastic bodies rolling over each other with pure creepage. *Wear*, vol. 2, 1968, p. 421–430.

[KAL 71] Kalker J. J., Pater A. D.
Survey of the theory of local slip in the elastic contact region with dry friction. *Soviet Applied Mechanics*, vol. 7, n° 5, 1971, p. 472–482.

[KAL 82] Kalker J. J.
A Fast Algorithm for the Simplified Theory of Rolling Contact. *Vehicle System Dynamics*, vol. 11, n° 1, 1982, p. 1–13.

[KAL 90] Kalker J. J.
Three-Dimensional Elastic Bodies in Rolling Contact, vol. 2 of *Solid Mechanics and Its Applications*. Springer Netherlands, Dordrecht, 1990.

[KAL 91] Kalker J. J.
Viscoelastic Multilayered Cylinders Rolling With Dry Friction. *Journal of Applied Mechanics*, vol. 58, n° 3, 1991, p. 666–679.

[KAR 87] Karami G., Fenner R. T.
A two-dimensional BEM method for thermo-elastic body forces contact problems. *Proc. Boundary Elements IX, Southampton (1987)*, vol. 417, 1987, p. 417–437. Publisher: Computational Mechanics Publications.

[KEN 87] Kennedy R., Padovan J.
Finite element analysis of steady and transiently moving/rolling nonlinear viscoelastic structure-II. Shell and three-dimensional simulations. *Computers & Structures*, vol. 27, n° 2, 1987, p. 259–273.

[KER 64] Kerr A. D.
Elastic and Viscoelastic Foundation Models. *Journal of Applied Mechanics*, vol. 31, n° 3, 1964, p. 491–498.

[KES 16] Kesavan D., Done V., Sridhar M., Billig R., Nélias D.
High temperature fretting wear prediction of exhaust valve material. *Tribology International*, vol. 100, 2016, p. 280–286.

[KIM 09] Kim J., Roque R., Byron T.
Viscoelastic Analysis of Flexible Pavements and Its Effects on Top-Down Cracking. *Journal of Materials in Civil Engineering*, vol. 21, n° 7, 2009, p. 324–332.

[KOM 88] Komvopoulos K.
Finite Element Analysis of a Layered Elastic Solid in Normal Contact With a Rigid Surface. *Journal of Tribology*, vol. 110, n° 3, 1988, p. 477–485.

[KOT 12] Kot M.
Contact mechanics of coating-substrate systems: Monolayer and multilayer coatings. *Archives of Civil and Mechanical Engineering*, vol. 12, n° 4, 2012, p. 464–470.

[KOU 14a] Koumi K. E., Nélias D., Chaise T., Duval A.
Modeling of the contact between a rigid indenter and a heterogeneous viscoelastic material. *Mechanics of Materials*, vol. 77, 2014, p. 28–42.

[KOU 14b] Koumi K. E., Zhao L., Leroux J., Chaise T., Nélias D.
Contact analysis in the presence of an ellipsoidal inhomogeneity within a half space. *International Journal of Solids and Structures*, , 2014, Page 14.

[KOU 15a] Koumi K. E.
Modélisation du contact entre matériaux hétérogène: Application au contact Aube/Disque. Thèse de doctorat, INSA Lyon, lyon, 2015.

[KOU 15b] Koumi K. E., Chaise T., Nélias D.
Rolling contact of a rigid sphere/sliding of a spherical indenter upon a viscoelastic half-space containing an ellipsoidal inhomogeneity. *Journal of the Mechanics and Physics of Solids*, vol. 80, 2015, p. 1–25.

[KUO 69] Kuo J. T.
Static response of a multilayered medium under inclined surface loads. *Journal of Geophysical Research*, vol. 74, n° 12, 1969, p. 3195–3207.

[KUS 17] Kusche S.
Frictional force between a rotationally symmetric indenter and a viscoelastic half-space: Elastomer friction. *ZAMM - Journal of Applied Mathematics and Mechanics / Zeitschrift für Angewandte Mathematik und Mechanik*, vol. 97, n° 2, 2017, p. 226–239.

[LAC 00] de Lacerda L. A., Wrobel L. C.
Frictional contact analysis of coated axisymmetric bodies using the boundary element method. *The Journal of Strain Analysis for Engineering Design*, vol. 35, n° 5, 2000, p. 423–440.

[LCP 10] LCPC
. « Manuel d'utilisation du logiciel ALIZE-LCPC version 1.3 », 2010.

[LEE 60] Lee E. H., Radok J. R. M.
The Contact Problem for Viscoelastic Bodies. *Journal of Applied Mechanics*, vol. 27, n° 3, 1960, p. 438–444.

[LER 13] Leroux J.
Modélisation numérique du contact pour matériaux composites. Thèse de doctorat, INSA Lyon, Lyon, 2013.

[LI 06] Li X., Wang M.
Hertzian Contact of Anisotropic Piezoelectric Bodies. *Journal of Elasticity*, vol. 84, n° 2, 2006, p. 153–166.

[LI 16] Li S., Guo Z., Yang Y.
Dynamic viscoelastic response of an instrumented asphalt pavement under various axles with non-uniform stress distribution. *Road Materials and Pavement Design*, vol. 17, n° 2, 2016, p. 446–465.

[LIA 10] Liao J., Sargand S.
Viscoelastic FE Modeling and Verification of a U.S. 30 Perpetual Pavement Test Section. *Road Materials and Pavement Design*, vol. 11, n° 4, 2010, p. 993–1008.

[LIU 00] Liu S., Wang Q., Liu G.
A versatile method of discrete convolution and FFT (DC-FFT) for contact analyses. *Wear*, vol. 243, n° 1-2, 2000, p. 101–111.

[LIU 02] Liu S., Wang Q.
Studying Contact Stress Fields Caused by Surface Tractions With a Discrete Convolution and Fast Fourier Transform Algorithm. *Journal of Tribology*, vol. 124, n° 1, 2002, p. 36–45.

[LIU 05] Liu S., Wang Q.
Elastic Fields due to Eigenstrains in a Half-Space. *Journal of Applied Mechanics*, vol. 72, n° 6, 2005, p. 871–878.

[LOV 52] Love A. E. H.
A treatise on the mathematical theory of elasticity. Cambridge University Press, 4 edition, 1952.

[LOY 15] Loy R. J., de Hoog F. R., Anderssen R. S.
Interconversion of Prony series for relaxation and creep. *Journal of Rheology*, vol. 59, n° 5, 2015, p. 1261–1270.

[LUB 91] Lubrecht A. A., Ioannides E.
A Fast Solution of the Dry Contact Problem and the Associated Sub-Surface Stress Field, Using Multilevel Techniques. *Journal of Tribology*, vol. 113, n° 1, 1991, p. 128–133.

[MAL 69] Malvern L. E.
Introduction to the mechanics of a continuous medium. Prentice-Hall series in engineering of the physical sciences Prentice-Hall, Englewood Cliffs, N.J, 1969.

[MAN 93a] Man K., Aliabadi M., Rooke D.
Bem frictional contact analysis: Load incremental technique. *Computers & Structures*, vol. 47, n° 6, 1993, p. 893–905.

[MAN 93b] Man K., Aliabadi M., Rooke D.
BEM frictional contact analysis: Modelling considerations. *Engineering Analysis with Boundary Elements*, vol. 11, n° 1, 1993, p. 77–85.

[MAN 19a] Manyo E. Y., Reynaud P., Picoux B., Tautou R., Nélias D., Allou F., Petit C.
Towards fast modelling of the tire-pavement contact. *European Journal of Environmental and Civil Engineering*, , 2019, p. 1–17.

[MAN 19b] Manyo Y. E.
Modélisation avancée du contact pneu-chaussée pour l'étude des dégradations des chaussées en surface. Thèse de doctorat, Universite de Limoges, 2019.

[MAN 21] Manyo E. Y., Picoux B., Reynaud P., Tautou R., Nélias D., Allou F., Petit C.
Approach of Pavement Surface Layer Degradation Caused by Tire Contact Using Semi-Analytical Model. *Materials*, vol. 14, n° 9, 2021, Page 14.

[MAR 86] Marshek K. M., Chen H. H., Connell R. B., Hudson W. R.
Experimental Determination of Pressure Distribution of Truck Tire-Pavement Contact. *Transportation Research Record*, vol. 1070, 1986, p. 9–14.

[MEN 14] Menga N., Putignano C., Carbone G., Demelio G. P.
The sliding contact of a rigid wavy surface with a viscoelastic half-space. *Proceedings of the Royal Society A: Mathematical, Physical and Engineering Sciences*, vol. 470, n° 2169, 2014, Page 20140392.

[MEN 16] Menga N., Afferrante L., Carbone G.
Effect of thickness and boundary conditions on the behavior of viscoelastic layers

in sliding contact with wavy profiles. *Journal of the Mechanics and Physics of Solids*, vol. 95, 2016, p. 517–529.

[MEN 21] Menga N., Carbone G., Dini D.
Exploring the effect of geometric coupling on friction and energy dissipation in rough contacts of elastic and viscoelastic coatings. *Journal of the Mechanics and Physics of Solids*, vol. 148, 2021, Page 104273.

[MIC 19] Michelin
MICHELIN et GM font rouler des voitures sur des pneus... sans air. *https://michelinmedia.com/michelin-uptis/*, , 2019.

[MIF 18] Miftakhova A. R.
Contact Problems for Rolling with Slip for Viscoelastic Solids. *Journal of Friction and Wear*, vol. 39, n° 1, 2018, p. 55–61.

[MIN 49] Mindlin R. D.
Compliance of Elastic Bodies in Contact. *Journal of Applied Mechanics*, vol. 16, n° 3, 1949, p. 259–268.

[MIN 53] Mindlin R. D., Deresiewicz H.
Elastic Spheres in Contact Under Varying Oblique Forces. *Journal of Applied Mechanics*, vol. 30, n° 3, 1953, p. 327–344.

[MON 94] Monismith C., Hicks R., Finn F., Sousa J., Harvey J., Weissman S., Deacon J., Coplantz J., G. Paulsen G.
Permanent deformation response of asphalt aggregate mixes. N° 415 Strategic Highway Research Program, SHRP-A Washington, DC, 1994. OCLC: 247456899.

[MUL 07] Mulungye R. M., Owende P. M. O., Mellon K.
Finite element modelling of flexible pavements on soft soil subgrades. *Materials and Design*, vol. 28, 2007, p. 739–756.

[MYE 99] Myers L. A., Roque R., Ruth B. E., Drakos C.
Measurement of Contact Stresses for Different Truck Tire Types To Evaluate Their Influence on Near-Surface Cracking and Rutting. *Transportation Research Record: Journal of the Transportation Research Board*, vol. 1655, n° 1, 1999, p. 175–184.

[NAC 04] Nackenhorst U.
The ALE-formulation of bodies in rolling contact. *Computer Methods in Applied Mechanics and Engineering*, vol. 193, n° 39-41, 2004, p. 4299–4322.

[NAG 08] Nagatani H., Imou A.
Contact Pressure and Shear Stress Analysis on Conforming Contact Problem. *Journal of Advanced Mechanical Design, Systems, and Manufacturing*, vol. 2, n° 6, 2008, p. 1055–1066.

[NAK 87] Nakajima Y., Padovan J.
Finite element analysis of steady and transiently moving/rolling nonlinear viscoelastic structure III. Impact/contact simulations. *Computers & Structures*, vol. 27, n° 2, 1987, p. 275–286.

[NÉL 06] Nélias D., Boucly V., Brunet M.
Elastic-Plastic Contact Between Rough Surfaces: Proposal for a Wear or Running-In Model. *Journal of Tribology*, vol. 128, n° 2, 2006, p. 236–244.

[NGU 20] Nguyen V. T., Hwu C.
Time-stepping method for frictional contact of anisotropic viscoelastic solids. *International Journal of Mechanical Sciences*, vol. 184, 2020, Page 105836.

[noa02] *Recommended performance-related specification for hot-mix asphalt construction: results of the WesTrack Project*. N° 455 NCHRP report Transportation Research Board, Washington, D.C, national cooperative highway research program edition, 2002. OCLC: ocm51299172.

[NOG 97] Nogi T., Kato T.
Influence of a Hard Surface Layer on the Limit of Elastic Contact-Part I: Analysis Using a Real Surface Model. *Journal of Tribology*, vol. 119, n° 3, 1997, p. 493–500.

[NOW 88] Nowell D., Hills D.
Tractive rolling of dissimilar elastic cylinders. *International Journal of Mechanical Sciences*, vol. 30, n° 6, 1988, p. 427–439.

[NOW 98] Nowell D., Dai D. N.
Analysis of Surface Tractions in Complex Fretting Fatigue Cycles Using Quadratic Programming. *Journal of Tribology*, vol. 120, n° 4, 1998, p. 744–749.

[ODE 84] Oden J. T., Martins J. A. C.
Models and computational methods for dynamic friction phenomena. *Computer Methods in Applied Mechanics and Engineering*, vol. 52, 1984, p. 527–634.

[ODE 86] Oden J. T., Lin T. L.
On the general rolling contact problem for finite deformations of a viscoelastic cylinder. *Computer Methods in Applied Mechanics and Engineering*, vol. 57, 1986, p. 297–367.

[OMA 21] Omairey E. L.
An equation-based multiphysics modelling framework for oxidative ageing of asphalt pavements. *Journal of Cleaner Production*, vol. 280, n° 124401, 2021, p. 1–19.

[O'S 88] O'Sullivan T. C., King R. B.
Sliding contact stress field due to a spherical indenter on a layered elastic half-space. *Journal of Tribology*, vol. 110, n° 2, 1988, p. 235–240.

[OUB 21] Oubahdou Y., Wallace E. R., Reynaud P., Picoux B., Dopeux J., Petit C., Nélias D.
Effect of the tire - Pavement contact at the surface layer when the tire is tilted in bend. *Construction and Building Materials*, vol. 305, 2021, Page 124765.

[PAD 87] Padovan J.
Finite element analysis of steady and transiently moving/rolling nonlinear viscoelastic structure-I. Theory. *Computers & Structures*, vol. 27, n° 2, 1987, p. 249–257.

[PAN 75] Panagiotopoulos P. D.
A nonlinear programming approach to the unilateral contact-, and friction-boundary value problem in the theory of elasticity. *Ingenieur-Archiv*, vol. 44, n° 6, 1975, p. 421–432.

[PAN 95] Pan G., Atluri S. N.
Dynamic response of finite sized elastic runways subjected to moving loads: A coupled BEM/FEM approach. *International Journal for Numerical Methods in Engineering*, vol. 38, n° 18, 1995, p. 3143–3166.

[PAP 96] Papagiannakis A. T., Amoah N., Taha R.
Formulation for Viscoelastic Response of Pavements under Moving Dynamic Loads. *Journal of Transportation Engineering*, vol. 122, n° 2, 1996, p. 140–145.

[PAR 85] Paris F., Garrido J. A.
On the Use of Discontinuous Elements in 2D Contact Problems. Boundary Elements VII. *Computational Mechanics Publications*, , 1985.

[PAU 81] Paul B., Hashemi J.
Contact Pressures on Closely Conforming Elastic Bodies. *Journal of Applied Mechanics*, vol. 48, n° 3, 1981, p. 543–548.

[PEL 74] Peltier W. R.
The impulse response of a Maxwell Earth. *Reviews of Geophysics*, vol. 12, n° 4, 1974, Page 649.

[PET 02] Petitjean J., Fabre C., Balay J. M.
A380 Flexible pavement experimental program. *Proceedings he 6th international conference on the bearing capacity of roads in airfields*, vol. 1, Lisbon, Portugal, 2002 p. 241–251.

[PET 09] Petit C., Diakhate M., Millien A., Phelipot-Mardele A., Pouteau B.
Pavement Design for Curved Road Sections: Fatigue Performance of Interfaces and Longitudinal Top-down Cracking in Multilayered Pavements. *Road Materials and Pavement Design*, vol. 10, n° 3, 2009, p. 609–624.

[PIC 09] Picoux B., Ayadi A. E., Petit C.
Dynamic response of a flexible pavement submitted by impulsive loading. *Soil dynamics and earthquake engineering*, vol. 29, n° 5, 2009, p. 845–854.

[PIS 61] Pister K. S.
Viscoelastic Plate on a Viscoelastic Foundation. *Journal of the Engineering Mechanics Division*, vol. 87, n° 1, 1961.

[PLU 98] Plumet S., Dubourg M.-C.
A 3-D Model for a Multilayered Body Loaded Normally and Tangentially Against a Rigid Body: Application to Specific Coatings. *Journal of Tribology*, vol. 120, n° 4, 1998, p. 668–676.

[POL 99] Polonsky I., Keer L.
A numerical method for solving rough contact problems based on the multi-level multi-summation and conjugate gradient techniques. *Wear*, vol. 231, n° 2, 1999, p. 206–219.

[POL 00] Polonsky I. A., Keer L. M.
A Fast and Accurate Method for Numerical Analysis of Elastic Layered Contacts. *Journal of Tribology*, vol. 122, n° 1, 2000, p. 30–35.

[POR 50] Porter O. J.
Development of the Original Method for highway Design: Symposium on Development of CBR Flexible Pavement Design Method for Airfields. *ASCE*, , 1950, p. 461–467.

[PRE 92] Press W. H., Teukolsky S. A., Vetterling W. T., Flannery B. P.
Numerical recipes in Fortran 77 - The art of scientific computing. *Cambridge unversity press*, vol. 1, 1992.

[PUT 14] Putignano C., Carbone G.
A review of boundary elements methodologies for elastic and viscoelastic rough contact mechanics. *Physical Mesomechanics*, vol. 17, n° 4, 2014, p. 321–333.

[PUT 15] Putignano C., Carbone G., Dini D.
Mechanics of rough contacts in elastic and viscoelastic thin layers. *International Journal of Solids and Structures*, vol. 69-70, 2015, p. 507–517.

[PUT 16] Putignano C., Carbone G., Dini D.
Theory of reciprocating contact for viscoelastic solids. *Physical Review E*, vol. 93, n° 4, 2016, Page 043003.

[PUT 18] Putignano C., Carbone G.
Viscoelastic reciprocating contacts in presence of finite rough interfaces: A numerical investigation. *Journal of the Mechanics and Physics of Solids*, vol. 114, 2018, p. 185–193.

[RAD 19] Radionov A. A., Kravchenko O. A., Guzeev V. I., Rozhdestvenskiy Y. V., Eds. *Proceedings of the 4th International Conference on Industrial Engineering: ICIE 2018*. Lecture Notes in Mechanical Engineering Springer International Publishing, Cham, 2019.

[REY 17] Reynaud P., Nasr S. B., Allou F., Chaise T., Nélias D., Petit C.
3D modelling of tyre-pavement contact pressure. *European Journal of Environmental and Civil Engineering*, vol. 21, n° 6, 2017, p. 712–729.

[ROD 10] Rodríguez-Tembleque L., Abascal R., Aliabadi M.
A boundary element formulation for wear modeling on 3D contact and rolling-contact problems. *International Journal of Solids and Structures*, vol. 47, n° 18-19, 2010, p. 2600–2612.

[SCA 17] Scaraggi M., Comingio D.
Rough contact mechanics for viscoelastic graded materials: The role of small-scale wavelengths on rubber friction. *International Journal of Solids and Structures*, vol. 125, 2017, p. 276–296.

[SET 94] SETRA-LCPC
Guide technique de Conception et Dimensionnement des Structures de Chaussees. december 1994.

[SET 98] SETRA-LCPC
Catalogue des structures types de chaussees neuves. N° 1151-1516 Guide technique / Laboratoire central des ponts et chaussees Laboratoire Central des Ponts et Chaussees, Service d'Etudes Techniques des Routes et Autoroutes, 1998.

[SET 03] SETRA
Guide technique - Construction des chaussees neuve sur le reseau routier national. Service d'etude technique des routes et autoroutes, march 2003.

[SHE 98] Shell
. ≪ Bisar 3.0 user manuel ≫, 1998.

[SHE 07a] Shen S., Carpenter S.
Development of an asphalt fatigue model based on energy principles. vol. 76 Asphalt Paving Technology AAPT-Proceedings, march 2007, p. 525–573.

[SHE 07b] Shen W., Kirkner D. J.
Non-linear Finite-Element Analysis to Predict Permanent Deformations in Pavement Structures Under Mo. *International Journal of Pavement Engineering*, vol. 2, n° 3, 2007, p. 187–199.

[SIM 19] Simulia D. S.
. « Abaqus », 2019.

[SIN 69] Singleton R.
An algorithm for computing the mixed radix fast Fourier transform. *Transactions on Audio and Electroacoustics*, vol. 17, n° 2, 1969, p. 93–103.

[SNE 51] Sneddon I. N.
Fourier Transforms. International series in pure and applied mathematics McGraw-hill Book Company, Inc., New York, 1951.

[SOO 04] Soon S.-C., Drescher A., Stolarski H. K.
Tire-Induced Surface Stresses in Flexible Pavements. *Transportation Research Record: Journal of the Transportation Research Board*, vol. 1896, n° 1, 2004, p. 170–176.

[SOU 05] Sousa J. B., Pais J. C., Way G. B.
A Mechanistic-Empirical Based Overlay Design Method for Reflective Cracking. *Road Materials and Pavement Design*, vol. 6, n° 3, 2005, p. 339–363.

[SPE 75] Spence D. A.
The hertz contact problem with finite friction. *Journal of Elasticity*, vol. 5, n° 3-4, 1975, p. 297–319.

[SPI 15] Spinu S., Frunza G.
The Hysteretic Behaviour of Partial Slip Elastic Contacts Undergoing a Fretting Loop. *Journal of Physics: Conference Series*, vol. 585, 2015, Page 012007.

[SPI 16] Spinu S., Cerlinca D.
A numerical solution to the cattaneo-mindlin problem for viscoelastic materials. *IOP Conference Series: Materials Science and Engineering*, vol. 145, 2016, Page 042033.

[SPI 17a] Spinu S., Cerlinca D.
Numerical simulations of rough contacts between viscoelastic materials. *IOP Conference Series: Materials Science and Engineering*, vol. 227, 2017, Page 012120.

[SPI 17b] Spinu S., Cerlinca D.
Modelling of Rough Contact between Linear Viscoelastic Materials. *Modelling and Simulation in Engineering*, vol. 2017, 2017, p. 1–11.

[SPI 18a] Spinu S.
Numerical Analysis of Elastic Contact between Coated Bodies. *Advances in Tribology*, vol. 2018, 2018, p. 1–13.

[SPI 18b] Spinu S.
Viscoelastic Contact Simulation under Harmonic Cyclic Load. *Advances in Tribology*, vol. 2018, 2018, p. 1–16.

[SPI 20] Spinu S., Cerlinca D.
The Fretting Contact of Coated Bodies. Part I – Contact Parameters. *IOP Conference Series: Materials Science and Engineering*, vol. 724, 2020, Page 012026.

[STE 15] Stepanov F. I.
Sliding of two smooth indenters on a viscoelastic foundation in the presence of friction. vol. 56, n° 6, 2015.

[STE 16] Stepanov F. I., Torskaya E. V.
Study of stress state of viscoelastic half-space in sliding contact with smooth indenter. *Journal of Friction and Wear*, vol. 37, n° 2, 2016, p. 101–106.

[STE 18] Stepanov F. I., Torskaya E. V.
Modeling of Sliding of a Smooth Indenter over a Viscoelastic Layer Coupled with a Rigid Base. *Mechanics of Solids*, vol. 53, n° 1, 2018, p. 60–67.

[STO 91] Stolle D.
Modelling of dynamic response of pavements to impact loading. *Computers and Geotechnics*, vol. 11, n° 1, 1991, p. 83–94.

[SUN 13] Sun L., Duan Y.
Dynamic response of top-down cracked asphalt concrete pavement under a half-sinusoidal impact load. *Acta Mechanica*, vol. 224, n° 8, 2013, p. 1865–1877.

[TAH 18] Taherkhani H., Jalali M.
Viscoelastic Analysis of Geogrid-Reinforced Asphaltic Pavement under Different Tire Configurations. *International Journal of Geomechanics*, vol. 18, n° 7, 2018, Page 04018060.

[TER 87] Terzopoulost D., Platt J., Barr A., Fleischert K.
Elastically Deformable Models. *Computer Graphics*, vol. 21, n° 4, 1987, p. 205–214.

[TER 88] Terzopoulos D., Fleiseher K.
Modeling Inelastic Deformation: Viscoelasticity, Plasticity, Fracture. *Computer Graphics*, vol. 22, n° 44, 1988, p. 269–278.

[THE 96] Theyse H. L., Beer M. D., Rust F. C.
Overview of South African Mechanistic Pavement Design Method. *Transportation Research Record*, , 1996, Page 12.

[TIE 87] Tielking J., Roberts F.
Tire Contact Pressure and Its Effect on Pavement Strain. *Journal of Transportation Engineering*, vol. 113, n° 1, 1987, Page 16.

[TIE 94] Tielking J. T., Abraham M. A.
Measurement of Truck Tire Footprint Pressures. *Transportation Research Record*, , n° 1435, 1994, p. 92–99.

[TOR 19] Torskaya E. V., Stepanov F. I.
Effect of Surface Layers in Sliding Contact of Viscoelastic Solids 3-D Model of Material. *Frontiers in Mechanical Engineering*, vol. 5, 2019, Page 26.

[TRA 04] Tran Q. D., Chabot A., Ehrlacher A., Tamagny P.
A simplified modelling for cracking in pavements. Limoges, France, may 2004 Page 9.

[UDD 04] Uddin W., Garza S.
3D-FE Modeling and Simulation of Airfield Pavements Subjected to FWD Impact Load Pulse and Wheel Loads. *Airfield Pavements*, Las Vegas, Nevada, United States, february 2004 American Society of Civil Engineers, p. 304–315.

[VER 64] Vermeulen P. J., Johnson K. L.
Contact of Nonspherical Elastic Bodies Transmitting Tangential Forces. *Journal of Applied Mechanics*, vol. 31, n° 2, 1964, p. 338–340.

[VER 85] Vergne F.
Calcul des déplacements et des contraintes dans un demi-espace élastique chargé en surface par des actions distribuées normales ou tangentielles quelconques. Rapport de DEA, INSA Lyon, Lyon, 1985.

[VES 69] Vesic A. S., Saxena S. K.
Analysis of Structural Behavior of Road Test Rigid Pavements. *Highway Research Record*, , n° 291, 1969, p. 165–158.

[WAL 20] Wallace E. R., Chaise T., Nélias D.
Three-dimensional rolling/sliding contact on a viscoelastic layered half-space. *Journal of the Mechanics and Physics of Solids*, vol. 143, 2020, Page 104067.

[WAN 03] Wang L. B., Myers L. A., Mohammad L. N., Fu Y. R.
Micromechanics Study on Top-Down Cracking. *Transportation Research Record: Journal of the Transportation Research Board*, vol. 1853, n° 1, 2003, p. 121–133.

[WAN 10] Wang Z.-J., Wang W.-Z., Wang H., Zhu D., Hu Y.-Z.
Partial Slip Contact Analysis on Three-Dimensional Elastic Layered Half Space. *Journal of Tribology*, vol. 132, n° 2, 2010, Page 021403.

[WAN 11a] Wang H., Al-Qadi I. L., Stanciulescu I.
Simulation of tyre–pavement interaction for predicting contact stresses at static and various rolling conditions. *International Journal of Pavement Engineering*, , 2011, Page 13.

[WAN 11b] Wang Z.-j., Wang W.-z., Meng F.-m., Wang J.-x.
Fretting Contact Analysis on Three-Dimensional Elastic Layered Half Space. *Journal of Tribology*, vol. 133, n° 3, 2011, Page 031401.

[WAN 12] Wang Z., Jin X., Keer L. M., Wang Q.
A Numerical Approach for Analyzing Three-Dimensional Steady-State Rolling Contact Including Creep Using a Fast Semi-Analytical Method. *Tribology Transactions*, vol. 55, n° 4, 2012, p. 446–457.

[WAN 15] Wang Z., Yu C., Wang Q.
An efficient method for solving three-dimensional fretting contact problems involving multilayered or functionally graded materials. *International Journal of Solids and Structures*, vol. 66, 2015, p. 46–61.

[WES 26a] Westergaard H. M.
Analysis of stresses in concrete pavements due to variations of temperature. *Highway Research Record*, vol. 6, 1926, p. 201–215.

[WES 26b] Westergaard H. M.
Stresses in concrete pavements computed by theoretical analysis. *Public Roads*, vol. 7, 1926, p. 25–35.

[WES 27] Westergaard H. M.
Theory of concrete pavement design. *Highway Research Record*, , 1927, p. 175–181.

[WES 67] Westmann R. A.
Viscoelastic Layered System Subjected to Moving Loads. *Journal of the Engineering Mechanics Division*, vol. 93, n° 3, 1967.

[WIL 66] Willis J.
Hertzian contact of anisotropic bodies. *Journal of the Mechanics and Physics of Solids*, vol. 14, n° 3, 1966, p. 163–176.

[WOL 16] Wollny I., Behnke R., Villaret K., Kaliske M.
Numerical modelling of tyre-pavement interaction phenomena: coupled structural investigations. *Road Materials and Pavement Design*, vol. 17, n° 3, 2016, p. 563–578.

[WRO 02] Wrobel L. C., Aliabadi M. H., Eds. *The boundary element method*. J. Wiley, Chichester ; New York, 2002.

[XI 21] Xi Y., Björling M., Almqvist A.
A Numerical Model for Solving Three-Dimensional Rolling Contact Problems with Elastic Coating Layers. *Tribology Letters*, vol. 69, n° 4, 2021, Page 139.

[XU 20] Xu J., Wang K., Liang X., Gao Y., Liu Z., Chen R., Wang P., Xu F., Wei K.
Influence of viscoelastic mechanical properties of rail pads on wheel and corrugated rail rolling contact at high speeds. *Tribology International*, vol. 151, 2020, Page 106523.

[YOO 08] Yoo P. J., Al-Qadi I.
The Truth and Myth of Fatigue Cracking Potential in Hot-Mix Asphalt: Numerical Analysis and Validation. *Association of Asphalt Paving Technologists Procedings*, , 2008, Page 35.

[YU 91] Yu H. Y., Sanday S. C.
Elastic fields in joined half-spaces due to nuclei of strain. *Proceedings of the Royal Society of London. Series A: Mathematical and Physical Sciences*, vol. 434, n° 1892, 1991, p. 503–519.

[YU 14] Yu C., Wang Z., Wang Q. J.
Analytical frequency response functions for contact of multilayered materials. *Mechanics of Materials*, vol. 76, 2014, p. 102–120.

[ZAA 09] Zaazaa K. E., Schwab A. L.
Review of Joost Kalker's Wheel-Rail Contact Theories and Their Implementation in Multibody Codes. *Volume 4: 7th International Conference on Multibody Systems, Nonlinear Dynamics, and Control, Parts A, B and C*, San Diego, California, USA, january 2009 ASMEDC, p. 1889–1900.

[ZAG 93] Zaghloul S., White T.
Use of a Three-Dimensional, Dynamic Finite Element Program for Analysis of flexible pavement. *Transportation Research Record*, vol. 1388, 1993, p. 60–69.

[ZHA 15] Zhao X., Li Z.
A three-dimensional finite element solution of frictional wheel–rail rolling contact in elasto-plasticity. *Proceedings of the Institution of Mechanical Engineers, Part J: Journal of Engineering Tribology*, vol. 229, n° 1, 2015, p. 86–100.

[ZHA 20] Zhang X., Wang Q. J., He T.
Transient and steady-state viscoelastic contact responses of layer-substrate systems with interfacial imperfections. *Journal of the Mechanics and Physics of Solids*, vol. 145, 2020, Page 104170.

[ZIE 08] Ziefle M., Nackenhorst U.
Numerical techniques for rolling rubber wheels: treatment of inelastic material properties and frictional contact. *Computational Mechanics*, vol. 42, n° 3, 2008, p. 337–356.

FOLIO ADMINISTRATIF

THÈSE SOUTENUE DEVANT L'INSTITUT NATIONAL DES SCIENCES APPLIQUÉES DE LYON

NOM: WALLACE DATE de SOUTENANCE: xx/02/2022

Prénoms: Efoé Rodrigue

TITRE: On the rolling contact between multi-layered bodies, application to tire-pavement modelling

NATURE: Doctorat Numéro d'ordre: xxxxxxxx

École doctorale: 162 MEGA

Spécialité: Mécanique - Génie Mécanique - Génie Civil

Cote B.I.U. - Lyon : T 50/210/19 / et bis CLASSE:

RÉSUMÉ:

The purpose of this thesis has been the development of a dimensioning tool for pavement design. In order to better understand their surface degradations (mainly rutting and cracking), a modelling study is carried out.
This modelling task has been performed with contact mechanics tools. Particularly, a semi-analytical model has been developed, based on Fast Fourier Transform (FFT) and Conjugate Gradient Method (CGM) algorithms. With view to achieve a more realistic modelling of the tire-pavement contact, the focus has been put on three aspects of the contact problem. Firstly, the multi-layered aspect of the pavement has been considered. Using the Papkovich-Neuber potentials, the influence coefficients have been found in the Fourier frequency domain. A numerical inversion using FFT algorithms has allowed to find the influence coefficients in the space domain.
Secondly, the viscoelastic behaviour of asphaltic materials, used in roads construction, has been accounted. To this aim, an Elastic/Viscoelastic correspondence has been proposed. This correspondence imposes to recalculate the influence coefficients at every time step. These additional calculations imply an increase of the computation time; however, the simulations remain straight and fast. In addition, the proposed correspondence is exact in some cases (especially in steady-state regime); and it is an approximation in the other cases where the committed error has been shown to be marginal.
Thirdly, the effects of the tangential overall forces have been integrated to the rolling contact. The goal is that the present tool can be able to simulate acceleration, braking, turnaround, etc. cases where tangential forces and/or moment are applied on the wheel in addition to the normal force (which is generally the weight of the car or truck). This tractive rolling contact has been solved between elastically dissimilar bodies submitted not only to tangential forces but also to a spinning moment.
All these aspects, introduced together in the model, have allowed to perform various parametric analyses for a better grasp of their influence on general contacts. Furthermore, an application of the developed model has allowed to simulate realistic cases of rolling contact between the tire and the pavement. From examples such as acceleration, turnaround and drift, it has been proven that the tangential forces increase significantly the overall stresses.

MOTS-CLÉS: Road pavement, contact modelling, tractive rolling contact, coating, multi-layered bodies, viscoelasticity, fretting contact, tire-pavement contact.

Laboratoire(s) de recherche: Laboratoire de Mécanique des Contacts et des Structures
UMR CNRS 5259 - INSA de Lyon
20 Avenue Albert Einstein
69621 Villeurbanne Cedex FRANCE

Directeur de thèse: Monsieur le Professeur Daniel NELIAS

Président du jury: xxxx

Composition du jury: David HILLS Giuseppe CARBONE
Antoine CHATEAUMINOIS Anne MILLIEN
Thibaut CHAISE Daniel NELIAS